UNIVERSITÉ DE MONTRÉAL

DEVELOPMENT OF POLYMER NANOCOMPOSITE FILMS AND THEIR POTENTIAL FOR PHOTOVOLTAIC CELL APPLICATIONS

AHMAD ZOHRE VAND

DÉPARTEMENT DE GÉNIE CHIMIQUE

ÉCOLE POLYTECHNIQUE DE MONTRÉAL

THÈSE PRÉSENTÉE EN VUE DE L'OBTENTION

DU DIPLÔME DE PHILOSOPHIAE DOCTOR

(GÉNIE CHIMIQUE)

FÉVRIER 2014

UNIVERSITÉ DE MONTRÉAL

ÉCOLE POLYTECHNIQUE DE MONTRÉAL

Cette thèse intitulée:

DEVELOPMENT OF POLYMER NANOCOMPOSITE FILMS AND THEIR POTENTIAL FOR PHOTOVOLTAIC CELL APPLICATIONS

présentée par : ZOHRE VAND Ahmad

en vue de l'obtention du diplôme de : Philosophiae Doctor

a été dûment acceptée par le jury d'examen constitué de :

M. CARREAU Pierre, Ph. D., président

M. AJJI Abdellah, Ph. D., membre et directeur de recherche

M. MIGHRI Frej, Ph. D., membre et codirecteur de recherche

Mme HEUZEY Marie-Claude, Ph. D., membre

Mme KONTOPOULOU Marianna, Ph. D., membre

DEDICATION

To my beloved family

ACKNOWLEDGMENTS

I would like to express my deep gratitude to my advisors *Professor Abdellah Ajji* and *Professor Frej Mighri* for giving me the opportunity of PhD studies under their supervision, and the trust they placed in me. Success of this project was impossible without their extensive supports, encouragements, knowledge, and experiences.

A sincere appreciation goes to *Professor Pierre J. Carreau*, *Professor Marie-Claude Heuzey*, and all the student members of the *Rheology Group* who have organized the group meetings and generously shared their knowledge and experiences with me during the productive discussions.

I would like to thank all the technical and administrative staffs of *Chemical Engineering Department of Ecole Polytechnique de Montreal*, *CREPEC*, and *3SPack*. Specially, I acknowledge *Ms. Mélina Hamdine*, *Ms. Claire Cerclé*, *Mr. Guillaume Lessard*, and *Dr. Babak Esmaeili* for their kind cooperation during my works in different labs.

I am also thankful to *Professor Eric David*, *Mr. Cyril Daran-Daneau,* and *Mr. Bouchaib Zazoum* from CREPEC in ÈTS Montreal for their help in electrical conductivity measurements.

Many thanks to *Ms. Sylvie St-Amour* and *Ms. Sylvie Sauriol* from FPInnovations (Pointe-Claire, Canada) for their help in MIP measurements.

My sincere thanks to *Professor Oumarou Savadogo*, *Mr. Ali Seifitokaldani*, and *Mr. Mohammad Shahrestani* from LANOMAT for their help in photo-electrochemical measurements.

I would like to thank *Ms. Marie Matet* for her kind help in translating abstract of this thesis from English to French.

I would like to thank all my professors in Amirkabir University of Technology (Polytechnic of Tehran) and Ecole Polytechnique de Montreal who have taught me from basic to advanced levels.

I would like to convey my heartfelt thanks to all my friends and colleagues who have supported and helped me during my PhD studies particularly *Mr. Ali Seifitokaldani*, *Mr. Nima Khadem Mohtaram*, *Mr. Shahir Karami*, *Mr. Ali Khadem Mohtaram*, *Mrs. Hadis Yarahmadi*, and *Mr. Omid Ebrahimpour*.

Definitely, my accomplishments in my studies would not have been possible without unconditional love and support of my beloved family and my lovely wife. My deepest gratitude

goes to my beloved parents, *Zahra & Reza*, my sisters & brother, and my lovely wife, friend, and classmate, *Maryam*.

RÉSUMÉ

La forte demande en énergie due à la croissance continue de la population, au développement industriel rapide, à l'épuisement des ressources conventionnelles d'énergie, et à leurs impacts sur l'environnement nécessite de trouver les nouvelles sources d'énergie. En attendant, le développement de dispositifs rentables et efficaces afin de produire des énergies bon marché, renouvelables et propres est un sujet intéressant qui a retenu l'attention à la fois de la recherche industrielle et de la recherche académique. L'énergie solaire est une des sources d'énergie renouvelable la plus disponible et qui peut être convertie en électricité par l'intermédiaire des cellules solaires. Parmi les différents types de cellules solaires, les cellules solaires à pigments photosensibles (DSSC de l'anglais dye-sensitized solar cell), qui sont des matériels à bas coût, ont un grand potentiel pour produire de l'électricité solaire rentable.

L'objectif de ce travail est de développer une photoélectrode flexible pour DSSC via un procédé rentable de mise en forme d'un polymère à température relativement basse. Des nanocomposites de polypropylène isotactique (iPP) et de dioxyde de titane (TiO_2) contenant jusqu'à 15 % volumique (45,5 % massique) de TiO_2 ont été produits par plusieurs passages en extrusion bi-vis à l'état fondu. L'effet de la quantité de particules de TiO_2 et de la présence de PP modifié par de l'anhydride (AMPP), en tant que compatibilisant, sur la microstructure des nanocomposites a été étudié. Pour une quantité inférieure à 5 % volumique des nanoparticules, la dispersion de ces dernières dans le nanocomposite est améliorée par l'addition du AMPP. Cependant, pour une quantité supérieure à 5 % volumique des nanoparticules, le nombre et la taille des agrégats de TiO_2, à la fois dans les nanocomposites compatibilisés ainsi que dans les non-compatibilisés, ont augmenté jusqu'à atteindre un réseau interconnecté de TiO_2. Une analyse micromécanique des nanocomposites a montré que la résistance interfaciale entre la matrice polymérique et les particules de TiO_2 était plus grande dans le système compatibilisé que dans le système non-compatibilisé.

Puisque la conductivité électrique des nanocomposites iPP/TiO_2 est une propriété importante exigée pour l'utilisation dans la photoélectrode, la corrélation entre la microstructure et la conductivité électrique des nanocomposites iPP/TiO_2 a été étudiée dans la partie suivante de cette recherche. Des mesures en courant continu (DC) de la conductivité électrique ont montré que les échantillons non-compatibilisés avaient un seuil de percolation électrique inférieur aux

échantillons compatibilisés. De plus, les propriétés rhéologiques des nanocomposites ont conclu à un seuil de percolation rhéologique plus faible pour les systèmes non-compatibilisés, ce qui est en accordance avec les propriétés électriques. Quantitativement, les seuils de percolation rhéologique (5-7 % en volume) des nanocomposites compatibilisés ou non étaient inférieurs aux seuils de percolation électrique (5,3-7,5 % en volume). Il a été montré que le seuil de percolation élevé des nanocomposites compatibilisés a été obtenu grâce à une meilleure dispersion des nanoparticules de TiO_2 en comparaison avec les systèmes non-compatibilisés. Cependant, en raison de la séparation des phases partielles de l'iPP et de l'AMPP et de la viscosité inférieure de la matrice polymérique dans le cas des nanocomposites compatibilisés contenant au minimum 7,5 % en volume de TiO_2, les agrégats de TiO_2 étaient plus denses dans ces systèmes que dans les nanocomposites non-compatibilisés. Des mesures rhéologiques non-linéaires ont aussi été effectuées afin d'étudier la microstructure des nanocomposites en-dessous et au-dessus de leur seuil de percolation. Des analyses échelonnées de tests de balayage en déformation ont montré une dimension fractale plus grande pour les systèmes compatibilisés que pour ceux non-compatibilisés, en concordance avec les observations morphologiques.

Après avoir déterminé les caractéristiques morphologiques, électriques et rhéologiques des nanocomposites à base de iPP et TiO_2 pour différentes compositions, des films nanocomposites basés sur les échantillons se situant au-dessus du seuil de percolation ont été préparés par extrusion de film. Ils ont été uniaxialement étirés pour préparer des films nanocomposites poreux. Les effets de la composition et des différents paramètres d'étirage pendant le procédé, comme la température d'étirage, le taux d'extension et le rapport d'étirage, sur la microstructure finale et les propriétés des films étirés ont été étudiés. Les observations au microscope électronique à balayage (MEB) ont montré que les pores été formés à cause du décollement interfacial entre le PP et les particules de TiO_2. La porosité et la taille des pores augmentent lorsque la température d'étirage diminue et lorsque le rapport d'étirage augmente. La surface des pores augmente avec la porosité, fournissant une surface plus grande pour l'adsorption d'un colorant photosensible.

Finalement, la fonctionnalité des films nanocomposites poreux comme électrodes pour DSSC a été examinée. Les films ont été sensibilisés avec un colorant inorganique (N719) et utilisés comme photoélectrode dans une structure sandwich DSSC. Les propriétés photo-électrochimiques des cellules ont été analysées par photocourant-tension (*J*-*V*) et par spectroscopie d'impédance électrochimique (SIE). Le photocourant de court-circuit (J_{SC}) ainsi

que la tension en circuit ouvert (V_{OC}) augmentent avec le rapport d'étirage des films nanocomposites. Le J_{SC} et la V_{OC} du DSSC des films nanocomposites étirés à 200 % étaient respectivement autour de 0.7 μA/cm^2 et de 126 mV et, le taux de remplissage (FF) du système autour de 32 %.

ABSTRACT

High demand for energy due to continuous growth of population, rapid industrial development, depletion of conventional sources of energy, and their environmental impacts necessitate finding new sources of energy. Meanwhile, developing cost-effective and efficient devices to produce cheap, renewable, and clean energies is an interesting topic which has attracted great attention from both industrial and academic researchers. Solar energy is one of the most available sources of renewable energies that can be converted to electricity by solar cell. Among different types of solar cells, Die-Sensitized Solar Cell (DSSC), which consists of low cost materials, has a great potential to produce cost effective solar electricity.

The objective of this work is to develop a flexible photoelectrode for DSSC via a cost-effective polymer processing method at relatively low temperatures. Nanocomposites of isotactic polypropylene (iPP) and titanium dioxide (TiO_2) containing up to 15 vol% (45.5 wt%) of TiO_2 were prepared by multi-pass melt twin-screw extrusion process. Effect of TiO_2 nanoparticle content and presence of anhydride modified PP (AMPP), as a compatibilizer, on microstructure of the nanocomposites were investigated. Adding AMPP improved dispersion of the nanoparticles at volume contents less than 5 vol%. However, number and size of TiO_2 aggregates in both compatibilized and uncompatibilized nanocomposites containing more than 5 vol% of TiO_2 increased enough to result in an interconnected network of TiO_2. A micromechanical analysis on the nanocomposites showed that interfacial strength between polymer matrix and TiO_2 nanoparticles in the compatibilized nanocomposites were stronger than in the uncompatibilized nanocomposites.

Since electrical conductivity of the iPP/TiO_2 nanocomposites is an important property required for the photoelectrode application, correlation between microstructure and electrical conductivity of the iPP/TiO_2 nanocomposites were studied in the other part of this research. DC electrical conductivity measurements showed lower electrical percolation threshold for the uncompatibilized samples compared to the compatibilized ones. In additional, rheological properties of the nanocomposites resulted in lower rheological percolation threshold for the uncompatibilized system. It was in a qualitative agreement with the results of electrical properties. Quantitatively, rheological percolation thresholds (5-7 vol%) of both uncompatibilized and compatibilized nanocomposites were lower than the electrical percolation

thresholds (5.3-7.5 vol%). It was shown that the higher percolation threshold in the compatibilized nanocomposites was due to their better dispersion of the TiO_2 nanoparticles compared to the uncompatibilized ones. However, TiO_2 aggregates in the compatibilized nanocomposites with TiO_2 content above 7.5 vol% were denser than those in the uncompatibilized nanocomposites. It was due to partial phase separation of iPP and AMPP and lower viscosity of the polymer matrices of the nanocomposites. Nonlinear rheological measurements were also performed to investigate microstructure of the nanocomposites below and over their percolation thresholds. Scaling analysis of strain sweep tests resulted in larger fractal dimension for the compatibilized samples confirming the morphological observations.

After identifying morphological, electrical, and rheological characteristics of the iPP/TiO_2 nanocomposites with different compositions, nanocomposite films based on the samples above the percolation threshold were prepared by film extrusion. They were uniaxially stretched to prepare porous nanocomposite films. Effects of composition and different stretching process parameters such as drawing temperature, extension rate, and stretching ratio on the final microstructure and properties of the stretched films were studied. SEM observation showed that the pores were formed due to interfacial debonding between PP and TiO_2. Porosity and average pore size increased by decreasing drawing temperature and increasing stretching ratio. Pore surface area increased with porosity, providing larger area for adsorption of a photosensitive dye.

Finally, functionality of the porous nanocomposite films as photoelectrodes for DSSC was examined. The films were sensitized with an inorganic dye (N719) and used as a photoelectrode in a sandwich-like DSSC. Photo-electrochemical properties of the cells were analyzed by photocurrent-voltage (*J*-*V*) and electrochemical impedance spectroscopy (EIS). Both short circuit photocurrent (J_{sc}) and open circuit voltage (V_{oc}) increased with stretching ratio of the nanocomposite films. J_{sc} and V_{oc} of the DSSC based on 200 % stretched nanocomposite films were around 0.7 $\mu A/cm^2$ and 126 mV respectively and, fill factor (*FF*) of the system was around 32 %.

TABLE OF CONTENTS

LIST OF TABLES

LIST OF FIGURES

INTRODUCTION

Consuming fossil fuels as the conventional sources of energy has resulted in different drawbacks such as environmental pollutions and depletion of the resources. Consequently, in order to reach a sustainable development, it is necessary to use renewable energies. Solar energy is one the most interesting type of the renewable energies that is widely available all over the world. Developing efficient and cost-effective solar cells is one of the most important topics in solar technology. Meanwhile, making light and flexible solar cells is an interesting way to increase applications of solar cells on different surfaces of buildings and vehicles.

Among different types of solar cells, die-sensitized solar cell (DSSC) which is composed of cheap materials has a great potential for being manufactured in large scale. However, there is a high-temperature (>450 °C) sintering process in making photoelectrode of DSSC from titanium dioxide (TiO_2). In order to make flexible DSSCs, it is needed to find a method to make the photoelectrode at a suitable temperature that does not damage the plastic substrates.

The main objective of this Ph.D. dissertation is to develop a novel method for making flexible photoelectrode of DSSC. To achieve this objective, an approach based on making nanocomposites via polymer melt processing method was used. One of the most important microstructure characteristics of the nanocomposites is presence of an interconnected network of TiO_2 nanoparticles through the blend of polymer and TiO_2. Moreover, porosity of the film is another important requirement of the photoelectrode of DSSC.

In the first part of this project, polymer nanocomposites based on polypropylene (PP) and TiO_2 with different concentration were prepared and, evolution of their microstructure and properties were studied. Effect of adding anhydride-modified PP (AMPP), as a macromolecular compatibilizer, on dispersion and electrical properties of the nanocomposites was investigated. In the other part of the work, rheology was utilized as a tool to study the microstructure of the nanocomposites and, attempts were made to compare electrical percolation threshold with rheological percolation threshold. Porous nanocomposite films were prepared by stretching nanocomposite film and, effect of different process conditions on microstructure of the porous film were examined. At the last part, functionality of the porous nanocomposite films as photoelectrodes of DSSC was analyzed.

Accordingly, this Ph.D. thesis consists of the following sections:

- **Chapter 1:** A literature review which summarize main points about photovoltaic properties, different type of solar cell and, specially, DSSCs. It also presents a summary about thermoplastic nanocomposites containing TiO_2 particles and developing porous film by stretching filled polymer films.
- **Chapter 2:** is on organization of the articles.
- **Chapter 3, 4, 5, and 6:** are presenting main findings of this project in the format of four journal articles.
- **Chapter 7:** is on general conclusions and recommendations
- **Appendix 1:** Microstructure and Mechanical Properties of iPP/TiO_2

CHAPTER 1 LITERATURE REVIEW

1.1 Introduction to Photovoltaic and Solar Cell Technology

Importance of energy in the life of human being is completely obvious. Extraordinary consumption of conventional sources of energy, such as coal, oil and natural gas, has led to depletion of the fossil energy sources and also environmental pollutions. Large demands of energy, limitation in the sources, and environmental considerations force all the stakeholders (companies, government, etc.) to find renewable and clean alternatives [1, 2]. Figure 1-1 depicts a perspective of the growth in using renewable energies in next 25 years in comparison with other kinds of energies. Table 1.1 reports that electricity generation from solar sources has the highest average annual percent change in the next 25 years compared to the other types of renewable electricity.

The sun provides a continuous energy current around 1.7×10^{17} W (1.5×10^{18} kWh/year) which is four order of magnitude larger than the current annual global energy consumption (10^{14} kWh/year) [3]. Therefore, different aspects of energy production from sun light has attracted

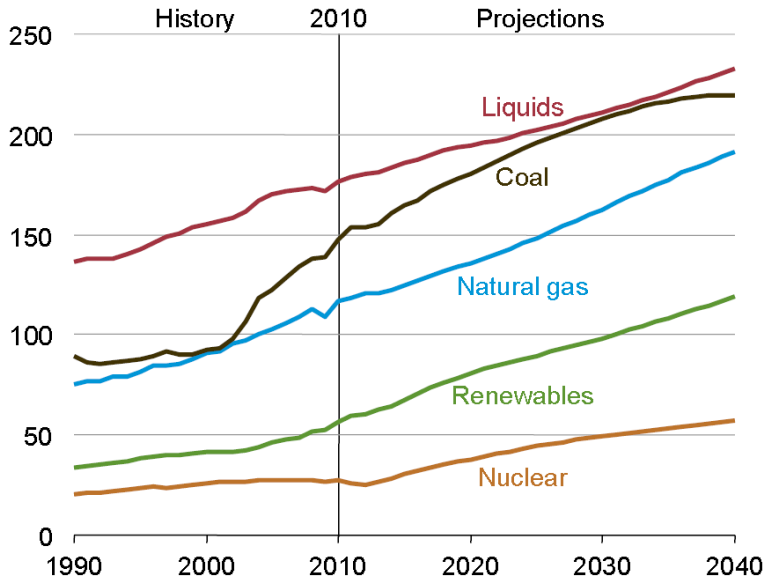

Figure 1-1: World energy consumption by fuel type, 1990-2040 (quadribillion) [4]

Table 1.1: World net renewable electricity generation by energy source, 2010-2040 (billion kilowatthours) [4]

	2010	2015	2020	2025	2030	2035	2040	Average annual percent change, 2010-2040
Hydroelectric	3,402	3,805	4,452	4,762	5,177	5,692	6,232	2.0
Wind	342	767	1,136	1,383	1,544	1,694	1,839	5.8
Geothermal	66	112	133	146	171	195	220	4.1
Solar	34	157	240	288	327	394	452	9.1
Other	332	427	549	643	729	800	858	3.2
Total World	**4,175**	**5,267**	**6,509**	**7,222**	**7,948**	**8,775**	**9,601**	**2.8**

great attention of scientific and governmental research centers [5]. One of the most important sectors of this research area is focused on producing electricity from sun light energy using solar cells. Solar cells or photovoltaic (PV) cells are devices which convert sunlight to electricity by means of photoelectric effect [6].

1.1.1 General Structure of Solar cells

Mostly, solar cells are made from semiconductor materials. In a crystal structure of an atom, different energy levels of electrons form a continuous energy band. The energy difference between the lower band, *valence*, and upper band, *conduction*, is called *band gap*, E_g, which is an important parameter in a semiconductor. Semiconductor materials have a band gap between 0.5-3 eV [2]. There are organic and inorganic semiconductors, e.g. Silicon (Si) and Germanium (Ge) are two widely used inorganic semiconductors [1].

The energy of a photon is

$$E = h\nu = \frac{hc}{\lambda} = \bar{h}\omega \tag{1.1}$$

where h and $\bar{h}$ are Planck's constant and Diarc constant ($\bar{h} = h/2\pi$), v, c, ω and λ are frequency, speed, angular frequency and wavelength of the light, respectively. Average energy of solar photons is about 1.35 eV [1].

When a photon of the light is absorbed by a photosensitive (semiconductor) material, its energy overcomes the band gap energy, excites an electron from the highest occupied molecular

orbital (HOMO) to the lowest unoccupied molecular orbital (LUMO) and forms an electron-hole pair which is called *exciton* [7]. This system usually consists of an electron donor (semiconductor) material and an electron acceptor (semiconductor) material. The former exports its electron to another semiconductor component, gains positive charges (therefore it is called p-type layer) and works as a hole carrier, while the later one works as electron carrier and has negative charge (n-type) [8].

Conversion of light into electricity can be summarized in the following steps [8]:

I. Photon absorption,
II. Exciton formation,
III. Exciton diffusion to the interface,
IV. Charge separation,
V. Charge transport to the electrodes.

Limitations and losses in each one of these steps result in reduction of cell performance.

In a general view, the basic structure and common parts of the solar cells can be explained by four main parts: two metallic electrodes and a layer composed of the photosensitive material (consist of two main sub-layers) enclosed between the electrodes. All of these parts are supported by a substrate, usually glass or plastics (see Figure 1-2). Practically, based on components of the active layer and its fabrication method, thickness of the layers varies and, some other (sub) layers are added to the system.

1.1.2 Different Types of Solar Cells

There are different methods of classification of the photovoltaic cells based on their semiconductor materials, morphology and fabrication technique.

1.1.2.1 Silicon-based Solar Cells

The most produced semiconductor-based solar cells are made from crystalline silicon (c-Si) (E_g=1.1 eV). The initial models are self-supporting films with a typical thickness around 200-300

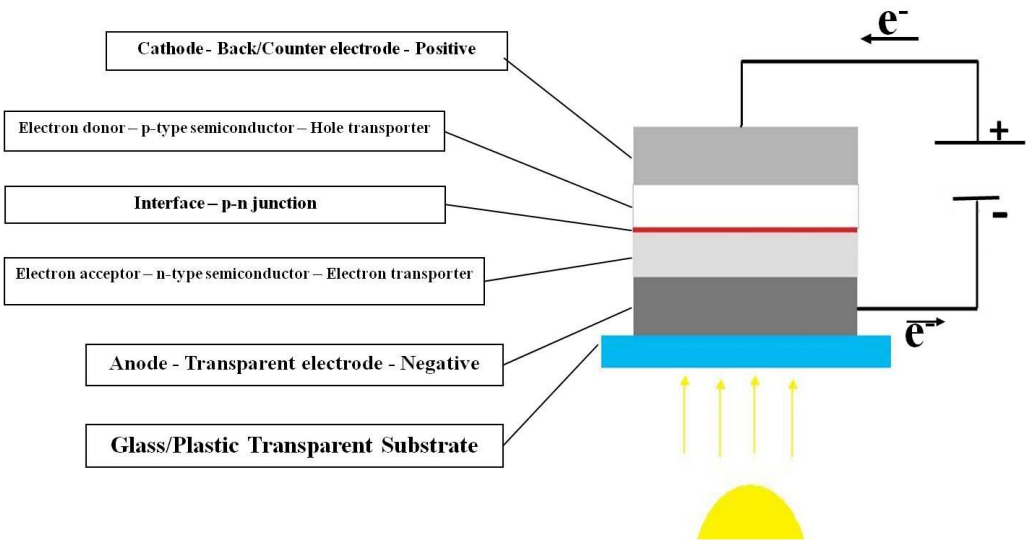

Figure 1-2: General view of a (heterojunction) solar cell

μm [2]. Because there is just one type of semiconductor material (Silicon with p and n doping), they are homojunction solar cells [5].

1.1.2.2 Thin Film Solar Cells

Reducing consumption of the expensive materials and developing an energy-efficient way led to development of thin film solar cells. For example, low temperature deposition of silicon from SiH_4 gas results in a thin film silicon solar cell that has a great potential to capture a large market of PV cells. These thin films are usually supported by a cheap substrate such as glass, steel or plastic. It is also possible to use different structures of silicon (e.g. amorphous, microcrystalline and single crystal) with different band gaps by thin film technology to make a wide range of light absorption [2]. The thickness range of such a film layer varies from a few nanometers to tens of micrometers.

1.1.2.3 Heterojunction Solar Cells

Thin film technology makes it possible to use different semiconductors, with different band gap energies, in the form of thin layer structures [2, 9]. Photovoltaic devices based on cadmium sulfide (CdS), copper indium diselenide ($CuInSe_2$ or CIS) and cadmium telluride (CdTe) are

leading candidates for large scale production of solar cells at low cost [10]. In these cells, the junction is formed by contacting two different semiconductors [5].

1.1.2.4 Organic Solar Cells

Due to presence of highly polarizable π-systems, conjugated polymers which have carbon-carbon double-bound in their molecular structure backbone, are electrically active (see Figure 1-3). Hybridization of the orbital and π-π* optical transition take place in the visible region of light spectral [7]. Hence, materials which have delocalized π electron systems can absorb energy of sunlight photons, create photogenerated charge carriers and transport the charges. Generally, organic semiconductors have wide band gap (~1.4 eV) [2, 7, 8].

1.1.2.5 Dye-sensitized solar cell (DSSC)

Dye-Sensitized Solar Cell (DSSC, DSC or DYSC) is a new class of solar cells which was first introduced by Michael Grätzel et al. in 1991 [11]. DSSC is composed of a dye-sensitized

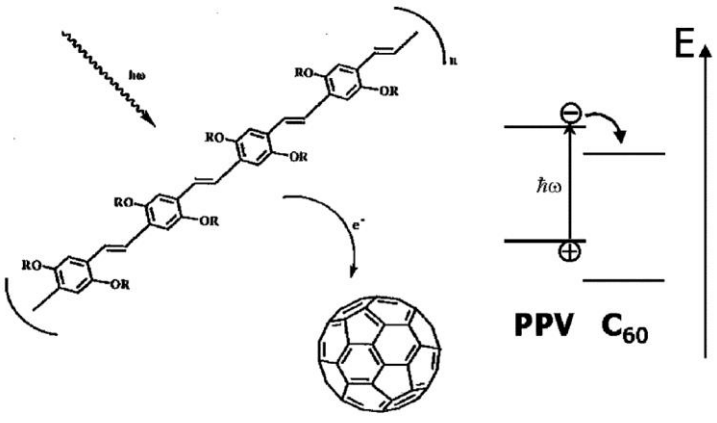

Figure 1-3: Illustration of the photoinduced charge transfer with (b) a sketch of the energy level. After excitation in PPV polymer as an organic semiconductor, the electron is transferred to fullerene (C_{60}) [8]

nanoporous TiO_2 electrode on a transparent conductive oxide (TCO) electrode, a platinum counter electrode placed on the top of the TiO_2 electrode and an electrolyte containing I^-/I_3^- redox couple filling the pore of the electrode [2]. Its low cost materials and manufacturing process, and mechanical robustness are attractive, but its low efficiency (about 11%) is still a problem which is a concern in relation to price-performance ratio [12]. Separation of the function of light absorption from charge carrier transport is the main difference in DSSCs from the conventional solar cell devices [11].

1.1.2.5.1 Operational principles

The principal operation of DSSC is schematically presented in Figure 1-4. The mesoporous oxide layer composed of nanometer-sized particles of anatase TiO_2 (or alternative wide band gap semiconductor oxide such as ZnO) is at the heart of the system. It is a high surface area electrically conductive network covered by a photosensitive chemical compound (dye). Photoexcitation of the monolayer of photosensitive dye (attached on the surface of TiO_2 layer) leads to the injection of an electron into the conduction band of the oxide. Subsequently, the dye

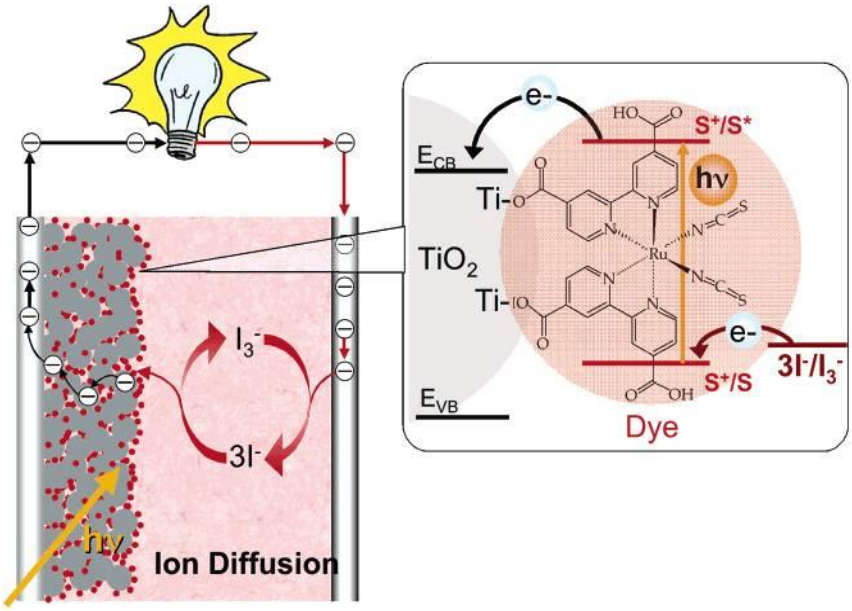

Figure 1-4: Schematic drawing of principal operation of DSSC [13]

goes back to its original state by electron donation from the electrolyte. The electrolyte, which is usually an organic solvent containing redox system (e.g. iodide/triiodide (I^-/I_3^-)), is regenerated by the reduction of I_3^- at the counter electrode and passing the electrons through the load, completes the circuit [14].

1.1.2.5.2 Fabrication

Preparation of the TiO_2 mesoporous layer and fabrication of the whole cell involve the following steps [2, 15, 16];

- Preparation of conductive transparent substrate (e.g. fluorinated tin oxide (FTO) SnO_2:F coated glass),
- Paste processing (applying the colloidal paste of the TiO_2 nanoparticles and a binder using processes such as doctor blading or screen printing)
- Drying and firing; the deposited layer is dried in air and then is fired (sintered) at around 450°C to burn the organic binder, pore formation and to connect the TiO_2 particle to each other and the support as well
- Sensitizing; typically by soaking the porous TiO_2 layer in a solution of a photosensitive dye for several hours followed by rinsing
- Applying a Pt-sputtered conducting glass as the counter electrode, sealing and filling the cell with an electrolyte

Schematically, Figure 1-5 shows a typical structure of a dye-sensitized solar cell (DSSC).

1.1.2.5.3 Morphology

Figure 1-6 shows microscopic images of the TiO_2 layer of a DSSC. Usually, it has a thickness around 5-20 μm. The porosity of layer is 50-65 % with the average pore size around 15 nm, area density of 1-4 mg/cm^2, and surface area of 50 m^2g^{-1} [2, 14]. Roughness factor, defined as the ratio between the real and the projected surface of the films, of the surface of these films for a 10 μm thick TiO_2 film was estimated about 1000 [17].

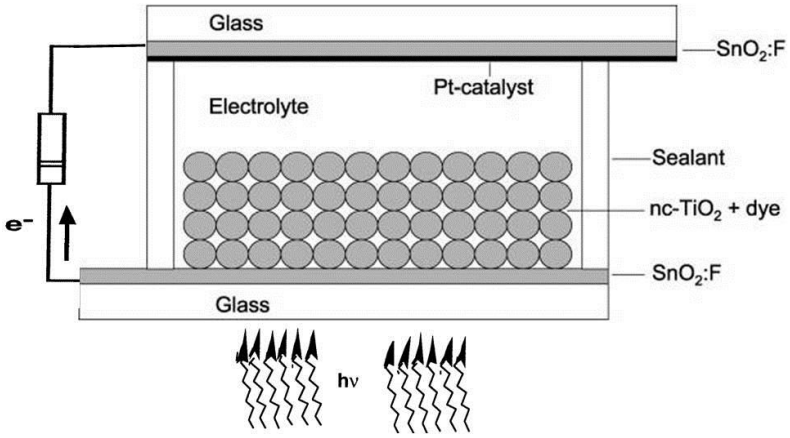

Figure 1-5: Schematic construction of a DSSC [15, 17]

1.1.2.5.4 Important Components of DSSCs

1.1.2.5.4.1 Titanium Dioxide (TiO_2)

Titanium dioxide (titanium oxide, titania) is a wide band gap (E_g=3.2 eV) semiconductor. Because of its high refractive index (~ 2.55-2.73 [18]), UV absorption, low cost, and availability, it is widely used as a white pigment in paint and plastic industries. TiO_2 has three forms of crystalline structures; rutile, anatase and brookite. Thermodynamically, rutile is the most stable

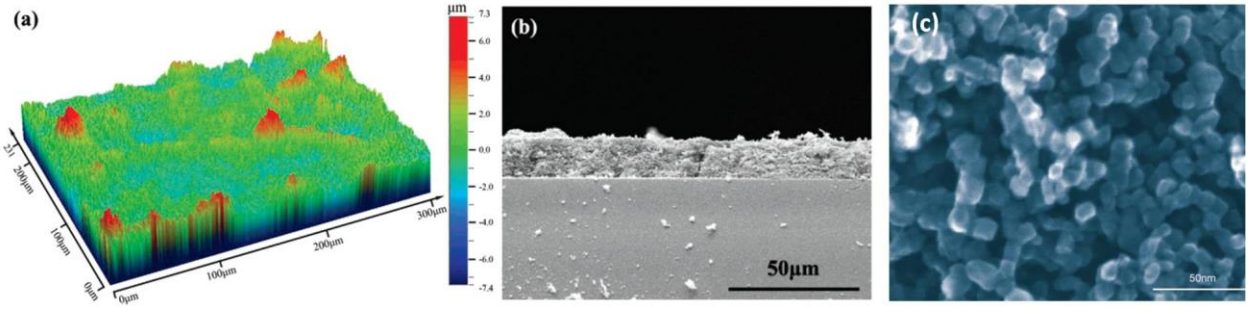

Figure 1-6: (a) Three-dimensional surface image and (b) cross-sectional SEM image of a TiO2 film coated on a conducting glass [19], (c) scanning electron micrograph of the surface of a mesoporous anatase film prepared from a hydrothermally processed TiO_2 colloid [20]

one and, compared to anatase. It has a smaller band gap energy and larger refractive index (E_g= 3.0 eV and RI= 2.73) [17]. Due to its surface chemistry and higher conduction-band edge energy, anatase has been widely used in DSSCs [21].

1.1.2.5.4.2 Sensitizing Dyes

Generally, two main types of sensitizers are used for DSSCs; inorganic (metal-based) and organic (metal free). A series of metal complex dyes based on Ruthenium polypyridyl (Ru) are currently highly efficient (11-11.3%) [22]. Figure 1-7 demonstrates the molecular structure of a group of these dyes. As can be seen, they have a metal center (ruthenium: Ru) which is responsible for light absorption and charge production. It injects the charge to organic ligand. Then the electrons are transferred to the semiconductor by hydroxyl groups (Figure 1-7). Stability, light absorption range and charge transfer rate are the most important characteristics that should be considered [2]. Ru is a rare and expensive metal. Hence, the need of cheap and available dyes encouraged developing less costly, but relatively less efficient organic dyes (8-9%) [2, 22]. Organic coumarin and indoline are examples of this group of dyes [23]. **Error! Reference source not found.** depicts other examples. Quantum sized (Quantum dot) particles such as PbS, CdS and Ag_2S are also used as photosensitizer [24].

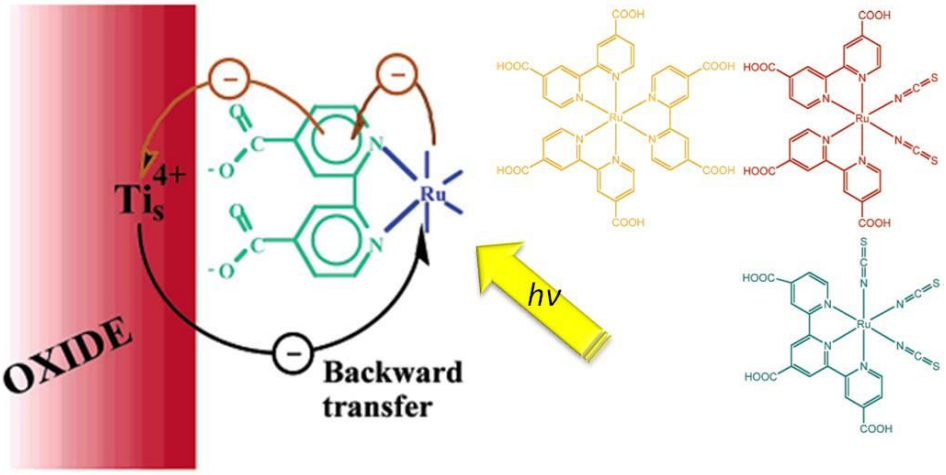

Figure 1-7: Schematic mechanism and molecular structure of Ruthenium-based dyes [13]

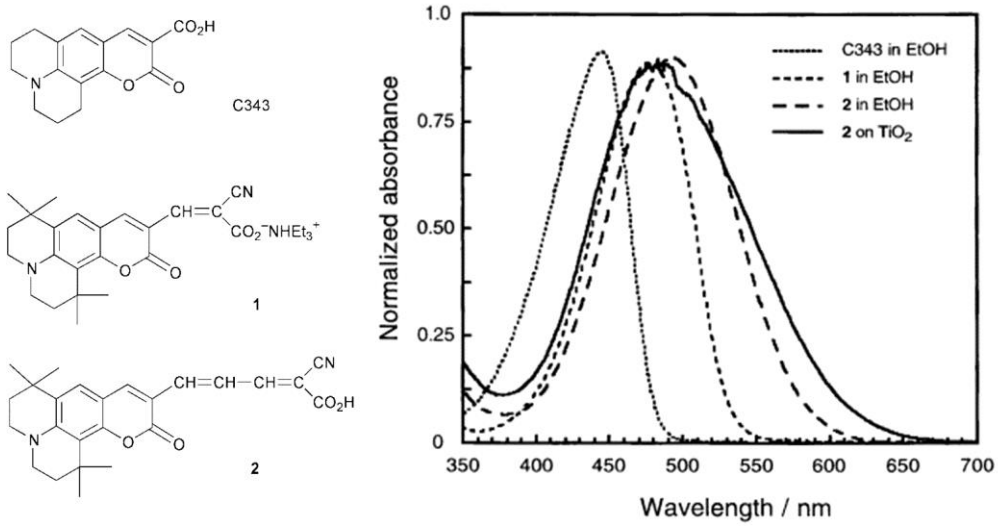

Figure 1-8: Molecular structure of coumarin derivative dyes and their absorption spectrum [25]

Up to here, some basic principles of solar cell technology and a brief introduction about DSSCs were presented. In the next section, works done on DSSCs based on flexible substrates and endeavors done toward mass production of PV cells will be reviewed. It is to be mentioned that the sintering operation of the TiO_2 layer at high-temperatures is the main part of the cell fabrication process that is addressed in the next section.

1.1.2.5.5 Electrodes on Plastic Substrates for DSSC

Lower weight, increased flexibility, higher impact resistance, lower cost, possibility of the roll-to-roll process are some of the advantages of using plastic substrates instead of the glass ones for DSSC. However, the main concern is the step of TiO_2 film deposition which includes an annealing process at high temperature (450 °C) that is responsible for removing the organic binder and forming an electrically connected network of TiO_2 particles. Because of thermal degradation of plastic substrates, mostly Poly(ethylene-terephthalate) (PET) coated with indium doped tin oxide (ITO-PET), the thermal treatment is limited to 150 °C [26].

Pichot et al. [27] prepared the TiO_2 electrodes from surfactant-free TiO_2 colloidal suspensions sintered at 100 °C. They compared their performances with regular electrodes.

Figure 1-9 compares cross sectional morphology and incident photon to current efficiency (IPCE) of the prepared electrodes. Relatively close photoaction spectrums of the different cells were attributed to compensation of efficiency loss of the low-temperature sintered cell by higher degree of dye absorption due to its larger internal surface. Hegfeldt and coworkers [28-30] developed a new method to prepare an interconnected network of TiO_2 nanoparticles on plastic substrates using static and dynamic mechanical compression. They deposited 20-25 %wt suspensions of nanoparticles in ethanol on the conductive PET substrates and applied a pressure around 1000 kg/cm^2 using a static press and a roller mill. Because of relatively higher applied pressure, the samples prepared by static pressure had better performance. The mentioned researchers claimed cell efficiency around 5.2 % at 0.1 sun.

Kim et al. [31, 32], used laser sintering as a technique to eliminate organic additives at lower temperatures. Although they obtained better results compared to unsintered samples, they were far from the cells prepared via the standard method. Figure 1-10 compares the characteristic photocurrent density-voltage (*I-V*) curves of the cells prepared via the standard method and the laser sintering. In another work [26], UV treatment was applied as an assistant for removing the organic additives in low temperatures.

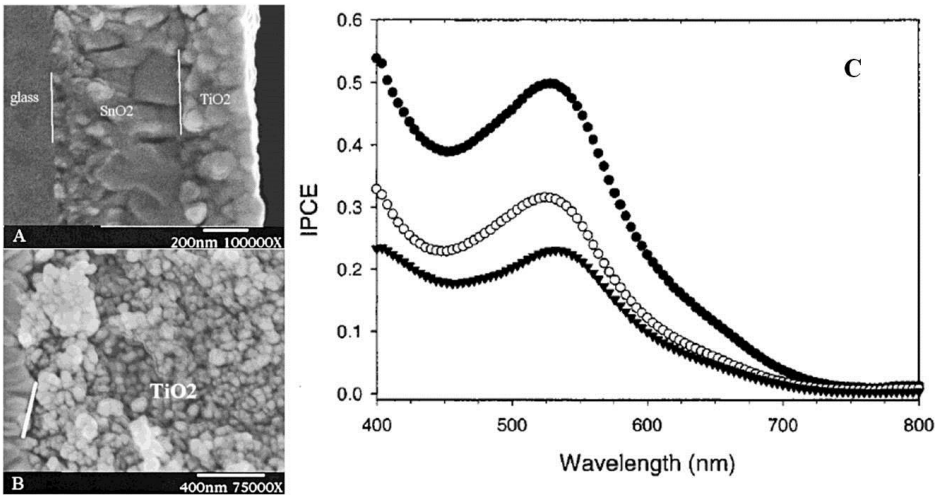

Figure 1-9: Cross sectional SEM pictures of TiO_2 samples sintered at (A) 100 (B) 450 °C and (C) comparison of IPCE of sintered at 100 °C (▼) and 450 °C (●) [27]

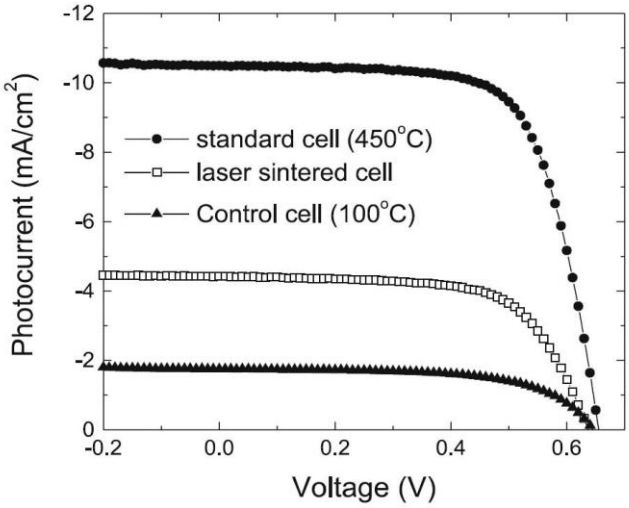

Figure 1-10: *I-V* characteristics for dye-sensitized solar cells fabricated with a laser-sintered TiO_2 (-□-), a non-laser-sintered TiO_2 electrode (control cell) (-▲-), and a high-temperature-sintered TiO_2 electrode (standard cell) (-●-) [32]

Drew et al. [33-35] reported an interesting work on using the electrospinning process to develop a porous structure from a mixture containing a polymer (PAN), a solvent (DMF), an azo-dye (congo red) and TiO_2 nanoparticles (Degusa P25). They measured the photocurrent response of the solar cells based on these electrospun electrodes. Table 1.2 summarizes the composition and properties of the samples based on polyacrylonitrile. Noteworthy, efficiency or efficiency range of the cells was not discussed. The intensity of UV absorption spectrum was used as a criterion to obtain the concentration of the absorbed dye. Figure 1-11 compares the photocurrent response of a cell based on electrospun electrode with one based on a spin coated film electrode. It is noticeable that the measured current of the cells are in the range of nanoampere. A current 294.43 nA per mol was measured for electrospun electrode while, it was 118.49 nA per mol for spin coated one. The authors did not report any significant effect for the presence of TiO_2 nanoparticles. In another work, they used PEO but did not report any morphological (porosity) details [35].

Recently, concept of polymer-inorganic composite was utilized to fabricate flexible photoelectrode of DSSC [36, 37]. In one approach, TiO_2/PMMA composite paste was prepared by solution blending and sintered at 150 °C followed by mechanical compression [36]. Figure 1-12 shows cross-sectional SEM images of the TiO_2/PMMA composite film with different

Table 1.2: Dye content and photocurrents from electrospun cells corrected for light scattering [34]

Sample Number	Wt% PAN	Wt% CR	Wt% TiO_2	Absorbance at 498 nm	Surface Dye Conc. (mol/cm^2)	Photo-current (nA/cm^2)	Current per mol of Dye (nA/mol)
1	10	3	0	0.0574	0.0143	0.60	41.92
2	10	3	0	0.1566	0.0391	0.75	19.20
3	10	3	0	0.2705	0.0675	1.20	17.79
4	10	3	0	0.1347	0.0034	2.00	595.40
5	10	3	0	0.1177	0.0030	0.62	211.23
6	10	3	0	0.6015	0.0150	5.30	353.33
7	10	3	1	0.0453	0.0113	0.35	30.98
8	10	3	1	0.0827	0.0206	0.70	33.94
9	10	3	1	0.0952	0.0237	1.06	44.65
10	10	3	1	0.1008	0.0251	0.86	34.21
11	10	3	1	0.2201	0.0055	4.05	737.87
12	10	3	1	0.2895	0.0072	2.36	326.89
13	5	5	0	0.0026	0.0006	1.63	2506.25
14	5	5	0	0.0578	0.0144	7.34	509.23

PMMA contents. Although adding PMMA improved flexibility of the photoelectrode, it resulted in reducing pore size and electric contact between nanoparticles. It was shown that short circuit current (J_{sc}) and efficiency of the cells decreased with PMMA concentration. However, open circuit voltage (V_{oc}) increased with PMMA content and fill factor (FF) remained unchanged. In

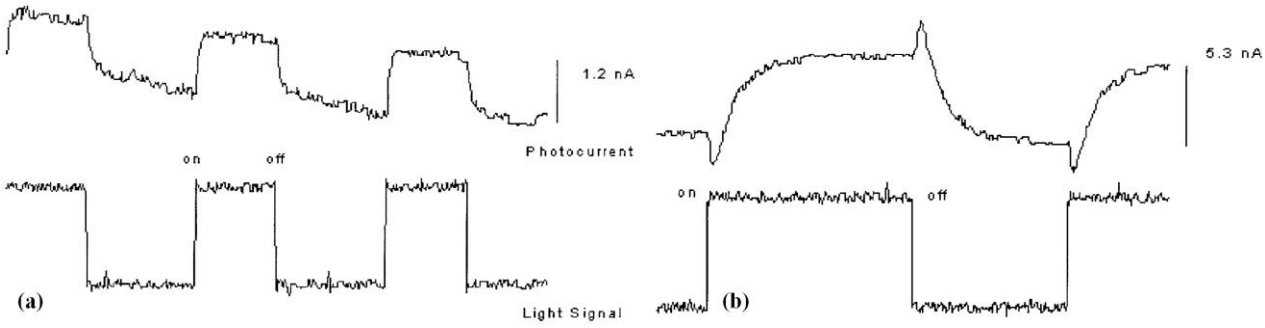

Figure 1-11: (a) Photocurrent response for sample 3, representative of all electro spun cells, (b) photocurrent response for a representative of all spin-coated cells [34]

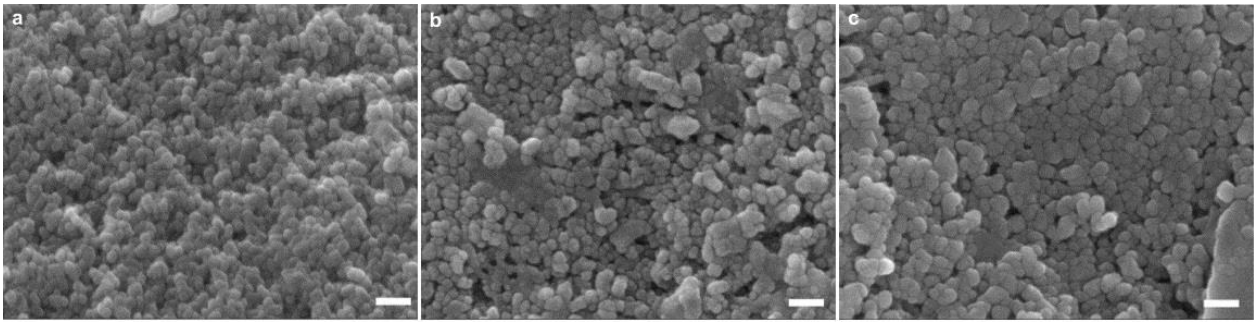

Figure 1-12: SEM images from cross-section of TiO_2/PMMA composite film with different PMMA concentrations; (a) 0 wt%, (b) 1 wt% and (c) 5 wt%, where the scale bar denotes a length of 100 nm [36]

another approach, composite photoelectrode based on PVDF nanofiber/TiO_2 was prepared by a spray-assisted electrospinning method (Figure 1-13a) [37]. Due to its structure, the photoelectrode prepared from this method had outstanding bending stability. In addition, its efficiency was comparable to the conventional DSSC.

1.2 Conductive Porous Polymer Film

In the previous sections, some basic points about the photovoltaic technology and a review on different kinds of solar cells were presented. Then, an interesting area of research regarding the development of cheap and efficient solar cells based on flexible plastic substrates was introduced. On the way of cost-effective production of electricity from solar energy, reducing production costs is as important as improving the efficiencies of the devices.

Since DSSCs are composed of relatively inexpensive materials, they have a great potential for large scale production on flexible substrates. But it depends on the development of a low-temperature process for TiO_2 deposition. The TiO_2 thin layer is a porous conductive network composed of interconnected TiO_2 nanoparticles. This kind of structure provides a large surface area for deposition of the dye compound and its pores are filled with a liquid electrolyte. Table 1.3 summarizes the typical morphological features and properties of a TiO_2 photoelectrode in the conventional method of preparation [2, 14].

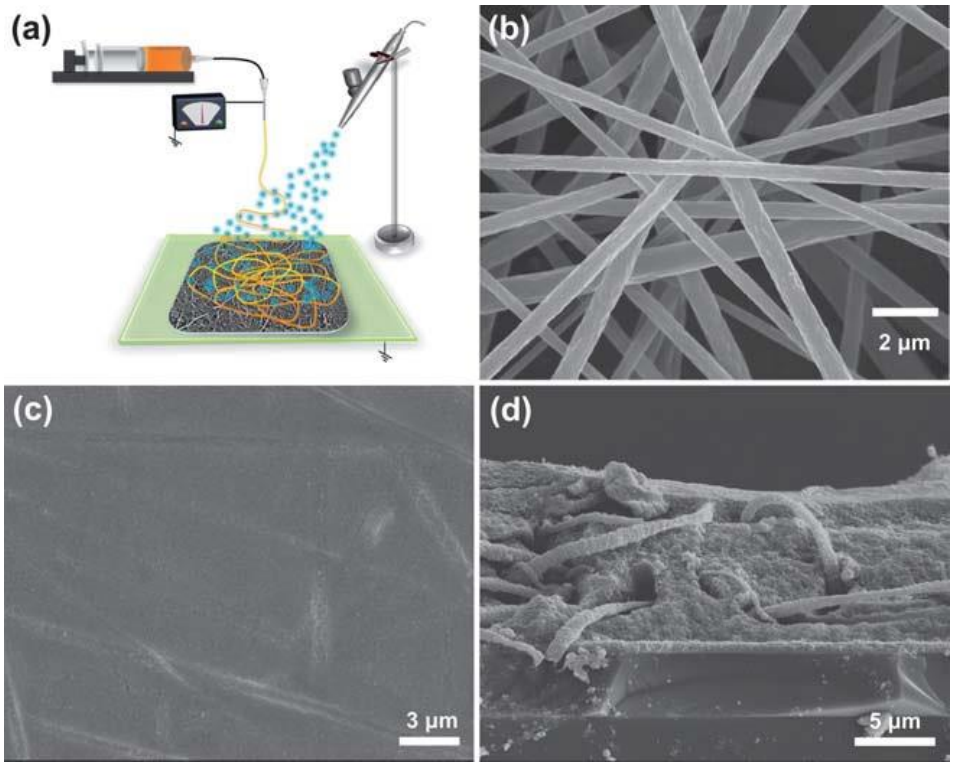

Figure 1-13: (a) Spray-assisted electrospinning system. SEM images of (b) as-spun PVDF nanofibers, (c) as-prepared PVDF/TiO2 composite film, and (d) cross section of a compressed PVDF/TiO2 composite film, that is, of the fiber-reinforced composite structure

Accordingly, in the present project, we are focusing on the development of an electrically conductive porous polymer film via melt processing to be used instead of pure TiO_2 photoelectrodes. Eliminating the high-temperature process, flexibility of the film and cost

Table 1.3: Important typical features of a TiO_2 photoelectrode of a DSSC [2, 14]

Feature	Value
Thickness	5-20 µm
Porosity	50-65 %
Average Pore Size	15 nm
Specific Surface Area (BET)	50 $m^2.g^{-1}$
Electrical Resistivity	10^{12} ohm.cm

effective mass production of the solar cells are some of the advantages of this process. In fact, we are investigating the possibility of making a percolated structure of TiO_2 nanoparticles in a thermoplastic porous matrix with morphological and electrical properties near to those presented in Table 1.3. Some similar works done on replacing porous conductive films with polymer nanocomposites structures will be reviewed.

1.2.1 Stretching Filled Composites

Yakisir et al. [38] made attempts to develop a continuous process for producing highly conductive microporous films to be used in different parts of fuel cells. They compounded polypropylene (PP) with different combinations of carbon black (CB) and graphite (GR) as two conductive fillers. Using a twin screw extruder, highly loaded blends containing up to 60 wt% of the fillers were prepared. Although they used a high melt flow rate resin (MFR=100 $dg.min^{-1}$), due to poor wetting of high surface filler by the polymer melt, it was not possible to incorporate more than 35 wt% of filler in a continuous mixing process.

Practically, obtaining a balance between processability of the compound and conductivity of the final product is a main challenge in such investigations because processability limits the final level of electrical conductivity. Rheological properties of the compounds were studied to find a suitable processable formulation for a film extrusion process. Figure 1-14 shows the apparent viscosity of the PP/CB/GR blends, with different concentrations, as a function of the imposed shear rate. Obviously, viscosity of the blend increases upon increasing the filler content and shows a power-law behavior.

In a post-extrusion stretching process, the prepared films were stretched up to 8-10 % at room temperature to create microvoids. As it can be seen in TEM images of Figure 1-15, the filler and polymer matrix were debonded at their interface. Then, a second stretching step at 160 °C was responsible for enlargement of the pores. Figure 1-16 demonstrates the proposed mechanism of the microporous structure formation during the two-stage stretching process. No significant reduction in electrical conductivity was observed due to stretching.

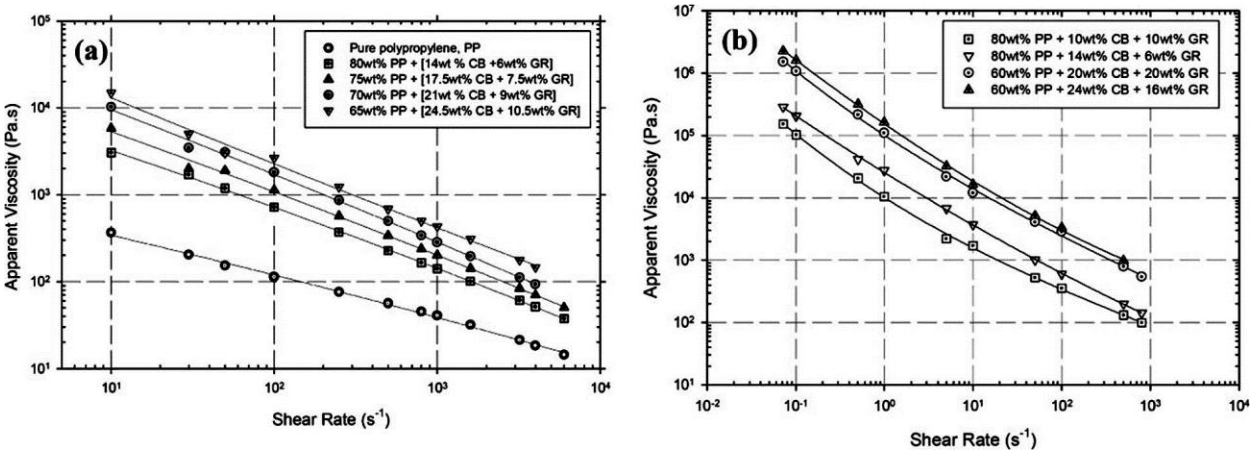

Figure 1-14: Apparent viscosity as a function of shear rate for PP/CB/GR blends at 230°C (a) CB/GR 70/30 wt%, (b) CB/GR 50/50 and 70/30 wt% [38]

1.2.2 Dispersed Phase Extraction

The previous researchers applied a polymer blending concept to achieve their goal in creating micropores in a conductive composite film [39]. They used blends of PP and PS, two immiscible polymers, as the polymer matrix. The PS phase was extracted after melt blending to prepare a porous structure. Figure 1-17 represents the changes of in-plane and through-plane film

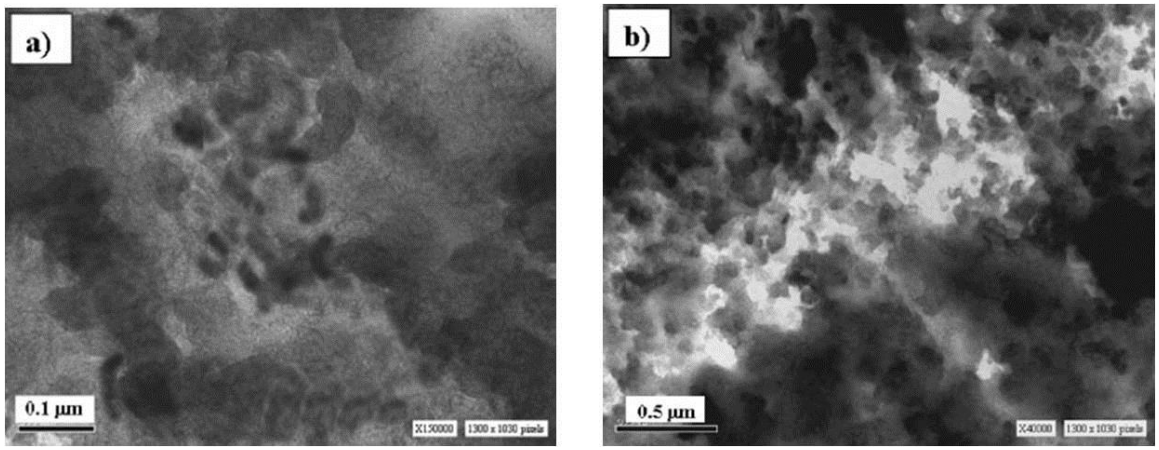

Figure 1-15: TEM of films made from 50 wt-% PP/25 wt-% CB/25 wt-% GR blend. (a) before stretching and (b) after stretching [38]

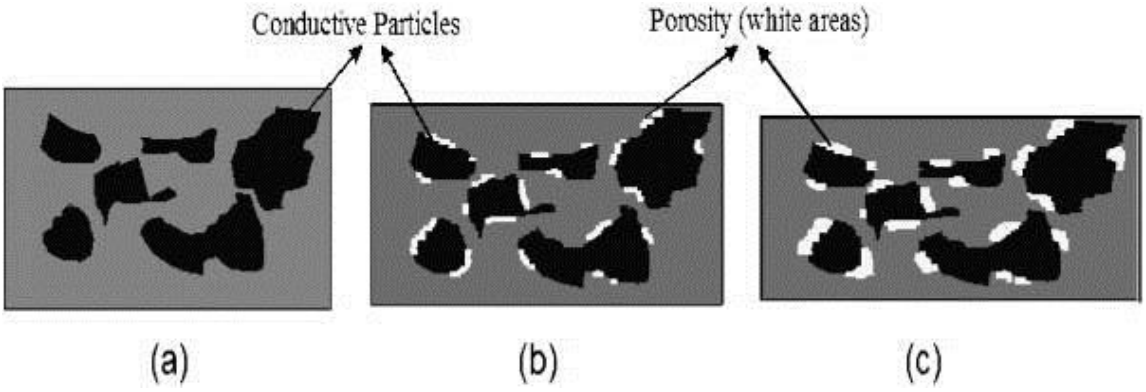

Figure 1-16: Schematic representation of microcracks upon stretching. (a) PP/CB/GR morphology before stretching; (b) initiation of microcraks upon stretching at room temperature; (c) growth of microcracks upon stretching at elevated temperature (≈160 °C) [38]

resistivity with CB/GR phase concentration and their corresponding blend viscosities. The difference between these quantities was attributed to orientation of asymmetric filler along the extrusion axis. A little change in resistivity of the samples after the extraction of PS dispersed phase is a good evident of proper filler incorporation into the PP matrix phase.

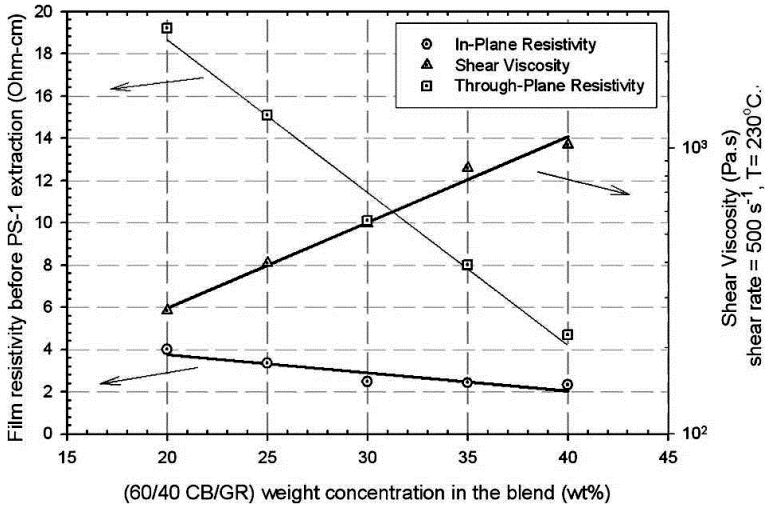

Figure 1-17: In-plane and through-plane film resistivities and their corresponding blend viscosities (at a shear rate of 500 s-1 and T=230 °C) as a function of CB/GR phase concentration [40]

Figure 1-18 shows results of BET measurements. Pore-size distribution characterization by BET and mercury intrusion techniques revealed existence of pores with different sizes in the prepared composites blends. Deyrail et al. [39, 41] continued the same approach with PA-11 and PET as the matrix phase and utilized the compatibilizing effect of organocly to obtain a finer droplet size of the PS dispersed phase.

1.3 Alternative Approach for the Porous Electrode of DSSCs

According to what is required for development of porous layer of TiO_2 in DSSCs, we need the presence of pores around the network of TiO_2 particles. Therefore, creating pores by stretching the filled polymer film is a possible method among the discussed approaches in the previous sections, because it yields the creation of pores at the polymer-filler interface. Hence, the next section reviews studies performed on producing porous films via stretching of filled polymer composites.

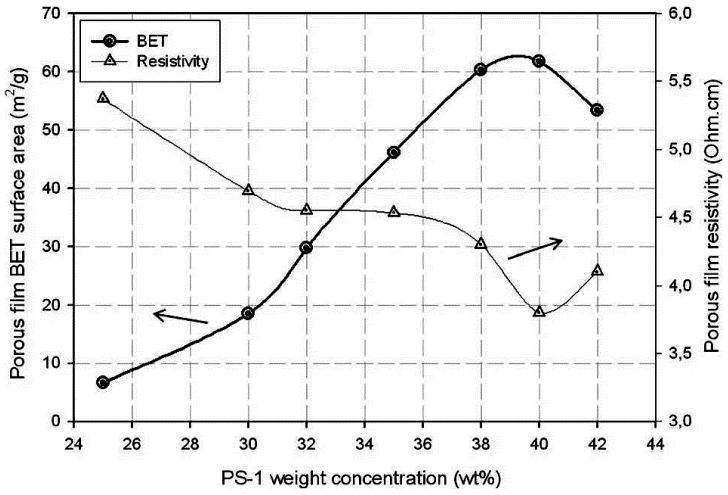

Figure 1-18: Resistivity and BET surface area of porous uncompressed films as a function of initial PS concentration [40]

1.4 Filled Membranes

One of the well-known methods of producing porous flexible thin films/sheets is based on stretching polymeric composite sheets containing rigid fillers. This kind of microporous films is made of a thermoplastic that is filled (40-70 %wt) with organic or inorganic fillers [42].

1.4.1 Pore Formation

Figure 1-19 shows a diagram of typical formulation and process steps of producing microporous polypropylene sheets containing $CaCO_3$ filler. The biaxial stretching of polymer composite sheets containing a fine dispersion of the filler causes to detachment of the two phases from the interface, due to stress concentration, and results in pore formation in the polymer sheet/film. Structural characteristics of the three dimensional network of interconnected pores, which is schematically depicted in Figure 1-20, is responsible for permeability of the films [43]. In the

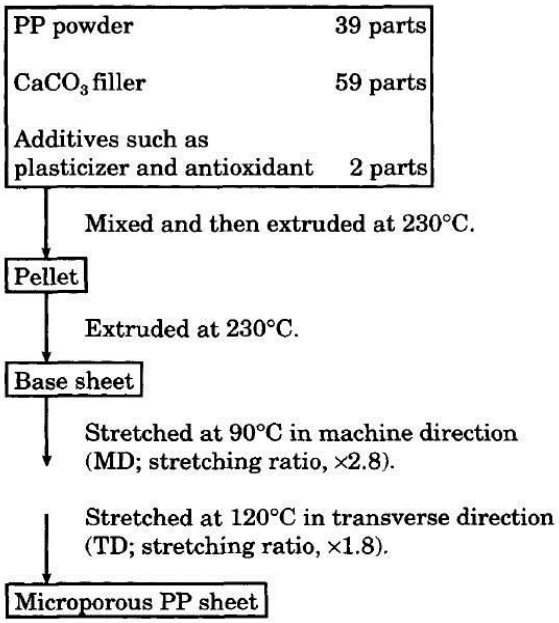

Figure 1-19: Schematic diagram of formulation and processing of microporous polypropylene sheets containing $CaCO_3$ [43]

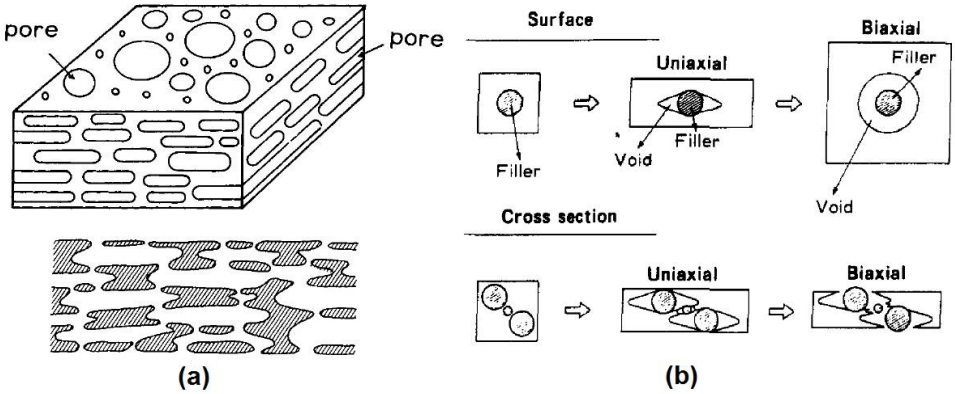

Figure 1-20: (a) Schematic structure of microporous sheet [43], (b) schematic mechanism of micropore formation [44]

step of machine direction (MD) stretching, initial voids are formed at the periphery of filler particles. Then, these initial voids are widened by stretching in transverse direction (T_D) (Figure 1-20b). The SEM micrographs of surface and cross section of a filled porous sheet are illustrated in Figure 1-21. Whereas the biaxial stretching yields to the circular/elliptical voids on the surface of the films, a layered structure of polymer matrix formed in parallel to the extension plane.

1.4.2 Effect of Particle Size

The final properties of the porous films are affected by material properties (e.g. characteristics of polymer matrix, filler nature, filler particle size etc.) and process conditions (such as mixing conditions, extension rate and temperature) [42, 44, 45]. Nago et al. [43] studied the effect of $CaCO_3$ particle size on the structure of biaxially stretched microporous PP sheets. They reported that using smaller particles leads to higher porosity and effective porosity. In addition, samples containing the smaller particles had lower tortuosities and smaller equivalent pore sizes (Figure 1-22b). It is to be mentioned that porosity is defined as ratio of the void volume to volume of the porous sample, while effective porosity is the density, or distribution per space unit, of the open pores that extend from wall to wall of the film [42]. At a constant filler concentration, the smaller the particle size, the higher the number of filler particles. Therefore, the number of stretch-

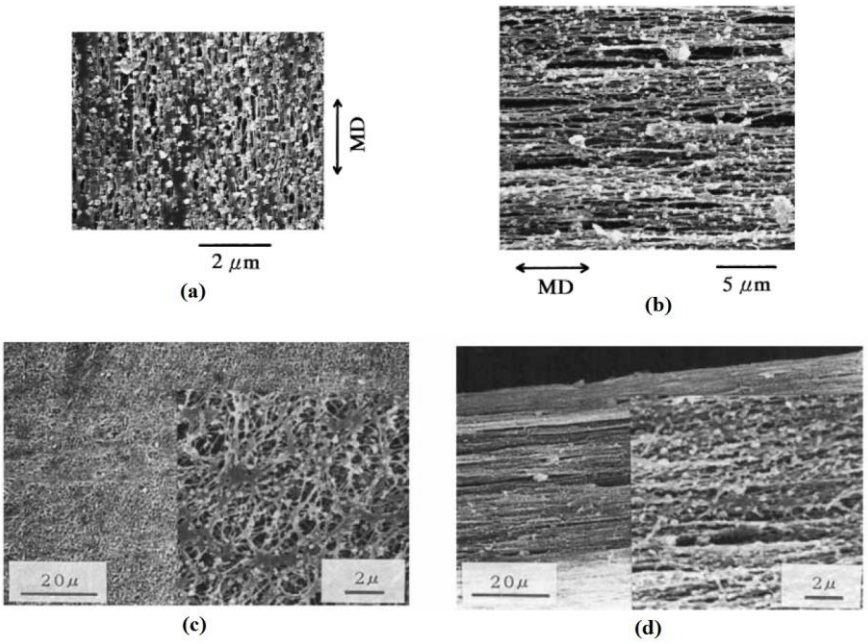

Figure 1-21: SEM micrograph of PP sheets containing $CaCO_3$ (0.08 μm); (a) surface after stretching in MD, (b) cross section after stretching in MD [46], (c) surface after biaxial stretching and (d) cross section after biaxial stretching [43]

induced pores and their interconnectivity increase [43].

1.4.3 Effect of Filler Type and Filler Concentration

Mizutani and coworkers reviewed the effects of different parameters on the properties of microporous polypropylene sheets [44]. They prepared PP-based composites containing different compositions of various inorganic fillers ($CaCO_3$, SiO_2 and diatomaceous SiO_2). Figure 1-23a represents the effect of filler type and filler concentration on maximum pore size (D_{max}). As can be seen, higher concentrations of filler result in relatively larger D_{max}. The difference among these dependencies for the different fillers was attributed to the particle shape as well as affinity of filler surface with the polymer matrix. One of the interesting points that should be mentioned is the effect of small particle aggregation on the structure of the pores. Figure 1-23b elucidates that aggregation of the smallest $CaCO_3$ particles leads to a broad particle size distribution and consequently broad distribution of pore size of the membranes.

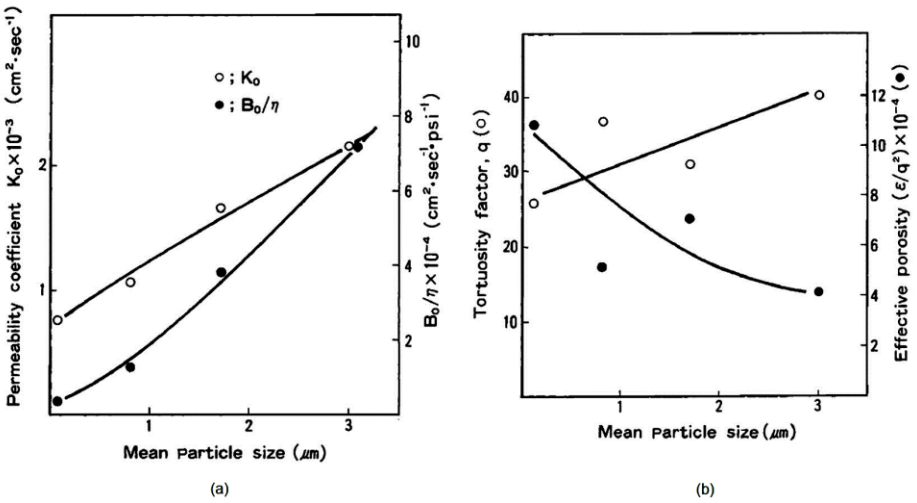

Figure 1-22: (a) relationship of permeability coefficient (K_0) to the mean particle size of fillers; (b) dependence of effective porosity (ε/q^2) and tortuosity factor (q) on mean particle size of fillers [43]

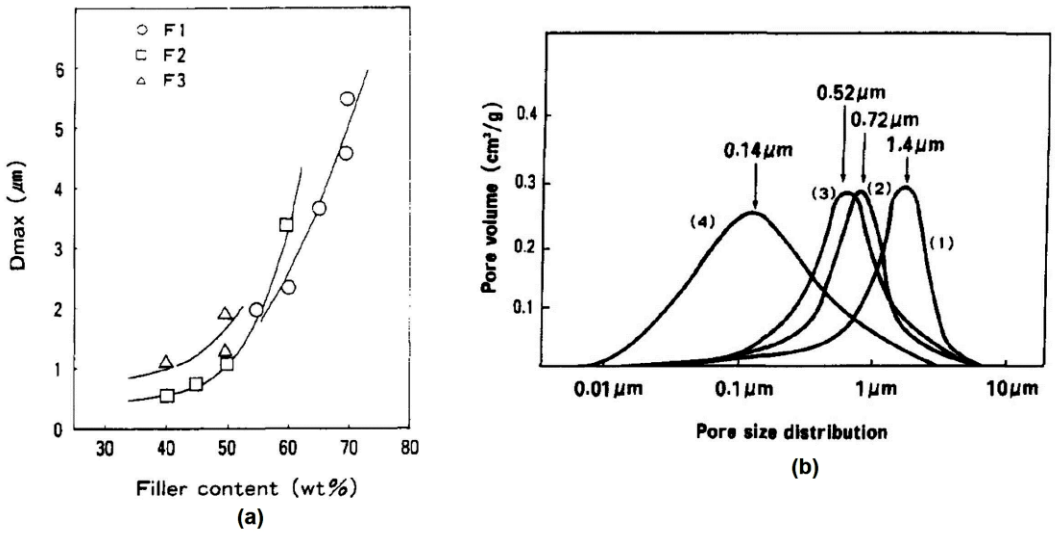

Figure 1-23: (a) Relations between filler content and D_{max}. Stretching temperature, 110 (MD) and 140 °C (TD). Stretching degree, 250 % in MD and 160 % in TD. Filler: ○, $CaCO_3$; □, SiO_2; Δ, diatomaceous SiO_2. (b) Pore size distribution of biaxially stretched microporous PP sheets containing $CaCO_3$ with different mean particle size; 1) 3.0, 2) 1.7, 3) 0.8 and 4) 0.08 μm [44]

In order to overcome the aggregation of small particles and to reach to a fine dispersion of the filler in the polymer matrix, Mizutani and Nago prepared composites of PP/SiO_2 using a sol-gel reaction of tetraethoxysilane (TES) in molten PP using an extruder [47]. Table 1.4 summarizes the structural properties of the obtained porous films. The ash content was used as a measure of SiO_2 content. As can be seen, the obtained pore sizes were in the range of few nanometers.

1.4.4 Effect of Stretching Ratio

Nago and Mizutani, in another work [48], studied the structure, permeability and mechanical properties of microporous sheets containing polymethylsilsesquioxane particles. They also investigated the effects of transverse direction (TD) stretching on structure and properties of PP sheets containing $CaCO_3$ [46, 49]. Effect of extracting the $CaCO_3$ particles by HCl treatment was also studied. The term "stretching ratio" was defined as total length after stretching divided by the original length before stretching. Figure 1-24 indicates that porosity (ε) and maximum pore size (D_{max}) increase with stretch ratio because of pores widening. Figure 1-25 shows the effects of stretching ratio on the effective porosity (ε/q^2), tortusity (q), and the equivalent pore size (m) of porous sheets containing particles with 0.08 μm average particle size. Although the tortusity factor slightly decreases with stretching ratio, its values are pretty large. On the other hand, small values of effective porosity imply complicated structure of fibrous texture of the polymer matrix.

Table 1.4: Effect of the ash content on the structure of microporous PP film

Sample No.	Ash Content (%)	Stretching Ratio	Porosity (%)	Pore Size (μm)	Specific Surface Area (m^2/g)	K (cm^2/s)
1	2.2	3.5	8.4	0.01	114	0.010
2	2.6	5	13.3	0.02	161	0.016
3	2.8	3	15.0	0.02	177	0.052
4	3.4	4	19.1	0.02	189	0.083

Stretching ratios were the same both in the machine and in the transverse directions at 150°C. Film thickness, 6–9 μm.

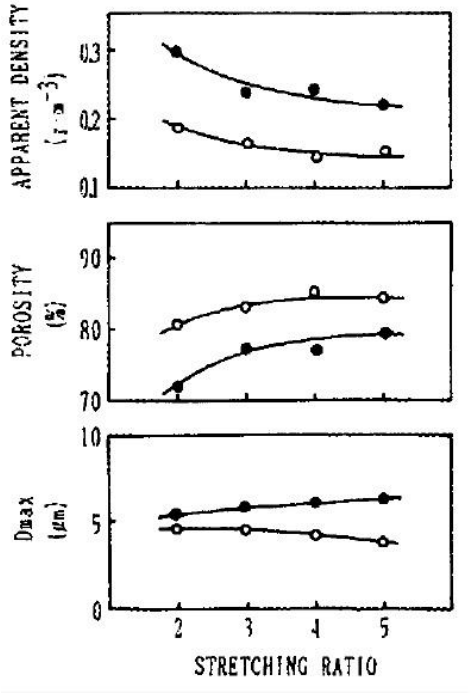

Figure 1-24: Effect of stretching ratio (D_{TD}) on some properties of the microporous sheets. ●: samples containing $CaCO_3$ (average particle size 3 μm). ○: samples after removing $CaCO_3$ [49]

1.4.5 Other Parameters

Stretching temperature is another important process parameter. Extension at elevated

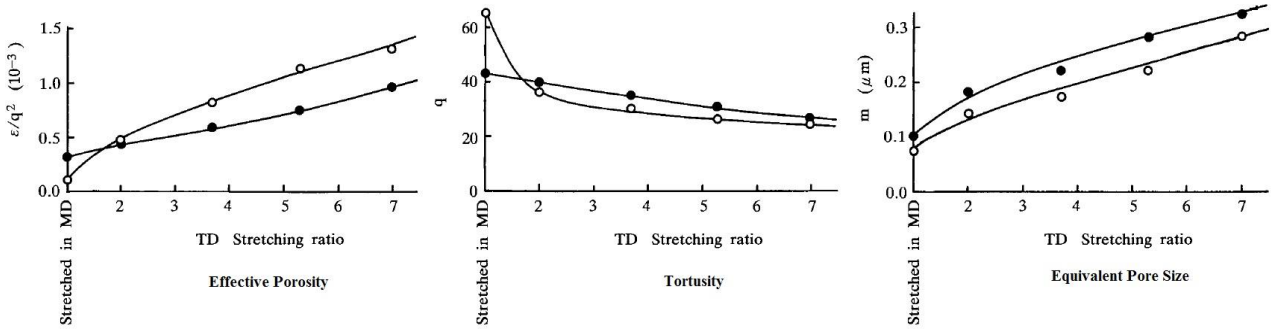

Figure 1-25: ε/q^2, q, and m versus TD stretching ratio: (○) before HCl treatment; (●) after HCl treatment [46]

temperatures does not result in an efficient pore structures. Typically, the optimum stretching temperature is between T_g and Vicat softening temperature. Deformation rate and film thickness also affect permeability properties [45]. In addition, rheological properties of the polymer matrix should provide an acceptable level of processability and extrudate stability as well [42].

1.5 Melt-Blended Thermoplastic/Titanium Dioxide Nanocomposites

According to the previous sections and the aim to develop a composite structure containing TiO_2 nanoparticles, a review on the works focused on melt-blending of thermoplastic polymers and TiO_2 are presented in this section.

Table 1.5 summarizes some of the recent works about polymer/TiO_2 micro- and nanocomposites prepared via melt processing. As can be seen, among the different thermoplastic resins which have been used for different applications, polyolefins are widely used. Polypropylene is the most utilized one. In the case of nanocomposites, it is difficult to find highly concentrated blends. However, some of most important aspects of this kind of filled polymer systems will be reviewed in the following sections.

Table 1.5: Summary of the recent works on melt-processed polymer/TiO_2 micro- and nano-composites

No.	Polymer	MW, MFR or IV	APS[1]	Max. Filler Loading	Process	Compatibilizer	Ref.
1	PBT	0.7 dL/g		1.5 wt%	Torque Rheometer	Titanate coupling agent	[50]
2	PP	4 dg/min	42.3 nm 130 nm	3 wt%	TSE[2]		[51]
3	iPP	M_w=184.7 kg mol^{-1}	<200 nm	40 wt%	Extruder/Compression molding		[52]
4	iPP	60 g/10 min		5 wt.%	Internal Mixer	Wax/PPgMA	[53]
5	PET/PP	(0.8 dl.g^{-1})/(2 g.10 min^{-1})	300 nm 15 nm	4 vol %	TSE	PPgMA	[54]
6	HDPE	6.5 g/10 min	30 nm	1 vol%	Internal Mixer	Surface modification	[55]
7	PET	0.6 dl/g	50 nm	3 wt%	TSE	Surface grafting	[56]
8	PMMA	Mw=93000 g mol^{-1}	21 nm	20 wt%	Internal Mixer/compression molding		[57]

[1] Average particle size

[2] Twin screw extruder

9	EVOH			13 wt %	Internal mixer/compression molding		[58]
10	iPP	4 g.(10 min)$^{-1}$		30 wt.%	TSE	Surface modification	[59]
11	PP		21 nm	5 wt %	TSE	Surface modification	[60]
12	PET	63.6±5.2 g×10 min^{-1}	21 nm	3 wt %	Injection Molding/ Extrusion-IM		[61]
13	EVOH		9 nm		Internal Mixer/Compression Molding		[62]
14	PP	10 g/10 min	Micro <44 μm Nano ~15	4.5 % Vol	TSE (Masterbatch method)		[63]
15	PS		5 ,15 nm Needle 10×40, 15 and 14 nm	5 wt%	TSE	Surface modification	[64]
16	LDPE	17.8 g/10 min	220 nm	70 wt %	Special equipment for high-concentration masterbatches		[65]

1.5.1 Dispersion Mechanisms of Titanium Dioxide in Polymer Melts

Factors such as interparticle forces (e.g. Van der Waals), the difference between specific surface energy of inorganic particles and polymeric matrix would result in agglomeration of the fillers [64]. The degree of filler dispersion/agglomeration has significant effects on mechanical, electrical, and optical properties of the composites. The hydrodynamic force applied by the flow field and cohesive force within particle agglomerates are two main competitive parameters in a dispersive mixing [66].

There are two main mechanisms for agglomerate breakup under hydrodynamic forces during the compounding process; rupture and erosion [66]. In the former mechanism, the agglomerates are split to small fragments due to high shear rates or particle defects while in the latter the radius of agglomerate gradually decreases. Processing conditions, cohesiveness of the agglomerates, agglomerate-medium interactions and medium penetration are the most important parameters affecting the agglomerate breakup. Infiltration of the fluid into structural pores of agglomerates and a good degree of wetting reduce the cohesive strength of the agglomerates and also helps to transfer the shear stress of the flow field to the particle agglomerates which lead to a better dispersion level [66, 67]. Figure 1-26 depicts the effect of agglomerate porosity on the erosion mechanism schematically. As can be seen, better wetting in the more porous particles results in the formation of larger eroded fragments. Equation 4 relates the change of particle size (agglomerate radius R) to the affecting parameters and describes the kinetics of the erosion process [67]

$$\frac{R_0 - R}{R_0} = \frac{k''}{\tau_c} W_a \, \mu \dot{\gamma} t \tag{1.2}$$

k'', W_a, τ_c, μ and $\dot{\gamma}$ are erosion rate constant, work of adhesion between the filler and fluid, the cohesive strength of the agglomerate, the fluid viscosity, and the shear rate respectively.

1.5.2 Processing Conditions

Wacharawichanant et al. [51] studied the effects of mixing conditions on mechanical properties of PP/TiO_2 nanocomposites. They prepared the nanocomposite samples at different screw speeds

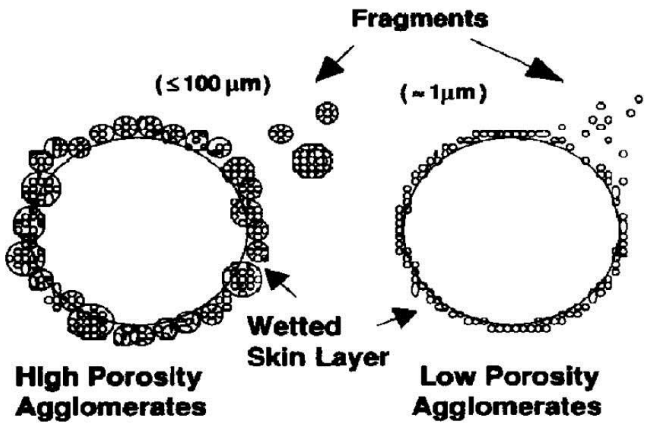

Figure 1-26: Structural models for high- and low-porosity TiO_2 agglomerates [66]

in a twin screw extruder and different numbers of mixing cycles as well. As can be seen in Figure 1-27, the nanocomposites prepared at lower screw speed (50 rpm) have better mechanical properties. The more improved mechanical properties of samples prepared at the lower mixing speed was attributed to the better dispersion of nanoparticle due to longer residence time. However, the effect of thermo-mechanical degradation, which is possible at higher screw speeds, was not considered in that study. The second cycle of melt mixing of PP/TiO_2 nanocomposites in the twin screw extruder improved the mechanical properties due to a better dispersion of nanoparticles.

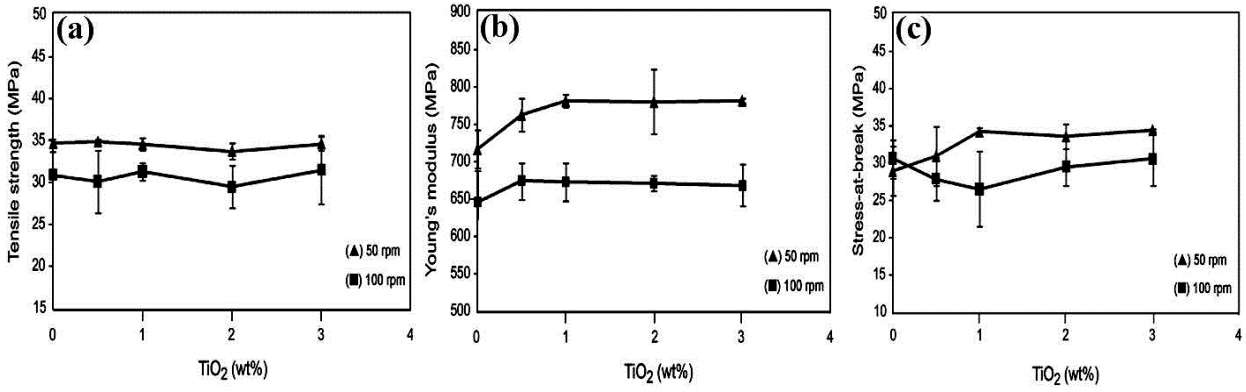

Figure 1-27: Mechanical properties of PP/TiO_2 (130 nm) at various concentration and different screw speeds of mixing; (a) tensile strength, (b) Young's modulus and (c) stress at break [51]

Chandra et al. [64], in a systematic study, investigated the optical, mechanical and morphological properties of PS based nanocomposites containing 5 wt% of different TiO_2 nanoparticles and several kinds of surfactants. Figure 1-28 shows different screw configurations used to prepare the PS/TiO_2 nanocomposites. The high shear configuration, equipped with kneading blocks in its metering section and without the reverse flight element, resulted in the best degree of dispersion and the smallest agglomerate size. It is noticeable that there was a mixture of large and small agglomerates in the nanocomposites. However, the majority of filler domains prepared by the high shear configuration were smaller than 100 nm (see Figure 1-29).

Mina et al. [52] investigated the effect of processing conditions and TiO_2 concentration on performance of iPP based micro-composites. They blended iPP with up to 40 wt% of TiO_2 (<0.2 μm diameter) using melt extrusion molding (EM) process and melt extrusion followed by compression molding. Figure 1-30 illustrates the changes of microhardness with TiO_2 concentration. Evidently, the microhardness (*H*) of the EM samples is lower than for the ECM ones, especially in the case of the most concentrated samples. This was attributed to a good adhesion between filler and polymer matrix.

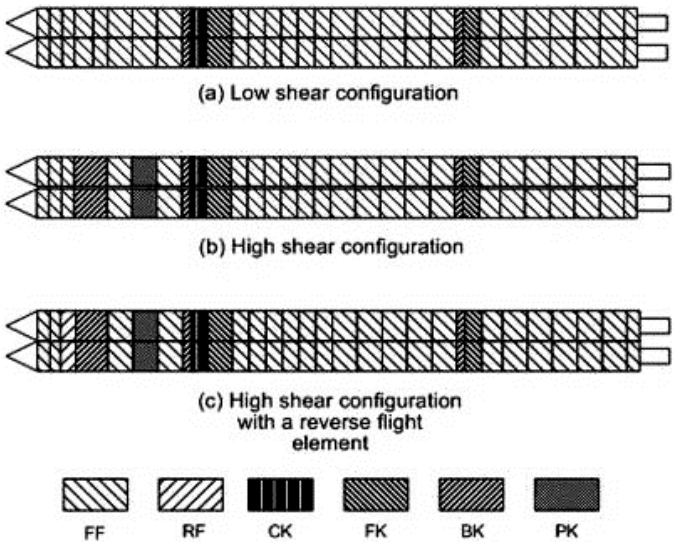

Figure 1-28: Screw configuration used during melt compounding (FF= forward feed, RF= reverse flight, CK= cross kneader, FK= forward kneader, BK= back kneader, PK= paddle kneader) [64]

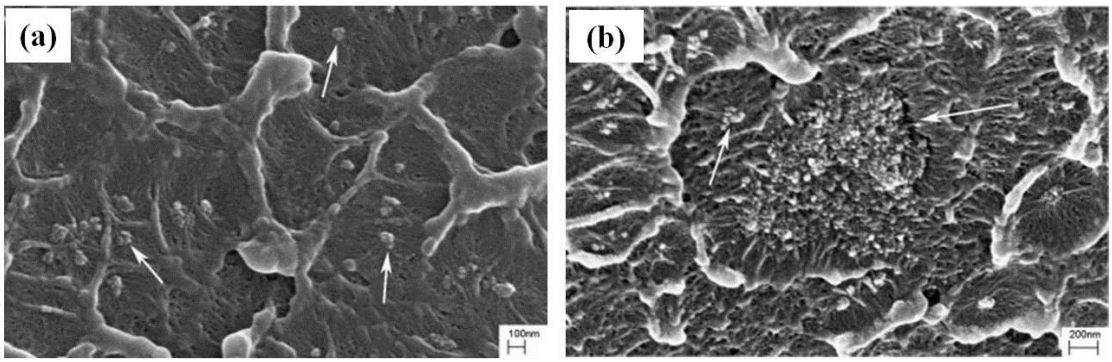

Figure 1-29: Polystyrene/anatase 15 nm TiO_2 processed using the high shear configuration without the reverse flight element taken at different locations [64]

1.5.3 Compatibilizers and Surface Treatments

Surface hydrophilicity of unmodified TiO_2 causes its poor compatibility with plastics and rubbers and high extent of agglomeration. Therefore, surface modification and addition of a compatibilizer component have important effects on dispersion of TiO_2 in a polymer matrix [50].

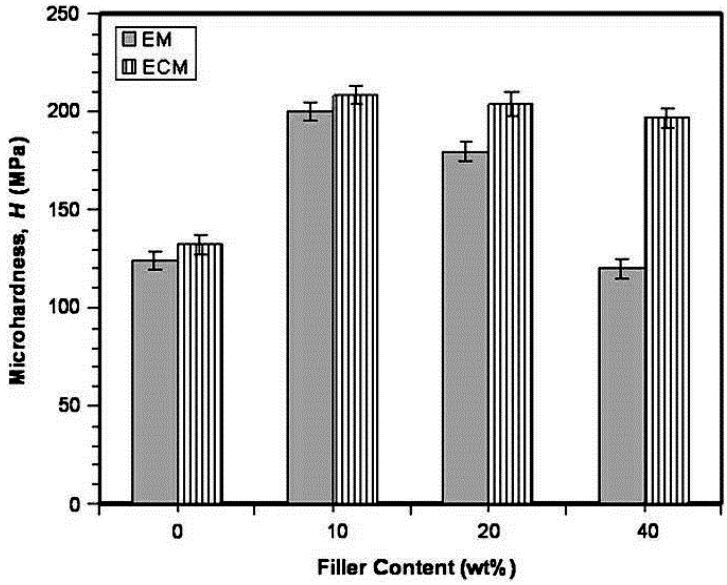

Figure 1-30: Change of microhardness at various concentrations of filler for both EM and ECM samples [52]

Figure 1-31 shows effect of adding a titanate coupling agent[3] on TiO_2 dispersion in PBT. It yields a better degree of filler dispersion and its enhanced nucleating effect on crystallization [50]. In fact, the surface modification decreases the surface energy of the modified particles, increases the space steric effect, and consequently improves the dispersion [50, 64]. Chandra et al. [64] also studied the effect of different surfactants on morphological and mechanical properties of PS/TiO_2 nanocomposites. Table 1.6 shows the effect of using different kinds of surfactants (10 wt% relative to the nanoparticles). It can be concluded that the silwet L-7280 (a copolymer of silicone, ethylene oxide, and propylene oxide) results in the best dispersion state.

Another advantage of using surface treatment is reducing the photocatalytic effect of the TiO_2 nanoparticles. Absorption of UV by TiO_2 causes the formation of electron-hole pair and, consequently, an extremely reactive $^{\bullet}OH$ radical at the surface of the particles which can degrade the polymer. Using surfactants and surface treatments protects the polymer matrix from degradation by creating a layer between TiO_2 and polymer [64].

Ou et al. [68] studied the compatibilizing effect of maleated polypropylene (PP-g-MAH) on

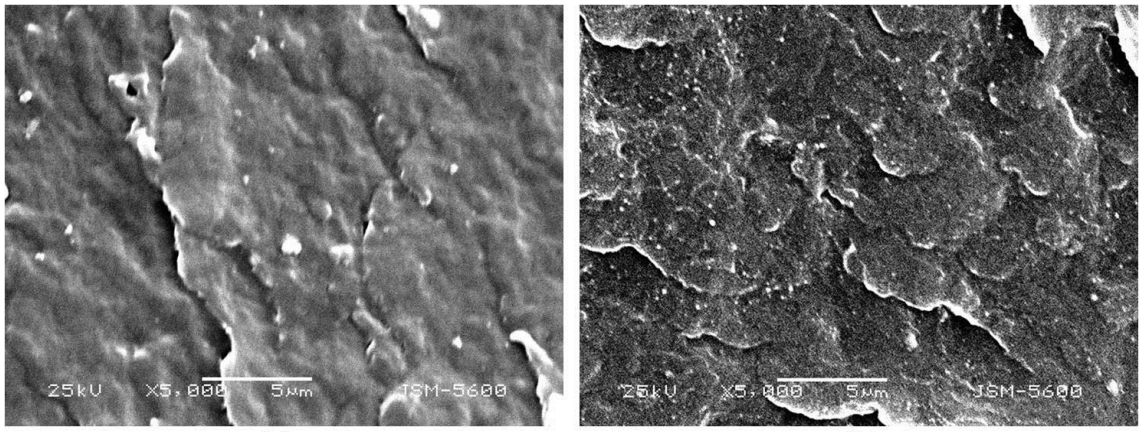

(a) (b)

Figure 1-31: SEM micrographs of PBT/TiO_2 containing; (a) pristine and (b) the titante surface modified particles [50]

[3] Isopropyl tri(dactyl phosphate) titante; $C_{51}H_{109}O_{13}P_3Ti$

Table 1.6: Effect of surfactants on anatase 15 nm TiO_2 agglomerate size [64]

Surfactants	Agglomerates sizes (μm)
None	8–14
Silwet L-7280	0.05–2
Disperbyk 111	5–12
Solsperse 2–1000	<0.20 and 3–5
Silquest A-137	0.1–12
Ken-React Lica 38	1–12

mechanical properties of injection molded polypropylene/polyamide 6/functionalized-TiO_2 nanocomposites. They added up to 7 phr of TiO_2 nanoparticles in the blend of PP/PA6. Using PP-g-MAH, as a compatibilizer, had a synergistic effect on the mechanical properties of the nanocomposite blends containing TDI[4]-functionalized TiO_2. This effect was attributed to the improvement of TiO_2 dispersion in PP phase as well as PA phase after compatibilization. A reaction between the carboxyl groups of PA6 and –NCO groups of treated TiO_2 was proposed as the main cause of the better dispersion and preferential location of TiO_2 nanoparticles in the PA dispersed phase. On the other hand, another reaction between PA6, PP and PP-g-MAH helps dispersing TiO_2 nanoparticles in the PP continuous phase. Figure 1-32 demonstrates the proposed chemical reactions.

The effect of adding nano-size TiO_2 on morphology and properties of PET/PP binary blends was investigated by Li et al. [54, 69, 70]. They prepared PET/PP blends containing 2 and 4 vol% of TiO_2 nanoparticle (15 nm). Because the surface of the nanoparticles was coated by a polyalcohol, interaction between hydroxyl groups of TiO_2 and carboxyl groups of PET and polar nature of TiO_2 resulted in preferentially presence of the nanoparticles in the PET dispersed phase [71]. Since maleic anhydride grafted polypropylene (PP-*g*-MA) can also react with hydroxyl groups of the TiO_2 nanoparticle, it coats the nanoparticles and prevents their migration from PP matrix to the PET droplets[70]. Figure 1-33 illustrates the possible chemical reactions. TEM micrographs of compatibilized and uncompatibilized blends are shown in Figure 1-34.

[4] Toluene-2,4-diisocyanate

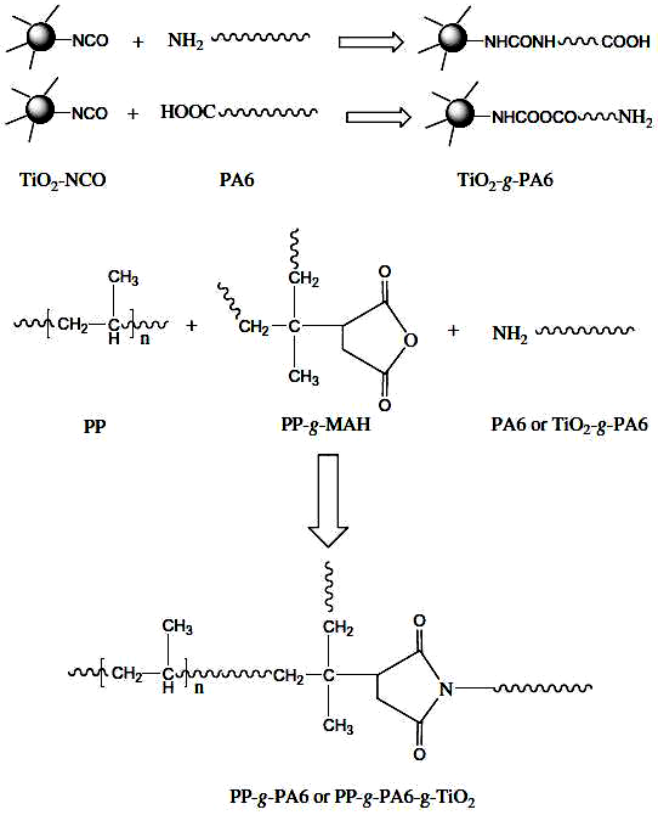

Figure 1-32: Possible chemical reactions between PP, PP-g-MAH, PA6 and TDI-functionalized TiO_2 nanoparticles [68]

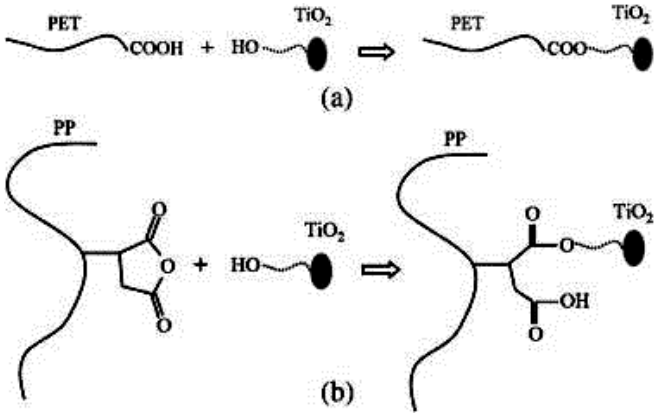

Figure 1-33: Possible chemical reactions between (a) PET and coated TiO_2 nanoparticles, (b) PP-g-MA and coated TiO_2 nanoparticles [70]

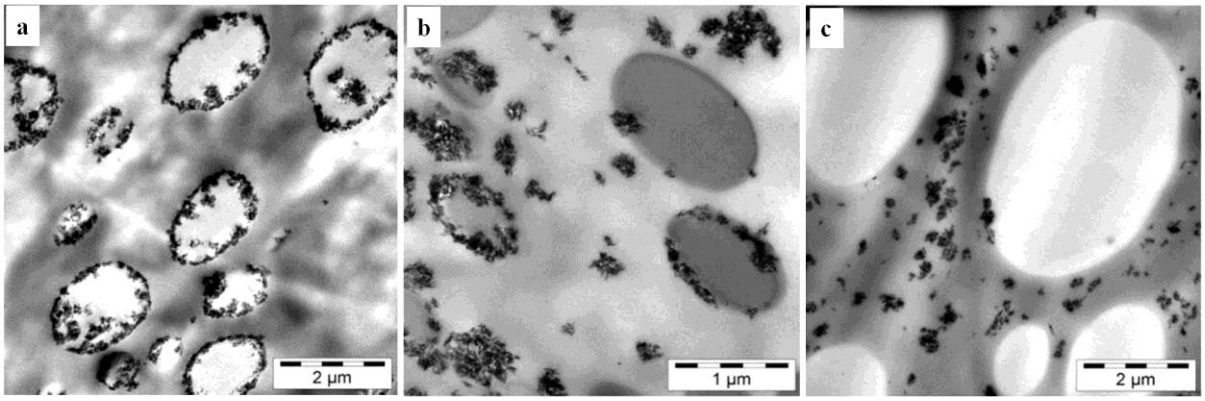

Figure 1-34: TEM images of PET(dispersed)/PP(continuous)/TiO_2(2 %wt) nanocomposites; (a) without PP-g-MAH, with (b) 3 %wt and (c) 6 %wt PP-g-MAH [70]

1.5.4 Concentrated nanocomposites

Lachachi et al. [57] prepared relatively concentrated nanocomposites (more than 10 %wt of nanoparticles) based on PMMA. They mixed the thermoplastic matrix with up to 20 wt% of TiO_2 nanoparticles, with 21 nm median particle size, in an internal mixer. Figure 1-35 shows SEM micrographs of the nano-composites with different concentrations and a micro-composite containing 15 wt% of TiO_2 micron-size particles. Obviously, a continuous network of the nanoparticles is formed in the samples containing more than 15 wt% of nano-TiO_2.

Figure 1-35 also shows the effect of particle size on the morphology of the composites. In other words, while adding 15 %wt of nanoparticles results in a percolated structure of fillers in the polymer matrix, the micro-composite, with the same concentration, has a dispersed morphology of particle agglomerates.

Dangtungee and Supaphol [59] prepared nanocomposites of iPP/TiO_2 in different concentrations (5-30 wt%) using a twin screw extruder. They studied the effects of composition and surface characteristics of rutile TiO_2 nanoparticles (50 nm, average particle size) on melt rheology and extrudate swell of the composites. Increasing the filler content led to a larger wall shear stress in the whole range of shear rates. As can be seen in Figure 1-36, the samples containing stearic acid coated particles had the lowest extent of shear stress. Although the shear viscosity increases with filler concentration, there is no significant increment in the viscosity of samples containing stearic acid coated particles up to 10 wt% of the filler. Lack of morphological

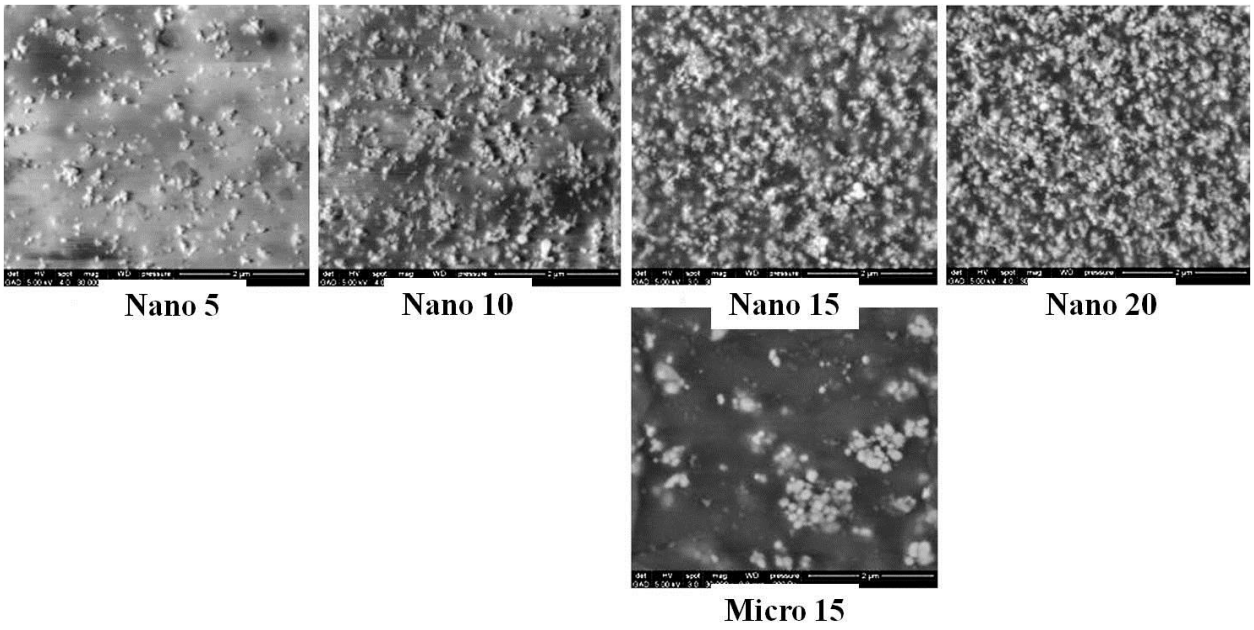

Figure 1-35: SEM images of PMMA-TiO_2 nano-composites and PMMA/TiO_2 (15 %wt) micro-composite (scale bar is 2 μm) [57]

studies does not allow drawing a conclusion about the effect of the surface coatings on filler dispersion and the cause of the changes in the rheological behaviors of the composites.

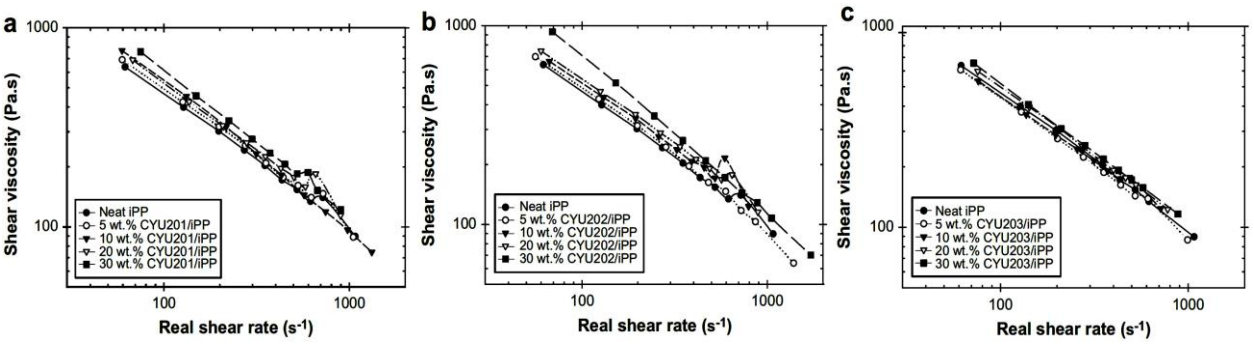

Figure 1-36: Shear viscosity as a function of real shear rate of the neat iPP melt and the iPP melt that had been filled with various contents of (a) uncoated, (b) SiO2-coated, and (c) stearic-coated TiO2 nanoparticles (i.e., CYU201, CYU202, and CYU203, respectively) [59]

1.5.5 Rheology of Polymer/TiO_2 Micro- and Nano-Composite

The presence of a network of filler particles that occupies a large volume fraction of the polymer matrix is responsible for the solid-like behavior of highly filled polymer based composites, even in their melt state [63]. On the other hand, interaction of two filler particles will be important if their separation distance becomes small enough in comparison with their sizes. The wall-to-wall distance D of randomly distributed monodisperse spherical particles with radius (R) can be estimated by

$$D = \left[\sqrt[3]{\frac{4\pi}{3\phi}} - 2 \right] R \tag{1.3}$$

where ϕ is the volume fraction of the particles [63]. From Equation (1.3), it could be concluded that D has the same order of magnitude of R and has a linear relation with the particle radius.

Acierno et al. [63] investigated the effect of particle size on linear viscoelastic behavior of PP-TiO_2 composites containing 4.5 %vol of micro- and nano-size TiO_2. The rheological and morphological studies revealed microstructural evolution in PP-TiO_2 nanocomposites due to thermal annealing, which was not observed in the case of micro-composites. Figure 1-37

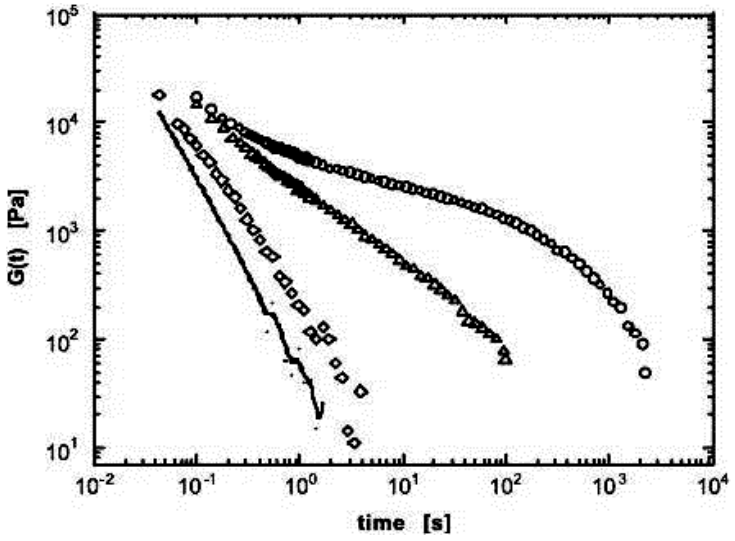

Figure 1-37: Stress relaxation moduli of PP45Micro (diamond), PP45Nano before (triangle) and after (circles) a two-hours thermal annealing, and neat polymer (solid line) [63]

compares stress relaxation behaviors of the PP-TiO_2 micro and nanocomposites. As can be seen, there is an obvious plateau in *G(t)* of the nanocomposite samples annealed at 190°C for two hours. Contrarily, annealing has no significant effect on the relaxation spectrum of the microcomposites. This rheological response was related to the formation of large particle clusters during the annealing time. Figure 1-38 compares the morphologies of the nanocomposites before and after annealing.

Lei and coworkers [65] studied time-dependant dynamic rheological behavior of concentrated (7-70 %wt) masterbatches of a micron-size TiO_2 pigment in a polyethylene matrix [65]. Figure 1-39 shows the changes of the dynamic viscosity with time for a PE sample containing 70 %wt of the TiO_2 filler. There are two time regions for the dynamic viscosities and tanδ of the TiO_2 masterbatches; a viscosity reduction region followed by a viscosity increase with time. The reduction in viscosity was attributed to thin sheet formation and the slippage effect. Migration of TiO_2 particles to the area with lower shear rate in outer edge of the rheometer was responsible for the viscosity increase in the second time region. Formation of a hard shell around the sample with higher concentration was proved by TGA analysis. Figure 1-40 shows the effect of TiO_2 concentration on the time-dependant behavior of the composites. Accordingly, it could be concluded that 30 %wt of the filler is a critical concentration for the time dependency of the compounds. For TiO_2 content greater than 30 %wt, a sudden increase in viscosity is observed.

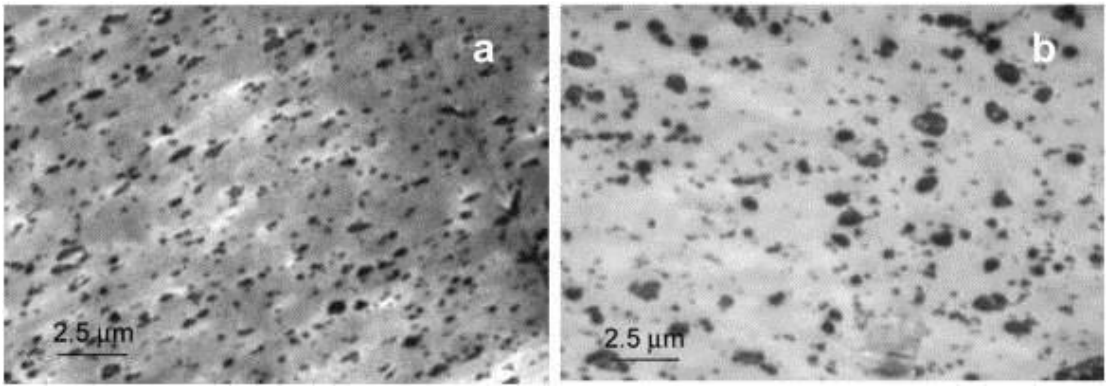

Figure 1-38: TEM images of the PP/TiO2 nanocomposite before (a) and after (b) the annealing [63]

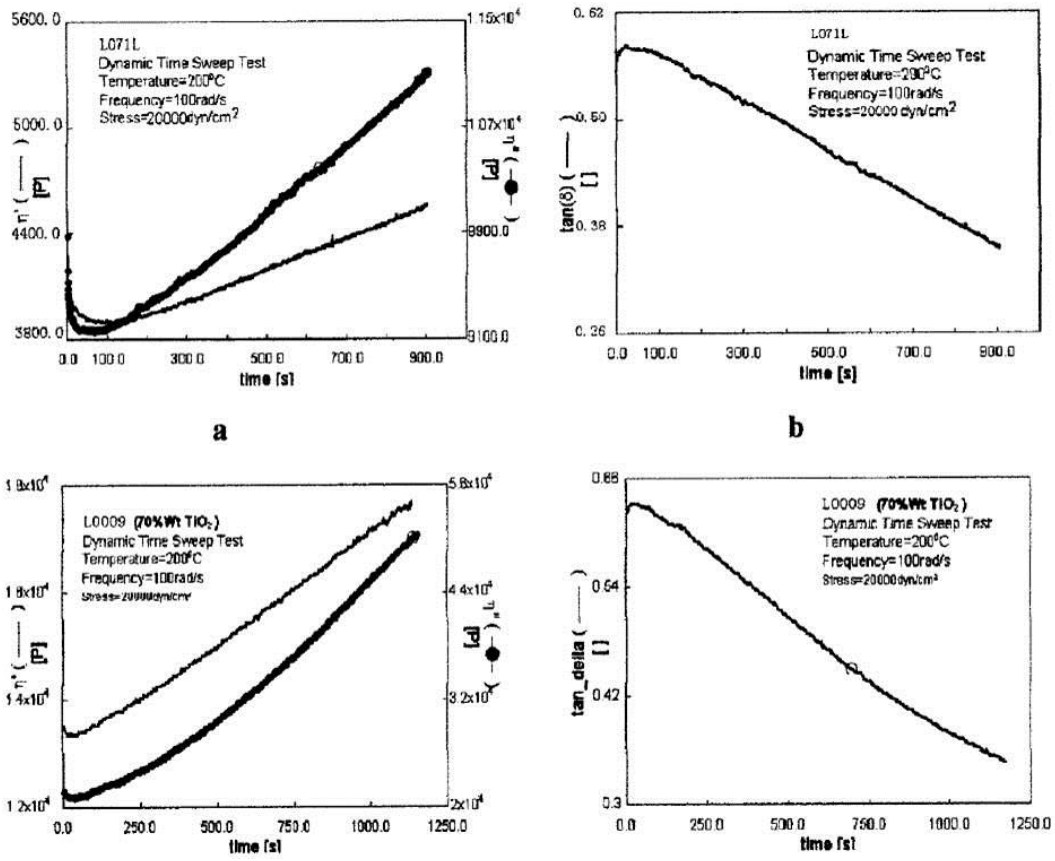

Figure 1-39: Time-dependant behavior of L071L and L0009 with 70 wt % contents [65]

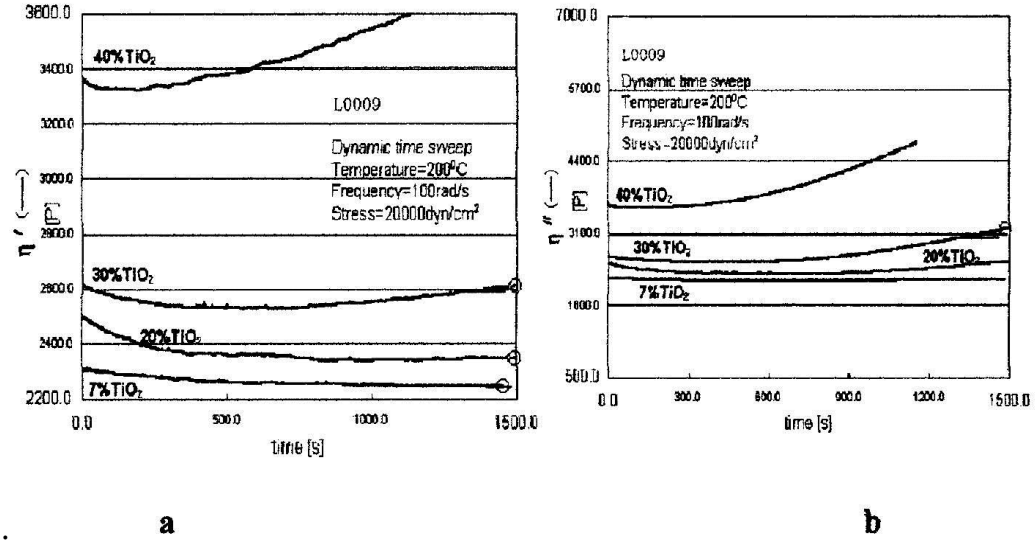

Figure 1-40: Effect of TiO2 content on the time-dependent behavior [65]

Wu et al. [72] studied the effect of particle dispersion on rheological properties of PP filled with micron-size $CaCO_3$. Figure 1-41 shows the variation of the rheological properties of the composites. As can be seen, at concentrations larger than 25 %wt, rheological properties increase significantly with time, which it was attributed to the buildup of a network due to the interaction between calcium carbonate particles. Interestingly, the loading at around 30-35 %wt was considered as a critical concentration at which the viscoelastic properties of the $CaCO_3$/PP systems were governed by particle interactions. Breakup of the agglomerates or their re-alignment may result in a decrease of the rheological properties of more concentrated composites with time. For instance, the destruction of the filler networks controls the rheology of 50 %wt filled composite and results in a viscosity reduction at long times. The contribution of each phenomenon depends on different parameters such as temperature, concentration and surface properties of filler.

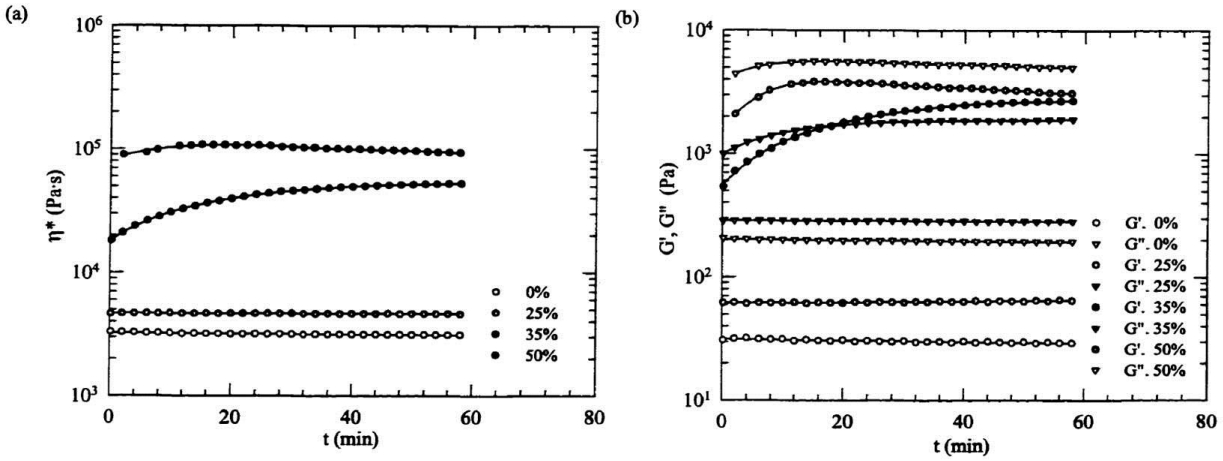

Figure 1-41: Variations of rheological properties of PP/$CaCO_3$ microcomposite with time measured at 200°C (0.01 Hz) [72]

1.6 Electrical Properties of TiO_2 Filled Composites

According to our interest in the development of an electrically conductive TiO_2 filled composite, the effect of adding titanium dioxide fillers on electrical properties of the polymer based composites has been investigated.

Figure 1-42 reports the variation of bulk electrical resistivity (ρ-ohm.m) of iPP-based composites with different TiO_2 contents and at different temperatures [52]. Evidently, adding TiO_2 decreases electrical resistivity. For concentrations lower than 10 wt%, the improvement of electrical conductivity is sharper than that for higher concentrations. It could be attributed to the formation of filler particle agglomeration at higher concentrations which provides a pathway for charge carriers. On the other hand, at elevated temperatures, the reduction rate of electrical resistivity decreases. Stabilizing effect of TiO_2 suppresses thermal generation of charge carriers in the composites and, leads to the smaller effect of temperature on conductivity of the composites, compared to the neat polymer.

1.7 Stretching the nanocomposites

Li et al. [69] also showed that drawing the nanocomposites of PET/PP/TiO_2 leads to void creation around the nanoparticles. Figure 1-43 schematically depicts mechanism of void formation due to nanoparticle debonding from PET phase. Figure 1-44 shows the enlargement of those voids after drawing.

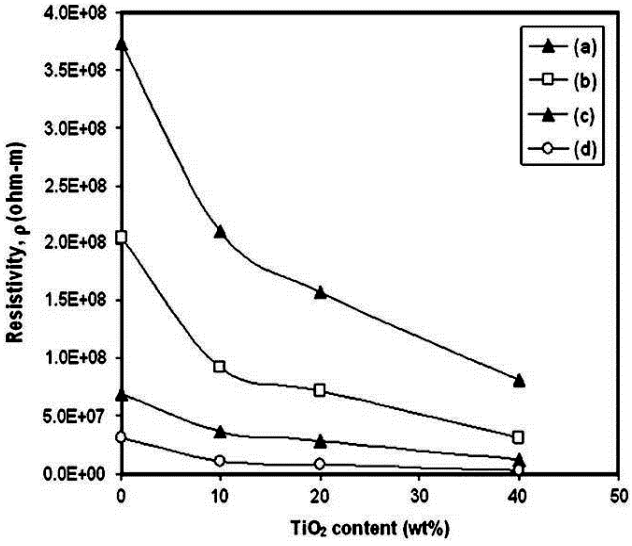

Figure 1-42: Variation of electrical resistivity with filler content at different temperatures: (a) 25 °C, (b) 50 °C, (c) 75 °C and (d) 100 °C [52]

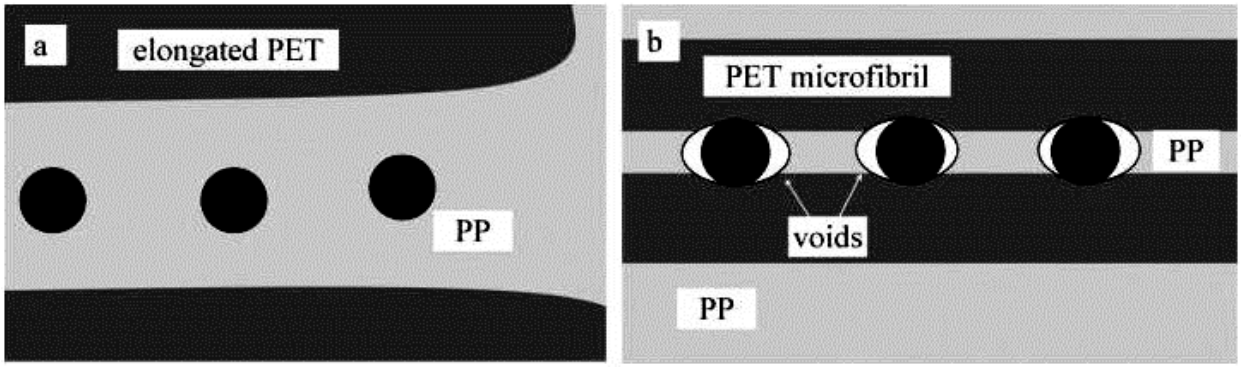

Figure 1-43: Schematic representation of (a) slightly drawn PET/PP/TiO_2 and (b) PET/PP/TiO_2 drawn strand [69]

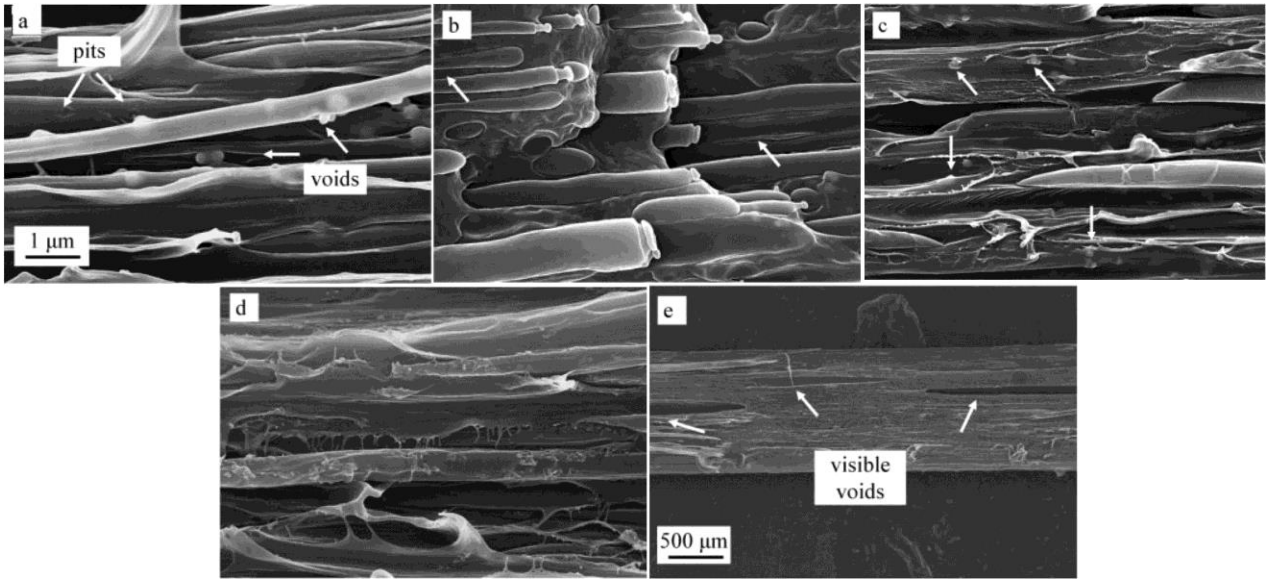

Figure 1-44: SEM images of drawn strands and slightly drawn extrudates: (a) PET/PP/2T300 drawn atrand, (b) PET/PP/C/2T300 slightly drawn extrudate, (c) PET/PP/C/2T300 drawn strand, (d) PET/PP/2T15 drawn strand, (e) PET/PP/2T15 drawn strand at low magnification [69]

1.8 Problem Identification and Originality of the Work

As it was summarized in the preceding sections of literature review, reducing the costs of mass production of solar cells is one of the main approaches to find reliable cost-effective renewable energy sources. Although simplicity and inexpensive materials of DSSCs have made them very interesting, the high temperature treatment of the TiO_2 layer brings a limitation in their cost-effectiveness and making light and durable flexible DSSCs based on plastic substrates. Therefore, developing a novel process to produce the photoelectrode at relatively low temperatures is necessary. In this PhD thesis, it is aimed to develop a porous composite film structure containing TiO_2 nanoparticles which can be used as the photoelectrode of DSSC. To the best of our knowledge, it is the first work on using polymer melt processing methods to produce a flexible polymer composite layer at relatively low temperatures that makes it possible to use plastic substrates. In the first stage, it is important to investigate electrical properties of the polymer composite containing TiO_2 because it is necessary to have a TiO_2 network to collect the photogenerated charges. Relation among composition, morphology and electrical properties of the blend of the thermoplastic polymer and TiO_2 nanoparticle is one of the most interesting subject that has not been well studied. Moreover, processability of the compound is a critical factor in polymer melt processing. Accordingly, it is essential to investigate the relation among morphology, rheology, and electrical properties with an emphasis on percolation of the TiO_2 phase in the thermoplastic matrix. As it was reviewed, stretching is an efficient route in generating pores in filled polymer films. However, the relation between stretching process conditions and final properties of the porous films should be extensively studied for the composite films containing TiO_2. Finally, the functionality of such composite film as photoelectrodes for DSSC should be examined.

1.9 Objectives

The main target of the present research is to develop a novel method to manufacture flexible solar cells from commodity polymers using common melt processes. Among the different types of photovoltaic cells, dye-sensitized solar cells (DSSC) were identified with a significant potential

to be produced via polymer melt-processing techniques. Therefore, the main objective in this PhD project is

"To prepare a conductive porous structure from a polymer/TiO_2 nanocomposite film applicable in photosensitive layer of DSSC".

In order to achieve this goal, different specific objectives are proposed:

I : To prepare/control the required morphology of polymer nanocomposites through melt-compounding of the polymer matrix and TiO_2 nanoparticles to obtain percolated conductive structure of TiO_2 in a nano/mesoporous polymer medium,

II : To develop a mesoporous thin film through stretching of nanocomposite film under controlled conditions,

III : To sensitize the flexible porous film with a photosensitive dye and to characterize the degree of sensitization

IV : To assemble and characterize a complete flexible cell using the prepared photosensitive polymer nanocomposite film

CHAPTER 2 ORGANIZATION OF ARTICLES AND THESIS STRUCTURE

In the chapters 3 to 6 of this thesis, main achievements of the work are presented in the format of four scientific journal papers. Each paper includes a concise introduction, experimental, and comprehensive results and discussion related to the findings of each part of the research work.

Chapter 3 studies the "Morphology and Properties of Highly Filled iPP/TiO_2 Nanocomposites". Morphology and thermal / mechanical properties of the compatibilized and uncompatibilized nanocomposites based on isotactic polypropylene (iPP) containing a wide range of TiO_2 nanoparticles were investigated. The effect of composition and anhydride-modifid PP (AMPP) addition (as a compatibilizer) on microstructure and dispersion of TiO_2 were investigated. A micromechanical analysis was utilized to assess the interfacial strength between polymer and TiO_2 phases. The article was published in the *Journal of Polymer Engineering and Science* [73].

Chapter 4 discusses about "Relationship between Rheological and Electrical Percolation in a Polymer Nanocomposite with Semiconductor Inclusions". In this paper, the effect of TiO_2 nanoparticles (as the semiconductive inclusions) on electrical and rheological properties of the nanocomposites was investigated. Percolation thresholds of the nanocomposites were determined based on the variation of their electrical and rheological properties with TiO_2 content. The paper has been accepted for publication in *Rheologica Acta* [74].

Chapter 5 is a paper on "Microstructure and Properties of Porous Nanocomposite Films: Effects of Composition and Process Parameters". The effects of different parameters of the stretching process on the microstructure and properties of the nanocomposite films were studied in detail. Porosity and surface area of the pores developed in the films due to stretching at different temperatures, extension rates, and draw ratios were two of the main characteristics that were investigated. The paper was submitted to the *Journal of Polymer International*.

Chapter 6 is particularly devoted to "Development of a Polymer Nanocomposite Film Based Flexible Photoelectrode for Dye-Sensitized Solar Cells". The functionality of the porous

nanocomposite film in generating electricity from light was examined in this work. This chapter is under preparation as an article for the *Journal of Nanoscience and Nanotechnology*.

A general discussion covering and connecting the different findings in the preceding chapters is presented in Chapter 7. At the end, a brief conclusion about the achievements of this PhD research project and some recommendations for future studies are given.

It should be mentioned also that Appendix 1 presents the results of a study on isothermal and non-isothermal crystallization of iPP/TiO_2 nanocomposites which is a side work in continuation of the findings of Paper 1 (Chapter 3).

CHAPTER 3 ARTICLE 1: MORPHOLOGY AND PROPERTIES OF HIGHLY FILLED IPP/TIO2 NANOCOMPOSITES

Ahmad Zohrevand, Abdellah Ajji*

Center for Research on High Performance Polymer and Composite Systems (CREPEC), Department of Chemical Engineering, Ecole Polytechnique du Montreal, Montreal, QC, Canada

Frej Mighri

Center for Research on High Performance Polymer and Composite Systems (CREPEC), Department of Chemical Engineering, Laval University, Quebec, QC, Canada

Abstract

Nanocomposites based on isotactic polypropylene (iPP) and titanium dioxide (TiO_2) nanoparticle containing 1-15 vol% (4.6 to 45.5 wt%) of the nanoparticle were prepared by the melt blending process. The effect of an anhydride-modified polypropylene as a compatibilizer on dispersion of TiO_2 nanoparticles was assessed using SEM. TGA and DSC analysis were performed in order to study the thermal properties of the nanocomposites. Crystalline structures of iPP in the presence of TiO_2 were analyzed by XRD. Mechanical properties of the nanoparticles were measured and a micromechanical analysis was applied to quantify interface interaction between the polymer and particle. SEM results revealed improvement of TiO_2 particle dispersion by adding the compatibilizer. It was shown that the thermal stability and crystalline structure of the nanocomposite are significantly affected by the state of particle dispersion. TiO_2 nanoparticles were shown to be strong β-nucleating agents for iPP, especially at concentrations less than 5 vol%. Presence of the β-structure crystals reduced the elastic modulus and yield strength of the nanocomposites. Micromechanical analysis showed enhanced interaction between organic and inorganic phases of the nanocomposites.

3.1 Introduction

In the last few years, most industrial and academic research focused on process-structure-properties relationship of polymer nanocomposites containing inorganic nanosized reinforcements [1-5]. Depending on their concentration, aspect ratio and state of dispersion into the polymeric matrix, nanoparticles provide large interfacial area with the matrix leading to outstanding properties of the corresponding nanocomposites [1-4]. Since there is a good balance between process parameters and final properties of isotactic polypropylene (iPP), the latter has attracted considerable attention as a thermoplastic matrix for the development of nanocomposites via melt blending process [5, 6]. Polypropylene-based nanocomposites containing different types of inorganic nanoparticles, such as nanoclay, calcite ($CaCO_3$) and silica (SiO_2), have been studied extensively [5, 7-9]. Among the various inorganic nanoparticles, titanium dioxide (TiO_2) is a wide band gap (E_g=3.2 eV) semiconductor with high refractive index (~ 2.6), good UV absorption ability, low cost and high availability. TiO_2 is added to a polymeric matrix to particularly modify its electrical, optical and mechanical properties [10-13]. Although micron-size TiO_2 particles have been widely used as white pigments in PP [14], there is a lack of comprehensive information about structure-properties relationship of PP/TiO_2 nanocomposites.

As a semi-crystalline polymer, properties of PP are strongly affected by its crystalline structure. Isotactic PP is known as a typical polymorphic polymer that, due to different packing of its molecular chain helix into the unit cell, exhibits four main crystalline forms; the monoclinic α-phase, the hexagonal β-phase, the orthorhombic γ-phase and the mesomorphic form namely smetic phase. In addition to tacticity, formation of these crystalline forms is also dependent on molecular weight and crystallization conditions [15-18]. The most thermodynamically stable and, consequently, the most common crystal form of iPP is the α-phase which is obtained under conventional processing conditions [19]. The *γ*-phase and the smetic phase form in low molecular weight or under pressure and due to quenching, respectively. However, the β-form crystal of iPP is a metastable phase which is occasionally observed as a minor crystal phase in iPP that tends to transform to *α*-form under mechanical to thermal stimulates [17, 18, 20-23]. Although presence of the β-phase leads to lower modulus and yield strength in iPP, its excellent effects on enhancement of toughness, impact strength and heat distortion temperature of iPP has attracted much attention from research and industrial applications [17-19, 24-26].

Isothermal crystallization, quenching, large temperature gradient, shear-induced crystallization and addition of extrinsic β-nucleating agents, other polymers or inorganic fillers may cause the formation of β-phase crystals in iPP [18, 19, 23, 25-29]. Addition of selective β-nucleating agents, which are generally crystallizable organic compounds with low molecular weight (e.g. quinacridone dye, triphenodithiazine and pimelic acid), is the common method to obtain high β-phase content in iPP [16, 18, 19, 22, 23, 26].

Conventional inactive fillers like $CaCO_3$, mica and glass fiber, which are inert components during crystallization, have been used to compensate stiffness of β-nucleated iPP retaining its toughness while, active fillers, like talc, strongly promote the *α*-modification of iPP [30]. However, effect of incorporation of different nanoparticles on crystalline structure of iPP, especially the β-phase, has been recently investigated. Due to α-heterogeneous nucleating ability of inorganic particles, it is hard to obtain β-iPP composites with high relative β-phase content. However, Dai *et al.* changed the α- nucleating ability of montmorillonite (MMT) by chemical surface modification using pimelic aid (HA) as a β-nucleator [24]. Effect of $CaCO_3$ nanoparticles with different surface modification on crystalline structure and mechanical properties of iPP have been studied extensively [9, 31]. Zhang *et al.* [9] and Wan *et al.* [31] reported a β nucleating role for $CaCO_3$ nanoparticles that could be promoted by using different surface modifiers based on polyethylene nonyphenol or aluminate and stearic acid coupling agents. Lin *et al.* [32] showed that PET fibers could have a synergistic effect on the β nucleating role for $CaCO_3$ nanoparticles in a PP/$CaCO_3$/PET ternary system. In contrary, negative or inert effects of $CaCO_3$ on β-phase crystal content of iPP have been reported by other authors [33, 34]. WAXD studies on crystalline structure of iPP nanocomposites containing SiO_2 nanoparticles, prepared by sol-gel method, revealed that presence of the nanoparticles results in formation of β-phase crystal [8]. However, Chen *et al.* [7] reported an opposite effect of SiO_2 nanoparticles in the nanocomposites based on iPP, prepared by twin-screw melt extrusion, that restrains crystallization of the β-phase. Medellín-Rodríguez *et al.* [28] observed that presence of an organomodified clay at low concentration cause to formation of β-phase but it was inhibited at high clay contents. In the case of iPP/ZnO nanocomposites, Zhao *et al.* [35] showed that ZnO nanoparticles can act as an inorganic β-nucleating agent for iPP while other authors did not report such effect [36]. Zeng *et al.* [29] recently reported strong effect of tetra-needle-shaped zinc oxide whisker (T-ZnOw) in inducing β-phase crystals. A stronger β-nucleating ability was also observed for silver

nanocrystals (Ag NC), compared to commercial silver nanoparticles (Ag NP) with no surface modification [19, 26]. Accordingly, one of the the main effects of nanoparticles on iPP is the alteration of its crystalline structure [8]. Noll and Knoer [37] reported a heterogeneous nucleation role of TiO_2 nanoparticles in the PP/TiO_2 nanocomposites containing up to 4 vol% of TiO_2.

On the other hand, there are many uncertainties about the effect of dispersed nanoparticles on thermal stability of the corresponding nanocomposites [1, 4]. Mina et al. [38] showed that adding 10-40 wt% (2.3-12.3 vol%) of TiO_2 microparticles increases the onset temperature of thermal degradation of PP/TiO_2 microcomposites during TGA analysis under inert (N_2) atmosphere. A similar effect was also observed for low content of TiO_2 nanoparticles (less than 2 wt%) in melt-spun PP fibers [39].

Achieving a good dispersion of hydrophilic TiO_2 nanoparticles in an organic polymeric matrix is the main challenge during the preparation of polymer/TiO_2 nanocomposites by melt blending methods [3]. In fact, surface hydrophilicity of unmodified TiO_2 nanoparticles causes its poor compatibility with PP and leads to a bad dispersion and high extent of TiO_2 agglomeration. Therefore, the addition of an adequate compatibilizer or surface modification of TiO_2 improves its dispersion in the polymer matrix [40]. Ou et al. [41] showed that the compatibilization effect of maleated polypropylene (PP-g-MAH) was evident on the improvement of the mechanical properties of injection molded PP/polyamide 6/functionalaized-TiO_2 nanocomposites.

From the above literature review, it is clear that there is no extensive study on morphology, thermal and mechanical properties of PP/TiO_2 blends. Therefore, the aim of the present study is to investigate the effect of adding TiO_2 nanoparticles at various volume concentrations, up to 15 vol% (45.5 %wt), on PP structure and the thermal and mechanical properties of PP/TiO_2 nanocomposites. Correlation of these properties to the nanocomposite microstructure is also considered. In order to achieve a better interaction between the organic (PP) and inorganic (TiO_2) phases, an anhydride modified PP was used as compatibilizer.

3.2 Experimental

3.2.1 Materials

An isotactic polypropylene (iPP) homopolymer (PP4712E1 from ExxonMobil) was used as the polymer matrix and an anhydride-modified polypropylene (AM-PP) supplied by DuPont (Bynel 50E571) was utilized as the compatibilizer. Table 3.1 summarizes the main characteristics of these two polymers.

A commercial grade TiO_2 nanoparticle (AEROXIDE TiO2 P 25 produced by Evonik) was used in this study. According to the information provided by the supplier, it consists of an hydrophilic fumed TiO_2 with a density ρ of 4.26 g/cm^3 and an average primary particle size of 21 nm and a nano crystalline structure composed of a mixture of anatase:rutile (79:21 wt%). Figure 3-1 shows a TEM image of the TiO_2 nanoparticles. Most of the particles are spherical with sizes ranging from 15 nm to 45 nm.

3.2.2 Nanocomposite preparation by twin-screw extrusion process

The compatibilized and uncompatibilized PP/TiO_2 nanocomposites containing 1 to 15 vol% (4.6 to 45.5 wt%) of TiO_2 were prepared via a masterbatch method using a tightly intermeshing co-rotating twin-screw extruder (Leistritz ZSE-18HP-40D, Germany) with Ø = 18 mm and L/D =

Table 3.1: Main characteristics of the resins

Polymer	Designation	Supplier	MA Content (%Wt)	MFR[a] (g/10 min)	Density (ρ) (g/cm^3)	η_0[b] (Pa.s)
iPP	PP4712E1	ExxonMobil	-	2.8	0.9	8000
AM-PP	Bynel® 50E571	DuPont	0.1[c]	3.5	0.89	5800

[a] ASTM D1238 (230°C/2.16 Kg)
[b] Zero-shear viscosity; obtained from complex viscosity measured in frequency sweep test at 205°C
[c] From the supplier

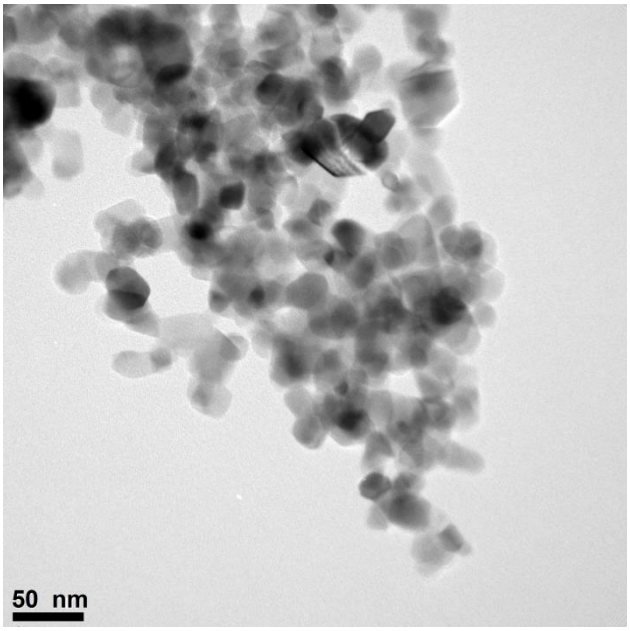

Figure 3-1: TEM image of the used TiO_2 nanoparticles

40 equipped with a typical compounding screw profile which is shown in Figure 3-2. Code GFA, in the Figure 3-2, represents the conveying elements, which all were 2-channel, and the last two numbers refer to the pitch size and total length of each element, respectively. The code KB refers to kneading blocks and the two last numbers are respectively the kneading disk thickness and their staggering angles. In the compounding process, first, two masterbatches based on PP and AM-PP matrices containing 18 vol% (51 wt%) of the TiO_2 nanoparticles prepared through two passes of extrusion. Then, in another extrusion run, the masterbatches were diluted to lower concentrations by adding neat PP. All nanocomposites were prepared using a constant screw speed of 200 rpm and the same temperature profile: 160, 190, 195, 200, 202, 205, 205 and 205°C (from the main hoper to the die, see Fig. 2). Neat iPP and AM-PP, nanocomposites and TiO_2 nanoparticles were vacuum dried at 80°C for 8 hours before each mixing run. Materials were fed to the extruder, from the main hopper, using a volumetric feeder (for the polymers and the composites) and a high-precision powder feeder (K-Tron, USA) for TiO_2 nanoparticles. In order to minimize thermo-mechanical degradation during intensive mixing, 3000 ppm of antioxidant (Ciba IRGANOX B 225) was added. Table 2 reports the compositions of the samples prepared. It is noticeable that the compositions of the samples, based on volume fractions (vol.%), were calculated using the densities of the related polymer matrices (iPP and AM-PP), as reported in

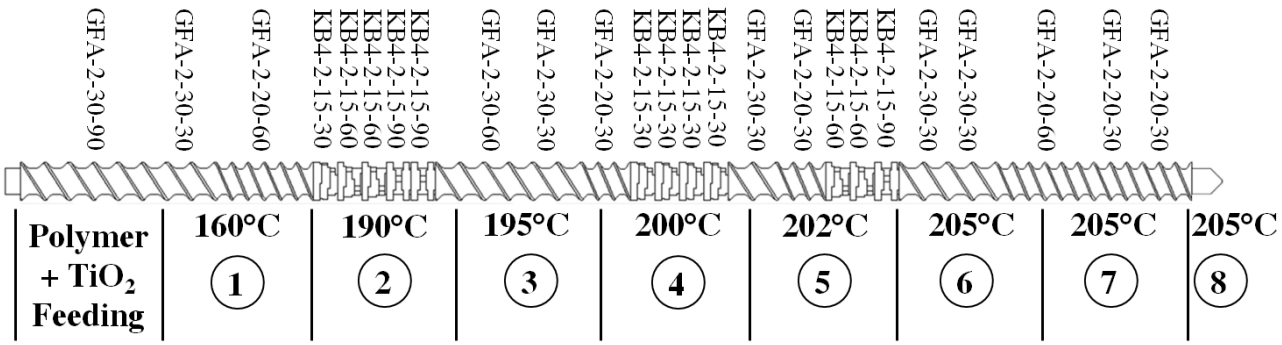

Figure 3-2: Schematic view of the screw configuration and the temperature profile used in the compounding process (GFA: co-rotating conveying free-meshing elements, KB: kneading blocks)

Table 3.1, and density of TiO_2 nanoparticles.

3.2.3 Sample Characterization

For further characterization, the dried compounded pellets were compression-molded into discs and dumbbell specimens using a Carver hot mini-press (Wabash, USA) under nitrogen atmosphere.

The dispersion of TiO_2 nanoparticles in the polymeric matrices was studied by using field emission gun scanning electron microscopy (JEOL 7600F FEG) operated at 2 kV. In order to have high-quality images, cross sections of the samples were cut under liquid nitrogen using a glass knife of a cryo-microtome (RM 2165, Leica, Germany) equipped with a cryo-chamber (LN 21).

In order to study the thermal stability of the composites and to characterize their composition, thermal gravimetric analysis (TGA) was performed using a TGA Q500 (TA Instruments, USA). During thermal characterization, the samples were heated under different atmospheres up to 800°C at a rate of 10°C/min.

Dynamic thermomechanical properties of the composites were measured using a dynamic mechanical and thermal analyzer (DMTA 2980, TA Instruments) equipped with a dual-cantilever

Table 3.2: Composition of the prepared PP/TiO_2 nanocomposites

Sample designation	TiO2 [vol%]	AM-PP [vol%]	iPP [vol%]
PP	-	-	100
AM-PP	-	100	-
PP-T-1	1	-	99
PP-T-3	3	-	97
PP-T-5	5	-	95
PP-T-10	10	-	90
PP-T-15	15	-	85
PP-AM-T-1	1	4.6	94.4
PP-AM-T-3	3	13.9	83.1
PP-AM-T-5	5	23.2	71.8
PP-AM-T-10	10	46.4	43.6
PP-AM-T-15	15	69.7	15.3

test fixture. During the characterization, samples were heated from -60 to 120°C at a heating rate of 2 °C/min and frequency of 1 Hz.

Thermal properties and crystallization behavior of PP in the presence of TiO_2 nanoparticles were analyzed by a differential scanning calorimeter (DSC Q1000, TA Instruments, USA). The samples were first heated up to 220°C at a rate of 10°C/min then kept at that temperature for 3 minutes to eliminate any prior thermal and mechanical histories. After the first heating run, the samples were cooled down to 50°C at a rate of 10°C/min, then they were heated again in a second heating cycle at 10°C/min to record the crystallization and melting thermograms.

The effect of TiO_2 nanoparticles on the crystalline structure of the polymeric phase was investigated through wide angle x-ray diffraction (WAXD) patterns recorded using a Philips X'PERT difractometer (PANalytical, The Netherlands) with the X-ray source of Cu-Kα (wavelength α=1.542 Å) and scanned from 2θ = 10 to 40 degrees.

Tensile characterization was carried out using an Instron 3365 Universal Testing System (USA) according to ASTM D638. The deformation speeds, used to measure the tensile modulus

and the ultimate tensile deformation, were 1 mm/min and 10 mm/min, respectively. Reported values correspond to the average of at least 5 tests on identical specimens.

3.3 Results and Discussion

3.3.1 Dispersion Characterization in Uncompatibilized and Compatibilized Nanocomposites

The state of dispersion of TiO_2 nanoparticles has a significant effect on the final properties of the TiO_2 based nanocomposites. A fine dispersion and distribution of these nanoparticles in the polymeric matrix can be achieved by an efficient mixing process, which breaks TiO_2 aggregates/agglomerates to provide a larger interfacial area between the TiO_2 nanoparticles and the surrounding polymer phase. Figure 3-3 representatively shows SEM micrographs of a cryo-microtomed cross section of uncompatibilized (PP-T) and compatibilized (PP-AM-T) samples containing 3 vol% (Figure 3-3a and 3b) and 5 vol% (Figure 3-3 and 3d) of TiO_2 nanoparticles. Figure 3-3 shows that there are smaller particle aggregates in the lower concentration (3 vol%, Figure 3-3a and 3b), compared to the concentrated samples containing 5 vol% TiO_2 (Figure 3-3c and 3d). In fact, the degree of dispersion and final TiO_2 aggregates size strongly depend on nanoparticle concentration. In other words, the probability of TiO_2 aggregation increases with decreasing the interparticle distance, i.e., with increasing TiO_2 concentration [42]. Figure 3-3 also shows the effect of adding the anhydride-modified PP (AM-PP), as a compatibilizer, on the morphologies of the nanocomposites. In the nanocomposite containing 3 vol% TiO_2, adding AM-PP significantly improved the dispersion of the nanoparticles. It can be seen that in the sample PP-AM-T-3 (Figure 3-3b), despite there are few particle aggregates larger than 1 µm, most of the aggregates have sub-micron size and even there are tiny aggregates formed from few single nanoparticles. This could be related to compatiblizing role of AM-PP that leads to a better distribution and dispersion of the TiO_2 nanoparticles, compared to PP-T-3 (Figure 3-3a). Reaction between the anhydride groups of AM-PP and the hydroxyl groups on surface of TiO_2 could be responsible for improving interactions between hydrophilic TiO_2 particles and the organic PP matrix [43]. As it can be seen in Figure 3-3c and 3d, by increasing TiO_2 content to 5 vol%, the number and size of TiO_2 aggregates increases and microstructures of compatibilized

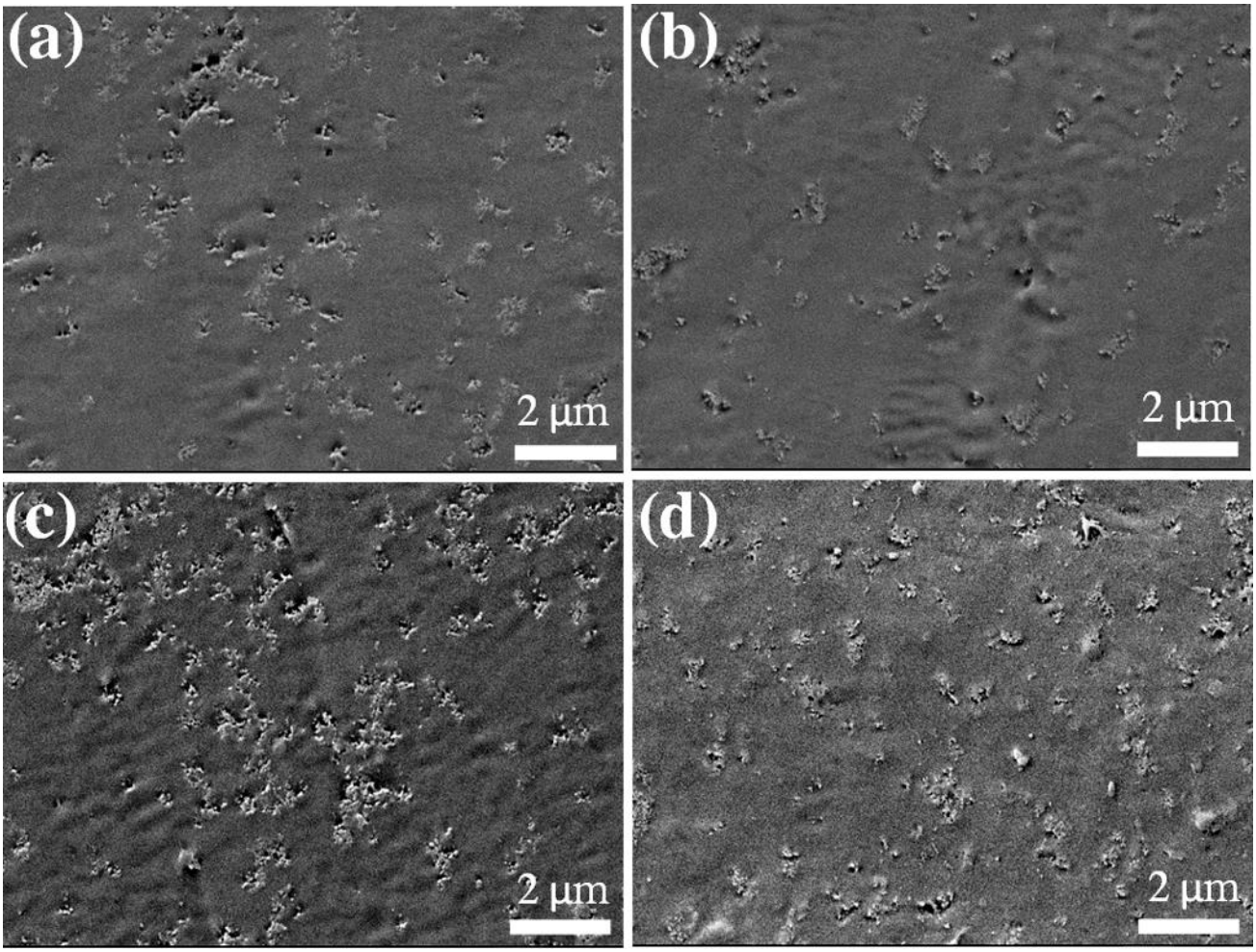

Figure 3-3: SEM micrographs of uncompatibilized (PP-T) and compatibilized (PP-AM-T) nanocomposite samples containing 3 and 5 vol% of TiO_2: (a) PP-T-3, (b) PP-AM-T-3, (c) PP-T-5, and (d) PP-AM-T-5

and uncompatibilized sample become more similar. However, the TiO_2 aggregates in PP-AM-T-5 were rather isolated spherical while the TiO_2 nanoparticles in PP-T-5 formed connected cluster structure.

3.3.2 Thermal Characterization of Compatibilized and Uncompatibilized Nanocomposites

Figure 3-4 shows TGA and differential thermogravimetric (DTG) curves of the PP and PP/TiO2 nanocomposites containing 1, 5 and 15 vol% of TiO_2 under air (Figure 3-4a) and N_2 (Figure 3-4b). Figure 3-5 summarizes the effect of TiO_2 nanoparticle on the thermal stability of PP in compatibilized and uncompatibilized nanocomposites in terms of T_{peak} (Figure 3-5a) and $T_{5\%}$ (Figure 3-5b). T_{peak} and $T_{5\%}$ are respectively the temperatures corresponding to the maximum peak in the derivative graphs and 5 wt% of PP loss. As it can be seen from the inset of Figure 3-4a and from Figure 3-5a, T_{peak} under oxidative atmosphere (air) was shifted to higher temperatures by adding TiO_2 nanoparticles and reached a plateau at TiO_2 concentrations higher than 5 vol%. However, stabilizing effect of TiO_2 nanoparticles under inert atmosphere (N_2) is not as much as that under the oxidative conditions. While adding 5 vol% TiO_2 increases the T_{peak}, under oxidative atmosphere, as high as ~65°C, it results to around 13°C higher T_{peak}, under inert atmosphere, followed by a reduction to the same value as neat PP in the nanocomposite. According to Figure 3-5, thermal stability of compatibilized nanocomposites is not significantly different from that of ncompatibilized ones and the differences are in the range of experimental errors. Figure 3-5a shows that presence of TiO_2, except in the nanocomposites with 1 vol% of TiO_2, did not significantly alter the PP onset degradation temperature ($T_{5\%}$) of under oxidative (air) atmosphere. On the other hand, T_{peak} of the nanocomposite under inert condition (N_2) reached a maximum value at 1 vol% of TiO_2 and decreases at higher TiO_2 concentration.

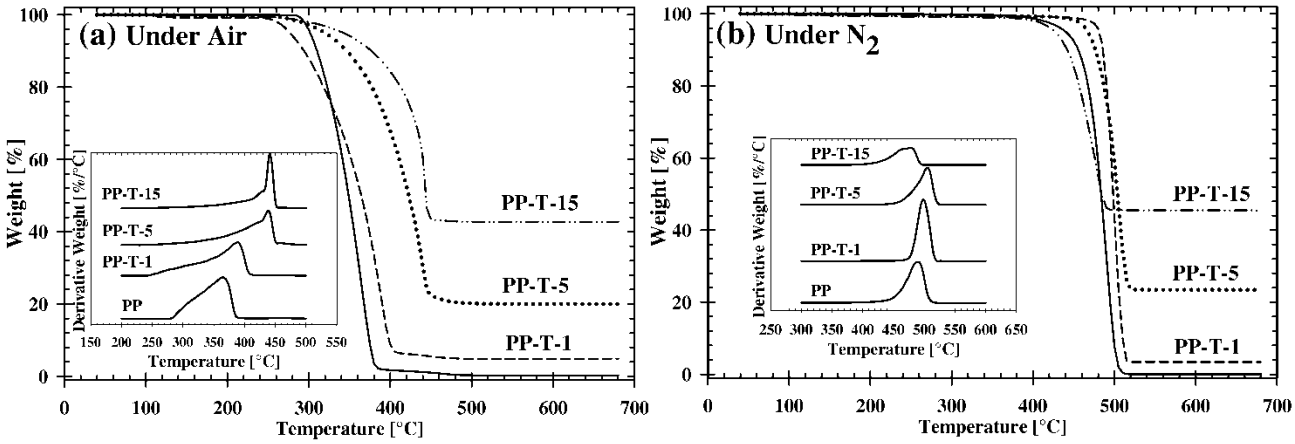

Figure 3-4: TGA graphs of uncompatibilized nanocomposites under (a) oxidative atmosphere and (b) inert atmosphere. Insets depict the derivative data

There are several chemical/physical mechanisms that could affect the stabilization effect of TiO_2 nanoparticles. These mechanisms include the reaction of the free radicals coming from the PP matrix with the metal groups of the TiO_2 nanoparticles, the adsorption of volatile degraded materials on TiO_2 surface, barrier effect of TiO_2 nanoparticles and the reduction of molecular mobility of polymers surrounding TiO_2 nanoparticles [44]. The significant increase of T_{peak} under oxidative atmosphere could be related to the barrier effect of TiO_2 nanoparticles, which decreases the diffusion of oxygen into the nanocomposites. In addition, the adsorption of volatile degraded materials on the surface of TiO_2 nanoparticles may retard the degradation process. Therefore, the increase of interfacial area between PP and TiO_2 with increasing TiO_2 concentration up to 5 vol% enhances the thermal stability (T_{peak}) of the nanocomposite. Accordingly, due to the formation of TiO_2 aggregates at higher TiO_2 concentrations, the PP/TiO_2interfacial area does not increase with TiO_2 content and, it results in the presence of a plateau in the T_{peak} curve under oxidative condition. The interaction between PP molecular chains and large surface area of TiO_2 nanoparticles reduces molecular mobility of PP macromolecules in their solid state and consequently increases the thermal stability of the PP/TiO_2 nanocomposite. It could be the main mechanism resulting in the relatively small stabilizing effect of TiO_2 under inert atmosphere.

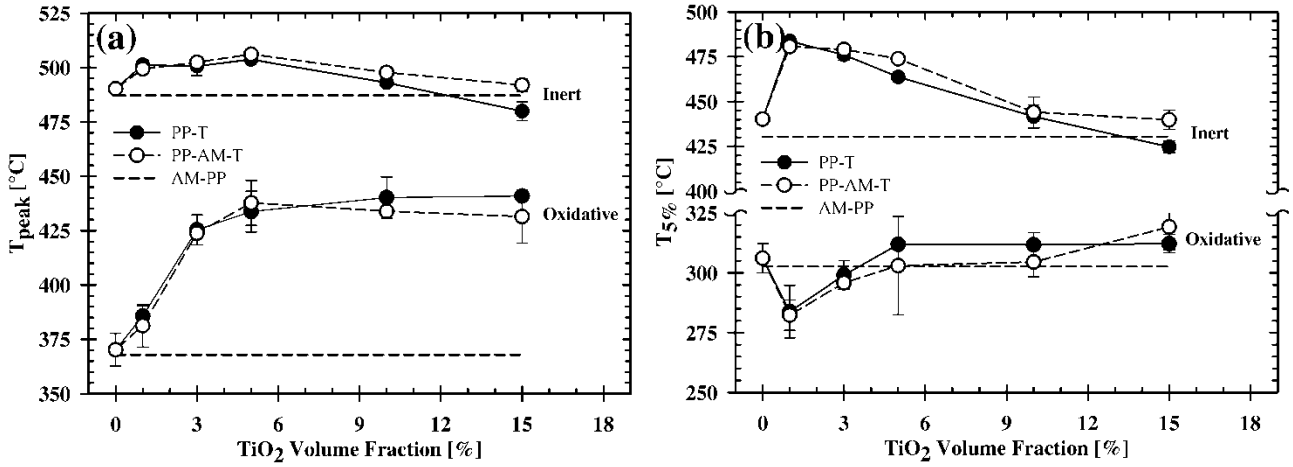

Figure 3-5: T_{peak}, and (b) onset temperature, $T_{5\%}$, of the PP/TiO_2 nanocomposites as a function of TiO_2 volume concentration

The glass transition temperatures (T_g) of neat PP and PP/TiO_2 nanocomposites can be determined from the peak of the loss factor (tan δ) curves versus temperature shown in Figure 3-6. As shown by the figure, addition of 1 vol% of TiO_2 increased T_g of PP from 5.3°C to 7.1°C. This is a good indication of the effect of TiO_2 on the reduction of PP molecular chain mobility. However, for higher TiO_2 volume concentrations (3, 5, 10 and 15 vol %), the T_g of the corresponding PP/TiO_2 nanocomposites decreased to 5.3, 5.0, 5.8 and 4.6°C. The larger inter-particle spacing in polymer/TiO_2 nanocomposites, due to the aggregation of TiO_2 nanoparticles, leads to enhance the mobility of PP molecular chains and consequently decreases the T_g of PP phase in the nanocomposites [45].

3.3.3 Crystalline Structure of PP/TiO_2 Nanocomposites

The properties of PP and its corresponding PP/TiO_2 nanocomposites are strongly controlled by PP crystalline structure. DSC characterization was performed in order to investigate the effect of TiO_2 nanoparticles on the crystalline structure of the PP phase. Figure 3-7 shows DSC curves of the first heating run and the cooling run for the neat polymers and the nanocomposites containing 1 to 15 vol % of TiO_2 nanoparticles. It should be noted that the DSC curves of the samples recorded during the second heating run are presented in Figure 3-10 of the supporting information

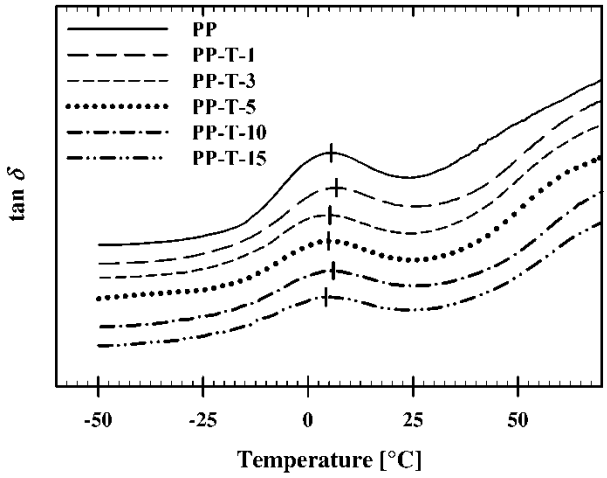

Figure 3-6: *tan* δ versus temperature for PP-T nanocomposites at various TiO_2 concentrations at 1 Hz

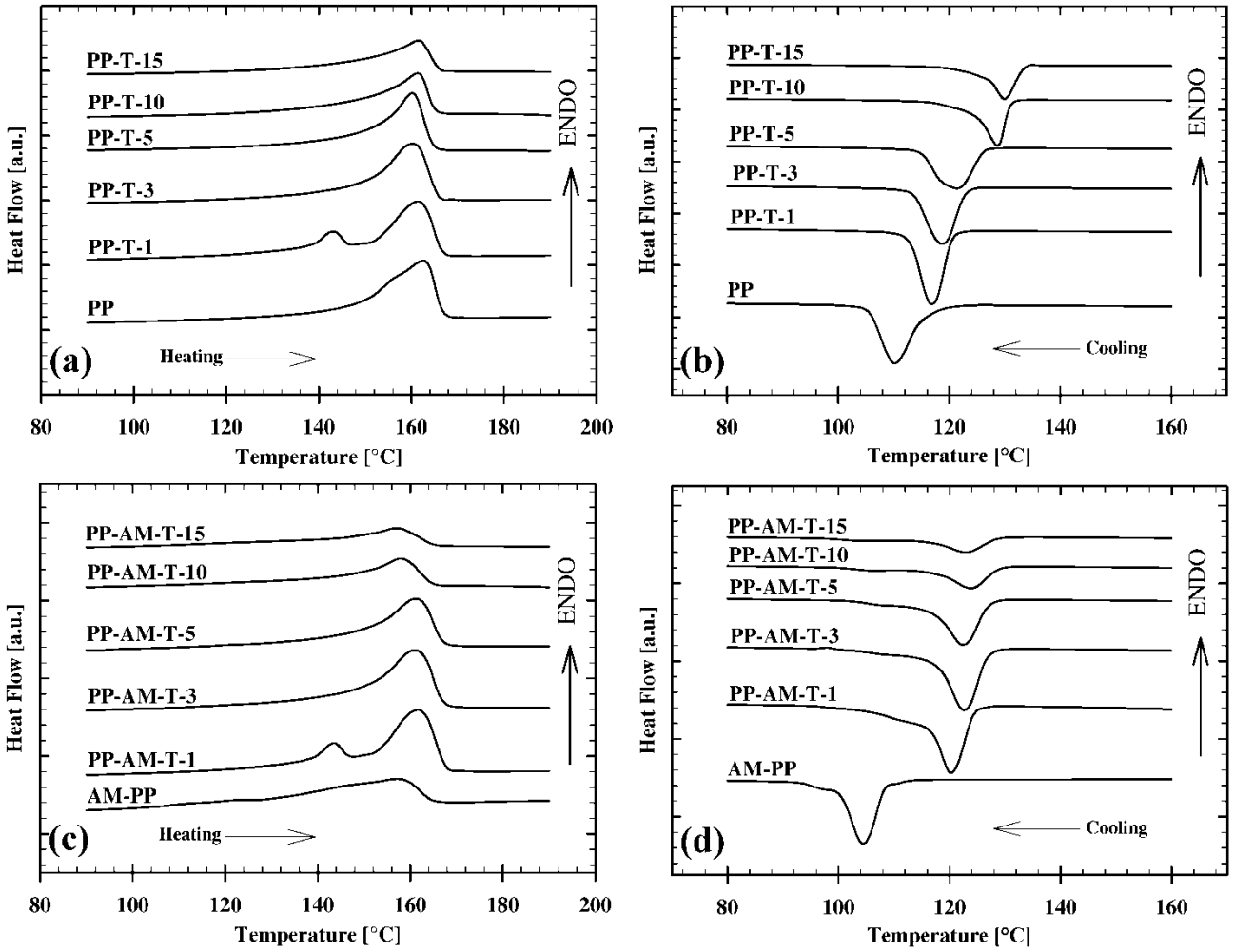

Figure 3-7: DSC thermograms of uncompatibilized (PP-T) and compatibilized (PP-AM-T) nanocomposites recorded during first heating (a),(c) and cooling (b),(d)

of this paper. As it can be seen in Figure 3-7a, the neat PP shows a melting endothermic peak at around 162°C, corresponding to α-iPP, and, addition of TiO_2 nanoparticles did not significantly change the melting temperature in the first heating run (T_{m1}). Figure 3-7a and Figure 3-7c show that, for PP/TiO_2 nanocomposite containing 1 vol% of TiO2 (PP-T-1 and PP-AM-T-1), there are two distinct melting peaks at 143 and 161°C while only one melting peak is observed for the other samples. It is well-known that iPP can form α-phase crystal with relative higher melting temperature ($T_{m\alpha}$) and β-phase with relative lower melting temperature ($T_{m\beta}$) [30]. As it will be discussed in the following sections, the XRD analysis confirmed the presence of β-phase crystals. On the other hand, Figure 3-7b and 7d shows that the crystallization temperature (T_c) of the

nanocomposites increases with TiO_2 concentration. Obviously, the heterogeneous nucleating effect of the TiO_2 nanoparticles leads to the increase in T_c of the nanocomposites. However, since the polymeric matrices in the compatibilized nanocomposites (PP-AM-T) are blends of PP and AM-PP with crystallization peak temperature (T_c) of 114 and 105, respectively, addition of TiO_2 did not increase their crystallization temperatures as much as for uncompatibilized nanocomposites (PP-T). Therefore, while T_c of uncompatibilized nanocomposites increases from 114°C for the neat PP to 132°C for PP-T-15, T_c of the compatibilized nanocomposites containing 15 vol% of TiO_2 (PP-AM-T-15) reaches to 123°C.

Table 3.3 summarizes the results obtained from DSC experiments for both compatibilized and uncompatibilized nanocomposites. In Table 3.3, T_{m1} and T_{m2} are melting peak temperatures measured at the first and second heating run, respectively. Noteworthy, in the case of PP-T-1 and PP-AM-T-1 where there are two melting peaks, T_{m1} and T_{m2} are the values of the highest melting peak temperatures associated to the α-phase iPP ($T_{m\alpha}$). ΔT, which is the difference between T_c and T_{m2}, corresponds to the degree of supercooling in each sample. As it can be seen in Table 3.3,

Table 3.3: Summary of DSC characterization results

Sample	T_{m1} [°C]	T_c [°C]	T_{m2} [°C]	$\Delta T = T_{m2} - T_c$ [°C]	ΔH_{m1} [J/g]	X_{m1} [%]	ΔH_c [J/g]	X_c [%]
PP	162	114	159	45	92.9	52.5	98.5	55.6
PP-T-1	161	116	159	43	84.5	51.5	90.6	53.4
PP-T-3	161	117	159	42	79.0	50.3	78.0	50.3
PP-T-5	161	120	160	40	73.8	53.1	75.3	54.1
PP-T-10	161	130	162	32	60.8	51.6	65.5	55.5
PP-T-15	162	132	161	29	49.5	50.5	51.8	52.8
PP-AM-T-1	162	120	160	40	84.1	49.6	84.1	49.7
PP-AM-T-3	161	123	161	38	74.5	48.0	76.1	49.1
PP-AM-T-5	161	123	160	37	62.6	45.5	62.0	45.0
PP-AM-T-10	158	124	159	35	44.9	41.9	41.6	38.9
PP-AM-T-15	157	123	158	35	31.1	32.7	30.4	31.9
AM-PP	157	105	158	53	61.6	29.5	68.5	38.7

ΔT decreases with increasing TiO_2 concentration for both compatibilized and uncompatibilized nanocomposites, which is another indication for heterogeneous nucleation effect of the TiO_2 nanoparticles. The same phenomena was also reported in literature for PP-based nanocomposites systems containing TiO_2, treated with polyalcohol, and silica (SiO_2) [7, 37] and, poly(ether ether ketone) (PEEK) containing carbon nanotubes [46]. There are two controlling phenomena in polymer crystallization: nucleation and diffusion. According to our results, it can be concluded that the presence of TiO_2 nanoparticles did not restrict the movement of the PP molecular chains in the molten state to hinder the diffusion of PP during crystal growth but they acted as a nucleating agent. Contrary to the higher concentrations of TiO_2, Table 3.3 shows that T_c of the compatibilized nanocomposites containing 1, 3 and 5 vol% of TiO_2 is higher than that of uncompatibilized nanocomposites containing the same TiO_2 concentration. Better dispersion and higher polymer-TiO_2 interactions cause more mobility restriction of PP macromolecules leading to higher T_c. This phenomenon was also reported in literature for compatibilized PP/fumed silica nanocomposites and PP/kenaf composites or nanocomposites of PA with surface treated nanoparticles [6, 47, 48].

Table 3.3 also reports crystalline contents of both compatibilized and uncompatibiized nanocomposites. Due to the polymorphism nature of iPP and the presence of considerable content of β-phase iPP in the PP-T-1 and PP-AM-T-1 samples, degree of crystallinity (X_{m1}) in these samples, was calculated from summation of contents of each present crystal phases (X_i where i = α or β):

$$X_{m1} = X_\alpha + X_\beta \tag{3.1}$$

Accordingly, X_i, which is the fraction of a particular crystalline PP modification i, was calculated using melting heat (ΔH_α or ΔH_β) measured during the first heating run by the following equation:

$$X_i\,[\%] = \frac{1}{1 - W_{TiO_2}} \times \frac{\Delta H_i}{\Delta H_i^0} \times 100 \tag{3.2}$$

where W_{TiO2}, ΔH_i and ΔH_i^0 are, respectively, the mass fraction of TiO_2 nanoparticles, the melting enthalpy and the theoretical enthalpy of fusion for 100% crystalline polypropylene containing only one of the crystalline iPP forms (α or β) [20]. It should be noticed that for the other samples, in which there were single melting peaks and, the β-phase contents were negligible (based on the

DSC thermograms), the X_{m1} was assumed identical to X_α. Moreover, the degree of crystallization during the cooling run of the DSC experiments (X_c) was calculated by Equation 3.2 using crystallization heat (ΔH_c) and assuming that only the α-phase crystals were formed.

Theoretical enthalpy of pure crystalline forms of iPP (ΔH_α^0 and ΔH_β^0) are critical parameters in determination of the degree of crystallinity and, in the literature, different values have been reported for them [30]. As previously reported [20, 30], ΔH_α^0 = 177.0 J/g and ΔH_β^0 = 168.5 J/g were used in Equation 3.2, as the most probable values, to calculate the degree of crystallinity. On the other hand, it is known that the metastable β-phase iPP transforms to the α-form during thermal or mechanical loads such as heating, annealing, or drawing through melt crystallization. Therefore, the peaks on the DSC profiles of the samples containing β-form crystals, recorded during heating runs, include a combination of overlapped peaks corresponding to melting of the β crystals (endotherm), the crystallization into the α-form (exotherm) and the final melting of the *α*-phase (endotherm). These overlapping of the α- and β-phase peaks causes difficulties in determination of enthalpy of fusion for each phase (ΔH_α and ΔH_β) [49] and, hence, different technique have been proposed to dissociate the peaks and to determine the enthalpy values [20, 26, 50, 51]. Li and Cheung [52] proposed a correction factor (or calibration factor), C_f, which can accurately determine the enthalpy of fusion of each crystalline phase in samples containing unknown mixtures of the α- and β-phases. In this technique, total heat of fusion (ΔH_{Total}), obtained from the area under the peaks of DSC thermograms, is divided into β-component, ΔH_β^* and α-component, ΔH_β^*, then, the real value of enthalpy of fusion of the β-phase (ΔH_β) is approximated using the correction factor (C_f):

$$\Delta H_\beta = C_f \times \Delta H_\beta^* \tag{3.3}$$

where

$$C_f = \left(1 - \frac{h_2}{h_1}\right)^{0.6} \tag{3.4}$$

and, as it is illustrated in a schematic DSC profile in Figure 3-11 of the supporting information, h_1 and h_2 are the heights from the base line to the β-phase peak and minimum point, respectively. Accordingly,

$$\Delta H_{\alpha} = \Delta H_{Total} - \Delta H_{\beta} = \Delta H_{\alpha}^{*} + \Delta H_{\beta}^{*} - \Delta H_{\beta} \quad (3.5)$$

More details on this calculation method could be found elsewhere [51-53] and, a schematic illustrating determination of the various parameters, used in Equations 3.3, 3.4, and 3.5, is shown in Figure 3-11 (in the supporting information). Since PP-T-1 and PP-AMT-1, compared to the other samples, contain significantly higher contents of β-phase, they showed two melting peaks (Figure 3-7a and b). Therefore, it was possible to apply the mentioned method to calculate crystal contents of each phase. Table 3.4 summarizes the DSC results and related parameters, used in Equation 3.5, for PPT-1 and PP-AM-T-1. It also reports the melting peak temperatures of β-phase iPP, recorded in the first and the second heating runs, and relative content of β-form crystals to all the crystal contents of the samples, ϕ_{β} which is defined as

$$\phi_{\beta} = \frac{X_{\beta}}{X_{m1}} = \frac{X_{\beta}}{X_{\beta} + X_{\alpha}} \quad (3.6)$$

Results presented in Table 3.4 indicate that, in both samples of PP-T-1 and PP-AM-T-1, β-phase content (X_{β}) is around 10.3 % which form around 19.9 and 20.7 % of total crystal contents (ϕ_{β}) in PP-T-1 and PP-AM-T-1, respectively. Tjong *et al.* [19] reported values of 13.04-14.09 % for X_{β} and 27.6-27.32 % for ϕ_{β} in nanocomposites based on iPP containing 0.1-1 wt.% of silver nanoparticles without applying the correction in calculation of the enthalpies of fusion. However, in a recent work [26], where Gaussian functions were used to deconvolute the DSC melting peaks, the relative contents of β-form (ϕ_{β}) in the iPP nanocomposites increased, with the inorganic content, up to 88 and 57% for 2 wt.% of silver nanocrystals (Ag NC) and commercial

Table 3.4: Summary of DSC characterization results and the values calculated using Eqs. 1-5 for the samples PP-T-1 and PP-AM-T-1

Sample	$T_{m\beta,1}$ [°C]	$T_{m\beta,2}$ [°C]	ΔH^{*}_{β} [J/g]	C_f	X_{β} [%]	$\phi_{\beta} = X_{\beta}/(X_{\beta} + X_{\alpha})$ [%]
PP-T-1	143.8	146.6	27.5	0.60	10.3	19.9
PP-AM-T-1	143.2	146.6	27.3	0.64	10.3	20.7

uncoated silver nanoparticles (Ag NP), respectively.

According to the data reported in Table 3.3, for all the studied TiO_2 concentrations, the degree of crystallinity of uncompatibilized nanocomposites is not significantly affected by the addition of TiO_2 nanoparticles. On the other hand, since presence of anhydride groups decreases regularity of polypropylene, AM-PP has lower degree of crystallinty compared to the iPP. Consequently, due to presence of higher content of AM-PP rather than PP in the compatibilized samples containing 10 and 15 vol% of TiO_2 nanoparticles (PP-AM-T-10 and PP-AM-T-15), they have lower crystalline content compared to the corresponding uncompatibilized nanocomposites (PP-T-10 and PP-T-15) and their crystallization behavior is closer to that of AM-PP rather than that of PP homopolymer.

In order to investigate the effect of TiO_2 nanoparticles on the crystalline structure of the developed nanocomposites, XRD characterization was performed on the neat PP and the PP/TiO2 nanocomposites. Figure 3-8 shows the XRD patterns of the TiO_2 nanoparticles, the neat PP and the PP/TiO_2 nanocomposites containing 1, 3 and 5 vol% of TiO_2 with the appropriate deconvolutions of Bragg's reflections to separate the crystalline and amorphous contributions in each diffraction pattern of the PP and nanocomposites. For neat PP sample, the main characteristic X-ray peaks of the monoclinic α-phase of isotactic PP are present at 2θ = 14.1, 16.9, 18.5, 21.1 and 21.9° corresponding respectively to the planes (110), (040), (130), (111) and (131). It is noticeable that reflections at 2θ = 25.4 and 28.6° associated with (060) and (220) plane of α-phase have negligible intensities. On the other hand, the presence of the characteristic peak of trigonal β-phase crystals at 2θ = 16.1° corresponding to the plane (300) is an indication of β-phase modification due to the presence of TiO_2 nanoparticles. In addition, the peak at 2θ = 21.1° could be correlated to both α(111) and β(311) phases. It is noteworthy that, since XRD pattern of TiO_2 nanoparticles (see Figure 3-8) have characteristic peaks of 2θ = 25.4, 27.5, 36.1, 37.0, 37.9 and 38.5°, intensities of the reflection peaks at 2θ = 25.4 and 27.5° (corresponding to anatase and rutile form of TiO_2) increase with TiO_2 content.

XRD and DSC results confirmed that the presence of TiO_2 nanoparticles induces β-form crystal formation in iPP. This β nucleating agent effect was also reported for other inorganic nanoparticles added to iPP [8, 9, 26, 29, 31, 35]. In order to quantify the effect of TiO_2 on β-form crystal formation, relative content of the β-phase (referred as K_β or K values) in crystalline iPP

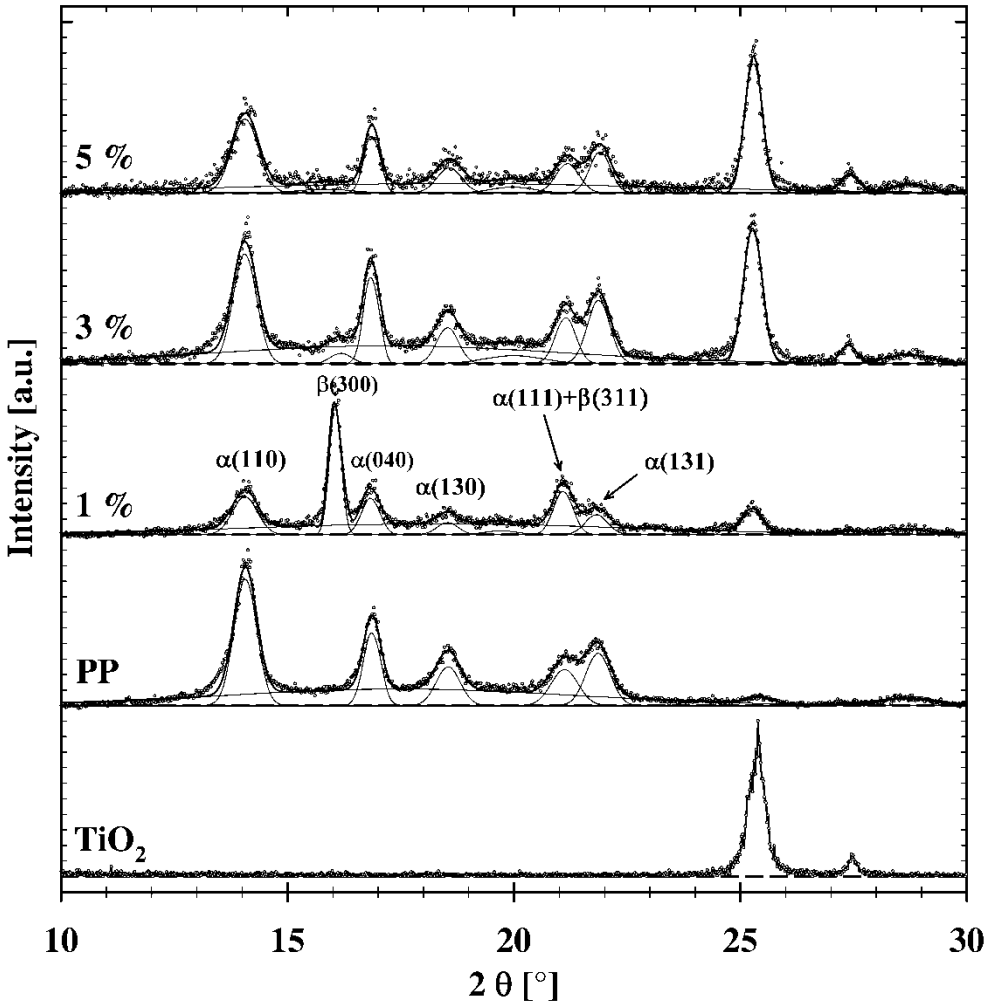

Figure 3-8: XRD patterns of the TiO_2 nanoparticle, the neat PP and PP-T nanocomposites with 1, 3 and 5 vol% of TiO_2 nanoparticles.

of uncompatibilized samples was described using the formula proposed by Jones and co-workers [54]:

$$K_{\beta,I} = \frac{I_\beta}{I_{\alpha_1} + I_{\alpha_2} + I_{\alpha_3} + I_\beta} \tag{3.7}$$

where $K_{\beta,I}$ is an empirical ratio that varies from zero, for no β-phase, to unity for 100% β-phase and, I_β, $I_{\alpha1}$, $I_{\alpha2}$ and $I_{\alpha3}$ are the diffraction intensities of β(300), α(110), α(040) and α(130) planes, respectively [55]. K values are used when β-phase is the minor crystalline form. The K values could be also defined based on the areas of the XRD peaks (noted as $K_{\beta,A}$). It should be noticed

that, since some of the specific peaks of α-phase and β-phase have almost the same 2θ values (e.g. $(111)_\alpha$ and $(301)_\beta$ at $2\theta \approx 21.1°$), it is hard to consider them in the calculation of the K values and, only the equatorial peaks are used in Equation 3.7. Therefore, these parameters are known as relative measures of the β-form crystal content in different samples and, they do not show absolute portion of β-phase in crystalline structures [55]. However, crystallinity of the samples can be estimated from the ratio of area the crystalline peaks (A_c) to the total peak area:

$$X_{XRD}[\%] = \frac{A_c}{A_c + A_a} \times 100 \tag{3.8}$$

where X_{XRD} is referred as the degree of crystallinity based on the XRD results and, A_c and A_a are areas of the crystalline peaks and the hollow amorphous bacground, respectively.

Table 3.5 reports the values of $K_{\beta,I}$ and $K_{\beta,A}$ for the neat PP, uncompatibilized nanocomposite (PP-T) and the sample PP-AM-T-1. As it can be seen, the relative β-phase contents of the nanocomposites containing 1 vol% of TiO_2 are significantly high and, it decreases dramatically to low values in the other samples containing more than 1 vol% of TiO_2. This behavior is in agreement with results reported by Mina et al. [38] for iPP/TiO_2 microcomposites containing more than 10 wt% (~2.3 vol%) of TiO_2. Although mechanisms of β-phase nucleation via incorporation of the extrinsic agents have been studied by several researchers, the effects of inorganic β-nucleators are still not well understood [19]. A widely accepted mechanism, for some β-nucleating agents, is the "dimensional lattice matching theory" proposed by Lotz and co-workers [56]. Based on this theory, the lattice matching between the c-axis periodicity of iPP (6.5 Å) and the corresponding distance in the substrate crystal face of the nucleating agent is

Table 3.5: *β*-form index (*K* value) and crystalline contents (X_{XRD}) of the uncompatibilized nanocomposites and PP-AM-T-1 sample calculated based on XRD results

	PP	PP-T-1	PP-T-3	PP-T-5	PP-T-10	PP-T-15	PP-AM-T-1
$K_{\beta,I}$	0	0.60	0.04	0.02	0.01	0.04	0.60
$K_{\beta,A}$	0	0.45	0.04	0.05	0.05	0.04	0.45
X_{XRD} [%]	56.3	53.6	54.6	57.6	52.2	53.5	53.3

responsible for the induction of the β-phase in iPP. Therefore, β-phase nucleating role of TiO_2 at the lowest concentration and the inverse relation between TiO_2 nanoparticle content and the β-phase content could be attributed to the size of the nanoparticle aggregates. In other words, the single nanoparticles and the small aggregates, dispersed in the matrices of PP-T-1 and PP-AM-T-1, were small enough to meet the crystallographic conditions of the β-crystal formation whereas the relatively larger particle aggregates present at the more concentrated nanocomposite lost this ability [28]. Crystal shape of the β-nucleator has been considered as another parameter which can affect the β-phase nucleation and, it was reported that plate or lumpish shape favor the growth of β-phase PP [57]. Thus, the irregular shape of the nanoparticle clusters in the concentration above 1 vol.% may reduce β-phase nucleation activity [19]. Formation of β-phase PP in low concentrations (5 wt.%) of $CaCO_3$ was attributed to smaller particle size due to the better dispersion [58]. In addition, as previously mentioned, TiO_2 nanoparticles are well-dispersed in the PP/TiO_2 nanocomposite containing 1 vol% and, it leads to a large interfacial area between the PP matrix and TiO_2 nanoparticles, which may enhances the β nucleating effect of TiO_2. In the more concentrated nanocomposites, there are more TiO_2 aggregates that are much larger than primary TiO_2 particle size.

Since XRD analysis investigates solid-state crystalline structure of materials, it is quite useful for studying the systems where the thermal transformations of the crystal forms (β-α), during DSC, causes the errors in calculation of crystal content [20]. Table 3.5 reports crystallinity of the nanocomposite samples calculated based on the XRD results (X_{XRD}). Comparison between values of crystallinity obtained from DSC and XRD (X_{m1} versus X_{XRD}) shows that in the case of neat PP where there is no β-phase and, in the case of PP-T-1 or PP-AM-T-1, where the correction factor (C_f) was applied to calculate the enthalpy of fusion, the values of crystallinity obtained from both techniques are very close to each other. It can be an indication of the acceptable accuracy of the correction method. On the other hand, the lower values of X_{m1}, compared to X_{XRD}, in PP-T-3 and PP-T-5 could be attributed to the assumption that there is only α-phase crystals with larger ΔH_α^0 (compared to ΔH_β^0) resulting in the lower degrees of crystallinity from Equation 4.2.

3.3.4 Mechanical Characterization of Uncompatibilized and Compatibilized Nanocomposites

Figure 3-9 summarizes results of the mechanical characterizations. It includes the Young's modulus (E), the tensile strain at break (ε_b) and the tensile strength at yield (σ_y) for neat PP and nanocomposites of PP-T and PP-AM-T at different TiO_2 volume concentrations. Obviously, the elastic moduli of the nanocomposites (Figure 3-9a) increased with increasing TiO_2 concentration, except for the nanocomposites containing 1 vol% of TiO_2. Since the matrices of compatibilized

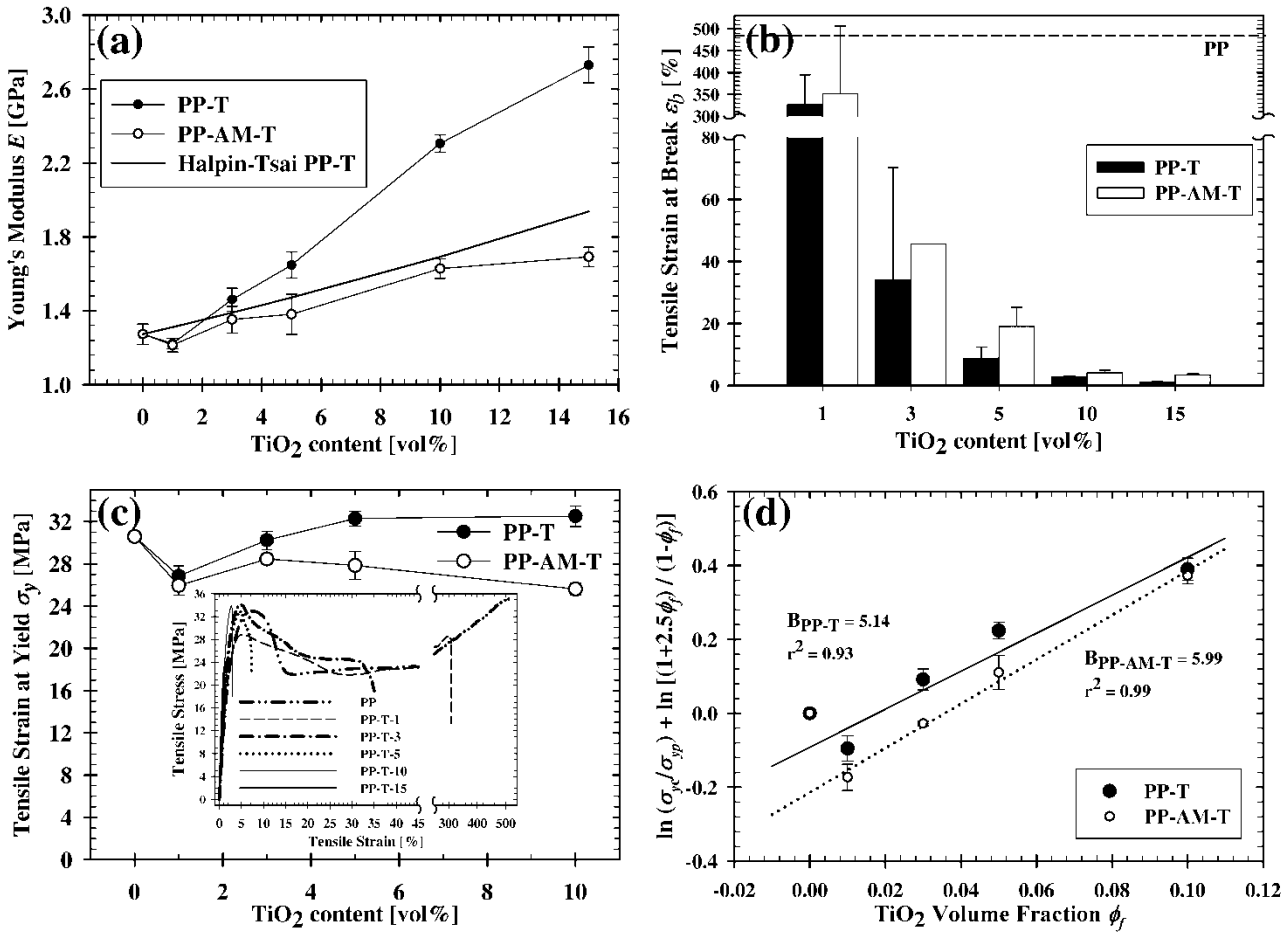

Figure 3-9: Mechanical properties of the nanocomposites; (a) Young's modulus E, (b) Tensile strain at break ε_b, (c) Tensile stress at yield σ_y (inset: representative tensile stress-strain curve of PP-T samples) and (d) results of $\ln(\sigma_{yc}/\sigma_{yp}) + \ln[(1+2.5\phi_f)/(1-\phi_f)]$ versus ϕ_f

nanocomposites are mixtures of PP with a low-modulus AM-PP (E=610 ±7.8 MPa), the moduli of uncompatibilized nanocomposites are higher than those of compatibilized ones for almost the whole range of the studied TiO_2 concentrations. Interestingly, adding 1 vol% of TiO_2 nanoparticles decreased the modulus of the corresponding nanocomposite. This could be attributed to the presence of β-form crystals, which typically leads to lower Elastic modulus and yield stress compared to α-iPP [49]. The Halpin-Tsai model [59] gives a simple prediction of the elastic modulus (E) of particulate composites using properties of the pure phases:

$$\frac{E_c}{E_m} = \frac{1+2f\phi_f\eta}{1-\eta\phi_f} \tag{3.9}$$

where E_c and E_m are respectively the moduli of the composite and the matrix; f and ϕ_f are the aspect ratio and the volume fraction of the dispersed particles and, $\eta = \frac{E_f/E_m - 1}{E_f/E_m + 2f}$, where E_f is the elastic modulus of the filler. The experimental values of E for the PP-T nanocomposites are compared with the predictions of the Halpin-Tsai model using f =1 and E_f =282.7 GPa for the TiO_2 nanoparticles [63]. Although an unrealistic perfect adhesion had been assumed in the model, it surprisingly underestimates the values, as already reported by Palza et al. [47] for the iPP/silica nanocomposites. Figure 3-9b shows the variation of the elongation at break (ε_b) with TiO_2 concentration. ε_b largely decreased with increasing TiO_2 concentration. Compatibilized nanocomposites have larger tensile strain at break compared to uncompatibilized ones due to the presence of the AM-PP with larger ε_b (579% ±90) compared to neat PP.

The tensile stress-strain curves of PP-T nanocomposites are representatively displayed in the inset of Figure 3-9c to show the effect of the TiO_2 nanoparticles on the tensile behavior of the samples. As it can be seen, except for PP-T-15 which shows a brittle break (no yielding), all the other samples have a ductile behavior with a characteristic yield stresses (σ_y), reported in Figure 3-9c versus TiO_2 loading. Except in PP-T-1, where adding TiO_2 nanoparticles led to a lower tensile stress at yield, σ_y of uncompatibilized samples increased with TiO_2 concentration. However, such effect is not observed in compatibilized PP-AM-T nanocomposites. It is noticeable that the presence of the nanoparticles eliminated strain hardening in the nanocomposite containing more than 1% TiO_2.

Interfacial interaction between polymer matrix and nanoparticles has a crucial effect on the mechanical properties of the resulting nanoparticle. Turcsányi et al. [64] proposed a micromechanical model to quantify filler/matrix interaction using yield properties of the composites. They introduced a constant B that has a direct relation to the interfacial properties, larger B values meaning stronger interactions:

$$\sigma_{yc} = \frac{1-\phi_f}{1+2.5\phi_f}\,\sigma_0 \exp\left(B\phi_f\right) \tag{3.10}$$

where σ_{yc} and σ_0 are tensile yield strength of the nanocomposite and matrix (PP), respectively. ϕ_f is the volume fraction of the particulate phase (TiO_2). Figure 3-9d shows the results of the predictions of the micromechanical analysis using $\ln(\sigma_{yc}/\sigma_0) + \ln[(1+2.5\phi_f)/(1-\phi_f)]$ versus volume fraction (ϕ_f). Linear regression on the data above 1% results yields B values of 5.14 and 5.99 for PP-T and PP-AM-T, respectively, indicating the role of the anhydride-modified polypropylene in improving adhesion between the organic PP and inorganic TiO_2 phases.

3.4 Conclusion

Study of structure and properties of the PP/TiO_2 nanocomposites containing a wide range of TiO_2 content revealed the development of the microstructure in the nanocomposites and its effect on thermal and mechanical properties of the nanocomposites. Presence of AM-PP yields better dispersion of the nanoparticles, particularly at the TiO_2 volume content lower than 5%. By increasing TiO_2 content, the number of aggregates increases and morphologies of the compatibilized and uncompatibilized samples became similar.

TGA results showed that the mechanism responsible for stabilizing effect of TiO_2 is dependent on TiO_2 content, the degree of particle dispersion and interfacial area between the two phases. Therefore, presence of larger interfacial area between PP and TiO_2 increases T_{peak} under inert and oxidative atmosphere, leading to the maximum at 5 vol% of TiO_2, while aggregation of TiO_2 nanoparticles at the higher nanoparticle contents causes to reach the plateau in T_{peak} versus volume content. On the other hand, interaction between PP and well-dispersed nanoparticles reduces molecular mobility of PP phase in solid state and enhances $T_{5\%}$ under inert atmosphere.

Higher T_g of the nanocomposites containing 1 vol% of TiO_2 confirmed suppression of the polymer molecular mobility by the nanoparticles.

DSC analysis revealed that TiO_2 nanoparticles have heterogeneous nucleation effect in PP crystallization. The decrease of the degree of supercooling with TiO_2 content indicates its nucleating role without significant effect on dynamics of crystal growth from melt-state. DSC result also showed that the presence of a small content (1 vol%) of TiO_2 induces formation of β phase crystal in PP/TiO_2 nanoparticles. However, results of XRD showed that increasing TiO_2 content to higher than 1 vol% leads to decrease of β phase content.

Measurement of mechanical properties showed that adding TiO_2 nanoparticles improves elastic modulus of PP except in the nanocomposites containing 1 vol% of the nanoparticles which, due to formation of β-type crystals, had lower Young's moduli. A micromechanical analysis based on Halpin-Tsai equation indicated stronger interfacial interactions between the polymer matrix and TiO_2 nanoparticles for the compatibilized nanocomposites.

Acknowledgments

This research was supported in part by the Natural Science and Engineering Research Council (NSERC) of Canada Strategic projects and discovery grants.

3.5 References

1. S. Wacharawichanant, S. Thongyai, T. Siripattanasak, and T. Tipsri, *Iran. Polym. J.* , **18**: 607 (2009).
2. P.A. Wheeler, R. Misra, R.D. Cook, and S.E. Morgan, *J. Appl. Polym. Sci.* , **108**: 2503 (2008).
3. D. Acierno, G. Filippone, G. Romeo, and P. Russo, *Macromol. Symp.* , **247**: 59 (2007).
4. S.G. Lei, S.V. Hoa, and M.T. Ton-That, *Compos. Sci. Technol.* , **66**: 1274 (2006).
5. S. Thomas, and G.E. Zaikov, *Recent Advances in Polymer Nanocomposites*, Brill Academic, Leiden (2009).
6. K. Chrissafis, and D. Bikiaris, *Thermochim. Acta.* , **523**: 1 (2011).
7. A. Kubacka, C. Serrano, M. Ferrer, H. Lunsdorf, P. Bielecki, M.L. Cerrada, M. Fernandez-Garcia, and M. Fernandez-Garcia, *Nano Lett.* , **7**: 2529 (2007).
8. N. Knor, R. Walter, and F. Haupert, *J. Thermoplast. Compos.* , **24**: 185 (2011).
9. J. Golebiewski, and A. Galeski, *Compos. Sci. Technol.* , **67**: 3442 (2007).
10. V. Vladimirov, C. Betchev, A. Vassiliou, G. Papageorgiou, and D. Bikiaris, *Compos. Sci. Technol.* , **66**: 2935 (2006).
11. M. Chen, G. Tian, Y. Zhang, C. Wan, and Y. Zhang, *J. Appl. Polym. Sci.* , **100**: 1889 (2006).
12. S. Jain, H. Goossens, M. Van Duin, and P. Lemstra, *Polymer* , **46**: 8805 (2005).
13. Q.-X. Zhang, Z.-Z. Yu, X.-L. Xie, and Y.-W. Mai, *Polymer* , **45**: 5985 (2004).
14. H. Abduljalil, A. Hashim, and A. Jewad, *Eur. J. Sci. Res.* , **63**: 231 (2011).
15. F. Bondioli, A. Dorigato, P. Fabbri, M. Messori, and A. Pegoretti, *Polym. Eng. Sci.* , **48**: 448 (2008).
16. D.N. Mccarthy, H. Stoyanov, D. Rychkov, H. Ragusch, M. Melzer, and G. Kofod, *Compos. Sci. Technol.* , **72**: 731 (2012).
17. A. Chandra, L.-S. Turng, S. Gong, D.C. Hall, D.F. Caulfield, and H. Yang, *Polym. Composites* , **28**: 241 (2007).

18. M. Burke, R.J. Young, and J.L. Stanford, *Polym. Bull.* , **30**: 361 (1993).

19. S.V. Meille, D.R. Ferro, S. Brueckner, A.J. Lovinger, and F.J. Padden, *Macromolecules* , **27**: 2615 (1994).

20. M. Obadal, R. Čermák, and K. Stoklasa, *Macromol. Rapid. Comm.* , **26**: 1253 (2005).

21. H. Bai, Y. Wang, L. Liu, J. Zhang, and L. Han, *J. Polym. Sci. Pol. Phys.* , **46**: 1853 (2008).

22. F. Luo, C. Geng, K. Wang, H. Deng, F. Chen, Q. Fu, and B. Na, *Macromolecules*, **42**: 9325 (2009).

23. S.C. Tjong, and S. Bao, *E-Polymers*, **139** (2007).

24. G.T. Offord, S.R. Armstrong, B.D. Freeman, E. Baer, A. Hiltner, J.S. Swinnea, and D.R. Paul, *Polymer* , **54**, 2577 (2013).

25. S.C. Tjong, R.K.Y. Li, and T. Cheung, *Polym. Eng. Sci.* , **37**: 166 (1997).

26. L. Xu, K. Xu, X. Zhang, F. Liu, and M. Chen, *Polym. Advan. Technol.* , **21**: 807 (2010).

27. L.-L. Xu, X.-J. Zhang, L.-H. Zhu, X.-N. Lian, K. Xu, and M.-C. Chen, *J. Macromol. Sci. B* , **50**: 89 (2010).

28. X. Dai, Z. Zhang, C. Wang, Q. Ding, J. Jiang, and K. Mai, *Compos. Part A-Appl. S.* , **49**: 1 (2013).

29. J. Duan, and Q. Dou, *J. Appl. Polym. Sci.* (2013). doi: 10.1002/app.39178.

30. Y. Shi, B. Sun, Z. Zhou, L.M. Wangatia, L. Chen, and M. Zhu, *J. Macromol. Sci. B* , **51**: 2505 (2012).

31. J. Varga, and G. Ehrenstein, *Colloid. Polym. Sci.* , **275**: 511 (1997).

32. F.J. Medellín-Rodríguez, J.M. Mata-Padilla, B.S. Hsiao, M.A. Waldo-Mendoza, E. Ramírez-Vargas, and S. Sánchez-Valdes, *Polym. Eng. Sci.* , **47**: 1889 (2007).

33. A. Zeng, Y. Zheng, Y. Guo, S. Qiu, and L. Cheng, *Mater. Design* , **34**: 691 (2012).

34. C. Grein, "Toughness of Neat, Rubber Modified and Filled β-nucleated Polypropylene: From Fundamentals to Applications," in *Intrinsic Molecular Mobility and Toughness of Polymers*, Vol. **2**, H.-H. Kausch, Ed., Springer Berlin, Heidelberg, 43 (2005).

35. W. Wan, D. Yu, Y. Xie, X. Guo, W. Zhou, and J. Cao, *J. Appl. Polym. Sci.* , **102**: 3480 (2006).

36. Z. Lin, C. Chen, Z. Guan, M. Li, G. Guo, J. Xian, and W. Li, *J. Therm. Anal. Calorim.* , 1 (2013).

37. M.-R. Meng, and Q. Dou, Journal *J. Macromol. Sci. B* , **48**: 213 (2009).

38. F. Ke, X. Jiang, H. Xu, J. Ji, and Y. Su, *Compos. Sci. Technol.* , **72**: 574 (2012).

39. H. Zhao, and R.K.Y. Li, *Polymer* , **47**: 3207 (2006).

40. J. Tang, Y. Wang, H. Liu, and L.A. Belfiore, *Polymer* , **45**: 2081 (2004).

41. A. Noll, and N. Knoer, *Mater. Sci. Forum* , **636/637**: 688 (2010).

42. M. Forhad Mina, S. Seema, R. Matin, M. Jellur Rahaman, R. Bijoy Sarker, M. Abdul Gafur, and M. Abu Hashan Bhuiyan, *Polym. Degrad. Stabil.* , **94**: 183 (2009).

43. C.-W. Chiu, C.-A. Lin, and P.-D. Hong, *J. Polym. Res.* , **18**: 367 (2011).

44. G.-J. Li, S.-R. Fan, K. Wang, X.-L. Ren, and X.-W. Mu, *Iran. Polym. J.* , **19**: 115 (2010).

45. B. Ou, D. Li, and Y. Liu, *Compos. Sci. Technol.* , **69**: 421 (2009).

46. W. Li, J. Karger-Kocsis, and R. Thomann, *J. Polym. Sci. Pol. Phys.* , **47**: 1616 (2009).

47. H. Palza, R. Vergara, and P. Zapata, *Compos. Sci. Technol.* , **71**: 535 (2011).

48. S.-P. Liu, J.-R. Ying, X.-P. Zhou, X.-L. Xie, and Y.-W. Mai, *Compos. Sci. Technol.* , **69**: 1873 (2009).

49. C. Rong, G. Ma, S. Zhang, L. Song, Z. Chen, G. Wang, and P.M. Ajayan, *Compos. Sci. Technol.* , **70**: 380 (2010).

50. D. Feng, D.F. Caulfield, and A.R. Sanadi, *Polym. Composites* , **22**: 506 (2001).

51. L.F. Giraldo, M. Echeverri, and B.L. López, *Macromol. Symp.* , **258**: 119 (2007).

52. J. Varga, *J. Macromol. Sci. B* , **41**: 1121 (2002).

53. Y. Yamamoto, Y. Inoue, T. Onai, C. Doshu, H. Takahashi, and H. Uehara, Macromolecules, **40**: 2745 (2007).

54. Z. Wei, W. Zhang, G. Chen, J. Liang, S. Yang, P. Wang, and L. Liu, *J. Therm. Anal. Calorim.* , **102**: 775 (2010).

55. J.X. Li, and W.L. Cheung, *J. Therm. Anal. Calorim.* , **61**: 757 (2000).

56. M. Liu, B. Guo, M. Du, F. Chen, and D. Jia, *Polymer* , **50**: 3022 (2009).

57. A.T. Jones, J.M. Aizlewood, and D.R. Beckett, *Die Makromolekulare Chemie* , **75**: 134 (1964).

58. P. Jacoby, B.H. Bersted, W.J. Kissel, and C.E. Smith, Journal of Polymer Science Part B: Polymer Physics, **24**: 461 (1986).

59. C. Mathieu, A. Thierry, J.C. Wittmann, and B. Lotz, *J. Polym. Sci. Pol. Phys*. , **40**: 2504 (2002).

60. J. Garbarczyk, and D. Paukszta, *Polymer* , **22**: 562 (1981).

61. T. Lozano, P.G. Lafleur, M. Grmela, and C. Thibodeau, *Polym. Eng. Sci.* , **44**: 880 (2004).

62. J.C. Halpin, and N.J. Pagano, *J. Compos. Mater.* , **3**: 720 (1969).

63. J.F. Shackelford and W. Alexander, *CRC Materials Science and Engineering Handbook*, 3rd edn., CRC, Boca Raton, FL, 766 (2000).

64. B. Turcsányi, B. Pukánszky, and F. Tüdõs, *J. Mater. Sci. Lett.* , **7**: 160 (1988).

3.6 Supporting Information

3.6.1 DSC Thermograms of the Second Heating Run

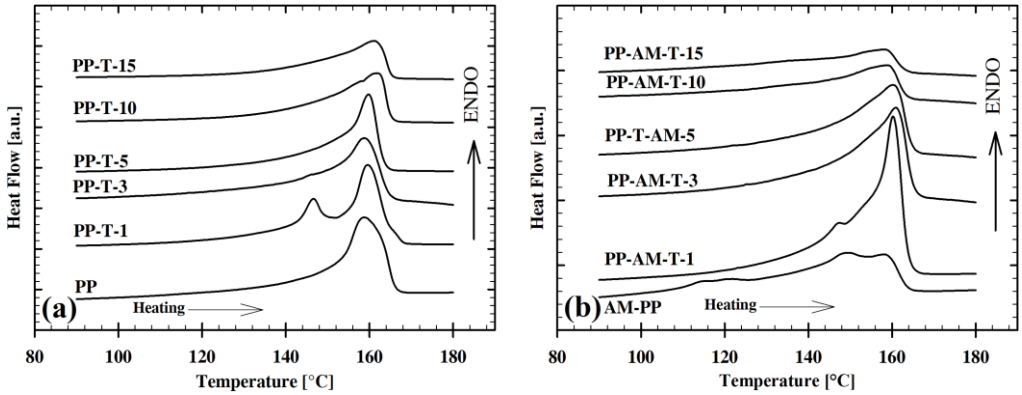

Figure 3-10: DSC thermograms of the uncompatibilized (PP-T) and the compatibilized (PP-AM-T) nanocomposites recorded during the second heating

3.6.2 Schematic showing how to determine different parameter used in Equations 3.3-3.5:

$$\Delta H_{\beta} = C_f \times \Delta H_{\beta}^{*} \tag{3.3}$$

$$C_f = \left(1 - \frac{h_2}{h_1}\right)^{0.6} \tag{3.4}$$

$$\Delta H_{\alpha} = \Delta H_{Total} - \Delta H_{\beta} = \Delta H_{\alpha}^{*} + \Delta H_{\beta}^{*} - \Delta H_{\beta} \tag{3.5}$$

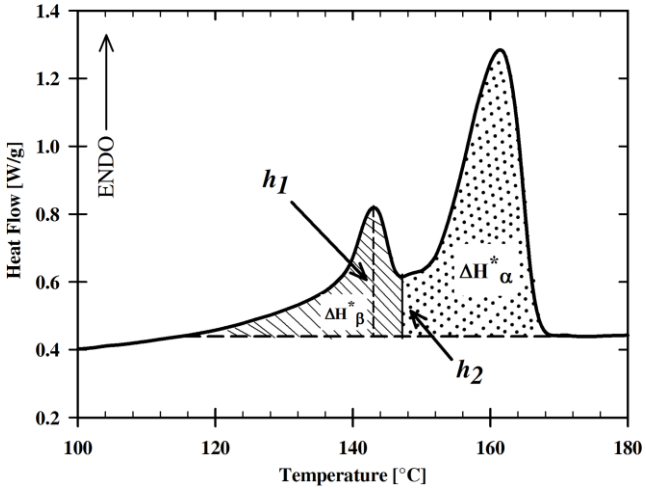

Figure 3-11: Melting curve of PP-T-1, recorded in the first heating run of DSC, to illustrate the method of determination of the different parameters, used in Eqs. 3-5, to calculate enthalpy of fusion for α- and β-phase of the samples.

CHAPTER 4 ARTICLE 2: RELATIONSHIP BETWEEN RHEOLOGICAL AND ELECTRICAL PERCOLATION IN A POLYMER NANOCOMPOSITE WITH SEMICONDUCTOR INCLUSIONS

A. Zohrevand, A. Ajji (Corresponding Author)

Center for Research on High Performance Polymer and Composite System (CREPEC)

Department of Chemical Engineering, Ecole Polytechnique de Montreal

2900 Édouard-Montpetit Blvd.

Campus of the University of Montreal

2500 chemin de Polytechnique

Montréal, Québec

H3T 1J4 Canada

abdellah.ajji@polymtl.ca

Tel.: (+1) 514-340-4711 (Ext.:3703)

Fax: (+1) 514-340-4159

F. Mighri

Center for Research on High Performance Polymer and Composite Systems (CREPEC)

Department of Chemical Engineering, Laval University

1065 ave. de la Médecine

Pavillon Adrien-Pouliot

Quebec, Quebec

G1V 0A6 Canada

Abstract

Microstructure, electrical conductivity and rheological properties of nanocomposites based on isotactic polypropylene (iPP) containing semiconductor nanoparticles of TiO_2 were studied. Compatibilized and uncompatibilized nanocomposites containing a wide range of TiO_2 concentrations (up to 15 vol%) were prepared by melt compounding in a twin screw extruder via a masterbatch method. An anhydride modified PP (AMPP) was used as the compatibilizer. AFM, SEM and image analysis techniques were utilized to study the morphology evolution in the samples. Analyzing the results of DC electrical conductivity measurements showed a lower percolation threshold for the uncompatibilized samples, compared to the compatibilized ones. In order to estimate the percolation threshold, linear and nonlinear melt-state viscoelastic properties of the samples were studied. Liquid-solid transition and non terminal behavior of the uncompatibilized samples were observed at relatively lower range of TiO_2 loading, compared to the compatibilized samples. This was an indication of lower rheological percolation threshold in the uncompatiblized nanocomposites which was in agreement with the electrical percolation threshold. Scaling analysis of strain sweep tests above the percolation thresholds of the nanocomposites resulted in a lower fractal dimension for the uncompatibilized samples.

Keywords Polymer nanocomposite, semiconductor nanoparticle, electrical percolation, rheological percolation

4.1 Introduction

Modifying electrical properties of organic polymer materials for different applications has been an area of research attracting both academic and industrial scientists. Improved mechanical properties, reduced costs of materials and production, enhanced flexibility in product geometrical design and reduced weight are some of the advantages of using functional polymer base materials (Ke et al. 2012). Since most of polymers are generally electrical insulators, their electrical properties are mostly tailored by adding different types of additives or fillers. These additives or fillers could be conductive or semi-conductive and organic or inorganic materials with various shape, size and concentration (Huang and Wang 2011; Pötschke et al. 2009). Carbon black (CB), carbon nanotubes (CNT), and metal nanoparticles are widely used as electrically conductive fillers to prepare high performance light-weight conductive polymer nanocomposites (Huang et al. 2009; Yakisir et al. 2006). Typically, these nanocomposites are percolated systems where formation of a network structure within the matrix is necessary to have the desired electrical properties (Huang et al. 2012). At a critical content of the conductive nanoparticles, known as electrical percolation threshold, a sudden increase of bulk electrical conductivity (σ) is observed. It is ascribed to formation of an interconnected network of the nanoparticles providing a pathway for a significant percentage of electrons through the sample and causing the transition from insulator to conductive. Nevertheless, determination of the critical particle content associated with percolation has shown intrinsic difficulties and uncertainties which led to wide differences in the reported values of percolation threshold even for similar systems (Shin et al. 2013; Pötschke et al. 2004; Bauhofer and Kovacs 2009; Huang and Wang 2011). In addition, the final performances of these materials and their electrical percolation threshold are not only affected by their compositions but are also strongly influenced by the state of dispersion of the nanoparticles (Huang et al. 2009).

Rheological properties of polymer nanocomposites are strongly affected by their microstructure. Hence, rheology could be utilized as a strong tool to investigate their microstructure (Ghanbari et al. 2013; Bailly and Kontopoulou 2013; Ndong and Russel 2012; Tan et al. 2011; Dorigato et al. 2010; Bailly et al. 2010; Bahloul et al. 2010; Romeo et al. 2009; Vermant et al. 2007; Lee et al. 2007; Acierno et al. 2007). Rheological percolation threshold is one of the most important characteristics of the nanocomposites containing electrical conductive

inclusions. At rheological percolation threshold, a transition from liquid-like to solid-like behavior in nanocomposite melts is observed. It is usually associated with an abrupt increase in their elasticity or viscosity values due to formation of a space filling network of the nanoparticles through the matrix.

Both electrical and rheological percolation thresholds are dependent on the type, size and geometry of the nanoparticles, the polymer matrix characteristics and process/test conditions (Huang and Wang 2011; Pan and Li 2013; Pötschke et al. 2009; Abbasi et al. 2009). Usually, the value of electrical/rheological percolation is defined as the onset of scaling power law dependence for electrical/rheological properties as a function of volume fraction of the particulate phase:

$$p \propto \left(\frac{\phi - \phi_{c_p}}{\phi_{c_p}} \right)^{n_p} \quad \text{for} \quad \phi > \phi_{cp} \tag{4.1}$$

where p is the property of the composite, ϕ is the volume fraction of the filler, ϕ_{cp} is the percolation threshold, and n_p is a scaling exponent (Du et al. 2004; Abbasi et al. 2009; Huang and Wang 2011).

Effect of the incorporation of nanofillers on linear and nonlinear viscoelastic properties of the polymer melts have been described by different mechanisms taking into account the possible interactions between polymer and filler as well as between filler and filler (Aranguren et al. 1992; Sternstein and Zhu 2002). Cassagnau (2008) distinguished between underlying causes of observing solid-like behavior in the linear viscoelastic properties of layered and spherical silicate (SiO_2) nanoparticles. In the former one, better dispersion (exfoliation) of the layered silicate nanoparticles led to the physical interaction of layered nanoparticles, the non terminal behavior and a lower percolation threshold. On the other hand, in the case of the spherical fumed SiO_2, better dispersion of the nanoparticles resulted in a higher percolation threshold. Accordingly, in order to describe long-time relaxations in solid-like behavior, three different types of polymer-filler interactions are generally considered as the main reasons for the formation of an immobilized layer around the nanoparticle (Aranguren et al. 1992; Bailly and Kontopoulou 2013): i) physical interactions, usually, due to absorption of the polymer chains onto the surface chemical groups of the particles; ii) chemical interaction via formation of covalent bonds between

polymer chain and surface functional groups of the particles and, iii) mechanical connection (bridging) due to chain entanglements. Depending on surface properties of the nanoparticles, intrinsic features of the polymer chains, and surface modification or macromolecular compatibilizers, these mechanisms may be taken into account.

Reduction of elastic modulus with strain (or stress) amplitude followed by a transition from linear to non-linear viscoelastic behavior (also known as *Payne* effect) is a nonlinear viscoelastic behavior which is strongly dependent on filler content, microstructure (state of dispersion) of the dispersed phase, and filler-filler or polymer-filler interactions. Hence, results of amplitude sweep tests provide valuable information about polymer-filler and filler-filler interactions and degree of filler dispersion. In the case of non-interacting particles, hydrodynamic effect or enhanced local deformation is a principal mechanism governing the non-linear behavior. Since the filler is solid, the global strain is concentrated on the polymer medium leading to the shorter linear zone compared to the neat polymer. Moreover, depending on filler concentration and polymer-filler interactions, two other possible mechanisms have been proposed for this non-linear behavior; breakdown of the particle network, and chain disentanglement (debonding) from surface of the nanoparticles (Cassagnau 2008; Sternstein and Zhu 2002). Shih et al. (1990) considered the particle network as an elastic structure composed of fractal aggregates and, developed a scaling relation which is used to quantitatively assess the nanoparticle aggregates at the concentrations above the percolation threshold ($\phi > \phi_c$) (Vermant et al. 2007; Durmus et al. 2007). Accordingly, the relation between the value of elastic modulus at the plateau ($G'p$) in the linear zone of the strain sweep curve and particle volume fraction (ϕ) is

$$G'_p \propto \phi^{(3+x)/3-d_f} \tag{4.2}$$

where d_f refers to fractal dimension of the aggregate network and, x is an exponent dependent on number of particles per aggregate. On the other hand, the critical strain value (γ_c) is:

$$\gamma_c \propto \phi^{-(1+x)/(3-d_f)} \tag{4.3}$$

Compared to other methods of polymer nanocomposite preparation, melt compounding of thermoplastics and nanoparticles is preferred. Because an intensive melt mixing could provide sufficient shear to break nanoparticle aggregates and disperse them through the matrix (Pötschke et al. 2002; Yu et al. 2011). Due to a good balance between process parameters and final

properties of isotactic polypropylene (iPP), it has been used as a thermoplastic matrix to develop nanocomposites via melt blending process (Lei et al. 2006; Vladimirov et al. 2006; Zohrevand et al. 2013; Pan and Li 2013; Serrano et al. 2012). Polypropylene-based nanocomposites containing different types of electrical conductive nanoparticles have been studied extensively (Bauhofer and Kovacs 2009). However, the relation between structure and electrical properties of thermoplastic-based nanocomposites containing semi-conductive metal oxide nanoparticles has been rarely investigated (David et al. 2011).

Among the various inorganic nanoparticles, titanium dioxide (TiO_2) is a wide band gap (E_g=3.2 eV) semiconductor with high refractive index (~ 2.6), good UV absorption ability, low cost, and high availability. It is added to polymeric matrices to particularly modify their electrical, optical and mechanical properties (Abduljalil et al. 2011; Bondioli et al. 2008; McCarthy et al. 2012; Chandra et al. 2007). TiO_2 has three crystalline structures; rutile, anatase and brookite. Due to the surface chemistry and higher conduction-band edge energy of anatase, it has been widely used in die sensitized solar cells (DSSC). An interconnected network of TiO_2 nanoparticles is needed as a photoelectrode of DSSCs to form a pathway for electrical charge collection (Kalyanasundaram and Grätzel 1998; Park et al. 2000).

Although micron-size TiO_2 particles have been widely used as reinforcement or pigment in PP (Burke et al. 1993), there is a lack of comprehensive information about the relationship between microstructure and electrical properties of PP/TiO_2 nanocomposites. To the best of our knowledge, it is hard to find a report on the relation between structure and electrical properties of thermoplastic containing TiO_2 nanoparticles. Mina et al. (2009) reported that the bulk electrical resistivity (ρ_v) of iPP-based composites decreases with content of micron-size TiO_2 at different temperatures. They also showed that, in the concentrations lower than 10 wt%, the improvement in electrical conductivity is sharper compared to the higher concentrations. It was attributed to formation of filler particle agglomerates. Wang *et al.* (2013) studied dielectric behavior of electrorheological (ER) suspensions based on silicon oil and TiO_2 nanoparticles. They found $\phi \approx$ 5 vol% as a critical TiO_2 content where the slope of conductivity (noted as κ) versus ϕ changed. This was attributed to aggregation of the nanoparticle and formation of a network structure. Guo et al. (2010) measured dielectric properties of nanocomposite of iPP containing different metal-oxide particles, including spherical and rod-shaped TiO_2 nanoparticles, prepared by in-situ

polymerization. They showed that the nanocomposite containing TiO_2 nanorods, compared to spherical TiO_2, have more tendencies to percolate at a volume content less than 5.1 vol%. In comparison to the nanocomposite containing conductive nanoparticles, there is a relatively small difference between electrical conductivity of the polymer and TiO_2 as a semiconductor. This could cause uncertainty in determining the percolation threshold and necessitates applying other methods for structural investigation on these nanocomposites.

Melt-state viscoelastic behavior of polymer nanocomposite containing conductive nanoparticles has been widely studied to find a relation between rheological and electrical percolation threshold (Kasgoz et al. 2012; Huang et al. 2012; Bangarusampath et al. 2009; Abbasi et al. 2009; Kota et al. 2007; Hu et al. 2006; Pötschke et al. 2004; Du et al. 2004; Pötschke et al. 2002). However, the relation among microstructure, rheology and electrical properties of polymer nanocomposite with semiconductor inclusions, such as TiO_2, has not been investigated. Linear viscoelastic properties of polymer nanocomposites containing spherical TiO_2 nanoparticles, as a model system, have been studied previously (Romeo et al. 2009; Romeo et al. 2008; Acierno et al. 2007). It was shown that due to the weak polymer-filler interaction, the viscoelastic response of the nanocomposite could be separated to two distinct parts with different kinetics: fast relaxation (short response) of polymer matrix, and slow relaxation (long time) of the particle aggregates. Nevertheless, the range of concentration investigated was limited.

To the authors' knowledge, the present study is the first report on relationship between melt-state viscoelastic properties of nanocomposites, based on a thermoplastic and TiO_2 nanoparticles, and their electrical properties in a wide range of ϕ focusing on percolation threshold of the system. Uncompatibilized and compatibilized nanocomposites of iPP/TiO_2 nanocomposites were prepared by twin-screw extrusion and, correlations between their morphology, rheology and electrical properties were investigated.

4.2 Experimental

4.2.1 Materials

Table 4.1 reports the main characteristics of the polymers used in this study. An isotactic polypropylene (PP) homopolymer (PP4712E1, ExxonMobil, USA) was used as the polymer matrix and an anhydride-modified polypropylene (AMPP) was utilized as the compatibilizer (Bynel 50E571, DuPont, USA).

Table 4.1: Characteristics of the polymeric materials

Polymer	Designation	Supplier	Density (ρ)	MFI[a]	η_0[b]	Maleic anhydride content[c]
			[g/cm^3]	[g/10 min]	[Pa.s]	[%Wt.]
PP	PP4712E1	ExxonMobil	0.9	2.8	8000	-
AMPP	Bynel® 50E571	DuPont	0.89	3.5	5800	0.1

[a] ASTM D1238 (230 °C/2.16 Kg)

[b] Zero-shear viscosity; obtained from complex viscosity measured in frequency sweep test at 205 °C

[c] From the supplier

A commercial grade TiO_2 nanoparticle (AEROXIDE TiO_2 P 25, Evonik, Germany) was used in this study. According to the information provided by the supplier, AEROXIDE P 25 consists of an hydrophilic fumed TiO_2 with a density ρ of 4.26 g/cm^3, an average primary particle size of 21 nm, and a nanocrystalline structure composed of a mixture of anatase/rutile (79/21 wt%). Figure 4-1 shows a TEM image of the TiO_2 nanoparticles. As can be seen in Figure 4-1, most of the particles are spherical with sizes ranging from 15 nm to 45 nm.

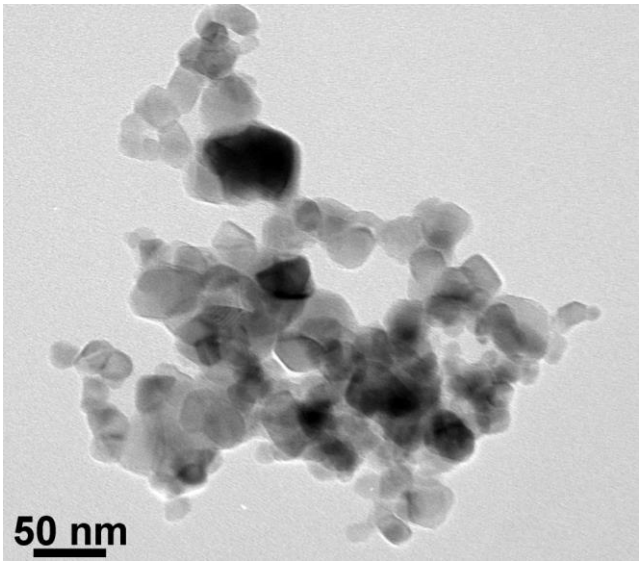

Figure 4-1: TEM image of the TiO_2 nanoparticles used in this work

4.2.2 Sample Preparation

The compatibilized and uncompatibilized PP/TiO_2 nanocomposites containing 1 to 15 vol% (4.6 to 45.5 wt%) of TiO_2 were prepared via a masterbatch method using a tightly intermeshing co-rotating twin-screw extruder (Leistritz ZSE-18HP-40D, Germany) with screw diameter Ø = 18 mm and length to diameter ratio L/D = 40, equipped with a typical compounding screw profile.

First, two masterbatches based on PP and AM-PP matrices containing 18 vol% (51 wt%) of TiO_2 nanoparticles were prepared through two extrusion passes. Then, in the third extrusion run, the masterbatches were diluted to lower concentrations by adding neat PP. All nanocomposites were prepared using a constant screw speed of 200 rpm and the same temperature profile: 160, 190, 195, 200, 202, 205, 205 and 205 °C (from hoper to die). Noteworthy, all the materials were vacuum dried at 80 °C for 8 hours before each mixing run. They were fed to the extruder, from the main hopper, using a volumetric feeder (for the polymers and the composites) and a high-precision powder feeder (K-Tron, USA) for the TiO_2 nanoparticles. In order to minimize thermo-mechanical degradation during the intensive mixing, 3000 ppm of an antioxidant (Ciba IRGANOX B 225, BASF) was added.

Table 4.2 reports the compositions of the samples prepared in this work. It summarizes both mass and volume contents of TiO_2 respect to the total content of the polymer matrices. The

matrices are neat PP and mixtures of PP and AMPP in uncompatibilized (PPT) and compatibilized (PPAMT) nanocomposites respectively. The compositions were presented in the form of volume content (vol%) to make comparison between the nanocomposites containing TiO_2 and the nanocomposite containing other types of particles with different densities. Since the polymer nanocomposites in the melt state could be considered as suspensions of the solid spherical nanoparticles in the liquid polymer melts, volume contents of TiO_2 in the melt state (at 205 °C) were also reported in Table 4.2. It shows that the contents of TiO_2 in the melt state in the both PPT and PPAMT samples are approximately identical.

Table 4.2: Compositions of the samples in solid and melt states

		Mass Content wt%			Volume Content vol%			
	Sample Code				(in solid state)			(in melt state[a])
		PP	AMPP	TiO_2	PP	AMPP	TiO_2	TiO_2
Uncompatibilized	PPT1	95.4	-	4.6	99	-	1	1.46
	PPT3	87.2	-	12.8	97	-	3	4.34
	PPT4	83.5	-	16.5	96	-	4	5.76
	PPT5	80.1	-	19.9	95	-	5	7.20
	PPT75	72.3	-	27.7	92.5	-	7.5	10.6
	PPT10	65.5	-	34.5	90	-	10	14.0
	PPT15	54.5	-	45.5	85	-	15	20.6
Compatibilized	PPAMT1	91.0	4.4	4.6	94.4	4.6	1	1.46
	PPAMT3	74.8	12.4	12.8	83.0	14.0	3	4.38
	PPAMT4	67.5	16.0	16.5	77.4	18.6	4	5.83
	PPAMT5	60.6	19.4	20.0	71.8	23.2	5	7.28
	PPAMT75	45.2	27.0	27.8	57.7	34.8	7.5	10.9
	PPAMT10	33.0	33.0	34.0	43.6	46.4	10	14.5
	PPAMT15	9.9	44.4	45.7	15.3	69.7	15	21.5

[a] at 205 °C

For further characterization, the dried compounded pellets were compression-molded into discs specimens using a Carver hot mini-press (Wabash, USA) at 200 °C applying up to 14 MPa pressure for 3 minutes under nitrogen atmosphere.

4.2.3 Morphological Characterization

The dispersion of TiO_2 nanoparticles in the polymeric matrices was studied by using field emission gun scanning electron microscopy (FEG-SEM, JEOL 7600F, Japan) operated at 2 KV. In order to obtain high-quality images, cross sections of the disc specimens were cut under liquid nitrogen using a glass knife of a cryo-microtome (RM 2165, Leica, Germany) equipped with a cryo-chamber (LN 21).

In addition, atomic force microscopy (AFM) at room temperature was utilized to characterize morphology of the samples. AFM images of the microtomed cross sections were captured by a Dimension™ 3100 (Bruker, USA) equipped with a Veeco Nanoscope V™ controller (Bruker). Intermittent contact imaging (i.e. TappingMode™) was performed at a scan rate of 1 Hz using etched silicon cantilevers (ACTA, Applied NanoStructures, USA) with a resonance frequency around 300 kHz, a spring constant around 42 N/m, and tip radius <10 nm. All images were acquired with a medium tip oscillation damping (20-30 %).

4.2.4 Rheological Measurements

All the rheological measurements were carried out, at 205 °C and under N_2 atmosphere, using a stress-controlled rotational rheometer (Bohlin Gemini HR nano, Malvern Instruments, UK) equipped with an environmental test chamber (ETC). The dynamic oscillatory tests were performed using a parallel-plate geometry with a diameter of 25 mm and a gap of 1 mm. 25-mm-diameter disk specimens, prepared by compression molding, were vacuum dried at 80 °C for 8 h prior to the tests to minimize degradation. The linear viscoelastic region (LVR) of the samples was determined by strain sweep tests from 0.01 to 1000 % at 1 rad/s. Thermal stability of the materials during the rheological experiments at 205 °C was examined by single-frequency time sweep test at 0.1 Hz and, accordingly, the test methods of each sample were defined such that their total test time was in the range of the time stability. Small amplitude oscillatory shear (SAOS) frequency sweep tests were performed in the range of 0.1-200 rad/s. Based on the morphological observations, it was assumed that the particles size was sufficiently smaller than

the gap distance and, there were negligible error due to wall or slip effect. This assumption was justified by changing the gap.

4.2.5 Electrical Resistivity Measurements

Volume resistivity (ρ_v) of the PP/TiO_2 samples was measured under direct current (DC) at room temperature. An electrometer/high resistance meter (6517A, Keithley, USA) connected to a two-probe resistivity test fixture (8009, Keithley, USA) was utilized to measure electrical current perpendicular to the surfaces (through plane) of the compression-molded specimens under different voltages. This equipment allows resistivity measurements up to 10^{17} Ω. The disk-shaped specimens with approximately 1.5 mm thickness and 10 cm diameter were dried overnight at 50 °C and cooled down to room temperature in a desiccator, just before the measurements. Then, they were placed between the two electrodes which applied electrical potentials from 250 to 1000 V and, measured electrical currents. Capacitance of the relatively high resistive samples causes an error in measuring real electrical current through the samples. In order to eliminate the error, the neat electrical currents were obtained by subtracting electrical current values during 100 s after cessation of voltage from the values during 100 s after applying the voltages. The electrical resistance (R) of each specimen was determined from the slope of the I-V curve and, converted to volume electrical conductivity σ (inverse of ρ_v) using the following relation

$$\sigma = \frac{1}{\rho_v} = \frac{t}{AR} \tag{4.4}$$

where t is the specimen thickness (≈1.5 mm) and A is the contact surface area of the electrodes (22.9 cm^2).

4.3 Results and Discussion

4.3.1 Electrical Properties

Since TiO_2 is an inorganic semiconductor, electrical properties of polymer/TiO_2 nanocomposites are significantly different from the systems containing conductive nanoparticles such as metal,

CB, and CNT (Huang et al. 2008; Huang et al. 2012; Bangarusampath et al. 2009). Two main concerns in measuring electrical conductivity of PP/TiO_2 nanocomposites are the relatively small difference between electrical conductivities of the two components and absorption of moisture on the hydrophilic surface of TiO_2 nanoparticles.

Figure 4-2a shows the variation of electrical currents with time through PPT5 sample after applying and, subsequently, interrupting different electric potentials (250, 500 and 1000 V). The results are presented in the form of charging (I_{ch}) and discharging (I_{dch}) currents respectively. As it can be seen, I_{ch} (black symbols) decreases with time to reach a steady state value. As expected, the steady state value increases with the applied voltage. The slowly decreasing current of I_{ch} is known as "absorption current" or "anomalous current". This behavior is attributed to the capacitance characteristic of the iPP/TiO_2 nanocomposite as a non-ideal dielectric (Smith et al. 2008). On the other hand, I_{dch} originates from depletion of the charges stored in the sample during applying voltage. In the early times after cessation of the voltage, I_{dch} has values close to I_{ch} but it reduces to the negligible values at the longer times (blank symbols in Figure 4-2a). In order to have the neat current due to electrical conductance of the sample, I_{dch} is subtracted from I_{ch} and noted as I_{ch}-I_{dch} (color symbols in Figure 4-2a).

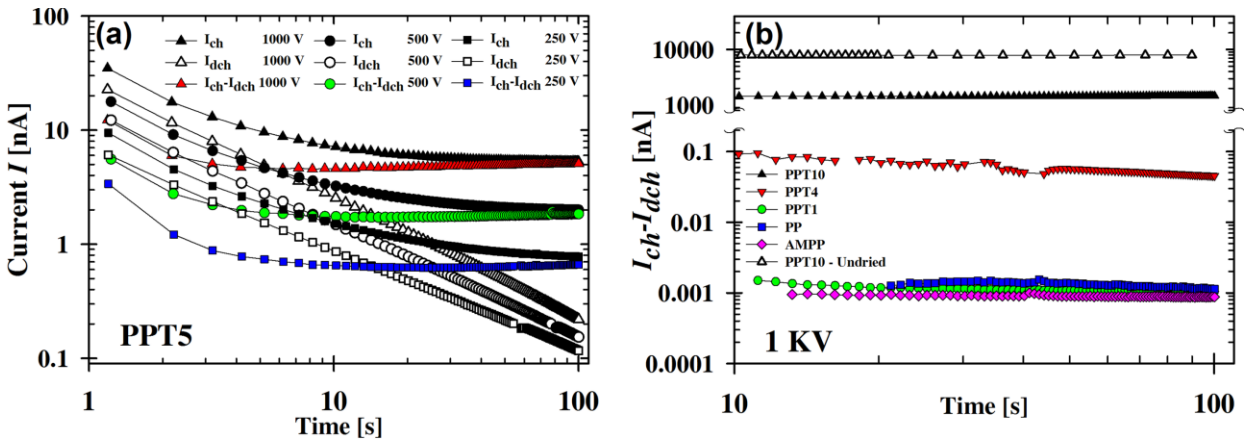

Figure 4-2: (a) Variation of electrical current with time through PPT5; after applying different voltages, (I_{ch}), after cessation of the voltages (I_{dch}), and the neat current (I_{ch}-I_{dch}), (b) variation of the neat current with time in the neat polymers, the uncompatibilized samples containing different TiO_2 contents, and undried PPT10

Figure 4-2b illustrates I_{ch}-I_{dch} versus time under 1000 V for the neat polymers and PPT nanocomposites containing different contents of TiO_2. As it can be seen, the neat electrical current passing through the samples increases with TiO_2 volume fraction. While extent of the current in PP, AMPP and PPT1 are in the range of pA, adding 4 and 10 vol% of TiO_2 increased the current more than 2 and 6 orders of magnitude, respectively. These significant increases could be attributed to the formation of an interconnected network of TiO_2 in the PP matrix which facilitates the movement of electrons between the two electrodes. Time dependency of DC conductivity is a characteristic of insulating materials (Huang et al. 2008). As it can be seen in Figure 4-2b, electric current through PPT10 had less time dependency indicating its higher conductivity compared to the other samples.

Effect of moisture on conductivity of PP/TiO_2 nanocomposites is illustrated in Figure 4-2b. The neat current through the undried PPT10 was around 9 times larger than the dried sample which might be due to the moisture adsorbed by the TiO_2 nanoparticles.

The change in the electrical conductivity of composite materials with composition can be interpreted in terms of the percolation theory, either qualitatively or quantitatively. Figure 4-3 shows σ as a function of TiO_2 volume fraction (ϕ) for the PPT and PPAMT nanocomposites. In both cases, three different regions for σ are observed. At low TiO_2 content ($\phi \leq 3$ %), there is no significant change in σ and, it is in the range of 10^{-16}-10^{-15} S/m that is close to conductivity of the neat polymers. Noteworthy, the measured values of bulk electrical conductivity for PP and AMPP were less than 10^{-15} S/m that were consistent with their insulating characteristic and the previously reported values (Huang et al. 2012). In the second region ($3 < \phi < 10$), electrical conductivity increased significantly with TiO_2 content and reached a high plateau at $\sigma \approx 10^{-9}$ S/m. This stepwise change of σ, by at least 6 orders of magnitude, could be attributed to the formation of the infinite conductive clusters of TiO_2 nanoparticles through the sample at the electrical percolation threshold ($\phi_{c\sigma}$). Since materials with electrical conductivity higher than 10^{-2} S/m are generally known as electrical conductors (Pötschke et al. 2009), at $\phi_{c\sigma}$ of the PP/TiO_2 nanocomposite system a transition from insulator to semiconductor took place. Measuring electrical conductivity of the TiO_2 powder, used in this work, gave a value around 10^{-8} S/m which is close to the high plateau value of σ in Fig. 3.

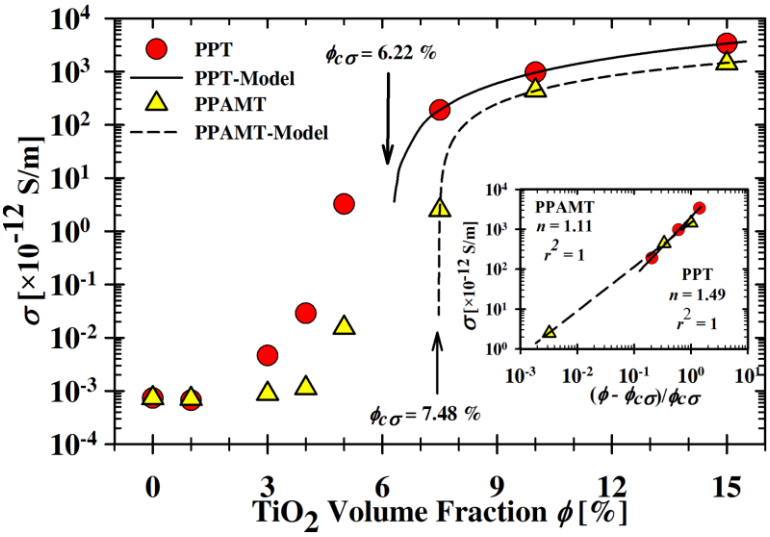

Figure 4-3: Electrical conductivity as a function of TiO_2 content. The lines are the best fits using Equation 4.5

It is generally accepted to use power-law relationships (e.g. Equation 4.1) between σ and ϕ, above the percolation threshold, to quantitatively determine $\phi_{c\sigma}$ in the filled systems (Du et al. 2004; Hu et al. 2006; Huang and Wang 2011). Figure 4-3 shows the results of fitting electrical conductivity using the following equation (Abbasi et al. 2009):

$$\sigma = \beta_{c\sigma}\left(\frac{\phi - \phi_{c\sigma}}{\phi_{c\sigma}}\right)^{n} \quad \text{for} \quad \phi \geq \phi_{c\sigma} \tag{4.5}$$

where $\beta_{c\sigma}$ and n are power-law constants, and $\phi_{c\sigma}$ is the electrical percolation threshold (in vol%). As can be seen in Figure 4-3 and its inset, the electrical conductivity data can be well fitted by Equation 4.5 at the volume fractions above the electrical percolation threshold giving $\phi_{c\sigma}$ of 5.29 and 7.48, for PPT and PPAMT nanocomposites respectively. The obtained values for $\phi_{c\sigma}$ are in the range of the percolation thresholds previously reported for the composite systems containing TiO_2 inclusions (Wang et al. 2013; Guo et al. 2010). The lower $\phi_{c\sigma}$ of the PPT samples, compared to PPAMT, should be attributed to the emergence of an interconnected microstructure at relatively low concentrations. These values for $\phi_{c\sigma}$ are much lower than the value predicted by percolation theory (16 vol%) as the critical volume fraction for random packing of hard spheres

in three dimensions (Stauffer 1985; McLachlan et al. 1990). However, $\phi_{c\sigma}$ of the PP/TiO_2 nanocomposite are quite high in comparison to most of the values reported for polymeric systems containing CNTs (Bauhofer and Kovacs 2009). It is because of the conductive nature and higher aspect ratio of CNT compared to the TiO_2 nanoparticles (Pötschke et al. 2009). On the other hand, $\phi_{c\sigma}$ around 5.6 (≈8.75 wt%), 9.7, and 6.1 vol% have been reported for the nanocomposites containing spherical conductive nanoparticles of CB, aluminum and copper respectively (Pötschke et al. 2009; Huang et al. 2009; Boudenne et al. 2005). They are relatively close to the values estimated for the PP/TiO_2 system in the present work.

4.3.2 Morphology

Properties of the nanocomposites are strongly affected by the state of dispersion of the nanoparticles in the host polymer. A fine dispersion and distribution of the dispersed TiO_2 particulate phase can be achieved by an efficient mixing process which breaks TiO_2 aggregates/agglomerates. SEM micrographs of the cryo-microtomed cross sections of PPT and PPAMT nanocomposites are shown in Figure 4-4a, Figure 4-4c and Figure 4-5. As can be seen, size of the dispersed domains of TiO_2 increases with nanoparticle content. In PPT1 and PPAMT1 (Figure 4-4a and Figure 4-4c), there are mostly individual nanoparticles or aggregates which are composed of few TiO_2 nanoparticles and, homogenously dispersed through the matrices. This is confirmed with the associated AFM images shown in Figure 4-4b and Figure 4-4d (showing higher magnification).

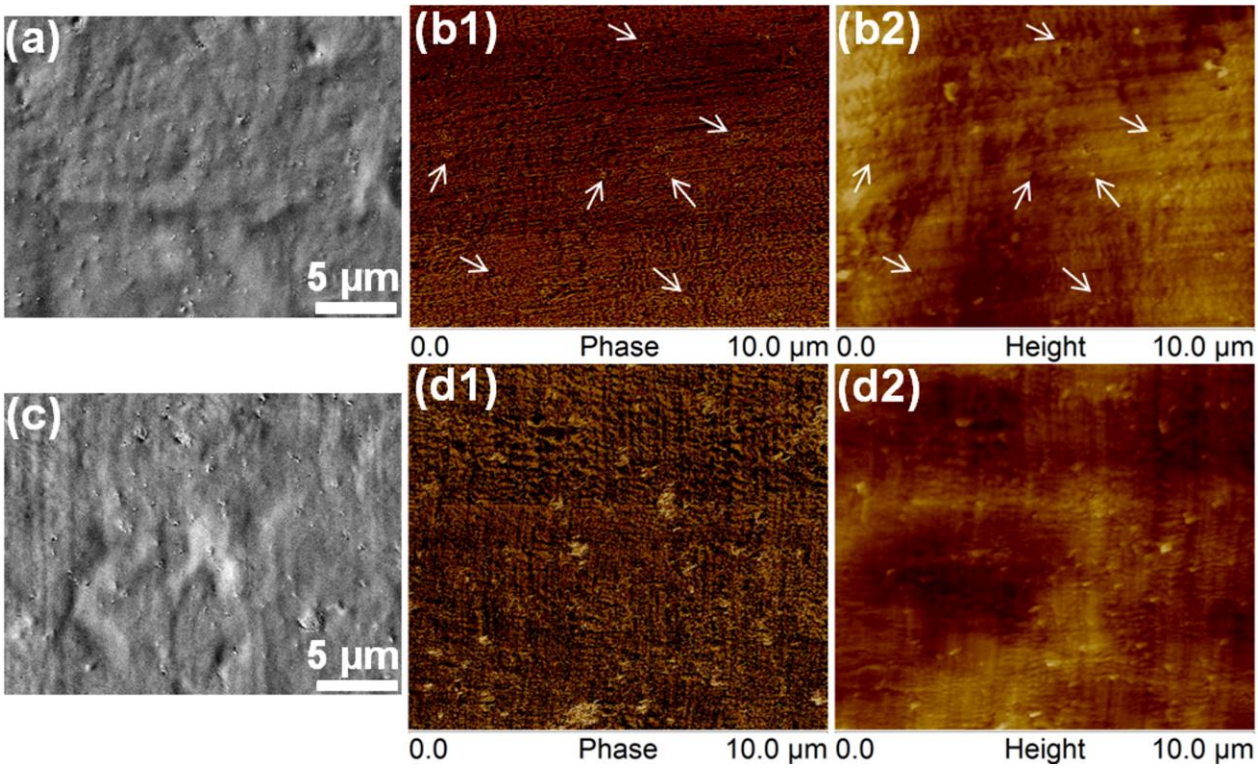

Figure 4-4: (a) SEM and (b) AFM images of PPT1, (c) SEM and (d) AFM images of PPAMT1. AFM images show higher magnification. Arrows indicate the TiO2 nanoparticles

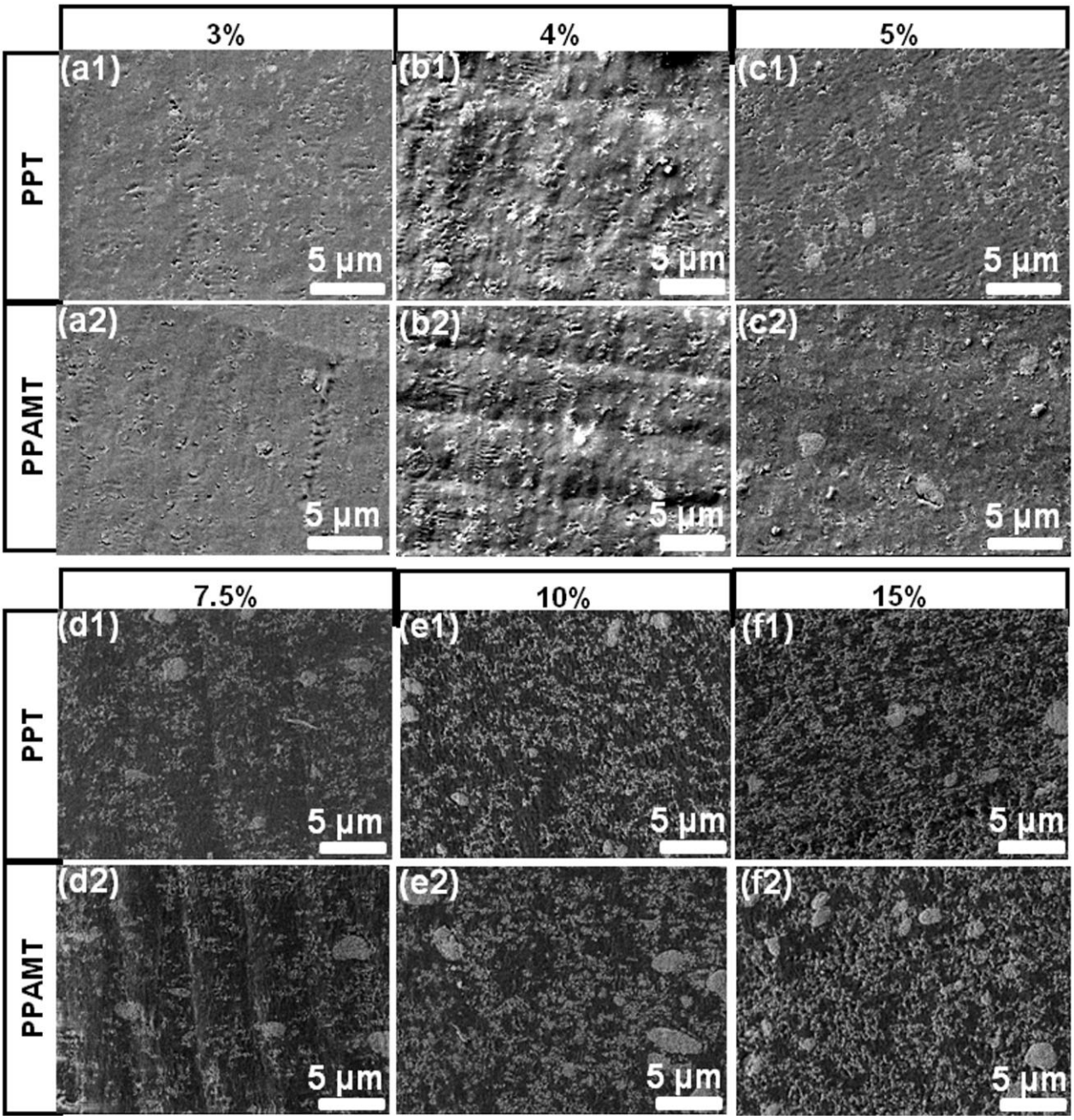

Figure 4-5: SEM micrographs of the nanocomposite samples containing different TiO_2 contents: (a) 3, (b) 4, (c) 5, (d) 7.5, (e) 10 and (f) 15 vol%

The number and size of the aggregates increase with TiO_2 volume fraction (Figure 4-5). Basically, higher nanoparticle content leads to shorter interparticle distance and higher probability of TiO_2 aggregation (Acierno et al. 2007; Bahloul et al. 2010). At vicinity of the

percolation threshold (ϕ_p), the interparticle distances decreases enough to result in contact between the nanoparticle subunits and formation of a space-spanning cluster network (Cassagnau 2008). Figure 4-5 shows that 5 vol% of TiO_2 is a critical composition close to or above the ϕ_p where an interconnected network of TiO_2 forms. Similarly to other particulate polymer nanocomposites, aggregates of the TiO_2 nanoparticles in PP have fractal structures (Bailly et al. 2010). Based on Figure 4-5d-5f, it is noticeable that aggregates of TiO_2 nanoparticles in the compatibilized nanocomposites (PPAMT) are more compact compared to the uncompatibilized ones (PPT).

Figure 4-5 also shows the effect of adding the anhydride-modified PP (AM-PP), as a compatibilizer, on the morphology of the nanocomposites. In the nanocomposites containing 3 vol% TiO_2, adding AM-PP significantly improved the dispersion of the nanoparticles. It can be seen in Figure 4-5a2 that most of the aggregates in sample PPAMT3 have sub-micron size. There are also some tiny aggregates of few single nanoparticles and few particle aggregates larger than 1 μm. This could be related to the compatibilizing role of AMPP that leads to the better distribution and dispersion of the TiO_2 nanoparticles compared to PPT3 (Figure 4-5a1). Reaction between the anhydride groups of AMPP and the hydroxyl groups on the surface of TiO_2 could be responsible for the improvement of interactions between hydrophilic TiO_2 particles and the organic PP matrix (Li et al. 2009). As it can be seen in Figure 4-5c1 and Figure 4-5c2, by increasing the TiO_2 content to 5 vol%, the number and size of the TiO_2 aggregates increases and, microstructures of the compatibilized and uncompatibilized samples become similar. However, TiO_2 aggregates in PPAMT5 were rather isolated and spherical while the TiO_2 nanoparticles in PPT5 formed connected cluster structure.

Figure 4-6 depicts results of image analysis for the SEM micrographs of the nanocomposites containing 1-7.5 vol% TiO_2 (Figure 4-4 and Figure 4-5) in the format of number fraction of the aggregates with different surface area (Figure 4-6a) and their contribution to total area (Figure 4-6b). It should be mentioned that there is no independent cluster structure in the samples containing 10 and 15 vol% of TiO_2 (Figure 4-5e and Figure 4-5f). The evolution of morphology with TiO_2 content in the nanocomposites could be realized by considering the two ranges of area in Figure 4-6; 10000-50000 and >200000 nm^2. Increasing TiO_2 loading results in fewer small aggregates and more large particle clusters. In order to have a quantitative

comparison among the microstructures observed by SEM, the area range that has the maximum fraction of particles in each sample was considered. As can be seen in Figure 4-6a, for all the PPT and PPAMT nanocomposites, except PPT75, the maximum fraction of particles are in the range of 10000-50000 nm^2. However, in the case of PPT75, there is a maximum in the range of 50000-100000 nm^2. This could be attributed to the fact that the less compact fractal microstructure of TiO_2 clusters in the PPT nanocomposite led to formation of the interconnected subunits in a lower TiO_2 content compared to PPAMT. In the other words, PPAMT samples have more isolated aggregates than PPT that is due to the better dispersion of the nanoparticles in the PPAMT system.

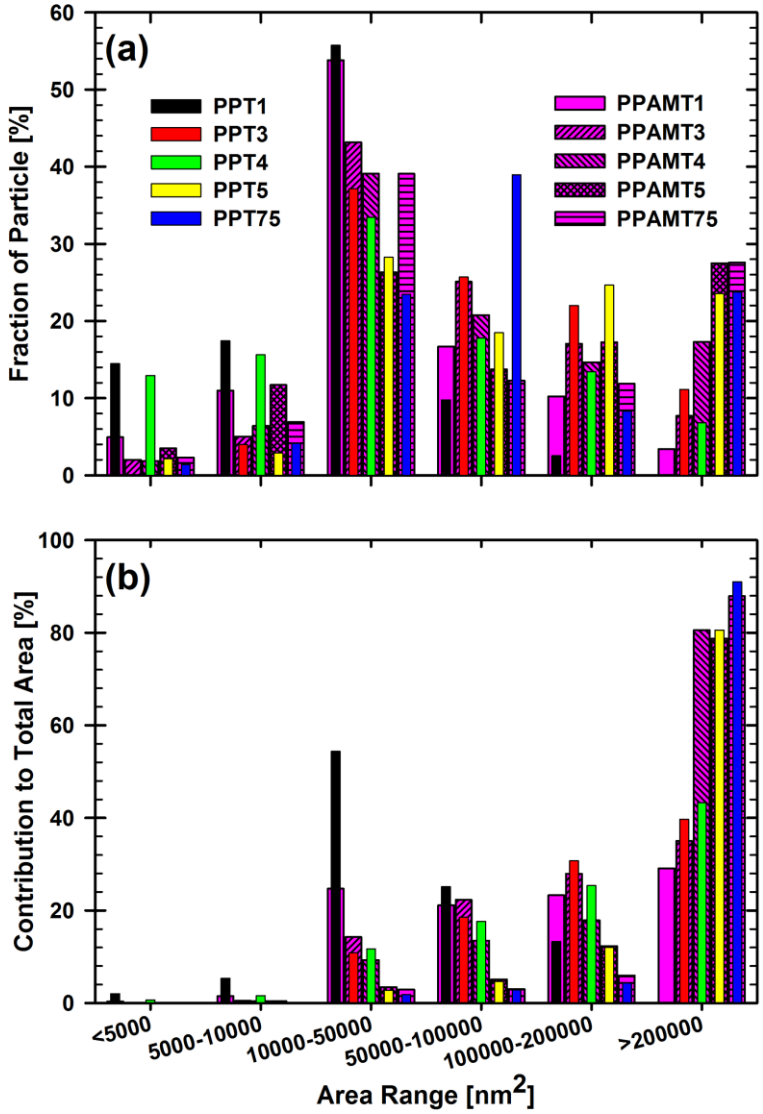

Figure 4-6: Results of image analysis of SEM micrographs (Figures 4-4 and 4-5) in the format of; (a) number fraction of the aggregate with a given range surface area, and (b) contribution to total area

4.3.3 Rheology

4.3.3.1 Linear Viscoelastic Properties

Rheology is an indirect method to obtain reliable data about bulk of the nanocomposites in the melt state. Linear viscoelastic properties are very sensitive to the microstructural changes in the polymer nanocomposites. Figure 4-7 shows the results of frequency sweep tests on the neat PP

and the compatibilized and uncompatibilized nanocomposites at 205 °C. It reports variation of complex viscosity (η^*) and elastic modulus (G') versus angular frequency (ω) for the samples with different contents of TiO_2. The insets in Figure 4-7c and Figure 4-7d representatively show variations of G' and η^* during the time sweep tests for the neat PP and the samples containing 4 and 7.5 vol% of TiO_2. They show that time dependency of the rheological properties increase with TiO_2 content. It could be attributed to the tendency of TiO_2 nanoparticles to form aggregates or agglomerates under oscillation in the melt-state particularly close to and above the percolation threshold (Bailly and Kontopoulou 2013). Accordingly, the frequency range lower than 0.1 rad/s was not accessible, because it required long-time of measurement.

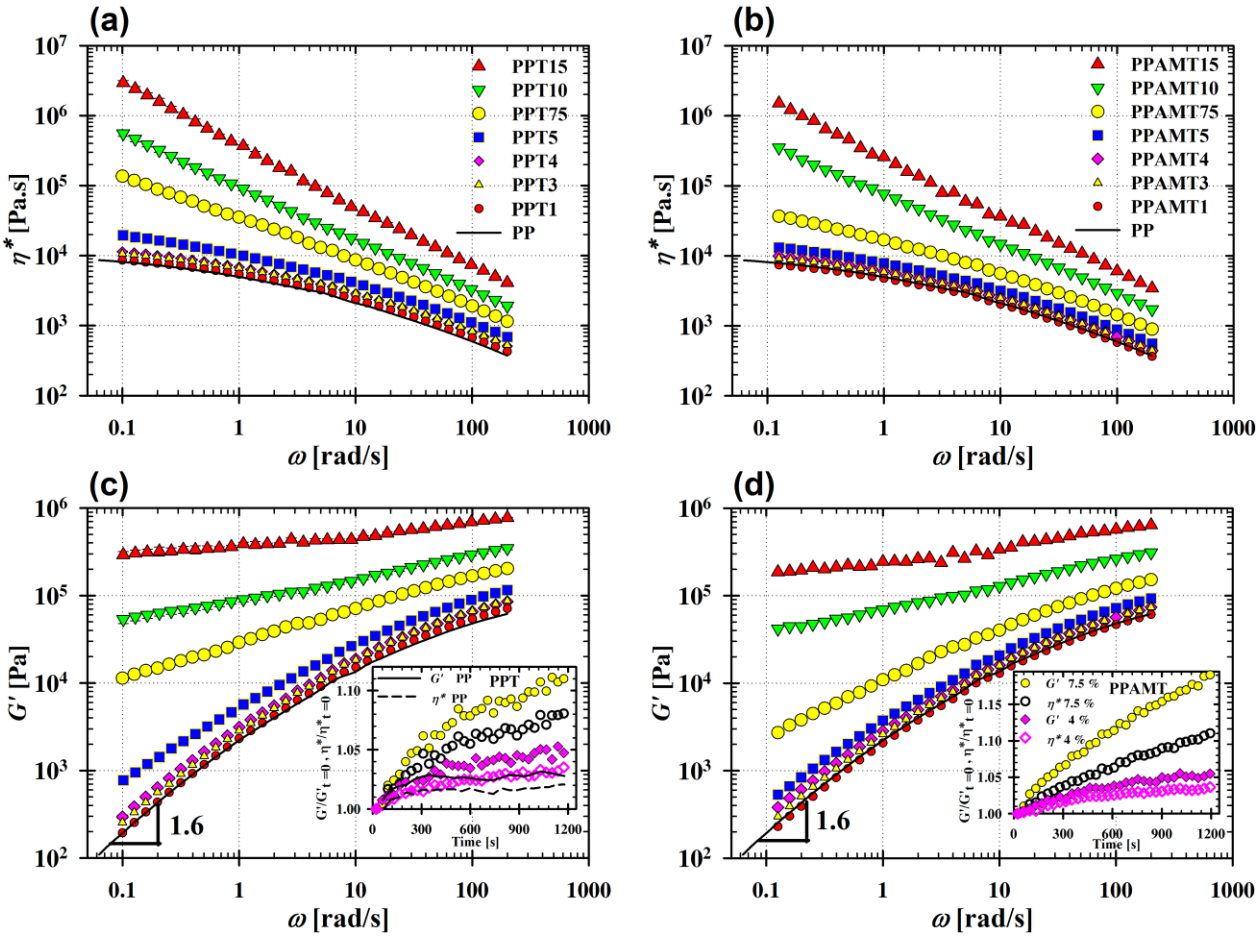

Figure 4-7: Complex viscosity (η^*) and elastic modulus (G') versus angular frequency of the nanocomposites samples: (a), (c) PPT, and PPAMT (b), (d). Insets in (c) and (d) show variation

normalized values of G' and η^* ($G'/G'_{t=0}$ and $\eta^*/\eta^*_{t=0}$) during the time sweep tests for the neat PP and the nanocomposites containing 4 and 7.5 vol% of TiO_2

Figure 4-7 shows that addition of TiO_2 nanoparticle leads to increase in both η^* and G' especially at low angular frequencies. The effect of TiO_2 content on the rheological properties of the PPT samples containing 5 and 7.5 vol% is more pronounced compared to PPAMT. Figure 4-7a shows that adding up to 3 vol% nanoparticles does not significantly change η^* over whole range of frequency. On the other hand, for $\phi \geq 4$, the behavior of the samples deviates obviously from that of the PP matrix. At high frequencies, where the viscoelastic properties of the suspending media are governing, the discrepancies are smaller. In the PPT nanocomposites, at $\phi \geq 7.5$ the pseudoplastic plateau disappeared, shear thinning increased and complex viscosity are significantly enhanced over the whole range of frequency. Moreover, dependency of η^* on frequency at low frequencies increased with TiO_2 content. Figure 4-7c-d show that adding TiO_2 nanoparticles decrease frequency dependency of dynamic elastic modulus (G') and leads to the formation of a plateau at low frequencies. This leads to flatness of the modulus curves at low frequencies for the most concentrated samples. The deviation from terminal behavior indicates that the presence of nanoparticles hinders long polymer chain relaxation. In order to quantitatively compare the changes in the rheological characteristics of the samples, η^* and G' at low frequencies ($0.1 \leq \omega \leq 0.5$ rad/s) were fitted using power-law type relations; $\eta^* \propto \omega^{n-1}$, $G' \propto \omega^m$ and $G'' \propto \phi^k$. In addition, zero-shear viscosity of the samples was determined using the four-parameter Carreau-Yasuda model;

$$\eta^* = \eta_0^* \left[1 + (\lambda\omega)^a\right]^{(c-1)/a} \tag{4.6}$$

where η_0^* is zero-shear viscosity, λ is the ratio of η_0^* to the shear stress at the transition from Newtonian to non-Newtonian behavior, a is the index that controls this transition and, c is the power-law index (Fontaine et al. 2013). The values of n, m, k and η_0^* are reported in Table 4.3. As can be seen, both m and n exponent decrease with ϕ showing the non-terminal behavior of the nanocomposites. The deviation of n from 1, represents a deviation from Newtonian behavior with increasing TiO_2 content. On the other hand, the significant increase in η_0^* with ϕ indicates the

formation of a space spanning network of TiO_2 nanoparticles. This abrupt change of η_0^* in PPT samples occurs at ϕ > 5 vol% where complex viscosity increases about two orders of magnitude. However, in PPAMT samples, this significant change takes place moderately. It could be attributed to the presence of AMPP with lower viscosity, compared to PP and smaller aggregate structures which need a higher TiO_2 content to reach the percolation threshold.

Table 4.3: Slope of rheological properties (Figure 4-7) at low frequencies and η_0^* from Equation 4.6

	PPT					PPAMT			
Sample	n [a]	m [a]	k [a]	η_0^* [b] [kPa.s]	Sample	n [a]	m [a]	k [a]	η_0^* [b] [kPa.s]
PP	0.81	1.10	0.78	12.5	AMPP	0.83	1.00	0.82	8.29
PPT1	0.83	1.12	0.79	12.3	PPAMT1	0.82	1.11	0.70	11.4
PPT3	0.81	1.08	0.79	16.3	PPAMT3	0.81	1.10	0.78	14.1
PPT4	0.80	1.06	0.77	16.9	PPAMT4	0.79	1.01	0.76	16.9
PPT5	0.73	0.85	0.70	49	PPAMT5	0.78	0.98	0.75	22.7
PPT75	0.40	0.38	0.43	3793	PPAMT75	0.67	0.70	0.65	395
PPT10	0.19	0.21	0.25	4748	PPAMT10	0.24	0.20	0.30	1630
PPT15	0.09	0.09	0.04	10890	PPAMT15	0.13	0.12	0.31	10693

[a] $\eta* \propto \omega^{n-1}$, $G' \propto \omega^m$ and $G'' \propto \phi^k$ at $.1 \leq \omega \leq 0.5$ rad/s

[b] obtained by fitting on Eq. 6

In order to investigate the effect of nanoparticles on elasticity of the molten nanocomposites, variation of G' versus ϕ at different frequencies are shown in Figure 4-8a and 8b respectively. In PPT samples at ω = 0.126 rad/s, G' rises slowly with ϕ up to 4 % followed by a steep increase in 4 < ϕ < 10. The same trend was observed at higher frequencies but with much smaller step increase. The critical volume fraction of the PPAMT samples, where the sharp increase of G' starts, is 5 %. It is higher than PPT and, is in agreement with the results of complex

viscosity (Figure 4-7a-b). It is noteworthy that the presence of TiO_2 increased G'' as well. However, G' is more sensitive to the nanocomposites microstructure.

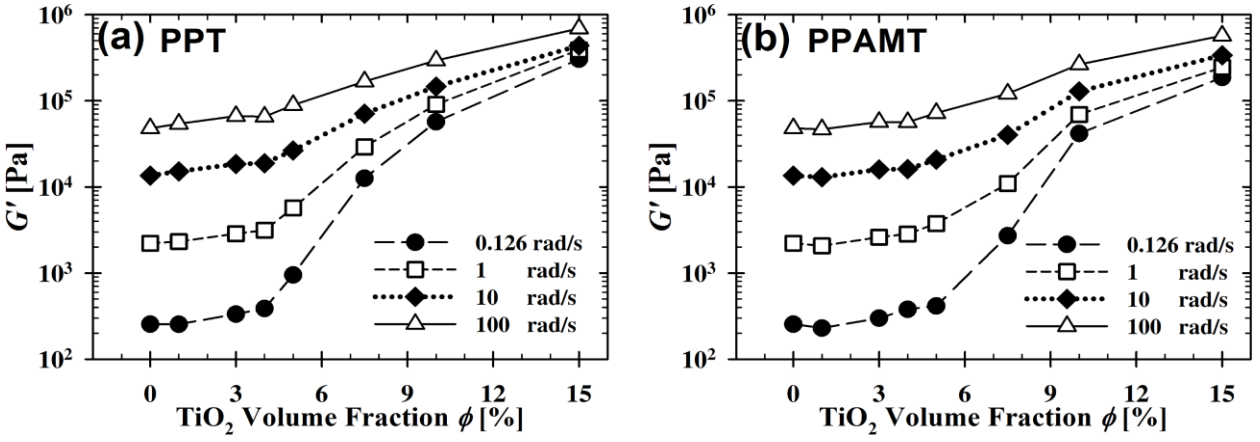

Figure 4-8: Variation of elastic modulus with nanoparticle content at different frequencies for (a) uncompatibilized and (b) compatibilized samples

To have a better observation about the changes in linear viscoelastic properties, imaginary part of complex viscosity (η'') versus real part (η') of the nanocomposites in the critical range of $4 \leq \phi \leq 7.5$ vol% are plotted in Figure 4-9 (*Cole-Cole* diagram). As can be observed for neat PP matrix in Figure 4-9, *Cole-Cole* diagrams of single phase systems with a single characteristics relaxation time are in the form of a semi-circle. However, in multi-phase complex systems, which have more than one relaxation time, the semi-circle diagram is distorted. In the PPT nanocomposites, the maximum of *Cole-Cole* diagram disappeared at $\phi \geq 5$ vol% indicating the presence of the interconnected aggregates of TiO_2 with long relaxation times. This change in *Cole-Cole* plot of the PPAMT samples is seen at 7.5 vol%. Intersection of the *Cole-Cole* plots with the line $\eta'' = \eta'$ represent the cross-over points where $G' = G''$. Table 4.4 summarizes the cross-over angular frequencies and the corresponding modulus. It can be seen that higher TiO_2 contents leads to lower angular frequency of cross-over points which is a characteristic of solid-like behavior. At $\phi \geq 7.5$ vol% in PPT and $\phi \geq 10$ vol% in PPAMT, values of elastic modulus exceed loss modulus without cross over which is another indication of lower percolation threshold in PPT.

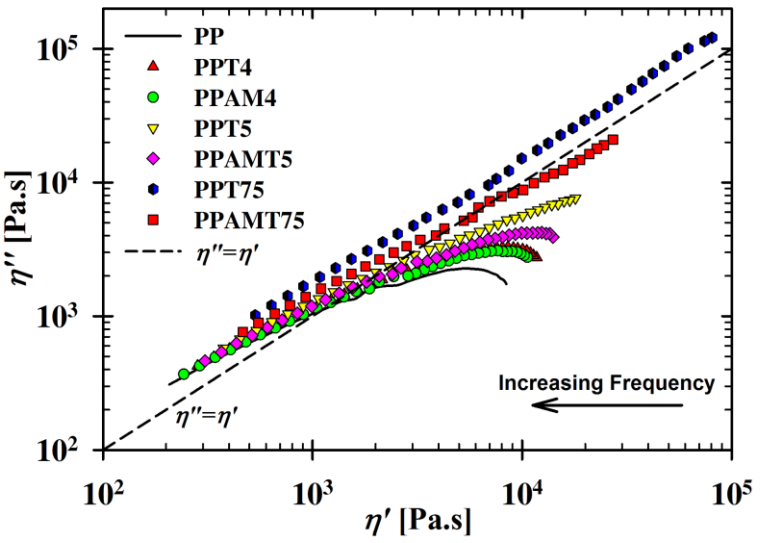

Figure 4-9: *Cole-Cole* diagrams of the samples with TiO_2 content of $4 \leq \phi \leq 7.5$ vol%

Table 4.4: Angular frequencies and values of the cross-over points where $G' = G''$

Sample	ω [rad/s]	G′=G″ kPa	Sample	ω [rad/s]	G′=G″ kPa
PPT1	20.0	23.7	PPAMT1	20.0	20.5
PPT3	20.0	28.9	PPAMT3	20.0	25.0
PPT4	15.9	25.7	PPAMT4	15.9	22.3
PPT5	14.7	34.4	PPAMT5	15.9	28.7
			PPAMT75	3.16	22.5

Loss factor ($tan\delta$), where δ is the phase angle ($tan\delta = G''/G'$), is a sensitive parameter to microstructural evolutions and transitions in multi-phase materials and, it is usually used to demonstrate liquid-solid transition at the percolation threshold. Figure 4-10 compares the variation of $tan\delta$ versus angular frequency in the nanocomposites undergoing the transition. The samples containing 4 vol% of TiO_2 exhibit behaviors similar to neat PP where $tan\delta$ decreases

with ω. Their plots have negative slopes indicating the higher elasticity of their melts at the higher angular frequencies. In PPT samples, $tan\delta$ at low angular frequencies significantly decreases with increasing ϕ from 4 to 5 vol%. This is due to the higher elasticity of the nanocomposites containing a percolated structure of nanoparticle at the concentrations above their percolation threshold. On the other hand, based on the results of $tan\delta$, the transition in PPAMT takes place at volume content between 5 and 7.5 vol%. Less dependency of $tan\delta$ on ω at high concentrations is another sign of the solid-like behavior.

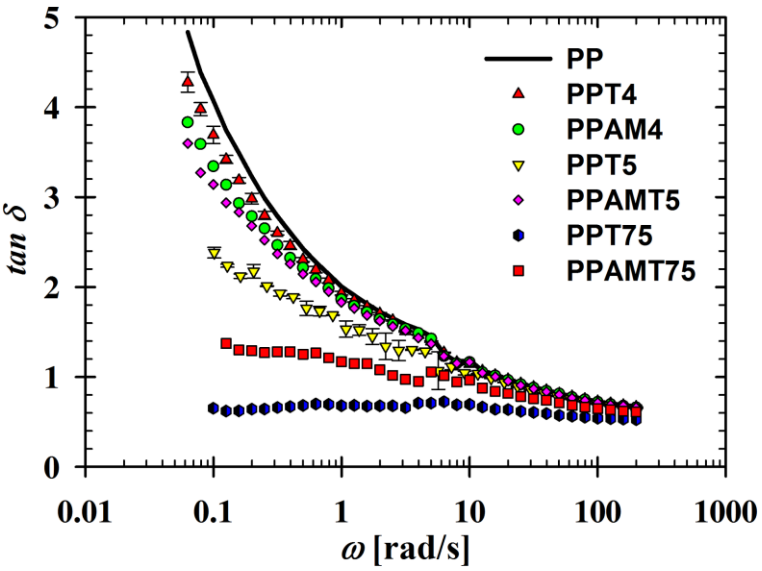

Figure 4-10: $tan\delta$ versus angular frequency for the samples containing 4-7.5 vol% of TiO_2

As shown in Figure 4-7, solid like behavior due to the formation of filler network leads to the yield behavior and the low-frequency plateau for G'. Presence of a finite yield stress could be clearly seen by plotting η^* versus G^*. Figure 4-11 shows that increasing TiO_2 content resulted in a divergence in η^*-G^* and, above 5 vol%, slopes of the curves became much steeper. This pronounced divergence in PPT75, compared to PPAMT75, indicates that 7.5 vol% was well above the percolation threshold of PPT nanocomposite. Therefore, the rheological percolation threshold in the uncompatibilized samples is lower than that in the compatibilized ones.

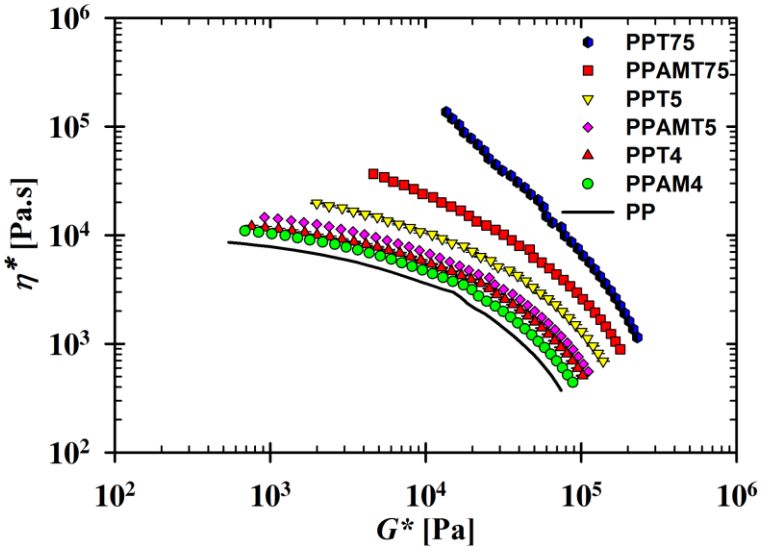

Figure 4-11: Plots of η^* versus G^* for the samples undergoing liquid-solid transition

In analogy with the electrical properties, rheological percolation threshold could be defined as a critical particle loading where an interconnected network of the filler is formed and liquid-solid transition occurs. It is generally admitted to describe the relation between the rheological properties and filler content above the percolation threshold by power-law equations. Similarly to Equation 4.1, we can use Equation 4.7;

$$p_R = \beta_{cp}\left(\frac{\phi - \phi_{cp}}{\phi_{cp}}\right)^n \quad \text{for} \quad \phi \geq \phi_{cp} \tag{4.7}$$

where β_{cp} and n are power-law constants, and ϕ_{cp} is the percolation threshold (vol%) determined based on the values of the rheological property p_R.

It was reported that, among the various rheological properties, estimating ϕ_{cp} based on G' gives the best description for experimental values (Kota et al. 2007). Since the polymer matrices of PPAMT samples are blends of PP and AMPP, their rheological properties are not the same as the PP matrice in PPT samples. Therefore, reduced values of the rheological properties of the nanocomposites relative to the properties of the corresponding matrices were used for fitting to the power-law relation. Huang and Wang (2011) used reduced form of G' relative to the matrix (G'_m) to compare percolation threshold in nanocomposites based on different grades of PS. Figure

4-12 shows the variation of reduced complex viscosities (η^*_r) and reduced elastic modulus (G'_r) with ϕ and the best fits of the results using Equation 4.7. Table 4.5 summarizes the obtained fitting results to find the rheological percolation threshold based on different criteria of G', G'_r, η^* and η^*_r. As can be seen, the type of considered rheological criterion does not affect the estimated value of ϕ_c for PPT samples. On the other hand, using η^* and η^*_r to determine ϕ_c of PPAMT samples led to lower values of percolation thresholds compared to those calculated based on G' and G'_r. It could be concluded that, regardless of fitting criterion, rheological percolation in uncompatibilized samples (PPT) are generally lower than those for compatibilized ones (PPAMT). This is in a qualitative agreement with the results of electrical percolation thresholds and, is directly due to the state of dispersion of TiO_2 nanoparticles. It should be noted that rheological percolation threshold in thermoplastic nanocomposite containing conductive nanoparticles is usually lower than electrical percolation threshold (Huang and Wang 2011; Pan and Li 2013; Pötschke et al. 2009; Abbasi et al. 2009; Sumfleth et al. 2011). Basically, it is believed that in the electrical percolation, the filler network is able to transfer electrons. On the other hand, in the rheological percolation it is able to transfer the stress (Kota et al. 2007; Huang et al. 2012). Accordingly, the lower rheological percolation threshold, compared to the electrical percolation threshold, could be attributed to the fact that a shorter interparticle distance is required for electron transfer. In addition, formation of a polymer bound layer around the nanoparticles enhances their effective volume fraction and, polymer chains might connect the nanoparticle aggregates by bridging. These phenomena enable the filler network to transfer the stress at lower nanoparticle contents resulting in the lower rheological percolation thresholds compared to the electrical ones.

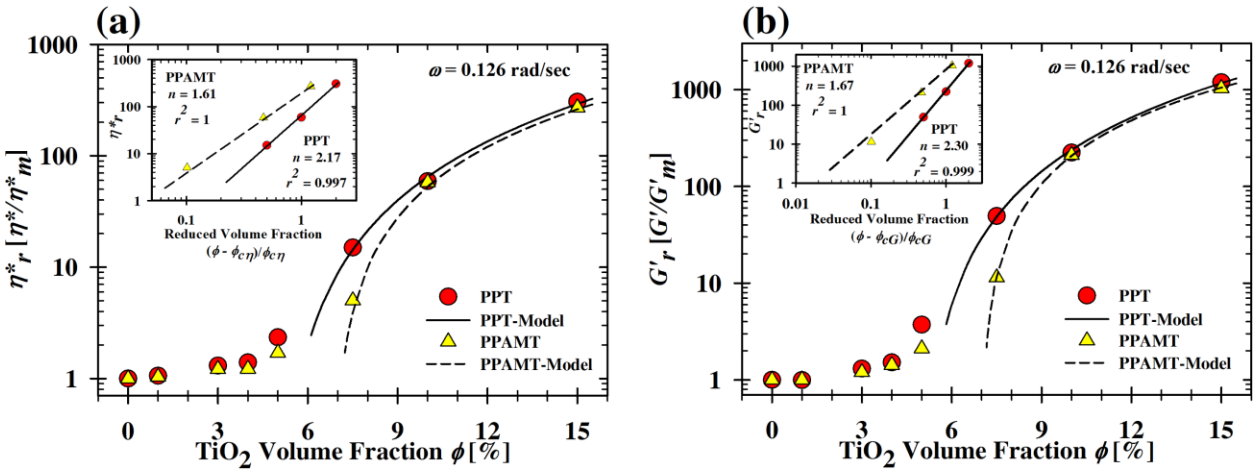

Figure 4-12: Reduced values of (a) η^* and (b) G', as functions of TiO_2 content. The lines are the best fits using Equation 4.7

Table 4.5: Rheological percolation thresholds and fitting parameters of Eq. 4.7 based on the values of different rheological properties

Sample Series	Fitting Criterion	Fitting Parameter			
		ϕ_c [%Vol.]	β	n	r^2
PPT	G′	5.0	60.2 kPa	2.30	0.999
	η*	5.0	513.6 kPa.s	2.17	0.997
PPAMT	G′	7.0	150.4 kPa	1.57	1
	G'_r	7.0	824.5	1.67	1
	η*	6.7	1000 kPa.s	1.62	1
	η^*_r	6.8	199.2	1.61	1

4.3.3.2 Non-Linear Viscoelastic Properties

Figure 4-13 shows results of the strain sweep tests for neat PP and PPT nanocomposites containing different contents of TiO_2 nanoparticles at ω = 1 rad/s. Generally, the length of linear viscoelastic region and corresponding critical strain limit (γ_c) decreases with filler contents. Figure 4-13a illustrates that increasing TiO_2 content leads to higher elastic modulus at plateau

(G'_p) and smaller linear viscoelastic zone. Normalized plots, relative to G'_p (i.e. G'/G'_p), depicted in Figure 4-13b, show the variation of γ_c (defined as a strain where 10% reduction in G' occurs) with TiO_2 content. Table 4.6 summarizes the results of strain sweep tests for both PPT and PPAMT samples. Interestingly, sudden decreases in γ_c with ϕ are observed in PPT and PPAMT that could be attributed to the presence of a particle network above the percolation threshold of each nanocomposite system. In agreement with frequency sweep results, the transition in non-linear viscoelastic behavior of PPT nanocomposites takes place at a lower ϕ compared to PPAMT. Increasing TiO_2 volume content from 4 to 5 % led to reduction of γ_c from 31 to 4.5 % in PPT samples while the reduction of γ_c for PPAMT samples was observed in the range of 5 to 7.5 vol% TiO_2. This is another indication of lower percolation threshold in the uncompatibilized system.

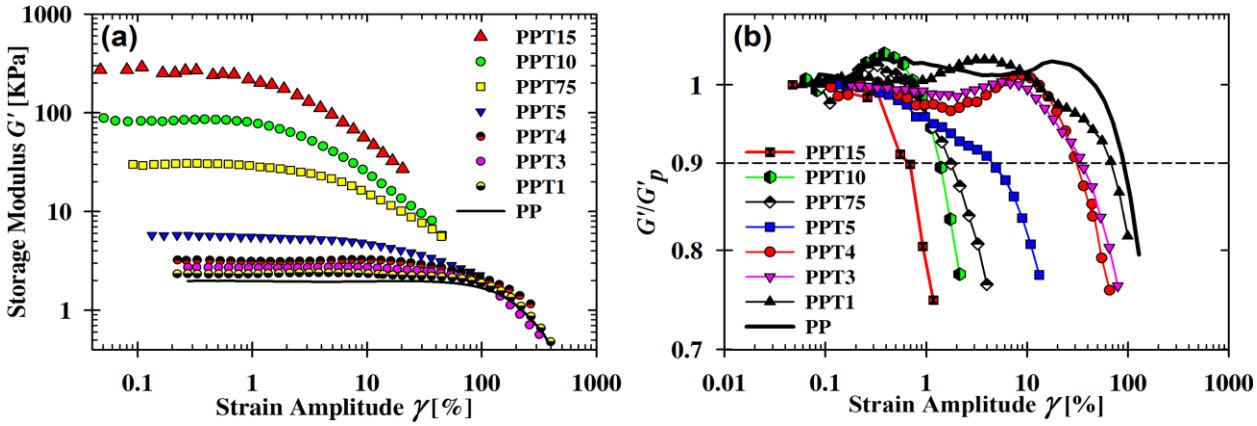

Figure 4-13: (a) variation of G' versus strain amplitude for neat PP and PPT samples at ω = 1 rad/s, (b) normalized values of G' to value of elastic modulus at the linear plateau (G'/G'_p)

Table 4.6: Key characteristics of the neat polymers and the nanocomposite samples obtained from strain sweep tests at ω = 1 rad/s and the elastic characteristic time λ

Sample	G'_p [kPa]	G''_p [kPa]	γ_c [%]	$\lambda = G'_p/G''_p\omega$ [s]
PP	1.35	3.04	85.4	0.707
AMPP	0.77	2.13	99.8	0.531
PPT1	2.35	4.87	68.2	0.483
PPT3	2.73	5.62	34.9	0.486
PPT4	3.22	6.14	31.0	0.524
PPT5	5.77	8.78	4.5	0.657
PPT75	30.1	22.1	1.7	1.362
PPT10	82.5	33.5	1.4	2.463
PPT15	271	39.9	0.7	6.792
PPAMT1	2.37	4.86	70.5	0.488
PPAMT3	2.29	4.63	65.3	0.495
PPAMT4	2.77	5.18	37.3	0.535
PPAMT5	3.21	5.66	22.8	0.567
PPAMT75	7.38	9.05	4.9	0.815
PPAMT10	86.0	35.1	1.3	2.450
PPAMT15	243	60.9	0.9	3.990

In order to investigate polymer-filler and filler-filler interactions, scaling analyses have been applied to interpret the rheological characteristics of polymer nanocomposites in both regimes; lower than the percolation threshold and above it. A general power-law relation between γ_c and ϕ is used for nanocomposites below their percolation;

$$\gamma_c \propto \phi^{-\nu} \tag{4.8}$$

where v is a parameter used to describe resistivity of the filled system to changing strain amplitude. Figure 4-14a shows γ_c for volume fractions below ϕ_c (1, 3 and 4 vol%) and its power-

law dependence according to Equation 4.8. The smaller exponent v for PPAMT nanocomposites compared to PPT (v = 0.35 versus v = 0.58) shows lower sensitivity to strain for the compatibilized nanocomposites. Bailly et al. (2010) reported values of 0.3 and 0.5 for nanocomposites based on ethylene octane copolymer (EOC) and fumed silica (SiO_2) containing up to 4.5 vol% of the nanoparticles with different polymer-particle interactions. Since filler loading was below the percolation threshold of the system, there was not the interconnected network of nanoparticles. Hence, lower strain resistivity of PPAMT could be attributed to a stronger interfacial interaction between PP and TiO_2 due to bonding with maleic groups (Bailly et al. 2010; Li et al. 2009). This was also confirmed in a previous study on mechanical properties of the same systems that showed a similar interfacial reinforcement through a micromechanical analysis (Zohrevand et al. 2013).

Figure 4-14b shows the results of the analysis using scaling relations $G'_p \sim \phi^m$ and $\gamma_c \sim \phi^{-t}$ at the volume fractions above the percolation thresholds of the nanocomposites (ϕ = 7.5-15 vol%). Simultaneous solving of Equations 4.2 and 4.3 using the values of exponents m and t gives d_f = 1.86 and 3.42 for PPT and PPAMT nanocomposites. Lower value of the fractal dimension for PPT could be attributed to less dense aggregates in the uncompatibilized nanocomposites compared to the compatibilized ones which is in agreement with the morphological observations.

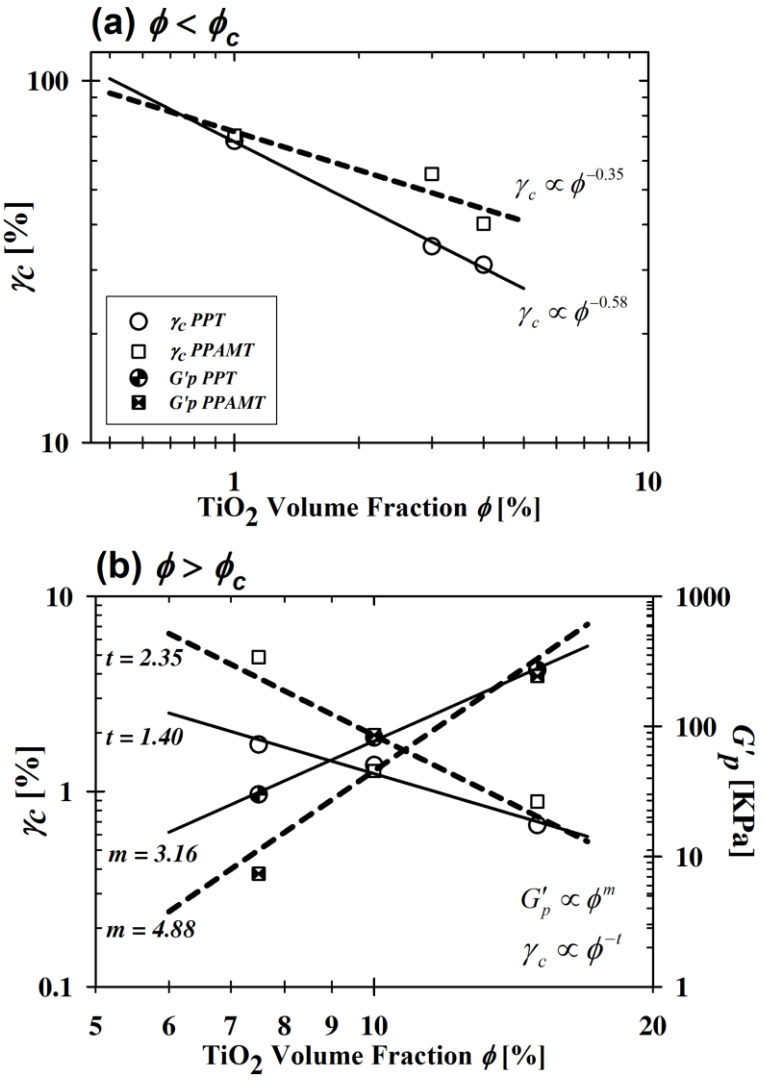

Figure 4-14: (a) critical strain as a function of TiO_2 volume fraction lower than the percolation thresholds of the samples. The lines are the best fits using Equation 4.8. (b) Variation of critical strain and elastic modulus at plateau with TiO_2 contents above the percolation threshold. The lines are results of fitting using Equation 4.2 and 4.3

4.4 General Discussion

Lee et al. (1995) correlated the rate of size reduction of filler agglomerates (R) in melt compounding to the main influencing factors, such as interactions among the components and hydrodynamic forces applied by an external flow field. He proposed a relation:

$$R \propto \frac{W_a}{\tau_c}\ \eta\dot{\gamma}$$

where W_a, τ_c, η and $\dot{\gamma}$ are work of adhesion between the fillers and fluid, the cohesive strength of the agglomerate, the fluid viscosity, and the shear rate respectively. Surface hydrophilicity of unmodified TiO_2 leads to weak interactions between PP and TiO_2, compared to TiO_2-TiO_2 ones and, it causes the aggregation during melt mixing process (Romeo et al. 2008). On the other hand, maleic anhydride groups of AMPP can react with hydroxyl groups of the TiO_2 nanoparticle forming the bound layer that can improve stress transfer, required for break-up, to the particle aggregate during the mixing (Li et al. 2009; Li et al. 2010). Bailly et al. (2010) utilized a rheological approach, based on the concept of "effective volume fraction" ϕ_e, to estimate the thickness of the bound layer in nanocomposites containing surface treated SiO_2. They described the relation between ϕ_e and ϕ using the expression in Equation 4.9

$$\phi_e = \frac{\left(d+2\Delta\right)^3 - 6d\Delta^2}{d^3}\phi \tag{4.9}$$

where d is average particle diameter and Δ the shell thickness. Accordingly, the value of Δ could be estimated by fitting the values of the elastic modulus on a combination of Equation 4.9 and the modified Guth-Smallwood equation (Equation 4.10) to describe the reinforcement effect of the TiO_2 nanoparticles

$$\frac{G'\left(\phi_e\right)}{G'_m} = 1 + 2.5\phi_e + 14.1\phi_e^{\,2} \tag{4.10}$$

where $G'(\phi_e)$ and G'_m are elastic modulus of the nanocomposite and matrix, respectively (Rooj et al. 2013; Jouault et al. 2012; White and Crowder 1974). Figure 4-15, representatively, shows the best fit on the experimental values of G' at ω = 0.126 rad/sec for PPT samples with the concentrations below the percolation. It was considered that d = 21 nm and Δ is the adjusting parameter in the combination of Equation 4.9 and Equation 4.10. The best fits on the experimental values gave Δ = 4.5 and 5 nm as the thicknesses of the bound layer shells in PPT and PPAMT nanocomposites, respectively. These values indicate thicker shell layers compared to those reported by. Bailly et al. (2010) which were 2.5 and 2.9 nm for the EOC/SiO_2 systems. However, this analysis qualitatively verifies the presence of bound layers in both PPT and

PPAMT samples. As expected, compatibilized PPAMT nanocomposites have thicker bound layer, compared to PPT, which is in agreement with the results of strain sweep.

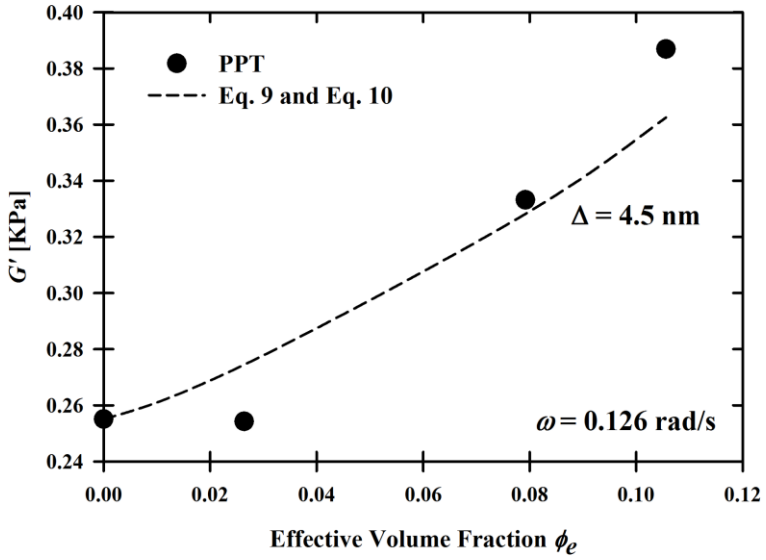

Figure 4-15: Experimental values of G' at ω = 0.126 rad/s (circles) for PPT nanocomposites and the best fit using the combination of Eq. 4.9 and Eq. 4.10 (dashed line)

On the other hand, in addition to polymer-filler interaction (W_a), appropriate extent of shear ($\eta\dot{\gamma}$) must be applied by the polymer melt to break and disperse the particle aggregates. Apparent shear rate in a typical conveying element of a twin-screw extruder ($\dot{\gamma}_{TSE}$) could be roughly estimated by

$$\dot{\gamma}_{TSE} \cong \frac{\pi N_s D_e}{h_m} \tag{4.11}$$

where N_s is screw speed, D_e is the equivalent screw diameter and h_m is the average channel depth of the twin-screw extruder (Goharpey et al. 2008). Using Equation 4.11 and corresponding geometrical characteristics of the twin-screw extruder used (D_e = 18 mm, h_m = 3.25 mm), the apparent shear rate at 200 rpm was around 58 s^{-1}. Assuming that Cox-Merz rule ($\eta(\dot{\gamma}) \approx \eta^*(\omega)$) is valid, corresponding values of apparent viscosity (η) and shear stress ($\eta\dot{\gamma}$) at ω = 58 rad/s for PP, AMPP and matrices of the compatibilized nanocomposites are reported in Table 4.7. As it

can be seen, the apparent shear stress ($\eta\dot{\gamma} \approx \eta^* \omega$), applied by the corresponding polymer matrices in the PPAMT samples, decreases with concentration of TiO_2. Therefore, although interactions between polymer-filler in compatibilized samples are higher than those in uncompatibilized ones, the induced shear stress from the corresponding matrices are lower.

Table 4.7: Values of complex viscosity (η^*) and $\eta^* \times \omega$ for the neat polymers and polymer matrices of different compatibilized samples at 205 °C and ω = 58 rad/s

Polymer Matrix	η* [Pa.s]	$\eta^*\omega \approx \eta\dot{\gamma}$ [kPa]
PP	840	48.6
PPAMT3	830	48.1
PPAMT10	750	43.3
PPAMT15	775	44.8
AMPP	765	44.2

Moreover, blends of PP and AMPP, depending on their compositions, can form one or two phases. Molecular weight and maleic anhydride content of AMPP are two important parameters which control miscibility of PP and AMPP as two crystalline polymers. High molecular weight and low maleic anhydride content of AMPP favor co-crystallization of PP/AMPP, which improves miscibility. AMPP used in the present work has a relatively low MA content (0.1 wt%) and high molecular weight which result in minor differences in chemical structure of PP and AMPP. In this case, where there are minor differences in chemical structure of PP and AMPP, their blend morphology could be result of one of two possible situations. In one situation, the phase separation is the dominant mechanism and, in the other one, co-crystallization is the main mechanism. In fact, in this kind of crystalline-crystalline polymer blends, crystallization kinetics has a more important role in determining the phase morphology compared to thermodynamics. A higher cooling rate may cause co-crystallization of PP and AMPP which decreases the phase separation (Duvall et al. 1994; Cho et al. 1999).

Figure 4-16 representatively shows AFM images of PP/AMPP blends with the same compositions as the matrices of the PPAMT3, PPAMT5, and PPAMT10 samples. They were prepared via the same process as used to prepare the nanocomposites. According to Table 4.2, the relative weight ratio of AMPP/PP in the mentioned samples are 14.2/85.8, 24.3/75.7, and 50/50, respectively. As can be seen in Figure 4-16a-c, there are separated domains (dark regions) dispersed into the PP matrices. Although the number and size of the droplets increased with AMPP content, the area ratio of the AMPP phase with respect to the total area are smaller than the content of AMPP in the blends. Figure 4-16d is an AFM image of the AMPP/PP 50/50 wt% blend at a lower magnification. Image analysis of Figure 4-16 shows that AMPP phase covers around 10 % of the total area which is lower than the expected 50 %. It could be attributed to dominance of co-crystallization over phase separation due to the high cooling rate (~50°C/min) during the compression molding process that hinders the phase separation.

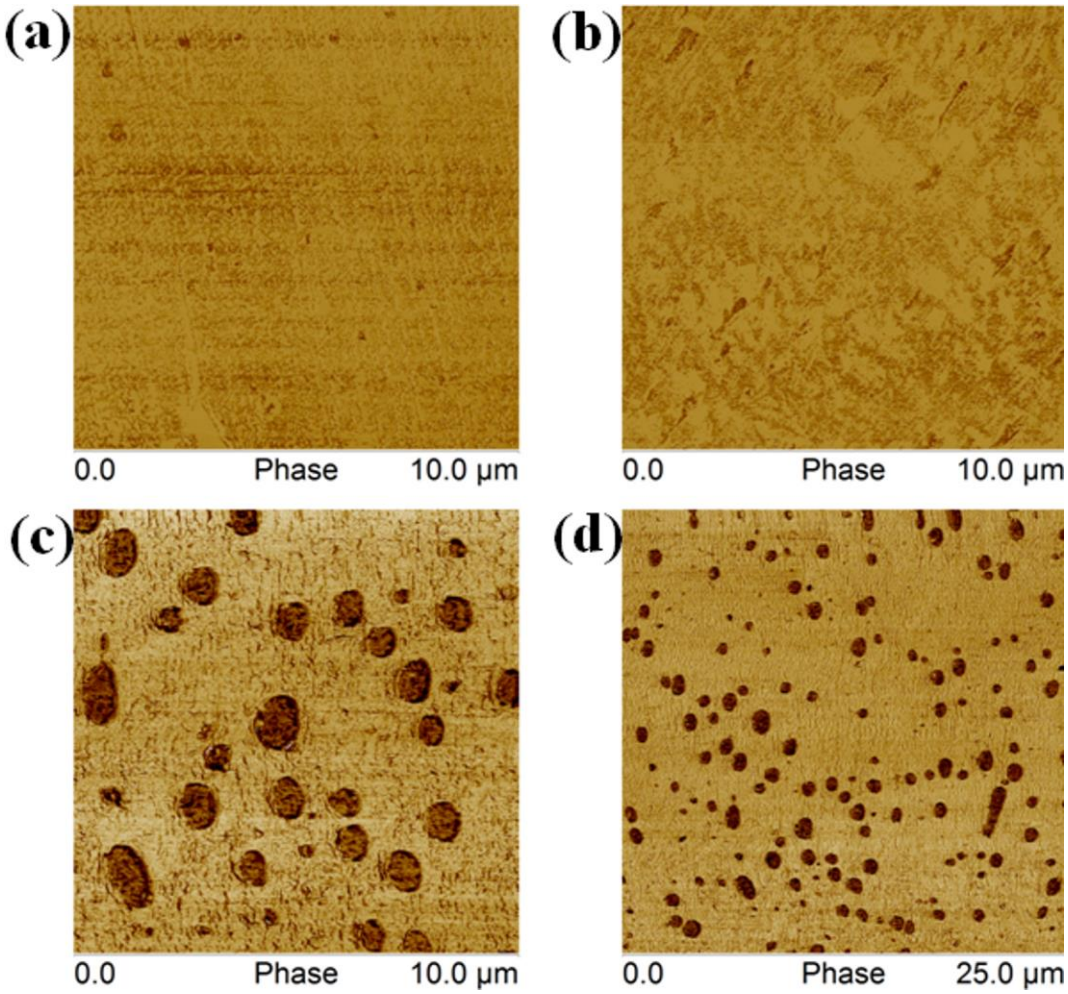

Figure 4-16: AFM images of the PP/AMPP blends with the same composition as in the matrices of the compatibilized nanocomposite samples; (a) PPAMT3, (b) PPAMT5, (c) PPAMT10, and (d) PPAMT10 (lower magnification)

The combination of the aspects discussed above, depending on the range of TiO_2 content, result in the different morphologies of the nanocomposites. At low particle content ($\phi \leq 5$ %), there is no matrix phase separation and, both factors of the high shear stress and stronger PP-TiO_2 interaction help in better dispersion of TiO_2 in PPAMT compared to PPT. They caused the better dispersion of TiO_2, formation of the smaller aggregates, and higher percolation thresholds in PPAMT system compared to PPT. On the other hand, at the higher TiO_2 contents ($\phi \geq 5$ %), the matrices of PPAMT samples have lower viscosities and, the applied hydrodynamic shear stress is not as much as in PPT samples. In addition, there is partial phase separation of PP/AMPP.

Therefore, the particle aggregates of PPAMT samples above the percolation threshold are denser compared to the PPT samples. It is in agreement with the values of d_f obtained from the scaling analysis of the amplitude sweep tests.

Based on tunneling model (Huang et al. 2009), interparticle tunneling conductivity σ_{tun} in a particulate polymer composite could be defined as

$$\sigma_{tun} \propto \exp\left(-\frac{r-d}{t}\right) \tag{4.12}$$

where r is the distance between the centers of the particles, d is the diameter of the particles, and t is a typical tunneling range that is assumed as a constant depending on the particle type. According to Equation 4.12, the contribution of any two spherical particles to the conduction of the composite decreases with r. This model shows that the electrical conduction of a nanocomposite is mainly due to charge transfer between the nearest particles or through the particle clusters. Figure 4-17 schematically depicts microstructure of PPT and PPAMT samples in the three ranges of nanoparticle concentrations; below percolation threshold ($\phi < \phi_c$: Figure 4-17a and d), in the vicinity of percolation ($\phi \approx \phi_c$: Figure 4-17b and e), and beyond the percolation ($\phi < \phi_c$: Figure 4-17c and f). Poor dispersion of TiO_2 at $\phi < \phi_c$ in PPT (Figure 4-17a) results in a lower average interparticle distance for PPT compared to PPAMT (Figure 4-17d). Therefore, electrical conductivity of PPT is higher than that of PPAMT and it has a lower electrical percolation threshold (Figure 4-17b has less particle compared to Figure 4-17e). At a concentration above ϕ_c (Figure 4-17c and f), interconnected networks of particle are formed but the aggregates in the PPAMT samples are denser compared to PPT.

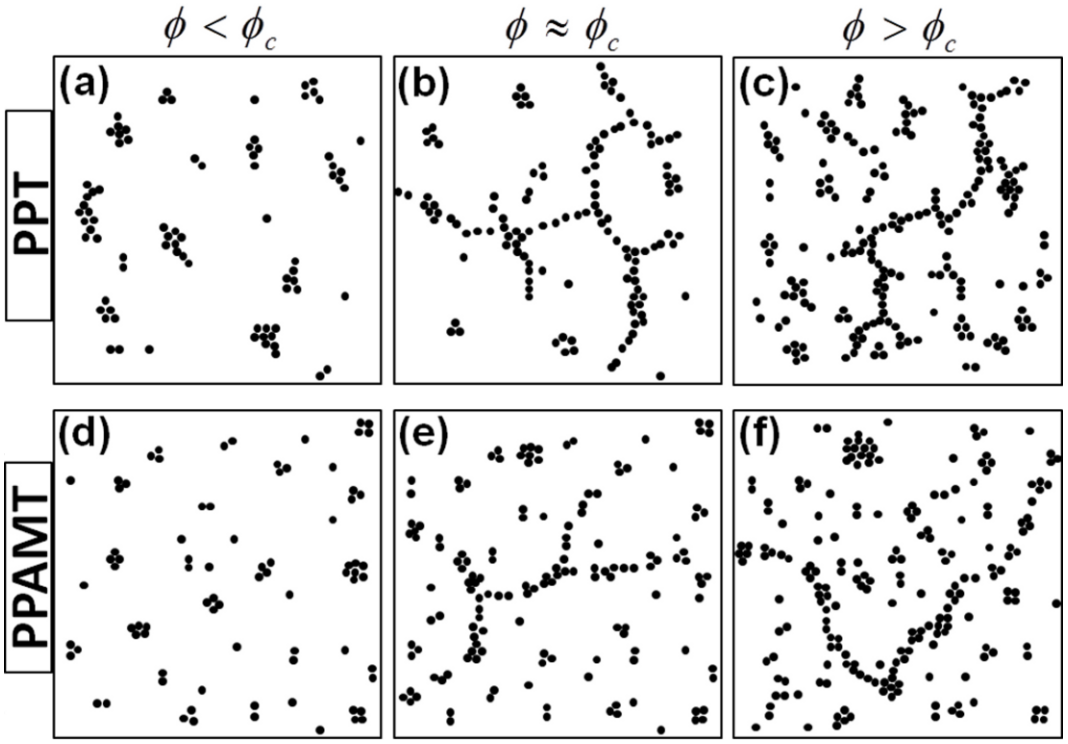

Figure 4-17: Schematic illustration of nanoparticle distribution in the PPT and PPAMT nanocomposites in three ranges of TiO_2 content respect to the critical volume fraction of ϕ_c in the percolation threshold (Number of particles in (a) and (c) is equal to that in (d) and (f) respectively but there more particle in (e) compared to (b))

4.5 Conclusions

A comprehensive study was performed on the evolution of morphology, electrical conductivity, and melt state viscoelastic properties of the compatibilized (PPAMT) and uncompatibilized (PPT) nanocomposites based on PP and TiO_2 nanoparticle as a semiconductor inclusion. Electrical measurements showed that the nanocomposites compatibilized with AMPP had a higher percolation threshold compared to PPT. It was in agreement with the SEM observations showing that the presence of the large clusters of nanoparticle aggregates in the PPT samples led to formation of the interconnected filler network at the lower TiO_2 content.

Based on the linear viscoelastic properties, a higher rheological percolation threshold was observed in the PPAMT system. It was attributed to the better dispersion of the spherical TiO_2

nanoparticles in the PPAMT system below the percolation, compared to PPT. It was also consistent with the results of the electrical conductivity measurement and the morphological studies. However, in the TiO_2 contents above the critical concentration of percolation ($\phi \geq 7.5$ vol%), the lower hydrodynamic shear stress during mixing and the partial phase separation in the matrices of the PPAMT samples could lead to the denser TiO_2 aggregates compared to PPT. The non-linear viscoelastic studies and the scaling analysis showed that the aggregate structures in the PPAMT samples, above their percolation, have larger fractal dimension (d_f) that was in agreement with their morphological features.

Acknowledgment

This research was supported in part by the Natural Science and Engineering Research Council of Canada (NSERC) Strategic projects and discovery grants. The authors would like to thank Professor Eric David, Mr. Cyril Daran-Daneau and Mr. Bouchaib Zazoum, from *CREPEC*, for their help in the electrical measurements.

4.6 References

Abbasi S, Carreau P, Derdouri A, Moan M (2009) Rheological properties and percolation in suspensions of multiwalled carbon nanotubes in polycarbonate. Rheologica Acta 48 (9):943-959

Abduljalil H, Hashim A, Jewad A (2011) The effect of addition titanium dioxide on electrical properties of poly-methyl methacrylate. European Journal of Scientific Research 63 (2):231-235

Acierno D, Filippone G, Romeo G, Russo P (2007) Rheological Aspects of PP-TiO2 Micro and Nanocomposites: A Preliminary Investigation. Macromolecular Symposia 247 (1):59-66

Aranguren MI, Mora E, DeGroot JJV, Macosko CW (1992) Effect of reinforcing fillers on the rheology of polymer melts. Journal of Rheology 36 (6):1165-1182

Bahloul W, Bounor-Legaré V, David L, Cassagnau P (2010) Morphology and viscoelasticity of PP/TiO2 nanocomposites prepared by in situ sol–gel method. Journal of Polymer Science Part B: Polymer Physics 48 (11):1213-1222. doi:10.1002/polb.22012

Bailly M, Kontopoulou M (2013) Linear viscoelastic properties of ethylene--octene copolymer/nanosilica composites investigated over a broad range of frequencies. Journal of Rheology 57 (2):407-426

Bailly M, Kontopoulou M, El Mabrouk K (2010) Effect of polymer/filler interactions on the structure and rheological properties of ethylene-octene copolymer/nanosilica composites. Polymer 51 (23):5506-5515. doi:10.1016/j.polymer.2010.09.051

Bangarusampath DS, Ruckdäschel H, Altstädt V, Sandler JKW, Garray D, Shaffer MSP (2009) Rheology and properties of melt-processed poly(ether ether ketone)/multi-wall carbon nanotube composites. Polymer 50 (24):5803-5811. doi:http://dx.doi.org/10.1016/j.polymer.2009.09.061

Bauhofer W, Kovacs JZ (2009) A review and analysis of electrical percolation in carbon nanotube polymer composites. Composites Science and Technology 69 (10):1486-1498. doi:http://dx.doi.org/10.1016/j.compscitech.2008.06.018

Bondioli F, Dorigato A, Fabbri P, Messori M, Pegoretti A (2008) High-density polyethylene reinforced with submicron titania particles. Polymer Engineering & Science 48 (3):448-457

Boudenne A, Ibos L, Fois M, Majesté JC, Géhin E (2005) Electrical and thermal behavior of polypropylene filled with copper particles. Composites Part A: Applied Science and Manufacturing 36 (11):1545-1554. doi:http://dx.doi.org/10.1016/j.compositesa.2005.02.005

Burke M, Young RJ, Stanford JL (1993) The relationship between structure and properties in titanium dioxide filled polypropylene. Polymer Bulletin 30 (3):361-368. doi:10.1007/bf00343073

Cassagnau P (2008) Melt rheology of organoclay and fumed silica nanocomposites. Polymer 49 (9):2183-2196. doi:10.1016/j.polymer.2007.12.035

Chandra A, Turng L-S, Gong S, Hall DC, Caulfield DF, Yang H (2007) Study of polystyrene/titanium dioxide nanocomposites via melt compounding for optical applications. Polymer Composites 28 (2):241-250

Cho K, Li F, Choi J (1999) Crystallization and melting behavior of polypropylene and maleated polypropylene blends. Polymer 40 (7):1719-1729. doi:http://dx.doi.org/10.1016/S0032-3861(98)00404-2

David E, Sami A, Couderc H, Frechette M (2011) Dielectric Response of Polyethylene Loaded with SiO2 Nanoparticles. Paper presented at the 8th International Conference on Isulated Power Cables (Jicable'11), Versailles - France, 19-23 June

Dorigato A, Pegoretti A, Penati A (2010) Linear low-density polyethylene/silica micro-and nanocomposites: dynamic rheological measurements and modelling. Express Polymer Letters 4:115-129

Du F, Scogna RC, Zhou W, Brand S, Fischer JE, Winey KI (2004) Nanotube Networks in Polymer Nanocomposites: Rheology and Electrical Conductivity. Macromolecules 37 (24):9048-9055. doi:10.1021/ma049164g

Durmus A, Kasgoz A, Macosko CW (2007) Linear low density polyethylene (LLDPE)/clay nanocomposites. Part I: Structural characterization and quantifying clay dispersion by melt rheology. Polymer 48 (15):4492-4502. doi:10.1016/j.polymer.2007.05.074

Duvall J, Sellitti C, Myers C, Hiltner A, Baer E (1994) Interfacial effects produced by crystallization of polypropylene with polypropylene-g-maleic anhydride compatibilitzers. Journal of Applied Polymer Science 52 (2):207-216. doi:10.1002/app.1994.070520208

Fontaine A, Guntzburger Y, Bertrand F, Fradette L, Heuzey MC (2013) Experimental investigation of the flow dynamics of rheologically complex fluids in a Maxblend impeller system using PIV. Chemical Engineering Research and Design 91 (1):7-17. doi:http://dx.doi.org/10.1016/j.cherd.2012.06.018

Forhad Mina M, Seema S, Matin R, Jellur Rahaman M, Bijoy Sarker R, Abdul Gafur M, Abu Hashan Bhuiyan M (2009) Improved performance of isotactic polypropylene/titanium dioxide composites: Effect of processing conditions and filler content. Polymer Degradation and Stability 94 (2):183-188

Ghanbari A, Heuzey M-C, Carreau P, Ton-That M-T (2013) Morphological and rheological properties of PET/clay nanocomposites. Rheologica Acta 52 (1):59-74. doi:10.1007/s00397-012-0667-1

Goharpey F, Foudazi R, Nazockdast H, Katbab AA (2008) Determination of twin-screw extruder operational conditions for the preparation of thermoplastic vulcanizates on the basis of batch-mixer results. Journal of Applied Polymer Science 107 (6):3840-3847. doi:10.1002/app.27401

Guo N, DiBenedetto SA, Tewari P, Lanagan MT, Ratner MA, Marks TJ (2010) Nanoparticle, Size, Shape, and Interfacial Effects on Leakage Current Density, Permittivity, and Breakdown Strength of Metal Oxide−Polyolefin Nanocomposites: Experiment and Theory. Chemistry of Materials 22 (4):1567-1578. doi:10.1021/cm902852h

Hu G, Zhao C, Zhang S, Yang M, Wang Z (2006) Low percolation thresholds of electrical conductivity and rheology in poly(ethylene terephthalate) through the networks of multi-walled carbon nanotubes. Polymer 47 (1):480-488. doi:10.1016/j.polymer.2005.11.028

Huang C-L, Wang C (2011) Rheological and conductive percolation laws for syndiotactic polystyrene composites filled with carbon nanocapsules and carbon nanotubes. Carbon 49 (7):2334-2344. doi:10.1016/j.carbon.2011.01.065

Huang S, Liu Z, Yin C, Wang Y, Gao Y, Chen C, Yang M (2012) Dynamic Electrical and Rheological Percolation in Isotactic Poly(propylene)/Carbon Black Composites. Macromolecular Materials and Engineering 297 (1):51-59. doi:10.1002/mame.201100150

Huang X, Kim C, Jiang P, Yin Y, Li Z (2009) Influence of aluminum nanoparticle surface treatment on the electrical properties of polyethylene composites. Journal of Applied Physics 105 (1):014105-014110

Huang X, Kim C, Ma Z, Jiang P, Yin Y, Li Z (2008) Correlation between rheological, electrical, and microstructure characteristics in polyethylene/aluminum nanocomposites. Journal of Polymer Science Part B: Polymer Physics 46 (20):2143-2154. doi:10.1002/polb.21547

Jouault N, Dalmas F, Boué F, Jestin J (2012) Multiscale characterization of filler dispersion and origins of mechanical reinforcement in model nanocomposites. Polymer 53 (3):761-775. doi:http://dx.doi.org/10.1016/j.polymer.2011.12.001

Kalyanasundaram K, Grätzel M (1998) Applications of functionalized transition metal complexes in photonic and optoelectronic devices. Coordination Chemistry Reviews 177 (1):347-414

Kasgoz A, Akın D, Durmus A (2012) Rheological behavior of cycloolefin copolymer/graphite composites. Polymer Engineering & Science:n/a-n/a. doi:10.1002/pen.23221

Ke K, Wang Y, Luo Y, Yang W, Xie B-H, Yang M-B (2012) Evolution of agglomerate structure of carbon nanotubes in multi-walled carbon nanotubes/polymer composite melt: A rheo-electrical study. Composites Part B: Engineering 43 (8):3281-3287. doi:http://dx.doi.org/10.1016/j.compositesb.2012.02.011

Kota AK, Cipriano BH, Duesterberg MK, Gershon AL, Powell D, Raghavan SR, Bruck HA (2007) Electrical and Rheological Percolation in Polystyrene/MWCNT Nanocomposites. Macromolecules 40 (20):7400-7406. doi:10.1021/ma0711792

Lee SH, Cho E, Jeon SH, Youn JR (2007) Rheological and electrical properties of polypropylene composites containing functionalized multi-walled carbon nanotubes and compatibilizers. Carbon 45 (14):2810-2822. doi:http://dx.doi.org/10.1016/j.carbon.2007.08.042

Lee Y-J, Manas-Zloczower I, Feke DL (1995) Analysis of titanium dioxide agglomerate dispersion in linear low density polyethylene and resulting properties of compounds. Polymer Engineering & Science 35 (12):1037-1045

Lei SG, Hoa SV, Ton-That MT (2006) Effect of clay types on the processing and properties of polypropylene nanocomposites. Composites Science and Technology 66 (10):1274-1279. doi:10.1016/j.compscitech.2005.09.012

Li G-J, Fan S-R, Wang K, Ren X-L, Mu X-W (2010) Modification of TiO2 with titanate coupling agent and its impact on the crystallization behaviour of polybutylene terephthalate. Iranian Polymer Journal (English Edition) 19 (2):115-121

Li W, Karger-Kocsis J, Thomann R (2009) Compatibilization effect of TiO_2 nanoparticles on the phase structure of PET/PP/TiO_2 nanocomposites. Journal of Polymer Science Part B: Polymer Physics 47 (16):1616-1624

McCarthy DN, Stoyanov H, Rychkov D, Ragusch H, Melzer M, Kofod G (2012) Increased permittivity nanocomposite dielectrics by controlled interfacial interactions. Composites Science and Technology 72 (6):731-736. doi:10.1016/j.compscitech.2012.01.026

McLachlan DS, Blaszkiewicz M, Newnham RE (1990) Electrical Resistivity of Composites. Journal of the American Ceramic Society 73 (8):2187-2203. doi:10.1111/j.1151-2916.1990.tb07576.x

Ndong R, Russel W (2012) Linear viscoelasticity of ZrO_2 nanoparticle dispersions with associative polymers. Rheologica Acta 51 (9):771-782. doi:10.1007/s00397-012-0633-y

Pan Y, Li L (2013) Percolation and gel-like behavior of multiwalled carbon nanotube/polypropylene composites influenced by nanotube aspect ratio. Polymer 54 (3):1218-1226. doi:http://dx.doi.org/10.1016/j.polymer.2012.12.058

Park NG, van de Lagemaat J, Frank AJ (2000) Comparison of Dye-Sensitized Rutile- and Anatase-Based TiO2 Solar Cells. The Journal of Physical Chemistry B 104 (38):8989-8994. doi:10.1021/jp994365l

Pötschke P, Abdel-Goad M, Alig I, Dudkin S, Lellinger D (2004) Rheological and dielectrical characterization of melt mixed polycarbonate-multiwalled carbon nanotube composites. Polymer 45 (26):8863-8870. doi:http://dx.doi.org/10.1016/j.polymer.2004.10.040

Pötschke P, Abdel-Goad M, Pegel S, Jehnichen D, Mark JE, Zhou D, Heinrich G (2009) Comparisons Among Electrical and Rheological Properties of Melt-Mixed Composites Containing Various Carbon Nanostructures. Journal of Macromolecular Science, Part A 47 (1):12-19. doi:10.1080/10601320903394397

Pötschke P, Fornes TD, Paul DR (2002) Rheological behavior of multiwalled carbon nanotube/polycarbonate composites. Polymer 43 (11):3247-3255. doi:10.1016/s0032-3861(02)00151-9

Romeo G, Filippone G, Fernández-Nieves A, Russo P, Acierno D (2008) Elasticity and dynamics of particle gels in non-Newtonian melts. Rheologica Acta 47 (9):989-997. doi:10.1007/s00397-008-0291-2

Romeo G, Filippone G, Russo P, Acierno D (2009) Effects of particle dimension and matrix viscosity on the colloidal aggregation in weakly interacting polymer-nanoparticle composites: a linear viscoelastic analysis. Polymer Bulletin 63 (6):883-895. doi:10.1007/s00289-009-0176-2

Rooj S, Das A, Stockelhuber KW, Wang D-Y, Galiatsatos V, Heinrich G (2013) Understanding the reinforcing behavior of expanded clay particles in natural rubber compounds. Soft Matter

Serrano C, Cerrada ML, Fernández-García M, Ressia J, Vallés EM (2012) Rheological and structural details of biocidal iPP-TiO2 nanocomposites. European Polymer Journal 48 (3):586-596. doi:10.1016/j.eurpolymj.2011.12.012

Shih W-H, Shih WY, Kim S-I, Liu J, Aksay IA (1990) Scaling behavior of the elastic properties of colloidal gels. Physical Review A 42 (8):4772-4779

Shin E-C, Seo H-H, Kim J-H, Ahn P-A, Park SM, Lim YW, Kim SJ, Kim CH, Kim DJ, Hong CK, Seo G, Lee J-S (2013) A new diagnostic tool for the percolating carbon network in the polymer matrix. Polymer 54. doi:http://dx.doi.org/10.1016/j.polymer.2012.12.057

Smith RC, Liang C, Landry M, Nelson JK, Schadler LS (2008) The mechanisms leading to the useful electrical properties of polymer nanodielectrics. Dielectrics and Electrical Insulation, IEEE Transactions on 15 (1):187-196. doi:10.1109/t-dei.2008.4446750

Stauffer D (1985) Introduction to Percolation Theory. 1st edn. Taylor & Francis, London

Sternstein SS, Zhu A-J (2002) Reinforcement Mechanism of Nanofilled Polymer Melts As Elucidated by Nonlinear Viscoelastic Behavior. Macromolecules 35 (19):7262-7273. doi:10.1021/ma020482u

Sumfleth J, Buschhorn S, Schulte K (2011) Comparison of rheological and electrical percolation phenomena in carbon black and carbon nanotube filled epoxy polymers. Journal of Materials Science 46 (3):659-669. doi:10.1007/s10853-010-4788-6

Tan Y, Yin X, Chen M, Song Y, Zheng Q (2011) Influence of annealing on linear viscoelasticity of carbon black filled polystyrene and low-density polyethylene. Journal of Rheology 55 (5):965-979

Vermant J, Ceccia S, Dolgovskij MK, Maffettone PL, Macosko CW (2007) Quantifying dispersion of layered nanocomposites via melt rheology. Journal of Rheology 51 (3):429-450

Vladimirov V, Betchev C, Vassiliou A, Papageorgiou G, Bikiaris D (2006) Dynamic mechanical and morphological studies of isotactic polypropylene/fumed silica nanocomposites with enhanced gas barrier properties. Composites Science and Technology 66 (15):2935-2944. doi:10.1016/j.compscitech.2006.02.010

Wang J, Zhao K, Zhang L (2013) Dielectric analysis of TiO2-based electrorheological suspensions. Rheologica Acta 52 (2):115-125. doi:10.1007/s00397-012-0666-2

White JL, Crowder JW (1974) The influence of carbon black on the extrusion characteristics and rheological properties of elastomers: Polybutadiene and butadiene–styrene copolymer. Journal of Applied Polymer Science 18 (4):1013-1038. doi:10.1002/app.1974.070180405

Yakisir D, Mighri F, Bousmina M (2006) Electronic Conductive Microporous Polymer-Based Structures. Macromolecular Rapid Communications 27 (18):1596-1602

Yu C-R, Wu D-M, Liu Y, Qiao H, Yu Z-Z, Dasari A, Du X-S, Mai Y-W (2011) Electrical and dielectric properties of polypropylene nanocomposites based on carbon nanotubes and barium titanate nanoparticles. Composites Science and Technology 71 (15):1706-1712. doi:10.1016/j.compscitech.2011.07.022

Zohrevand A, Ajji A, Mighri F (2013) Morphology and properties of highly filled iPP/TiO2 nanocomposites. Polymer Engineering & Science (in press)

CHAPTER 5 ARTICLE 3: MICROSTRUCTURE AND PROPERTIES OF POROUS NANOCOMPOSITE FILMS: EFFECTS OF COMPOSITION AND PROCESS PARAMETERS

Ahmad Zohrevand[a], Abdellah Ajji[b*], and Frej Mighri[c]

[a] Center for Research on High Performance Polymer and Composite Systems (CREPEC), Department of Chemical Engineering, Ecole Polytechnique du Montreal, C.P. 6079, succ. Centre-Ville, Montreal, QC, Canada, H3C 3A7, *ahmad.zohre-vand@polymtl.ca*

[b] Center for Research on High Performance Polymer and Composite Systems (CREPEC), Department of Chemical Engineering, Ecole Polytechnique du Montreal, C.P. 6079, succ. Centre-Ville, Montreal, QC, Canada, H3C 3A7, *abdellah.ajji@polymtl.ca*

[*] Corresponding Author: Tel.: (+1) 514-340-4711 (Ext.:3703),Fax: (+1) 514-340-4159

[c] Center for Research on High Performance Polymer and Composite Systems (CREPEC), Department of Chemical Engineering, Laval University, 1065 ave. de la Médecine, Pavillon Adrien-Pouliot, Quebec, QC, Canada, G1V 0A6, *Frej.Mighri@gch.ulaval.ca*

Abstract

Porous Nanocomposites films based on polypropylene (PP) and titanium dioxide (TiO_2) nanoparticles were prepared by melt extrusion followed by uniaxial stretching. Effects of drawing temperature, extension rate, stretching ratio, and composition of the base films on final properties and microstructure of the stretched films were studied. Water vapor permeability results showed significant decrease in permeability of the films stretched at temperatures higher than 60°C. Porosity, pore size, and water vapor transmission rate (WVTR) in the porous nanocomposite films had a direct relation with nanoparticle content, extension rate and stretching ratio. Study on morphology of the stretched films, using SEM, revealed that the pores form due to PP/TiO_2 interfacial debonding at low stretching ratio and, higher stretching ratios causes an enlargement of the pores and formation of PP fibril structure parallel to the stretching direction. Quantification of dye adsorption revealed that the quantity of adsorbed dye increased with porosity and surface area of the pores

Keywords: porous film, polymer nanocomposite, stretching, porosity, process-structure relationship

5.1 INTRODUCTION

Simplicity, efficiency, and cost-effectiveness of the methods for producing high-performance functional products based on polymer materials are some of the strong motivations to develop polymer nanocomposites. Polymers can be blended with different kinds of nanoparticles to modify their mechanical, electrical, or other physico-chemical properties for different applications [1, 2]. One of the interesting applications of the functional polymer nanocomposites is in the area of clean energies.

Proton exchange membrane fuel cells and flexible solar cells are examples of devices in which polymer nanocomposite can be used to replace some parts in order to reduce their weight, production cost or improve their mechanical properties [3, 4]. In the area of solar cell applications, dye-sensitized solar cells (DSSC) (which were first introduced by Michael Grätzel et al [5]) have attracted a great attention due to their low cost materials and high efficiency. They have a photoactive anode composed of a mesoporous thin layer of nanocrystalline TiO_2 doped with photosensitive dye molecules [6]. The TiO_2 layer provides an interconnected porous network of TiO_2 nanoparticles, needed as a pathway for electrical charge collection, and a large surface area over which the dye can be adsorbed [7, 8]. Figure 5-1 illustrates a typical structure of a DSSC showing its main parts. As it is shown, the pores of the TiO_2 layer are usually filled with a liquid electrolyte and a platinum counter electrode is placed on the top of it [9].

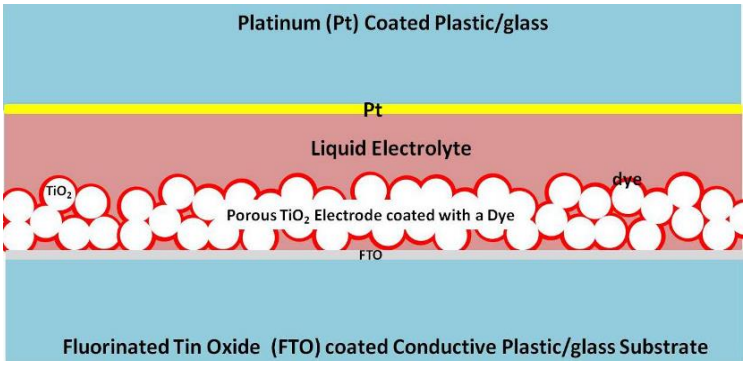

Figure 5-1: Typical structure of a dye-sensitized solar cell

A high-temperature (> 450 °C) sintering process is needed for the preparation of the TiO2 structure, which is a limiting factor in the fabrication of the porous TiO_2 layer on plastic substrates to manufacture flexible DSSCs. Different methods such as chemical sintering [10], laser sintering [11], and mechanical compression have been proposed to make the flexible porous TiO_2 layer. Among the different techniques that have been used to manufacture DSSCs via more convenient rout, utilizing polymer nanocomposite materials could be a promising one. Drew et al. [12-14] reported an interesting work on using electrospinning process to develop a porous structure from a mixture containing a polymer (PAN), a solvent (DMF), an azo-dye (congo red) and TiO_2 nanoparticles. Recently, Li et al. [4] proposed a method based on spray-assisted electrospinning to develop composite photoelectrode of DSSCs composed of TiO_2 nanoparticles and PVDF nanofibers.

In another approach, a continuous process was used to produce highly conductive microporous films for different parts of fuel cells where a thermoplastic polymer was compounded with different combinations of conductive fillers followed by stretching or solvent extraction techniques to create pores in the nanocomposite films [15]. One of the well-known solvent-free methods of producing porous flexible thin films is based on stretching polymeric composite films containing rigid fillers [16, 17]. Uniaxial/biaxial stretching of the polymer composite films containing a fine dispersion of the filler causes the detachment of the two phases from the interface (due to stress concentration) and results in pore formation in the film [18, 19]. The final properties of such porous films are affected by material properties (e.g. characteristics of the polymer matrix, filler nature, filler particle size etc.) and process conditions (such as mixing conditions, extension rate and temperature). It was reported that using smaller particles leads to smaller pore size, higher porosity and effective porosity in the final film [18, 20-23]. Polyolefins are widely used to produce microporous films. Because of their excellent physical properties, chemical resistance and easy processing, polypropylene (PP) is one of the best candidate polymers [18, 20, 21].

The aim of the present work is to develop a method to produce a flexible porous photoelectrode layer for DSSCs through melt processing followed by stretching. Therefore, PP based nanocomposite films containing a percolated structure of TiO_2 nanoparticle were prepared, and, the effects of different material compositions and process parameters on the formation of porosity due to stretching was studied. Since there is a poor compatibility between PP and TiO_2,

it is difficult to achieve a good dispersion of the nanoparticle via melt blending. Therefore, as previously reported [1, 2], an anhydride modified PP (AMPP) was added to enhance the dispersion of nanoparticles. The nanocomposite based film containing different nanoparticle contents or AMPP were prepared by cast extrusion and stretched under different conditions. Then, morphology, permeability and other properties of the porous films were analyzed to obtain an optimum processing window.

5.2 EXPERIMENTAL

5.2.1 Materials

An isotactic polypropylene (iPP) homopolymer (PP4712E1, ExxonMobil, USA) was used as the polymer matrix and an anhydride-modified polypropylene (Bynel 50E571, Dupont, USA) denoted as AMPP, was utilized as the macromolecular compatibilizer. Table 5.1 summarizes the main characteristics of the two polymers.

Table 5.1: Main characteristics of the resins

Polymer	Designation	Supplier	MA Content (%Wt)	MFI[a] (g/10 min)	Density (ρ) (g/cm^3)	η_0[b] (Pa.s)
PP	PP4712E1	ExxonMobil	-	2.8	0.9	8000
AM-PP	Bynel® 50E571	DuPont	0.1[c]	3.5	0.89	5800

[a] ASTM D1238 (230°C/2.16 Kg)
[b] Zero-shear viscosity; obtained from complex viscosity measured in frequency sweep test at 205°C
[c] From the supplier

A commercial grade TiO_2 nanoparticle (AEROXIDE TiO_2 P25, Evonik, Germany) was used in this study. According to the information provided by the supplier, it consists of an hydrophilic fumed TiO_2 with a density ρ of 4.26 g/cm^3 and an average primary particle size of 21 nm and a nano crystalline structure composed of a mixture of anatase:rutile (79:21 wt%). Figure

5-2 shows typical TEM image of the TiO_2 nanoparticles and their particle size distribution in a dispersion in water (inset of Figure 5-2).

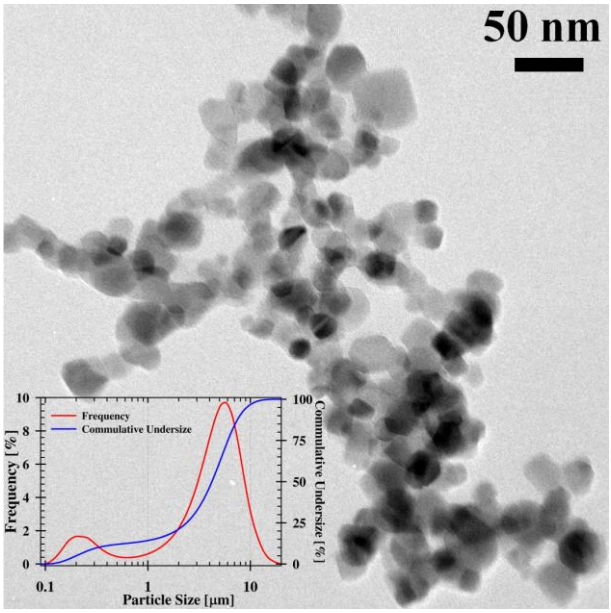

Figure 5-2: TEM micrographs of the TiO_2 nanoparticles used in this work (Inset: Particle size distribution of an aqueous dispersion of the TiO_2 nanoparticle)

5.2.2 Preparation of base nanocomposite films by twin-screw extrusion process

The compatibilized and uncompatibilized nanocomposite base films containing 10 and 12.5 %Vol. (around 34 and 40 %Wt) of the TiO_2 nanoparticles were prepared via diluting two masterbatches based on PP and AMPP. The masterbatches containing 18 %Vol (≈ 51%Wt) of TiO_2 were prepared using a tightly intermeshing co-rotating twin-screw extruder (Leistritz ZSE-18HP-40D, Germany) with diameter Ø = 18 mm and ratio of length to diameter L/D = 40 equipped with a typical compounding screw profile shown in Figure 5-3. Code GFA, in Figure 5-3, represents the conveying elements, which were all 2-channel, and the last two numbers refer to the pitch size and total length of each element, respectively. The code KB refers to kneading blocks and the two last numbers are respectively the kneading disk thickness and their staggering angles.

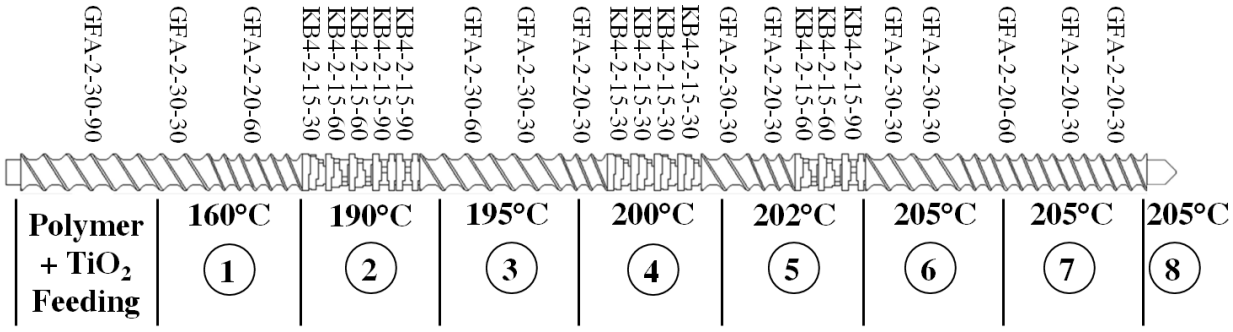

Figure 5-3: Schematic view of the screw configuration and the temperature profile used in the compounding process (GFA: co-rotating conveying free-meshing elements, KB: kneading blocks)

In the compounding process, the two masterbatches were, initially, prepared through two extrusion passes. Then, in another extrusion run, the masterbatches were diluted to lower concentrations by adding neat PP and the resulting compounds were extruded through a slit die at 210°C to produce the base nanocomposite films with an average thickness of 120 μm. In all of the extrusion runs, a constant screw speed of 200 rpm and the same temperature profile: 160, 190, 195, 200, 202, 205, 205 and 205°C (from the main hoper to the die, see Figure 5-3) were applied. Pure PP and AMPP, nanocomposites and TiO_2 nanoparticles were vacuum dried at 80°C for 8 hours before each mixing run. Materials were fed to the extruder, from the main hopper, using a volumetric feeder (for the polymers and the composites) and a high-precision powder feeder (K-Tron, USA) for TiO_2 nanoparticles. In order to minimize thermo-mechanical degradation during intensive mixing, 3000 ppm of antioxidant (Ciba IRGANOX B 225) was added. Table 5.2 reports the complete compositions of the samples.

Table 5.2. Composition of the nanocomposite samples

Sample Code	PP Content	AMPP Content	TiO_2 Content	
	%Wt	%Wt	%Wt	%Vol
PPT125	60	-	40	12.5
PPT10	65.5	-	34.5	10
PPAMT125	21.4	38.7	39.9	12.5

5.2.3 Post extrusion stretching and porous film preparation

The base films were uniaxially stretched parallel to extrusion (Machine) direction (MD) at different stretching temperatures, extension rates and draw ratios using a dynamic tensile machine (Instron ElectroPuls E3000, USA) equipped with an environmental chamber. The samples were cut as 6 cm rectangle and the initial distances between two grips of the machine were set at 20 mm to 40 mm. The films were stretched up to 200% draw ratio at different temperatures (60, 90 and 120°C) with different extension rates (5, 50, 200 and 500 mm/min). It is to be noted that the draw ratio was defined as;

$$\text{Draw Ratio [\%]} = 100 \times (L_f - L_0)/L_0 \quad (5.1)$$

where L_f and L_0 are final and initial lengths of the samples between the two grips. The samples were kept for 3 minutes at the desired stretching temperatures before drawing and slowly cooled at the end.

5.2.4 Nanocomposite Sample Characterization

5.2.4.1 Scanning Electron Microscopy (SEM)

Microstructure of the nanocomposite base films and the porous stretched films were characterized using field emission gun scanning electron microscopy (JEOL 7600F FEG) operated at 2 kV. In order to observe the cross sections of the film, samples were cryo-fractured under liquid nitrogen.

5.2.4.2 Water Vapor Transmission Rate (WVTR)

Water vapor permeation through the film samples was measured, according to ASTM E96, using a permeation test system (PERMATRAN-W Model 101K, MOCON, USA) at room temperature. In this equipment, the sample film is placed between an upper chamber with 100% relative humidity (RH) and a lower chamber connected to a RH sensor. Water vapor diffuses through the sample from the upper chamber to the lower one and then, it is swept by a flow of nitrogen to the sensor.

5.2.4.3 Mercury Intrusion Porosimetry

The average pore size, pore size distribution, and porosity of the films were measured by mercury intrusion porosimetry (MIP) (AutoPore IV 9500, Micromeritics, USA). This technique measures the amount of mercury penetrated into pores of a porous media as a function of the applied pressure. Pressure required to penetrate mercury into a certain size of pore is a function of the pore diameter.

The porosity of the films was also calculated by using the apparent density of the base films and the stretched films obtained by measuring their dimensions and weights. In this method the relation between porosity and density is defined as;

$$\text{Porosity \%} = \left(1 - \frac{\rho_{porous\ film}}{\rho_{base\ film}}\right) \times 100 \tag{5.2}$$

where $\rho_{porous\ film}$ and $\rho_{base\ film}$ are densities of the porous (stretched) samples and the base films respectively.

5.2.4.4 BET Measurements

Specific surface areas of the porous films, which are related to their porosity, were measured by BET method (Autosorb, Quantachrome, USA). In this technique, a nitrogen and helium gas mixture is continuously fed through the sample cell kept at liquid nitrogen temperature. At

different pressures, the total volume of nitrogen gas adsorbed on the surface was measured. The volume of gas needed to create an adsorbed monomolecular layer is calculated by Brunauer-Emmet-Teller [24] equation;

$$\frac{p}{v(p_0 - p)} = \frac{1}{v_m c} + \frac{c-1}{v_m c}\frac{p}{p_0} \tag{5.3}$$

where p is the experimental pressure, p_0 is the saturation pressure, v is the volume of the adsorbate, v_m is the volume of gas required to form an absorbed monomolecular layer, and c is a constant. The detailed procedure of this technique could be found elsewhere [3].

5.2.4.5 DMA Measurements

The mechanical properties of the prepared films and membranes and their evolution with temperature are very important properties during their use. In order to measure variation of elastic modulus of the PP matrix with temperature, its dynamic thermomechanical properties were measured using a dynamic mechanical and thermal analyzer (DMTA 2980, TA Instruments) equipped with a dual-cantilever test fixture. During the characterization, samples were heated from -60 to 120°C at a heating rate of 2 °C/min and frequency of 1 Hz.

5.3 Results and Discussion

5.3.1 Particle Size and Particle Size Distribution

Particle size and particle size distribution are important factors affecting microstructure and properties of the porous films prepared by stretching. Generally, the pore size and pore size distribution of the films are in a direct relation with the size and size distribution of the particles. In the case of inorganic nanoparticle, due to larger specific surface area and significant interparticle forces, compared to traditional fillers, aggregates are formed. Figure 5-2 shows a typical TEM image of the TiO_2 and their particle size distribution of (inset of Figure 5-2). As it can be seen in the TEM image, there are nanoparticles with diameter size from 20 nm to 50 nm that are connected to each other to form aggregates with different sizes. Particle size analysis

shows two maxima around 200 nm and 5.9 μm indicating size of aggregate that should be broken down into smaller domains through melt compounding.

5.3.2 Dispersion of the Nanoparticles in the Base Films

The state of dispersion of TiO_2 nanoparticles in the polymer matrices is another important parameter which has a significant effect on the final properties of the porous nanocomposite films. An efficient melt compounding process breaks the aggregates/agglomerates of the filler leading to a fine level of dispersion and distribution of the inorganic phase. Figure 5-4 shows SEM micrographs of cryo-fractured cross sections of the base nanocomposite films containing different concentrations of TiO_2 and AMPP as a compatibilizer. The particles are homogenously distributed through the samples. According to our previous work [1], the TiO_2 contents of the films are above the percolation threshold of the PP/TiO_2 nanocomposite systems. Therefore, isolated clusters structure of TiO_2 is not distinguishable. In fact, the TiO_2 dispersed phase consists an interconnected network of the nanoparticles aggregates/agglomerates (with fractal structures), small aggregates containing few nanoparticles, and individual primary nanoparticles. As expected, size of the dispersed domains of TiO_2 increases with nanoparticle content from 10 %Vol to 12.5 %Vol.

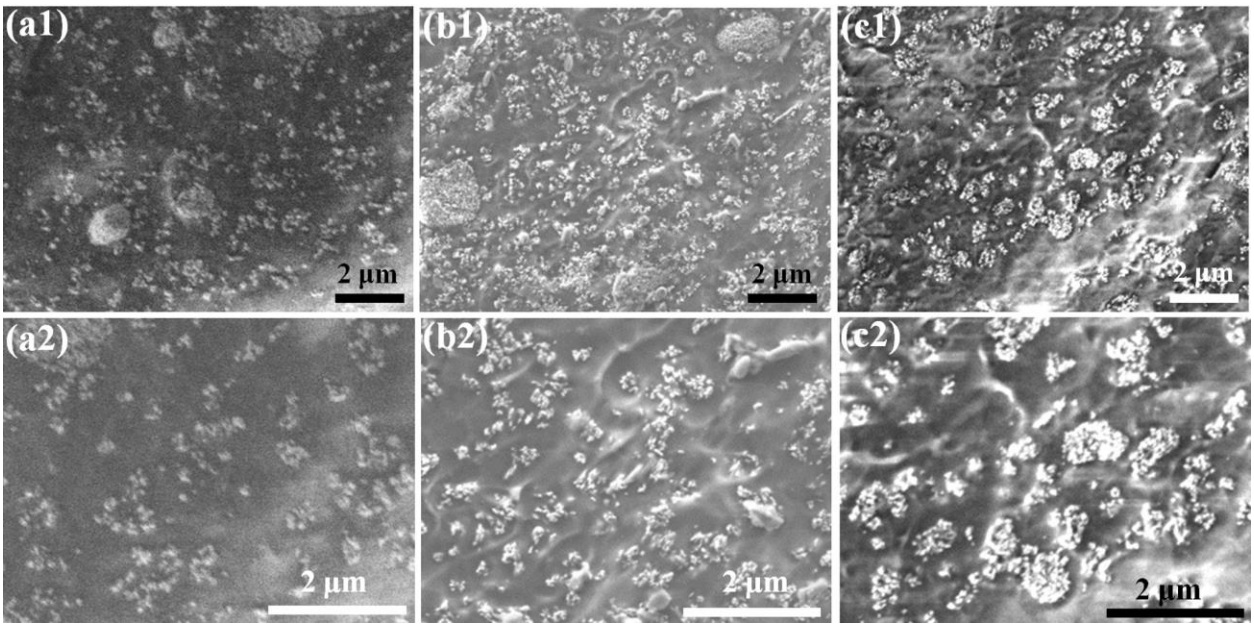

Figure 5-4: SEM micrographs from cross-section of the base nanocomposite film samples containing different TiO2 contents and AMPP as the compatibilizer: (a) PPT10, (b) PPT125, and (c) PPAMT125 in two magnifications

Figure 5-4c shows the effect of adding the anhydride-modified PP (AM-PP), as a compatibilizer, on the morphology of the nanocomposites films. The aggregates of TiO_2 nanoparticles in the compatibilized sample PPAMT125 are more compact compared to PPT125. This could be related to the less-viscous matrix of PPAMT samples compared to PPT which applies lower shear stress during melt mixing that does not break the particles aggregates [1].

5.3.3 Effect of drawing temperature and extension rate

Drawing temperature and extension rate are two important process conditions affecting microstructure and properties of the porous films, particularly their porosity. In order to initiate the pores from the interface of polymer and filler, the base films could be stretched in a wide range of temperatures lower than the melting point of the polymer. Drawing at the temperatures far from the melting point may cause sample breakage and, on the other hand, drawing at the temperatures close or above it may result in orientation without efficient pore formation.

Figure 5-5 illustrates the effect of drawing temperature on BET surface area and the apparent porosity (P_a) of the PPT125 stretched 100 % at the given extension rate (200 mm/min). Increasing the drawing temperature led to lower porosity values. In the other words, pore formation decreases with drawing temperature. BET surface area represents the total surface of the pores inside the porous samples. As the apparent porosity of the samples decrease from 60 % to 43 %, BET surface area of the porous films decrease dramatically from 7 to 1 m^2/g. It is another indication of the low pore formation at elevated temperatures.

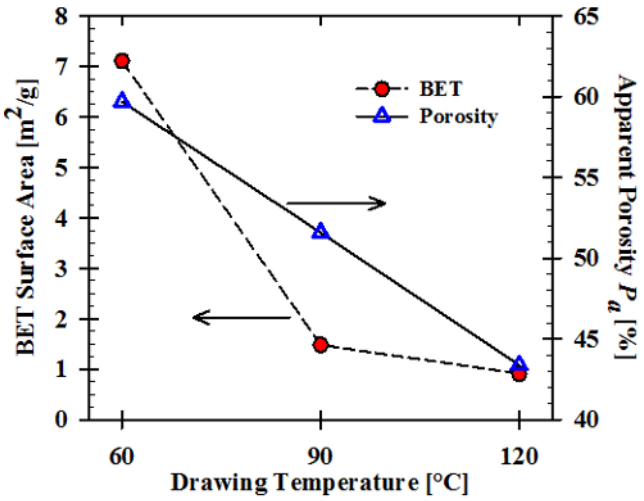

Figure 5-5: Variation of BET surface area (left axis) and the apparent porosity P_a (right axis) with stretching temperature for the porous films based on PPT125 for a draw ratio of 100 % stretched at 200 mm/min

Figure 5-6 illustrates effects of extension rate and drawing temperature on water vapor transmission rate (WVTR) of 100% stretched PPT125 nanocomposite. As can be seen, increasing stretching temperature above 60 °C led to a dramatic reduction in WVTR through the samples. The effect of extension rate on WVTR of the porous nanocomposite films is ambiguous. However, transmission rate increased more than three times by increasing extension rate from 50 to 200 mm/min at 60°C.

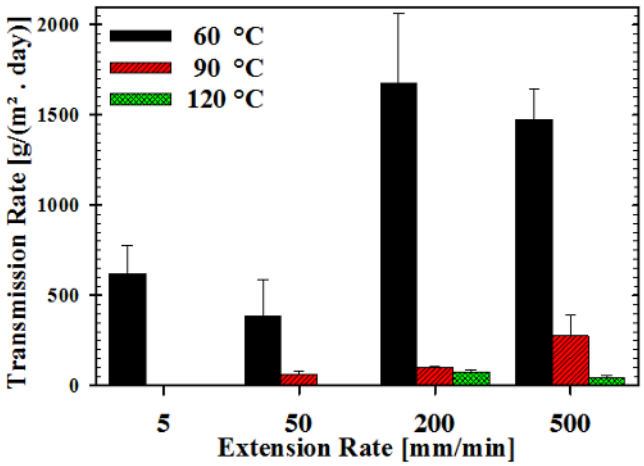

Figure 5-6: Water vapor transmission rate (WVTR) versus extension rate of 100% stretched for PPT125 nanocomposite films at different stretching temperatures

In porous films, WVTR depends on the number and size of the pores, pore size distribution, and the number of interconnected pores [19, 25]. Figure 5-7 shows SEM micrographs from the cross section and surface of PPT125 samples stretched 100 % using 200 mm/min at different stretching temperatures. From the cross section view of Figure 5-7a, it can be seen that fibril structure of PP were formed parallel to the stretching direction (MD) and, the TiO_2 nanoparticles are detached from the polymer phase causing the effective void formation. On the other hand, although the samples stretched at 90 and 120 °C (Figure 5-7b1 and c1) are oriented, the fibril formation and the detachment did not happen as much as in the case of 60 °C. Surface image of the samples (right side) reveal that the number and size of the pores on the surface of the films decrease with stretching temperature.

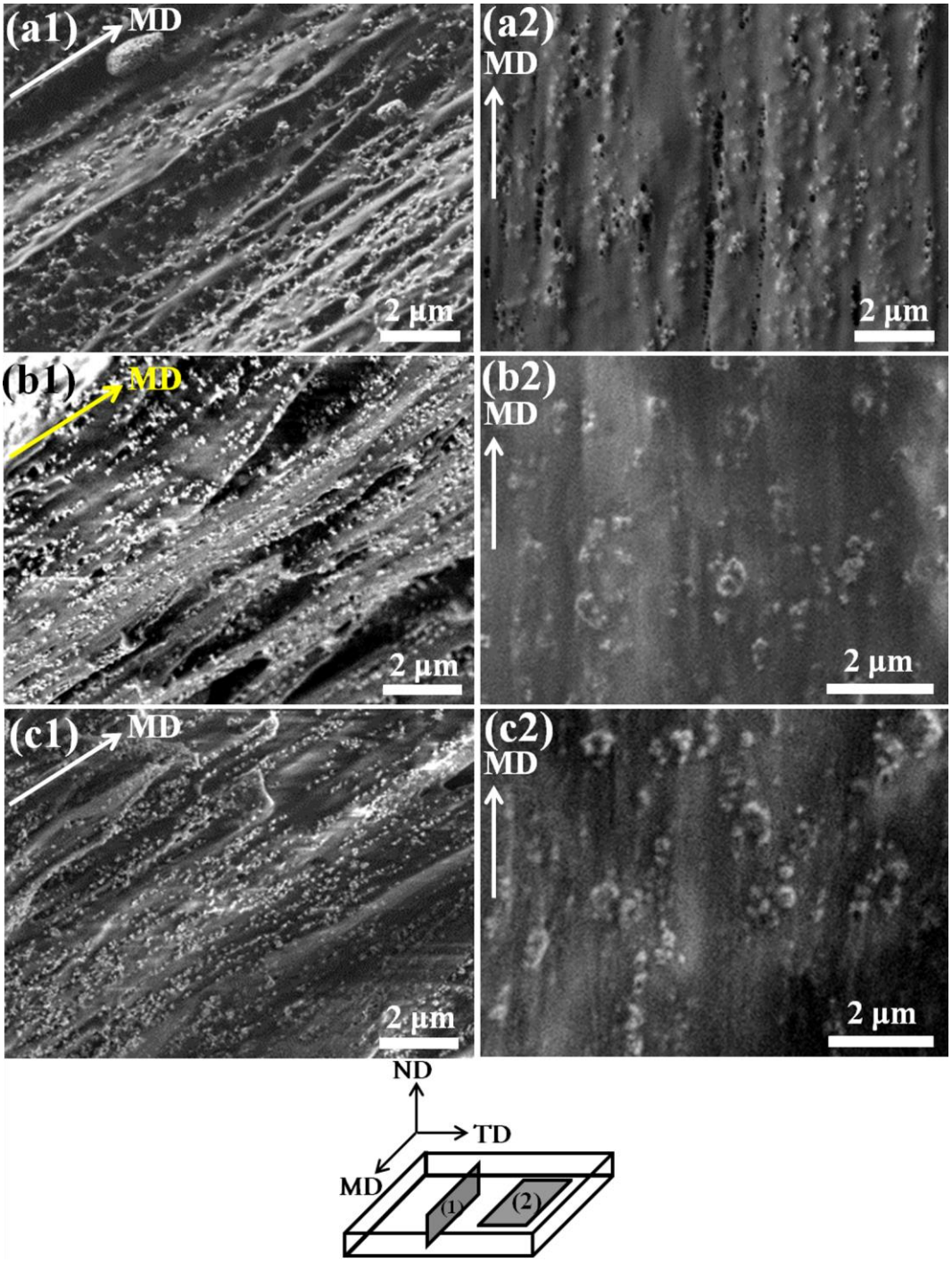

Figure 5-7: SEM images from cross-section and surface of the PPT125 film samples stretch up to 100 % at 200 mm/min and different stretching temperatures (a) 60, (b) 90, and (c) 120 °C (images number 1 are from cross-section and number 2 are from surface of the samples)

Figure 5-8 shows pore size distribution of the samples stretched at different temperatures measured by the mercury porosimetry method (MIP). As can be seen, peak of the curves shifted to lower values by increasing the drawing temperature suggesting a reduction in pore size. On the other hand, the area under the curves decreased with drawing temperatures. It shows that porosity of the stretched films decreases with the drawing temperature.

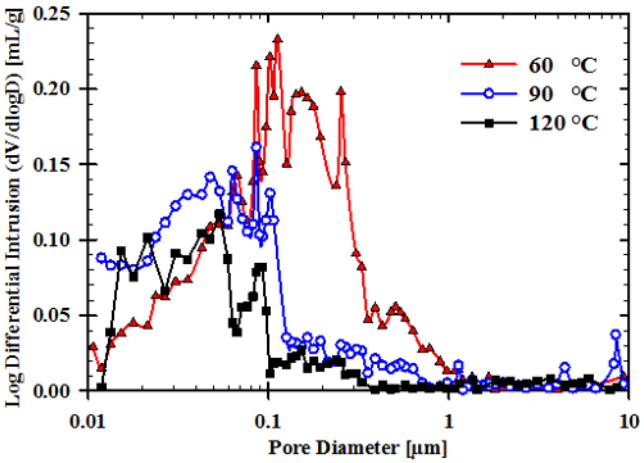

Figure 5-8: Pore size distribution of the samples stretched at different stretching temperatures (PPT125, 200 mm/min, 100 %) obtained from the MIP measurements

Table 5.3 summarizes results of MIP measurements for the samples, stretched at different drawing temperatures. It also compares the results of porosity and pore surface area obtained from MIP with the results of apparent porosity and BET surface area. The table reports that porosity, average pore size, and pore surface area of the samples decrease with drawing temperature. The difference between the values of porosity calculated based on density and obtained from MIP could be attributed to larger uncertainty in measuring the thickness of the samples (±20 %) compared to MIP method that its error is less than 5 %. Moreover, since in MIP method mercury could not penetrate to very small pores, it reports smaller values of porosity compared to the apparent porosity.

Table 5.3: Summary of pore size distribution obtained from MIP measurement for PPT125 sample stretched up to 100 % with 200 mm/min at different stretching temperatures

Stretching Temperature [°C]	Porosity [%]		Average Pore Size [μm]	Total Pore Area [m^2/g]	
	Density	MIP		MIP	BET
60	59.7	32.5	0.066	16.0	7.1
90	51.6	25.1	0.040	11.2	1.5
120	43.4	24.2	0.033	10.8	0.9

Depending on the drawing temperature and extension rate, several micro mechanisms are acting during the deformation of the particulate polymer composite. At low temperature and high strain rate, local cavitation mechanisms (e.g. micro-voiding, crazing, and micro-cracking) followed by the debonding of the particles are the governing failure mechanisms. On the other hand, local shear yielding dominates at low strain rates and elevated temperatures and, it has a much larger contribution compared to the cavitational mechanisms [26].

Detachment of the TiO_2 particles from the PP matrix is the main mechanism of the pore formation in the nanocomposite films. The required stress for the detachment, called as debonding stress, is a key parameter describing the effects of the process conditions on the properties of the porous nanocomposite film [26]. Pukanszky and Vörös [27] proposed a model to define the debonding stress in a polymer composite as:

$$\sigma_D = -C_1\sigma_T + C_2\left(\frac{W_{AB}E}{R}\right)^{\frac{1}{2}} \tag{5.4}$$

where C_1 and C_2 are constants, σ_T is the thermal stress induced by the different thermal expansion of the components, W_{AB} is the reversible work of adhesion, E is the tensile modulus of the matrix, and R is the radius of the particles.

Stress-strain behavior of the samples during the stretching process is presented in Figure 5-9a. Figure 5-9b depicts the variation of storage modulus (E') and *tan* δ of PP with temperature as measured by DMA. As expected, with increasing the temperature, both draw tension (stress) and E' decrease. Based on Equation 5.4, the debonding stress (σ_T) is proportional to the square

root of the modulus (E) of the matrix. However, as it can be seen in Figure 5-9b, there are two peaks in the curve of *tan* δ versus temperature for PP, at 5.3 ± 0.4 °C and 109 ± 8 °C, which are respectively associated with β and α relaxations of PP molecular chains. Increasing the drawing temperature, from 60 °C to 90 and 120 °C, leads to higher molecular mobility of the amorphous and crystalline parts of PP matrix and lower yield stress under deformation. Therefore, it could be concluded that the reduction in yield stress, at the high drawing temperatures, is more significant than for the square root of the modulus. It causes shear yielding and orientation in the PP matrix instead of debonding at its interface with the TiO_2 phase [26]. It should be mentioned that, since debonding stress is strongly dependent on particle size, larger particle aggregates detach from the matrix at lower temperatures. Figure 5-7b1 shows formation of the pores around the larger particle aggregates in the samples stretched at 90 °C.

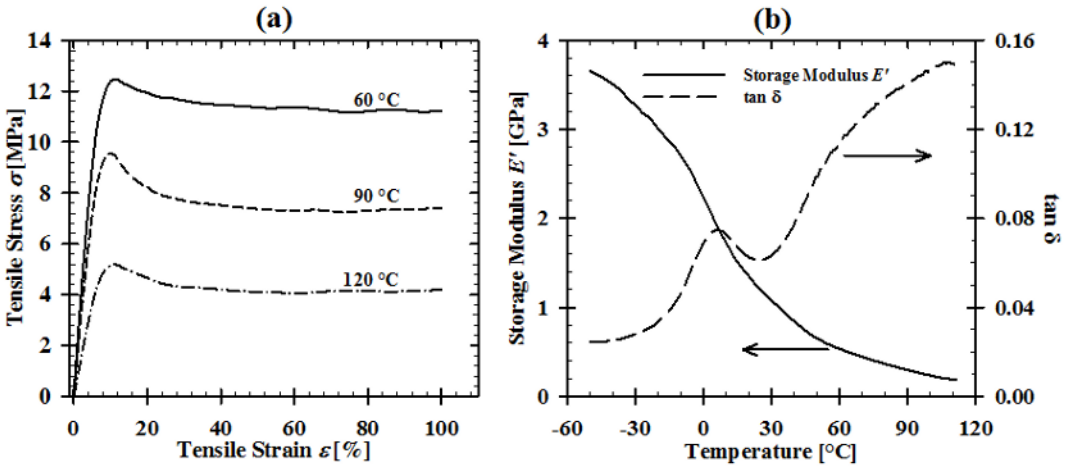

Figure 5-9: (a) stress-strain curves recorded during stretching at 200 mm/min and different stretching temperatures, (b) storage modulus *E'* and *tan* δ versus temperature for neat PP

5.3.4 Effect of draw ratio

Another important process condition that has a significant effect on the properties of the porous films is draw ratio (defined in Equation 5.1). Since the most desirable results of the previous sections were obtained for the lowest stretching temperature of 60 °C, the influence of draw ratio was investigated at 60 °C. Figure 5-10a reports the variation of WVTR with extension rate and

draw ratio for the nanocomposite samples stretched at 60 °C. An increase in draw ratio leads to higher WVTR. For the samples stretched at 200 and 500 mm/min, WVTR is between 1400 to 2560 g/(m^2.day) which is in the range of WVTR of other filled porous films with interconnected pores [19]. In the case of an extension rate of 50 mm/min, the change in WVTR with draw ratio is more significant compared to the other extension rates where it increased more than four times. It could be related to the presence of interconnected pores with less tortuosity in the samples stretched at 50 mm/min compared to the other samples.

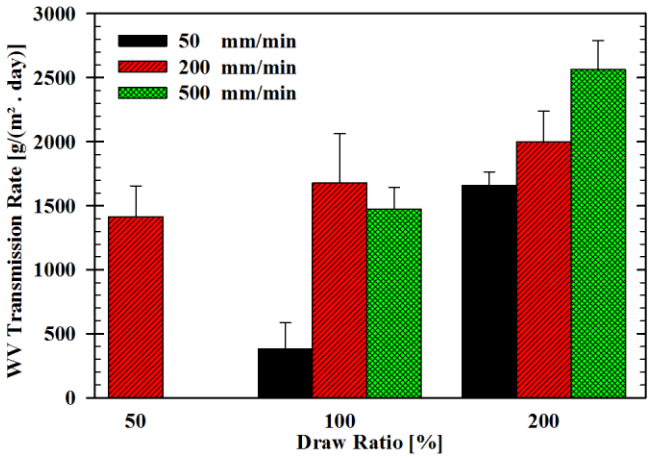

Figure 5-10: Water vapor transmission rate (WVTR) versus draw ratio for 100% stretched PPT125 nanocomposite films at 60 °C and different extension rates

Figure 5-11 shows SEM micrographs from the surface and cross section of the stretched PPT125 films to different stretching ratios parallel to machine direction (MD) at 60 °C. Figure 5-11a-b show surface morphology of the porous films. As it can be seen, the number and size of pore opening on the surface increased with draw ratio. As it was expected, the pores mostly initiated from the debonding of PP phase from the surface of TiO_2 particles. Cross-sectional SEM micrographs (Figure 5-11d-f) show that oval shape pores formed around the particles after 50% uniaxial stretching. The size of the pores is a function the aggregate that they initiate from; the larger the aggregate, the larger the pore. By increasing the stretch ratio to 100% (Figure 5-11e), the pore size increased, the pores elongated and fibril structure of PP were formed. Stretching up

to 200% enhanced the formation of PP fibrils and led to compaction of the PP fibril layers and merging of the neighboring pores.

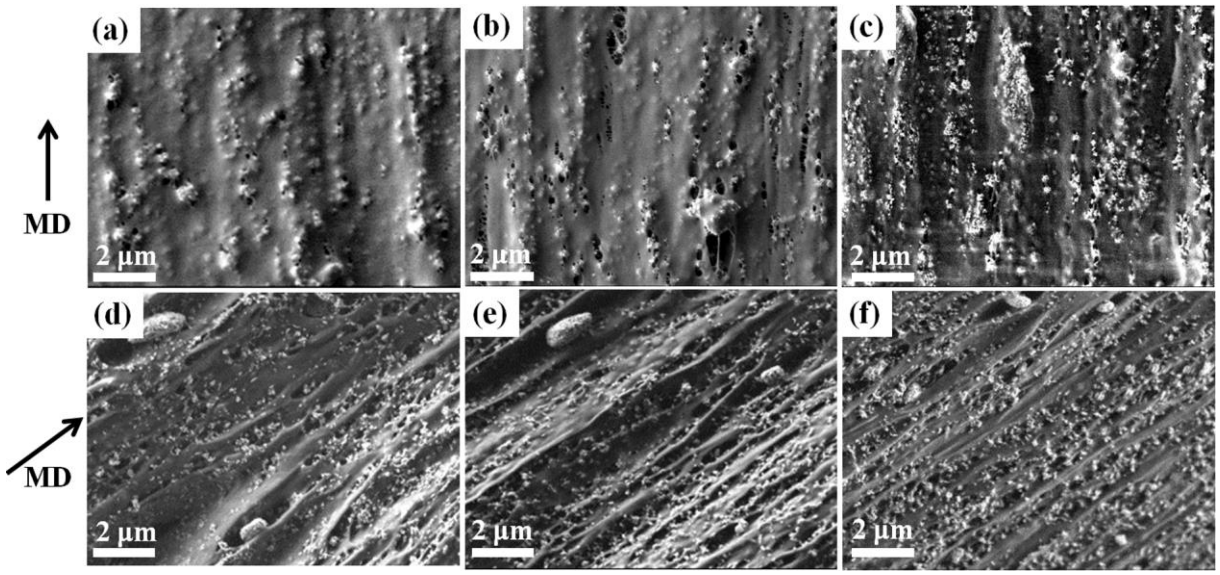

Figure 5-11: SEM images from surface of the PPT125 film samples stretched at 60 °C and 200 mm/min with different draw ratios (a) 50, (b) 100, (c) 200 % and cross-sectional SEM image of the samples stretched at 60 °C and 200 mm/min with different draw ratios (d) 50, (e) 100, and (f) 200 %

The number of interconnected pores between the two surfaces of the porous films and the tortuosity or structural complexity of the pores are two competing parameters affecting WVTR. Although the number of pores increases with draw ratio, the oriented layers of fibrillar PP may results in compaction of the pores that reduces transmission rate and, in total, WVTR and WVP do not increase significantly with draw ratio in the range of 50 to 200 % (Figure 5-10). Nago and Mizutani [28] reported the same effect in porous films based on PP and $CaCO_3$.

Figure 5-12 shows the effect of draw ratio on BET surface area and apparent porosity of the films stretched at 60 °C and 200 mm/min. The porosity of the films increases with draw ratio from 27 to 60 % and then slightly decreases. According to the previous SEM results (Figure 5-11) and WVTR (Figure 5-10), it could be concluded that the compaction of PP fibrils leads to a denser porous films and does not significantly change the apparent porosity calculated based on

the density (Equation 5.2) [28]. On the other hand, due to the formation of the pores which provides larger internal surface area, BET surface area of the porous films increases with draw ratio up to 9 m^2/g which is in the range of the previously reported values obtained by mercury porosimetry for stretched filled fibers [29].

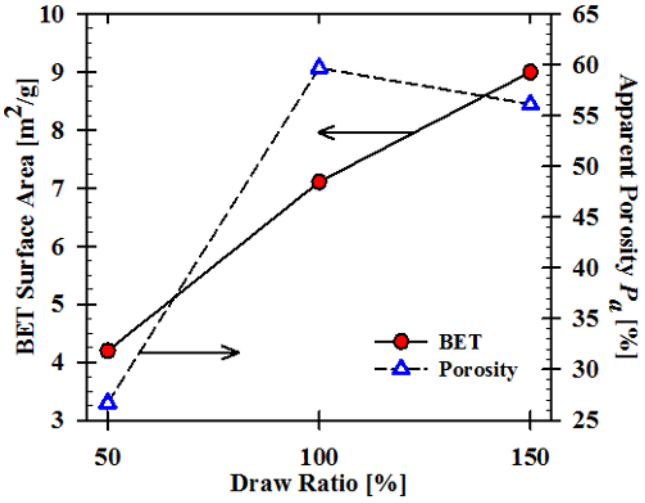

Figure 5-12: Variation of BET surface area (left axis) and the apparent porosity P_a (right axis) with draw ratio for the porous films based on PPT125 at stretching temperature of 60 °C stretched at 200 mm/min

Figure 5-13 compares results of MIP for porous films obtained with different draw ratios. It clearly shows that the volume of the pores which are in the range of 0.01-10 μm increases with draw ratio. However, the peak position in the pore size distribution curve did not significantly change and is around 0.1 μm. Analysis of pore size distribution in the whole accessible range of the MIP instrument (0.006-100 μm) resulted in porosity value of 40 % while around 47 % of the pores are in the range of 0.01-10 μm and, the average pore diameter was 0.08 μm. According to the results presented in Table 5.3, porosity increased with draw ratio. It is in contradiction with the results of apparent porosity (Figure 5-12) and could be attributed to MIP test mechanism where mercury diffuses to the pores under the applied pressures that may affect the pore structure. As it was discussed in section 5.3.3, the lower values of porosity from MIP compared

to the values calculated based on density could be due to the probable error in film thickness measurement and limited range of pore size considered in MIP.

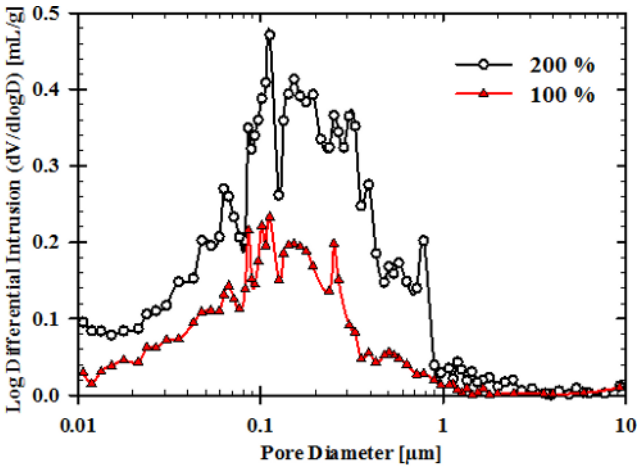

Figure 5-13: Pore size distribution of the samples stretched at different draw ratio (PPT125, 200 mm/min, 60 °C) obtained from the MIP measurements

5.3.5 Effect of TiO2 content and compatibilizer

Figure 5-14 compares WVTR in the porous films based on uncompatibilized nanocomposite films containing different volume contents of TiO_2 and the compatibilized ones containing AMPP which were uniaxially stretched in MD to a draw ratio of 100 % at 60 °C. As can be seen, WVTR of PPT125 is more than two times higher than that of PPT10, and the WVTR in PPAMT125 is surprisingly low.

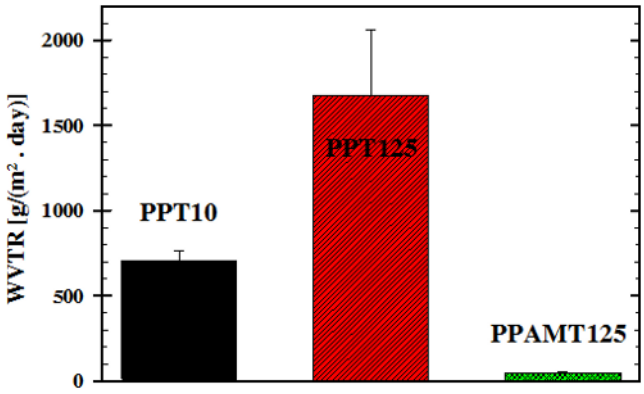

Figure 5-14: Comparison of WVTR in the porous film based on the uncompatibilized nanocomposite films PPT10, PPT125 with different TiO_2 contents, and the compatibilized nanocomposite film PPAMT125 containing AMPP and 12.5 %Vol. of TiO_2 (All the samples were stretched to draw ratio of 100 % at 60 °C)

Figure 5-15 shows an SEM image of PPAMT125 sample stretched 100%. Although few number of PP fibrils are observed, there is less number of pores created due to debonding between PP and TiO_2 compared to the uncompatibilized samples. Two reasons are possibly responsible for this difference; stronger interface between PP and TiO_2 and lower degree of crystallinty of the polymer matrix due to presence of AMPP which cause more flexibility of the polymer chains.

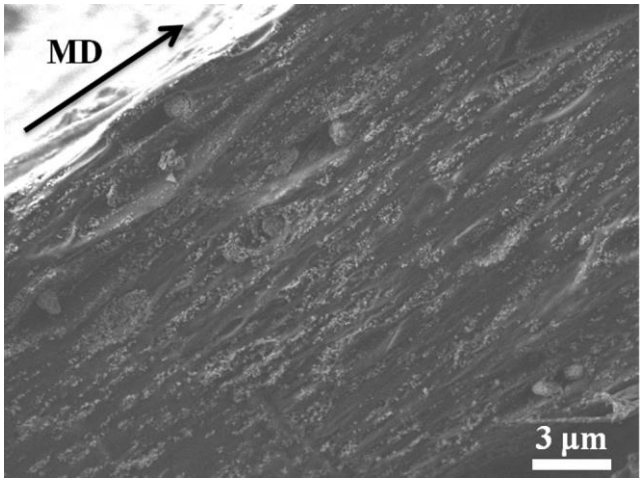

Figure 5-15: SEM images from cross-section of PPAMT125 film samples stretched at 60 °C and 200 mm/min 100 %

5.3.6 Dye adsorption

In order to quantify the capability of the porous film in absorbing a photosensitive dye, the concentration of desorbed dye from the porous nanocomposite film was analyzed using UV- Vis spectroscopy. Figure 5-16 shows the absorption spectra of the solvents containing the desorbed dye. As can be seen, UV absorption intensity increases with stretching ratio. It shows that increasing stretching ratio provides larger surface area to be covered by absorption of the dye. This is in agreement with BET surface area results (Figure 5-12) that showed that increasing draw ratio leads to higher values of surface area of the pores.

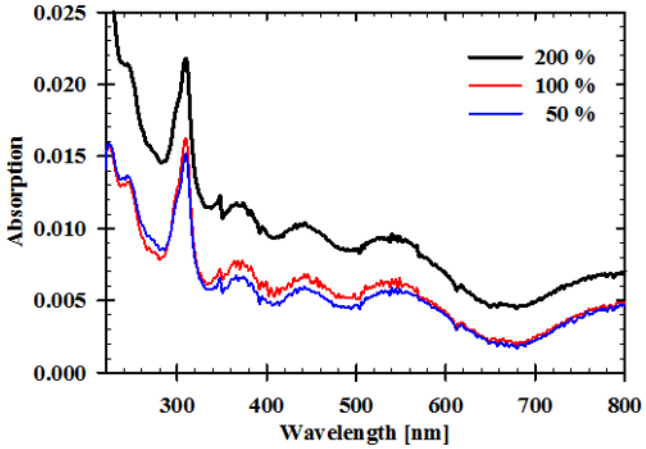

Figure 5-16: UV-Vis spectrums of the desorbed dye from stretched nanocomposite to 0.1 N solution of NaOH

5.4 CONCLUSION

Porous PP based nanocomposite films containing TiO_2 nanoparticles were prepared by melt mixing followed by uniaxial stretching. Final microstructure and properties of the porous films are strongly affected by their composition and different process parameters such as drawing temperature, stretching ratio and extension rate. Porosity and pore size of the films were strongly affected by drawing temperatures. Stretching at lower temperatures led to higher porosity and larger average pore size. It, consequently, resulted in larger WVTR through the films and larger surface area of the porous nanocomposites. Moreover, a direct relation between extension rate and WVTR was observed. Number of pore, pore size, and porosity increased with stretching ratio. Higher interfacial strength and polymer matrix flexibility in the compatibilized films, containing AMPP, caused less pore formation due to polymer-particle debonding and lower WVTR of the samples. Quantifying dye adsorption showed that the larger porosity of the films provides larger surface area covered by the dye.

Acknowledgments

This research was supported in part by the Natural Science and Engineering Research Council of Canada (NSERC) Strategic projects and discovery grants. The authors would like to thank Sylvie

St-Amour and Sylvie Sauriol from FPInnovations (Pointe-Claire, Canada) for their help in the MIP measurements.

5.5 REFERENCES

[1] A. Zohrevand, Relationship between rheological and electrical percolation in a polymer nanocomposite with semiconductor inclusions, Rheologica Acta, in press (2013).

[2] A. Zohrevand, A. Ajji, F. Mighri, Morphology and properties of highly filled iPP/TiO2 nanocomposites, Polymer Engineering & Science, (2013) doi: 10.1002/pen.23625.

[3] D. Yakisir, F. Mighri, M. Bousmina, Development of Porous Electrode Gas Diffusion Layers for Proton Exchange Membrane Fuel Cells, Journal of Fuel Cell Science and Technology, 5 (2008) 031008-031009.

[4] Y. Li, D.-K. Lee, J.Y. Kim, B. Kim, N.-G. Park, K. Kim, J.-H. Shin, I.-S. Choi, M.J. Ko, Highly durable and flexible dye-sensitized solar cells fabricated on plastic substrates: PVDF-nanofiber-reinforced TiO2 photoelectrodes, Energy & Environmental Science, 5 (2012) 8950-8957.

[5] B. O'Regan, M. Gratzel, A low-cost, high-efficiency solar cell based on dye-sensitized colloidal TiO2 films, Nature, 353 (1991) 737-740.

[6] T. Soga, Nanostructured Materials for Solar Energy Conversion, in, Elsevier, Amsterdam, 2006.

[7] K. Kalyanasundaram, M. Grätzel, Applications of functionalized transition metal complexes in photonic and optoelectronic devices, Coordination Chemistry Reviews, 177 (1998) 347-414.

[8] N.G. Park, J. van de Lagemaat, A.J. Frank, Comparison of Dye-Sensitized Rutile- and Anatase-Based TiO2 Solar Cells, The Journal of Physical Chemistry B, 104 (2000) 8989-8994.

[9] M. Grätzel, Dye-sensitized solar cells, Journal of Photochemistry and Photobiology C: Photochemistry Reviews, 4 (2003) 145-153.

[10] T. Miyasaka, M. Ikegami, Y. Kijitori, Photovoltaic Performance of Plastic Dye-Sensitized Electrodes Prepared by Low-Temperature Binder-Free Coating of Mesoscopic Titania, Journal of The Electrochemical Society, 154 (2007) A455-A461.

[11] H. Kim, R.C.Y. Auyeung, M. Ollinger, G.P. Kushto, Z.H. Kafafi, A. Piqué, Laser-sintered mesoporous TiO2 electrodes for dye-sensitized solar cells, Applied Physics A: Materials Science & Processing, 83 (2006) 73-76.

[12] C.P. Drew, Electrospinning of polymeric photovoltaic cells, in: Plastic Engineering, University of Massachusetts Lowell, Lowell, 2000, pp. 89.

[13] C. Drew, X. Wang, K. Senecal, H. Schreuder-Gibson, J. He, J. Kumar, L.A. Samuelson, ELECTROSPUN PHOTOVOLTAIC CELLS, Journal of Macromolecular Science, Part A: Pure and Applied Chemistry, 39 (2002) 1085 - 1094.

[14] C. Drew, X. Wang, L.A. Samuelson, J. Kumar, The Effect of Viscosity and Filler on Electrospun Fiber Morphology, Journal of Macromolecular Science, Part A: Pure and Applied Chemistry, 40 (2003) 1415 - 1422.

[15] D. Yakisir, F. Mighri, M. Bousmina, Electronic Conductive Microporous Polymer-Based Structures, Macromolecular Rapid Communications, 27 (2006) 1596-1602.

[16] S. Sängerlaub, M. Böhmer, C. Stramm, Influence of stretching ratio and salt concentration on the porosity of polypropylene films containing sodium chloride particles, Journal of Applied Polymer Science, 129 (2013) 1238-1248.

[17] K. Trommer, B. Morgenstern, Nonrigid microporous PVC sheets: Preparation and properties, Journal of Applied Polymer Science, 115 (2010) 2119-2126.

[18] Y. Mizutani, S. Nakamura, S. Kaneko, K. Okamura, Microporous polypropylene sheets, Industrial & Engineering Chemistry Research, 32 (1993) 221-227.

[19] P.C. Wu, G. Jones, C. Shelley, B. Woelfli, Novel microporous films and their composites, Journal of Engineered Fibers and Fabrics, 2 (2007) 49-59.

[20] P.P. Kundu, S. Choe, Transport of Moist Air Through Microporous Polyolefin Films, Polymer Reviews, 43 (2003) 143-186.

[21] A.Z. Moss, Microporous Polymeric Films and Process for Their Manufacture, in, E. I. Du Pont Nemours and Company, 1987.

[22] J.-S. Park, S.-J. Gwon, Y.-M. Lim, Y.-C. Nho, Influence of the stretching temperature on an alumina filled microporous high density polyethylene membrane, Materials & Design, 31 (2010) 3215-3219.

[23] D.L. Green, L. McAmish, A.V. McCormick, Three-dimensional pore connectivity in bi-axially stretched microporous composite membranes, Journal of Membrane Science, 279 (2006) 100-110.

[24] S. Brunauer, P.H. Emmett, E. Teller, Adsorption of Gases in Multimolecular Layers, Journal of the American Chemical Society, 60 (1938) 309-319.

[25] W.R. Hale, J. McGuire, I.D. Sand, K.K. Dohrer, Heat setting of stretched and microvoided PE/CaCO3 films, Journal of Applied Polymer Science, 82 (2001) 2454-2471.

[26] M. Jerabek, Z. Major, K. Renner, J. Móczó, B. Pukánszky, R.W. Lang, Filler/matrix-debonding and micro-mechanisms of deformation in particulate filled polypropylene composites under tension, Polymer, 51 (2010) 2040-2048.

[27] B. Pukanszky, G. VÖRÖS, Mechanism of interfacial interactions in particulate filled composites, Composite Interfaces, 1 (1993) 411-427.

[28] S. Nago, Y. Mizutani, Preparation of microporous polypropylene sheets containing CaCO3 filler: Effect of draft ratio, Journal of Applied Polymer Science, 61 (1996) 31-35.

[29] S. Nagó, Y. Mizutani, Microporous polypropylene fibers containing CaCO3 fillers, Journal of Applied Polymer Science, 62 (1996) 81-86.

CHAPTER 6 ARTICLE 4: DEVELOPMENT OF POROUS POLYMER NANOCOMPOSITE FILM BASED FLEXIBLE PHOTOELECTRODE FOR DYE-SENSITIZED SOLAR CELL

A. Zohrevand[1], A. Ajji[2]* and F. Mighri[3]

[1]*CREPEC, Department of Chemical Engineering, Ecole Polytechnique de Montreal – ahmad.zohrevand@polymtl.ca*

[2] *CREPEC, Department of Chemical Engineering, Ecole Polytechnique de Montreal,C.P. 6079, succ. Centre-Ville, Montreal, QC, Canada H3C 3A7 – abdellah.ajji@polymtl.ca*

[1]*CREPEC, Department of Chemical Engineering, Laval University – frej.mighri@gch.ulaval.ca*

Abstract

In the present work, a novel method based on polypropylene (PP) - TiO_2 porous nanocomposite film is introduced to prepare flexible photoelectrodes for dye-sensitized solar cells (DSSC). Highly-filled nanocomposites films, prepared by twin screw extrusion of PP and TiO_2 nanoparticles, were uniaxially stretched up to 200% at elevated temperatures in order to obtain porous films containing a percolated structure of the nanoparticles. The nanocomposite films were sensitized by an inorganic dye (N719) and used as a photoelectrode in a sandwich-like DSSC. Mercury intrusion porosimetry (MIP), BET surface analysis, and UV absorption techniques showed that higher stretching ratio leads to higher porosity and dye uptake in the nanocomposite photoelectrode layer. Photo-electrochemical properties of the cells were analyzed by photocurrent-voltage (*J*-*V*) and electrochemical impedance spectroscopy (EIS). Both short circuit photocurrent (J_{sc}) and open circuit voltage (V_{oc}) increased with the stretching ratio of the nanocomposite films. The results of this research can lead to the development of a cost-effective method for the production of flexible DSSC at low temperatures.

Keywords: nanocomposite, film extrusion, DSSC, photoelectrode, porosity

6.1 Introduction

Dye-sensitized solar cell (DSSC) is a type of solar cell that, due to its relatively high efficiency and low material cost, has attracted extensive attention from both academic and industrial researchers as a potential next generation photovoltaic device [1]. The photo electrode of DSSC is typically made of a thin layer composed of TiO_2 nanoparticles which are sensitized by a photosensitive dye. The TiO_2 nanoparticles are interconnected porous structure on a transparent conductive oxide (TCO) layer of the substrate, filled with a liquid electrolyte [2]. The conventional manufacturing process of the TiO_2 layer includes a high-temperature (450-500°C) sintering step that leads to the connection among the nanoparticles and the formation of the pores [3]. Since there is a considerable interest in manufacturing flexible solar cells on plastic substrates, the development of a new method as an alternative for the high temperature sintering is an important challenge. Different methods such as hydrothermal crystallization, electrophoretic deposition, microwave irradiation, chemical sintering, and mechanical pressing have been proposed in the past few years to prepare the photoelectrodes at low temperatures and avoid degradation of the plastic substrates [4].

Nanocomposite-based materials and their fabrication methods could offer promising solutions to produce the photoelectrodes [5, 6]. Continuous polymer melt processes can be used to produce highly filled conductive porous films where stretching or solvent extraction is applied to create the pores in the nanocomposite [7]. Stretching polymeric composite sheets containing rigid fillers is a well-known method to produce porous flexible thin films/sheets. This kind of porous films are made of a thermoplastic that is highly filled (15-35 %vol.) with organic or inorganic fillers [8].

In the present work, a novel preparation method of DSSC photoelectrode through film extrusion of highly-filled nanocomposite, containing TiO_2 nanoparticles, followed by uniaxial stretching is proposed. The structure and functionality of the porous nanocomposite films, prepared under different condition, were characterized and discussed in terms of porosity, dye adsorption and photovoltaic response.

6.2 Experimental

6.2.1 Materials

An isotactic PP (iPP) (PP4712E1, ExxonMobil, USA), having a melt flow index MFI = 2.8 dg/min and density ρ = 0.9 g/cm^3, was used as the polymer matrix. A commercial grade TiO_2 nanoparticle (AEROXIDE TiO2 P 25, Evonik, Germany) with an average primary particle size of 21 nm, containing a mixture of anatase: rutile with the ratio of 79:21 wt%, and ρ = 4.26 g/cm^3 was used as the nanoparticle. Solvents and other chemicals were purchased from Sigma-Aldrich Canada.

6.2.2 Preparation of the Porous PP/TiO2 Nanocomposite Films

PP/TiO_2 nanocomposite base films containing 12.5 %vol (40 %wt) of TiO_2 were prepared via a masterbatch method using a melt compounding process in a tightly intermeshing co-rotating twin-screw extruder (Leistritz ZSE-18HP-40D, Germany). First, a masterbatch based on PP containing 18 %vol (50 %wt) of the TiO_2 nanoparticles was prepared by two passes of extrusion. Then, in a third extrusion run, the masterbatch was diluted to 12.5 %vol by adding neat PP and the compounds were extruded through a slit die to produce base nanocomposite films with an average thickness of 120 μm.

The base films were uniaxially stretched parallel to extrusion direction (MD) at 60°C using a dynamic tensile machine (Instron ElectroPuls E3000, USA) equipped with an environmental chamber. The samples were cut as 6 × 6 cm rectangles and the initial distance between the grips of the machine were set at 20 mm to 40 mm. The films were stretched using an extension rate of 200 mm/min and different draw ratios up to 200%. It is to be noted that the draw ratio was defined as;

$$\text{Draw Ratio \%} = 100 \times (Lf - L0) \,/\, L0 \qquad (6.1)$$

where L_f and L_0 are final and initial lengths of the samples between the grips.

6.2.3 Characterization of the Porous Nanocomposite

The morphology of the porous nanocomposite films was characterized using SEM (JEOL 7600F FEG). The specific surface area of the samples was measured by BET method (Autosorb, Quantachrome, USA). The porosity of the films was measured by mercury intrusion porosimetry (MIP) (AutoPore IV 9500, Micromeritics, USA).

6.2.4 DSSC Fabrication

The porous samples were vacuum dried and immersed into a 0.3 mM solution of a ruthenium-based dye (N719, Sigma-Aldrich) in ethanol for 36 h. Then, they were rinsed using acetonitril and dried at room temperature. The amount of absorbed dye was estimated from UV absorption of the dye molecules dissolved into 0.1 M NaOH during 60 s and using a UV-Vis spectrometer (Cary 5000, VARIAN, USA). Transparent conducting FTO/glass (8 Ω/sq) substrates were used. Pt counter electrodes were prepared by thermal reduction of 7 mM solution of $H_2PtCl_6.6H_2O$ at 400°C for 20 min. The liquid electrolyte was a solution composed of 0.5 M LiI, 0.05 M I_2 and 0.5 M 4-tert-butylpiridine (tBP) in a mixture of acetonitrile and valeronitrile (v/v 85:15).

6.2.5 Photovoltaic Cell Measurements

The electrochemical impedance spectra (EIS) and photocurrent/voltage (*J*-*V*) measurements were obtained using a potentiostat equipped with a frequency response analyzer (Solarton). The frequency ranged from 10^{-1} to 10^{6} Hz. The magnitude of the alternative signal was 10 mV. A typical incandescent lamp was used as a light source. The amount of total light during the experiment was around 1100 lux.

6.3 Results and Discussion

Figure 6-1 shows SEM images from the cross section of the porous nanocomposite stretched parallel to machine direction (MD), with different stretching ratios. As can be seen, there is a good dispersion of TiO_2 nanoparticles through the PP phase. The TiO_2 dispersed phase consists

mainly in small aggregates composed of few primary nanoparticles. Although there are aggregates of few microns in diameter, it could be concluded that melt compounding is able to break TiO_2 nanoparticles large aggregates to smaller entities.

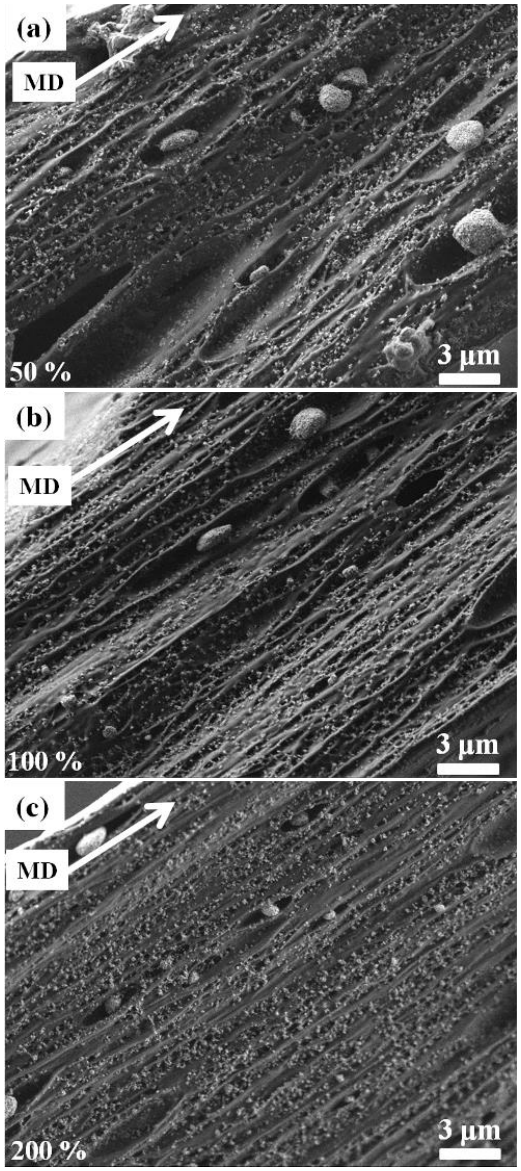

Figure 6-1: SEM image from cross section of the uniaxially stretched porous nanocomposite films up to; (a) 50%, (b) 100% and (c) 200%

Figure 6-1(a) shows that oval shaped pores formed around the particles due to the debonding between PP phase and nanoparticle surface after 50% uniaxial stretching. The size of the pores is a function of the aggregate that they initiate from; the larger the aggregate, the larger the pore. By increasing the stretch ratio to 100% (Figure 6-1(b)), the pore size increased, the pores elongated and PP fibrillar structures were formed. Stretching up to 200% enhanced the formation of PP fibrils but also led to their compaction and the merging of neighbor pores.

Figure 6-2 shows pore size distribution of 100% and 200% uniaxially stretched nanocomposite films. As can be seen, peak value in the distribution curve increased with stretch ratio from 107 nm for 100% to 126 nm for 200%. This is in agreement with SEM observations. In addition, porosity of the samples also increased from 28.4% to 40.0% with stretch ratio. Inset of Figure 6-2 reports the variation of BET surface area of the porous nanocomposite films with stretch ratio. Same as for porosity, increasing stretch ratio leads to higher values of BET surface area.

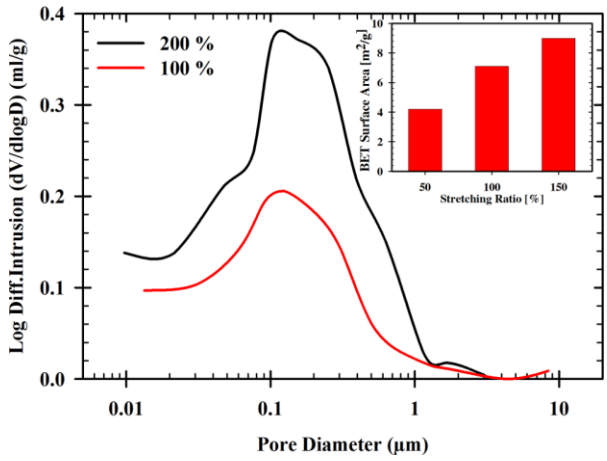

Figure 6-2: Pore size distribution for porous nanocomposites stretched to 100% and 200%. The inset shows BET surface area of the samples versus stretching ratio

In order to quantify the capability of the porous film in absorbing the photosensitive dye, the concentration of desorbed dye from the porous nanocomposite film was analyzed by UV-Vis spectroscopy. Figure 6-3 shows UV absorption spectra of the solvent containing the desorbed

dye. As can be seen, UV absorption intensity increases with stretch ratio. It shows that increasing stretch ratio provides larger surface area to be covered by adsorbed dye.

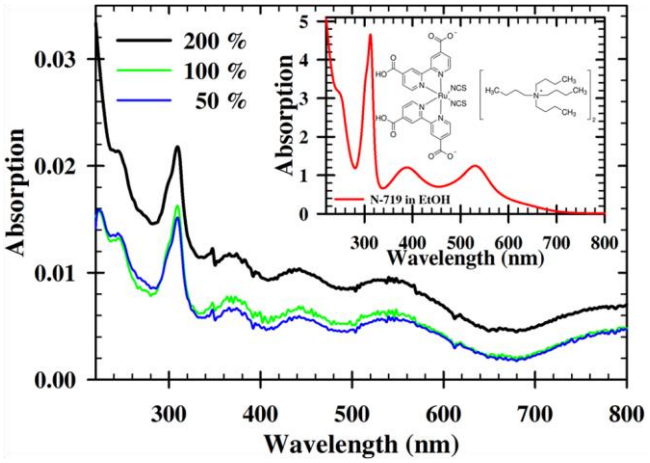

Figure 6-3: UV-Vis spectrum of the desorbed dye from the porous nanocomposites with different stretch ratio. The inset shows a typical absorption spectrum and chemical structure of N719 dye)

The photocurrent/voltage (*J*-*V*) curves are presented in Figure 6-4. Both short-circuit current (J_{sc}) and open-circuit voltage (V_{oc}) increased with stretch ratio. The increase of J_{sc} can be attributed to the increased dye absorption due to the larger surface in the porous film [9]. It should be mentioned that J_{sc} is much lower than that in DSSC prepared from conventional method. It could be attributed to the light source used for the experiments and larger resistance in the system. However, the result is promising.

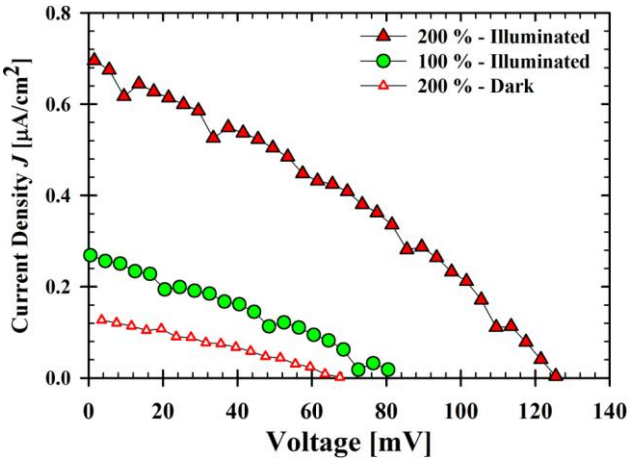

Figure 6-4: Photocurrent-voltage curves of the DSSC based on the nanocomposite photoelectrodes

6.4 Conclusions

A novel method, through melt extrusion of a concentrated nanocomposite followed by stretching, was proposed to produce porous nanocomposite films for DSSC photoelectrode applications. Porosity and pore size of the nanocomposite increased with stretch ratio because of the large surface area provided for absorption of photosensitive dye. Both short circuit photocurrent (J_{sc}) and open circuit voltage (V_{oc}) increased with stretching of the nanocomposite films.

Acknowledgements

Financial support from the Natural Science and Engineering Council of Canada Strategic projects and discovery grants is acknowledged. Authors would like to thank LANOMAT of Ecole Polytechnique de Montreal and FP Innovation for providing the opportunity of using their equipments.

6.5 References

1. B. O'regan; M. Gratzel *Nature* 1991, *353*, 737.

2. S. Mori; S. Yanagida in *Nanostructured Materials for Solar Energy Conversion*, T. Soga, Ed.; Elsevier, Amsterdam, 2006; 191-273.
3. M. Grätzel; *J. Photoch. Photobio. C* 2003, *4*, 145.
4. Y. Li; K. Yoo; D.-K. Lee; J.H. Kim; N.-G. Park; K. Kim; M.J. Ko; *Curr. Appl. Phys.* 2010, *10*, e171.
5. C.P. Drew, MSc Thesis, University of Massachusetts Lowell, 2000.
6. H. Lindström; A. Holmberg; E. Magnusson; L. Malmqvist; A. Hagfeldt; *J. Photoch. Photobio. A*, 2001, *145*, 107.
7. D. Yakisir; F. Mighri; M. Bousmina *Macromol. Rapid Comm.*, 2006, *27*, 1596.
8. P.P. Kundu; S. Choe *Polym. Rev.*, 2003, *43*, 143.
9. Y. Li; D.-K. Lee; J.Y. Kim; B. Kim; N.-G. Park; K. Kim; J.-H. Shin; I.-S. Choi; M.J. Ko *Energ. Environ. Sci.*, 2012, *5*, 8950.

CHAPTER 7 GENERAL DISCUSSION

In order to replace the photoelectrode of DSSCs with flexible polymer-based materials, different concerns regarding microstructure of the materials should be considered. The functional layer must be able to collect the photogenerated electrons, providing a pathway for electrical current. Porosity of the photoelectrode layer is another essential feature that is needed to complete the electrical circuit of the solar cell. The pores are filled with an electrolyte that is responsible for regeneration of dye by electron donation. Utilizing polymer composite approach is one of the most promising methods to prepare DSSCs on plastic substrate with relatively low process temperatures. TiO_2 nanoparticles were mixed with a thermoplastic polymer via melt blending and, composite films were prepared as precursors. Stretching the composite films is another step to make the porous film structure and that may be affected by both material and process parameters.

In the first step of the present work, structure and properties of iPP and TiO_2 nanocomposites in a wide range of TiO_2 content was investigated. State of dispersion of the nanoparticles is the key morphological characteristic that had a strong effect on final properties of the nanocomposites. Among different factors controlling microstructure of the nanocomposites, interactions between the polymer matrix and TiO_2 nanoparticles have significant roles in dispersion during mixing and strength of polymer-particle interface. SEM observations showed that adding AMPP, as a macromolecular compatibilizer, improves dispersion of the TiO_2 nanoparticles in concentrations lower than the percolation threshold of the system. Better dispersion of TiO_2 leads to smaller aggregates and larger surface area. It could result in higher porosity and more dye adsorption at a given particle content. However, our mechanical studies and the micromechanical analysis showed that presence of AMPP strengthens interfacial interactions between polymer matrix and TiO_2 nanoparticles. It improves the dispersion by increasing stress transfer from the polymer melt during blending. However, since the origin of pore formation in the filled polymer films is debonding of the TiO_2 particles from the PP phase during stretching, strong interfacial interactions between two phases affect on the microstructure of the porous nanocomposite films. Moreover, adding AMPP into PP changed rheological and mechanical properties of polymer matrices in the nanocomposites that had significant on the

morphology of the nanocomposite above the percolation threshold and microstructure of the stretched nanocomposite films.

As mentioned, electrical properties of the nanocomposite are very important. Because of the semiconductive nature of the TiO_2 nanoparticles, electrical conductivity of PP/TiO_2 nanocomposites is different from the nanocomposites containing conductive inclusions. Since the PP/TiO_2 nanocomposite film is used instead of the all-TiO_2 layer, its electrical conductivity must be as close as possible to electrical conductivity of TiO_2 layer. In other words, an interconnected network of TiO_2 embedded in the PP phase is required for electron transfer. Therefore, variation of electrical conductivity of nanocomposites with TiO_2 content was studied to find electrical percolation threshold of the system where the TiO_2 network forms. Measuring DC electrical conductivity of the samples showed that the uncompatibilized nanocomposites had lower percolation threshold compared to the compatibilized one containing AMPP. Like other composite systems, the electrical percolation is directly dependent on the microstructure of the PP/TiO_2 nanocomposites particularly the state of dispersion of the nanoparticles. In order to transfer the electrons, TiO_2 nanoparticles should be connected to each other to form the electron pathway. As observed in the morphological results, adding AMPP improved dispersion of TiO_2 and, resulted in smaller particle aggregate. The TiO_2 aggregates in the compatibilized composites are separately dispersed while the TiO_2 in the uncompatibilized nanocomposite form larger cluster aggregates. Therefore, the TiO_2 clusters in the uncompatibilized nanocomposites form the interconnected network at lower particle content compared to the compatibilized nanocomposites. Using a power-law relation between electrical conductivity and particle content quantitatively showed the lower percolation threshold of uncompatibilized sample.

Since one of the objectives of this work is to produce nanocomposite films via a melt processing method, their rheological properties are very important. The nanocomposites above the percolation threshold are highly-filled systems. Viscosity of molten nanocomposites increased significantly with TiO_2 content and, affected their processability. On the other hand, rheological properties of the PP/TiO_2 nanocomposites strongly depend on characteristics of the polymer matrices, particle content, and their microstructure including the state of the nanoparticle dispersion. Therefore, rheology was utilized as an important tool in characterizing the nanocomposites. Attempts were made to find a correlation between rheological and electrical percolation.

Analyzing linear viscoelastic properties of the nanocomposites showed the evolution of their microstructures with TiO_2 content. Once TiO_2 content reached the rheological percolation of the composite systems, low-frequency terminal behavior of their melts disappeared. It was attributed to the formation of the TiO_2 network that result in the abrupt jumps in G' and η^* at low frequencies. Similar to the analysis of electrical conductivity, quantification of rheological percolation using the power-law relation resulted in a lower percolation threshold for the uncompatibilized system compared to the compatibilized one. It is in a qualitative agreement with the result obtained for electrical percolation threshold. It should be mentioned that in both systems of the compatiblized and uncompatibilized nanocomposites, rheological percolation thresholds were lower than the electrical ones. It could be attributed to different mechanisms responsible for electrical percolation and rheological percolation. Interparticle distance required for electron transfer in the TiO_2 network at the electron percolation threshold is shorter than the interparticle distance required for stress transfer at the rheological percolation threshold. Moreover, polymer bound layer around the particles could reduce electron transfer while enhances the effective volume fraction of the particles.

In the nonlinear rheological investigations, particularly strain sweep test, nonlinear viscoelastic properties were correlated to the microstructure of the samples below and above the rheological percolation. The lower strain sensitivity of the rheological properties of the compatibilized samples, compared to the uncompatibilized ones, was attributed to the strong interfacial interaction between PP and TiO_2. Scaling analysis above the percolation threshold led to a larger fractal dimension of the TiO_2 aggregates above the percolation. It was in agreement with the microscopic studies where denser aggregate were observed in the compatibilized nanocomposite. Percolation threshold, as one of the most important characteristics of the samples, is strongly dependant on the degree of dispersion. Although presence of compatibilizer improves stress transfer during melt mixing, lower viscosity of the polymer matrices in the compatibilized samples led to lower shear stress during mixing. In addition, partial phase separation of PP and AMPP resulted to the denser TiO_2 aggregates in the compatibilized samples. Rheological analysis also showed thicker bound layer around TiO_2 nanoparticles in the compatibilized nanocomposites that is in analogy with results of the micromechanical analysis.

After the systematic study on morphological, electrical, and rheological properties of the compatibilized and uncompatibilized PP/TiO_2 nanocomposites, porous films were prepared by

stretching the nanocomposite precursor film. TiO_2 content of the precursor film was higher than the electrical percolation threshold. Different process and material parameters affect structure and properties of the final film after stretching. Drawing temperature, extension rate, stretching ratio, and composition of the films were the important factors studied in this work. Molecular chain flexibility of polymer matrix and interfacial strength (between PP and TiO_2) at the drawing temperature had strong effect on pore formation. In the compatibilized samples, molecular flexibility of matrix and the interfacial strength were high. These parameters were not favorable for debonding of TiO_2 particles from polymer, which is the main mechanism of pore formation in the nanocomposite films.

Functionality of the porous film prepared via melt mixing followed by stretching was examined. Final porosity and pore surface were two important factors on photo-chemical properties of the cells based on the porous nanocomposite films. As the porosity and pore surface are increased, higher amount of the photosensitive dye are adsorbed. It led to enhancement of photocurrent and voltage of the solar cell made based on the composite photoelectrode.

CONCLUSION AND RECOMMENDATIONS

In this PhD research project, a novel porous polymer film based on PP/TiO_2 nanocomposite was developed to be used as the photoelectrode in DSSC. Main axes of the work were on investigation of the microstructure and properties of the nanocomposite with and without AMPP as a compatibilizer. The effect of composition and microstructure on electrical conductivity of the nanocomposites with an emphasis on percolation of the blend system was studied. Rheological properties were analyzed as indicators of processability and microstructure to build correlation between electrical and rheological percolation thresholds. Finally, attempts were made to find a process window for stretching the precursor film to efficiently induce porosity and, functionality of the nanocomposite films in a DSSC was assessed.

7.1 Conclusion

Based on the results of the various studies of this work, the following conclusion could be drawn:

1. Morphological observation revealed that adding AMPP improves the dispersion of the TiO_2 nanoparticles in PP for concentrations lower than 5 vol%. In this range of particle content, TiO_2 were well-dispersed single particle or aggregates in the compatibilized samples while they form larger cluster aggregates. Although particle network formed at concentrations above 5 vol%, the aggregates in the compatibilized sample were denser compared to the uncompatibilized nanocomposites.

2. The formation of β-form crystals led to lower elastic modulus in the nanocomposites containing 1 vol% of TiO_2, adding TiO_2 increased modulus of the other samples compared to their matrices. Micromechanical analysis showed that the interfacial interaction between polymer and nanoparticles in the compatibilized nanocomposite and AMPP improved adhesion between PP and TiO_2.

3. DC electrical measurement showed that blend of PP and TiO_2 nanoparticles are non-ideal dielectric materials with capacitance characteristics. Comparison between dried and non-dried samples revealed enhanced electrical conductivity due to the presence of moisture. Electrical conductivity of the nanocomposite containing more than 4 vol% of TiO_2 significantly increased

with nanoparticles content. It was attributed to the formation of an electrically-conductive network of nanoparticles at the electrical percolation system. Quantifying the results of electrical conductivity using a power-law relation resulted in a lower percolation threshold for the uncompatibilized nanocomposite compared to the compatibilized one.

4. Measuring linear rheological properties of the nanocomposite in the melt state showed that their viscoelastic behavior strongly deviate from terminal behavior by increasing TiO_2 content above the rheological percolation. Qualitative and quantitative analysis showed that the compatibilized nanocomposites have lower rheological percolation threshold compared to the compatibilized one. However, rheological percolation threshold of both nanocomposite system were lower than their electrical percolation.

5. Analyzing linear and nonlinear viscoelastic properties showed that thickness of polymer bound layer in the compatibilized system is larger than that in the uncompatibilized one. Scaling analysis resulted in a larger fractal dimension for aggregates of compatibilized system above their percolation, confirming the morphological observations.

6. Two main reasons were indicated for the formation of denser TiO_2 aggregates in compatibilized nanocomposites above the percolation threshold: partial phase separation of PP and AMPP in the matrices, and their lower viscosities compared to the uncompatibilized nanocomposites

7. Final microstructure and properties of the porous nanocomposite films based on PP/TiO_2 nanocomposites could be customized by applying different compositions and process parameter for uniaxial stretching. Porosity, pore size and, consequently, pore surface area and WVTR through the films increased significantly with decreasing the drawing temperature. Number of pores, pore size, and porosity of the films increased with stretching ratio.

8. The amount of adsorbed photosensitive dye increased with porosity and pore surface area of the PP/TiO_2 nanocomposites. It led to enhancement of both photocurrent and open circuit voltage of the DSSC based on the porous nanocomposite photoelectrode.

7.2 Recommendations

At the end of this PhD thesis, the following subjects are recommended for future works in continuing the research in this area:

1. Since melt mixing is one of the most important part of the work, it is recommended to study the effect of different extrusion conditions such as screw configuration and feeding order on dispersion and microstructure of PP/TiO_2 nanocomposites,

2. As the composition and molecular characteristics of the polymer matrices has important effect on morphology and rheology of the precursor nanocomposite and final porous film, investigation on different grade of PP with different molecular weight or structure, and AMPP with different MA content and composition can be informative,

3. One of the interesting method to achieve a highly dispersed TiO_2 throughout the PP matrix is in-situ synthesis of TiO_2 via sol-gel method during melt mixing that could be studied,

4. Improving electrical conductivity of the PP/TiO_2 nanocomposites by adding a conductive component to the system and making a hybrid composite material,

5. Systematic investigation on reducing the thickness of nanocomposite film as a photoelectrode layer,

6. Investigating bi-axial stretching, simultaneously or sequential, on final microstructure of the nanocomposite films,

7. To study on mechanical properties and durability of the porous nanocomposite film,

8. To develop the porous composite structure via electrospinning that could be combined with the in-situ synthesis of the TiO_2,

9. To examine functionality of the PP/TiO_2 nanocomposite film in DSSCs using plastic substrates.

REFERENCES

[1] P. Wufrel, *Physics of solar cells : from principles to new concepts*. Weinheim: Wiley-VCH, 2005.

[2] T. Soga, Ed., *Nanostructured Materials for Solar Energy Conversion*. Amsterdam: Elsevier, 2006, p.^pp. Pages.

[3] G. G. Wallace, *et al.*, "Nanoelectrodes: energy conversion and storage," *Materials Today*, vol. 12, pp. 20-27, 2009.

[4] "International Energy Outlook 2013," U.S. Energy Information Adminstration, Washington DOE/EIA-0484(2013), July 25, 2013 2013.

[5] *Solar Energy Source*. Available: http://www.energy.gov/energysources/solar.htm

[6] E. Serrano, *et al.*, "Nanotechnology for sustainable energy," *Renewable and Sustainable Energy Reviews*, vol. 13, pp. 2373-2384, 2009.

[7] A. C. Mayer, *et al.*, "Polymer-based solar cells," *Materials Today*, vol. 10, pp. 28-33, 2007.

[8] S. Gunes, *et al.*, "Conjugated Polymer-Based Organic Solar Cells," *Chemical Reviews*, vol. 107, pp. 1324-1338, 2007.

[9] A. Luque and S. Hegedus, Eds., *Handbook of Photovoltaic Science and Engineering*. Wiley, 2003, p.^pp. Pages.

[10] V. P. Singh, *et al.*, "Thin-Film Solar Cells Based on Nanostructured CdS, CIS, CdTe and Cu2S," in *Nanostructured Materials for Solar Energy Conversion*, T. Soga, Ed., ed Amsterdam: Elsevier, 2006.

[11] B. O'Regan and M. Gratzel, "A low-cost, high-efficiency solar cell based on dye-sensitized colloidal TiO2 films," *Nature*, vol. 353, pp. 737-740, 1991.

[12] G. D. Sharma, *et al.*, "Quasi solid state dye sensitized solar cells employing a polymer electrolyte and xanthene dyes," *Materials Science and Engineering: B*, vol. 162, pp. 32-39, 2009.

[13] M. Gratzel, "Solar Energy Conversion by Dye-Sensitized Photovoltaic Cells," *Inorganic Chemistry*, vol. 44, pp. 6841-6851, 2005.

[14] M. Grätzel, "Dye-sensitized solar cells," *Journal of Photochemistry and Photobiology C: Photochemistry Reviews*, vol. 4, pp. 145-153, 2003.

[15] M. Späth, *et al.*, "Reproducible manufacturing of dye-sensitized solar cells on a semi-automated baseline," *Progress in Photovoltaics: Research and Applications*, vol. 11, pp. 207-220, 2003.

[16] Y. Saito, *et al.*, "Morphology control of mesoporous TiO2 nanocrystalline films for performance of dye-sensitized solar cells," *Solar Energy Materials and Solar Cells*, vol. 83, pp. 1-13, 2004.

[17] K. Kalyanasundaram and M. Grätzel, "Applications of functionalized transition metal complexes in photonic and optoelectronic devices," *Coordination Chemistry Reviews,* vol. 177, pp. 347-414, 1998.

[18] *Titanium Technologies*. Available: http://www2.dupont.com/Titanium_Technologies/en_US/tech_info/literature/

[19] W. Xu, *et al.*, "New Triphenylamine-Based Dyes for Dye-Sensitized Solar Cells," *The Journal of Physical Chemistry C,* vol. 112, pp. 874-880, 2008.

[20] M. Gratzel, "Photoelectrochemical cells," *Nature,* vol. 414, pp. 338-344, 2001.

[21] N. G. Park, *et al.*, "Comparison of Dye-Sensitized Rutile- and Anatase-Based TiO2 Solar Cells," *The Journal of Physical Chemistry B,* vol. 104, pp. 8989-8994, 2000.

[22] D. Shi, *et al.*, "New Organic Sensitizer for Stable Dye-Sensitized Solar Cells with Solvent-Free Ionic Liquid Electrolytes," *The Journal of Physical Chemistry C,* vol. 112, pp. 17478-17485, 2008.

[23] H. Choi, *et al.*, "Highly Efficient and Thermally Stable Organic Sensitizers for Solvent-Free Dye-Sensitized Solar Cells," *Angewandte Chemie International Edition,* vol. 47, pp. 327-330, 2008.

[24] R. Vogel, *et al.*, "Quantum-Sized PbS, CdS, Ag2S, Sb2S3, and Bi2S3 Particles as Sensitizers for Various Nanoporous Wide-Bandgap Semiconductors," *The Journal of Physical Chemistry,* vol. 98, pp. 3183-3188, 2002.

[25] K. Hara, *et al.*, "A coumarin-derivative dye sensitized nanocrystalline TiO_2 solar cell having a high solar-energy conversion efficiency up to 5.6%," *Chemical Communications,* pp. 569-570, 2001.

[26] A. F. Nogueira, *et al.*, "Polymers in dye sensitized solar cells: overview and perspectives," *Coordination Chemistry Reviews,* vol. 248, pp. 1455-1468, 2004.

[27] F. Pichot, *et al.*, "Low-Temperature Sintering of TiO2 Colloids: Application to Flexible Dye-Sensitized Solar Cells," *Langmuir,* vol. 16, pp. 5626-5630, 2000.

[28] H. Lindström, *et al.*, "A new method for manufacturing nanostructured electrodes on glass substrates," *Solar Energy Materials and Solar Cells,* vol. 73, pp. 91-101, 2002.

[29] H. Lindstrom, *et al.*, "A New Method for Manufacturing Nanostructured Electrodes on Plastic Substrates," *Nano Letters,* vol. 1, pp. 97-100, 2001.

[30] H. Lindström, *et al.*, "A new method to make dye-sensitized nanocrystalline solar cells at room temperature," *Journal of Photochemistry and Photobiology A: Chemistry,* vol. 145, pp. 107-112, 2001.

[31] H. Kim, *et al.*, "Laser processing of nanocrystalline TiO_2 films for dye-sensitized solar cells," *Applied Physics Letters,* vol. 85, pp. 464-466, 2004.

[32] H. Kim, *et al.*, "Laser-sintered mesoporous TiO_2 electrodes for dye-sensitized solar cells," *Applied Physics A: Materials Science & Processing,* vol. 83, pp. 73-76, 2006.

[33] C. P. Drew, "Electrospinning of polymeric photovoltaic cells," M.S.Eng., Plastic Engineering, University of Massachusetts Lowell, Lowell, 2000.

[34] C. Drew, *et al.*, "ELECTROSPUN PHOTOVOLTAIC CELLS," *Journal of Macromolecular Science, Part A: Pure and Applied Chemistry,* vol. 39, pp. 1085 - 1094, 2002.

[35] C. Drew, *et al.*, "The Effect of Viscosity and Filler on Electrospun Fiber Morphology," *Journal of Macromolecular Science, Part A: Pure and Applied Chemistry,* vol. 40, pp. 1415 - 1422, 2003.

[36] Y. Li, *et al.*, "Highly bendable composite photoelectrode prepared from TiO_2/polymer blend for low temperature fabricated dye-sensitized solar cells," *Current Applied Physics,* vol. 10, pp. e171-e175, 2010.

[37] Y. Li, *et al.*, "Highly durable and flexible dye-sensitized solar cells fabricated on plastic substrates: PVDF-nanofiber-reinforced TiO2 photoelectrodes," *Energy & Environmental Science,* vol. 5, pp. 8950-8957, 2012.

[38] D. Yakisir, *et al.*, "Electronic Conductive Microporous Polymer-Based Structures," *Macromolecular Rapid Communications,* vol. 27, pp. 1596-1602, 2006.

[39] Y. Deyrail, *et al.*, "Polyamide/Polystyrene Blend Compatibilisation by Montmorillonite Nanoclay and its Effect on Macroporosity of Gas Diffusion Layers for Proton Exchange Membrane Fuel Cells," *Fuel Cells,* vol. 7, pp. 447-452, 2007.

[40] D. Yakisir, *et al.*, "Development of Porous Electrode Gas Diffusion Layers for Proton Exchange Membrane Fuel Cells," *Journal of Fuel Cell Science and Technology,* vol. 5, pp. 031008-9, 2008.

[41] Y. Deyrail, *et al.*, "Electrically conductive polymer-based blends for proton exchange membrane fuel cell gas diffusion layers," Honolulu, HI, United states, 2007, pp. 155-163.

[42] P. P. Kundu and S. Choe, "Transport of Moist Air Through Microporous Polyolefin Films," *Polymer Reviews,* vol. 43, pp. 143-186, 2003.

[43] S. Nago, *et al.*, "Structure of microporous polypropylene sheets containing CaCO3 filler," *Journal of Applied Polymer Science,* vol. 45, pp. 1527-1535, 1992.

[44] Y. Mizutani, *et al.*, "Microporous polypropylene sheets," *Industrial & Engineering Chemistry Research,* vol. 32, pp. 221-227, 1993.

[45] A. Z. Moss, "Microporous Polymeric Films and Process for Their Manufacture," 4,698,372, 1987.

[46] S. Nago and Y. Mizutani, "Microporous polypropylene sheets containing CaCO3 filler: Effects of stretching ratio and removing CaCO3 filler," *Journal of Applied Polymer Science,* vol. 68, pp. 1543-1553, 1998.

[47] Y. Mizutani and S. Nago, "Microporous polypropylene films containing ultrafine silica particles," *Journal of Applied Polymer Science,* vol. 72, pp. 1489-1494, 1999.

[48] S. Nago and Y. Mizutani, "Microporous polypropylene sheets containing polymethylsilsesquioxane filler," *Journal of Applied Polymer Science,* vol. 50, pp. 1815-1822, 1993.

[49] S. Nago, *et al.*, "Structure of Microporous Polypropylene Sheet," *J Electron Microsc (Tokyo),* vol. 41, pp. 107-112, April 1, 1992 1992.

[50] G.-J. Li, *et al.*, "Modification of TiO2 with titanate coupling agent and its impact on the crystallization behaviour of polybutylene terephthalate," *Iranian Polymer Journal (English Edition),* vol. 19, pp. 115-121, 2010.

[51] S. Wacharawichanant, *et al.*, "Effect of Mixing Conditions and Particle Sizes of Titanium Dioxide on Mechanical and Morphological Properties of Polypropylene/Titanium Dioxide Composites," *Iranian Polymer Journal,* vol. 18, pp. 607-616, 2009.

[52] M. Forhad Mina, *et al.*, "Improved performance of isotactic polypropylene/titanium dioxide composites: Effect of processing conditions and filler content," *Polymer Degradation and Stability,* vol. 94, pp. 183-188, 2009.

[53] A. Kubacka, *et al.*, "Boosting TiO2-anatase antimicrobial activity: Polymer-oxide thin films," *Applied Catalysis B: Environmental,* vol. 89, pp. 441-447, 2009.

[54] W. Li, *et al.*, "Study of PET/PP/TiO_2 microfibrillar-structured composites, Part 2: Morphology and mechanical properties," *Journal of Applied Polymer Science,* vol. 113, pp. 3300-3306, 2009.

[55] F. Bondioli, *et al.*, "High-density polyethylene reinforced with submicron titania particles," *Polymer Engineering & Science,* vol. 48, pp. 448-457, 2008.

[56] X. Zhu, *et al.*, "Synthesis and Non-isothermal Crystallization Behavior of PET/Surface-treated TiO2 Nanocomposites," *Journal of Macromolecular Science, Part B: Physics,* vol. 47, pp. 1117 - 1129, 2008.

[57] A. Laachachi, *et al.*, "The catalytic role of oxide in the thermooxidative degradation of poly(methyl methacrylate)-TiO2 nanocomposites," *Polymer Degradation and Stability,* vol. 93, pp. 1131-1137, 2008.

[58] M. L. Cerrada, *et al.*, "Self-Sterilized EVOH-TiO2 Nanocomposites: Interface Effects on Biocidal Properties," *Advanced Functional Materials,* vol. 18, pp. 1949-1960, 2008.

[59] R. Dangtungee and P. Supaphol, "Melt rheology and extrudate swell of titanium (IV) oxide nanoparticle-filled isotactic polypropylene: Effects of content and surface characteristics," *Polymer Testing,* vol. 27, pp. 951-956, 2008.

[60] P. A. Wheeler, *et al.*, "Polyhedral oligomeric silsesquioxane trisilanols as dispersants for titanium oxide nanopowder," *Journal of Applied Polymer Science,* vol. 108, pp. 2503-2508, 2008.

[61] L. V. Todorov and J. C. Viana, "Characterization of PET nanocomposites produced by different melt-based production methods," *Journal of Applied Polymer Science,* vol. 106, pp. 1659-1669, 2007.

[62] A. Kubacka, *et al.*, "High-Performance Dual-Action Polymer-TiO2 Nanocomposite Films via Melting Processing," *Nano Letters,* vol. 7, pp. 2529-2534, 2007.

[63] D. Acierno, *et al.*, "Rheological Aspects of PP-TiO2 Micro and Nanocomposites: A Preliminary Investigation," *Macromolecular Symposia,* vol. 247, pp. 59-66, 2007.

[64] A. Chandra, *et al.*, "Study of polystyrene/titanium dioxide nanocomposites via melt compounding for optical applications," *Polymer Composites,* vol. 28, pp. 241-250, 2007.

[65] C. Lei, *et al.*, "Time-dependent rheological behavior of low-density polyethylene white color masterbatches under dynamic stress field," *Journal of Applied Polymer Science,* vol. 85, pp. 2793-2799, 2002.

[66] Y.-J. Lee, *et al.*, "Dispersion of titanium dioxide agglomerates in viscous media," *Chemical Engineering Science,* vol. 48, pp. 3363-3372, 1993.

[67] Y.-J. Lee, *et al.*, "Analysis of titanium dioxide agglomerate dispersion in linear low density polyethylene and resulting properties of compounds," *Polymer Engineering & Science,* vol. 35, pp. 1037-1045, 1995.

[68] B. Ou, *et al.*, "Compatibilizing effect of maleated polypropylene on the mechanical properties of injection molded polypropylene/polyamide 6/functionalized-TiO2 nanocomposites," *Composites Science and Technology,* vol. 69, pp. 421-426, 2009.

[69] W. Li, *et al.*, "Study of PET/PP/TiO_2 microfibrillar-structured composites, part 1: Preparation, morphology, and dynamic mechanical analysis of fibrillized blends," *Journal of Applied Polymer Science,* vol. 113, pp. 1471-1479, 2009.

[70] W. Li, *et al.*, "Compatibilization effect of TiO_2 nanoparticles on the phase structure of PET/PP/TiO_2 nanocomposites," *Journal of Polymer Science Part B: Polymer Physics,* vol. 47, pp. 1616-1624, 2009.

[71] W. Li, *et al.*, "Effect of viscosity ratio on the morphology of PET microfibrils in uncompatibilized and compatibilized drawn PET/PP/TiO_2 blends," *Journal of Polymer Science Part B: Polymer Physics,* vol. 47, pp. 555-562, 2009.

[72] M. Wu, "Effects of dispersion on rheological properties of filled polypropylene," M.Sc.A., Chemical Engineering, Ecole Polytechnique, Montreal (Canada), 1999.

[73] A. Zohrevand, *et al.*, "Morphology and properties of highly filled iPP/TiO2 nanocomposites," *Polymer Engineering & Science,* p. doi: 10.1002/pen.23625, 2013.

[74] A. Zohrevand, "Relationship between rheological and electrical percolation in a polymer nanocomposite with semiconductor inclusions," *Rheologica Acta,* vol. in press, 2013.